University of Alberta

# First Observation of the Rare Decay $K^+ \to \pi^+\gamma\gamma$

by

Richard Andrew Soluk

©

A thesis submitted to the Faculty of Graduate Studies and Research in partial fulfillment of the requirements for the degree of Doctor of Philosophy.

Department of Physics

Edmonton, Alberta

Fall 1998

National Library of Canada
Acquisitions and Bibliographic Services
395 Wellington Street
Ottawa ON K1A 0N4
Canada

Bibliothèque nationale du Canada
Acquisitions et services bibliographiques
395, rue Wellington
Ottawa ON K1A 0N4
Canada

Your file Votre référence

Our file Notre référence

The author has granted a non-exclusive licence allowing the National Library of Canada to reproduce, loan, distribute or sell copies of this thesis in microform, paper or electronic formats.

L'auteur a accordé une licence non exclusive permettant à la Bibliothèque nationale du Canada de reproduire, prêter, distribuer ou vendre des copies de cette thèse sous la forme de microfiche/film, de reproduction sur papier ou sur format électronique.

The author retains ownership of the copyright in this thesis. Neither the thesis nor substantial extracts from it may be printed or otherwise reproduced without the author's permission.

L'auteur conserve la propriété du droit d'auteur qui protège cette thèse. Ni la thèse ni des extraits substantiels de celle-ci ne doivent être imprimés ou autrement reproduits sans son autorisation.

0-612-34838-5

Canada

**University of Alberta**

**Library Release Form**

**Name of Author: Richard Andrew Soluk**

**Title of Thesis: First Observation of the Rare Decay $K^+ \to \pi^+\gamma\gamma$**

**Degree: Doctor of Philosophy**

**Year this Degree Granted: 1998**

Permission is hereby granted to the University of Alberta to reproduce single copies of this thesis and to lend or sell such copies for private, scholarly, or scientific research purposes only.

The author reserves all other publication and other rights in association with the copyright in the thesis, and except as hereinbefore provided, neither the thesis nor any substantial portion thereof may be printed or otherwise reproduced in any material form whatever without the author's prior written permission.

3422 37 Street
Edmonton, Alberta
T6L 6L1

*September 29, 1998*

**University of Alberta**

**Faculty of Graduate Studies and Research**

The undersigned certify that they have read, and recommend to the Faculty of Graduate Studies and Research for acceptance, a thesis entitled **First Observation of the Rare Decay $K^+ \to \pi^+\gamma\gamma$** submitted by Richard Andrew Soluk in partial fulfillment of the requirements for the degree of Doctor of Philosophy.

Dr. Peter Kitching

Dr. Faqir C. Khanna

Dr. James L. Pinfold

Dr. Arthur Olin

Dr. D. Gingrich

Dr. M. deMontigny

Date: September 17, 1998

## Abstract

The first observation of the decay $K^+ \to \pi^+\gamma\gamma$ is reported. A total of 31 events are observed with an estimated background of 5.1±3.3 in the $\pi^+$ momentum range 100–180MeV/c. The partial branching ratio, $BR(K^+ \to \pi^+\gamma\gamma, 100 < P_{\pi^+} < 180\text{MeV/c})$, is $(5.8\pm1.5\pm0.6\pm0.6)\cdot10^{-7}$, where the errors are from statistics, experimental systematics and theoretical systematics respectively. The results are compared with the predictions of chiral perturbation theory. The construction of a low mass drift chamber is also discussed.

*To my parents, Helen and Tony, who always supported and encouraged me in my undergraduate and graduate pursuits even though they can't be here to see the completion of this thesis.*

## Acknowledgements

I would like to thank my supervisor, Dr. Peter Kitching, whose astonishing patience and support made this thesis possible. I would also like to thank Dr. Takashi Nakano without whose excellent work the observation of $K^+ \to \pi^+\gamma\gamma$ could never have been made. The hardware and software used to acquire and analyze the data in this experiment was the result of hundreds of man-years of labor by the members of the E787 collaboration making this, without question, a group effort.

The extremely painstaking construction of the UTC would have been impossible without TRIUMF technician Chapman Lim and his unsurpassed genius in inventing and building new tools. Finally I'd like to thank my friends and fellow students Vincent Kujala and Vighen Pacradouni, for their help in assembling and understanding the UTC, as well as Jean Roy for his insights into data analysis.

# Contents


**1 Introduction** **1**

**2 Theory** **2**
2.1 Quantum Electrodynamics(QED) . . . . . 2
2.2 Quantum Chromodynamics(QCD) . . . . . 8
2.3 Electroweak Theory . . . . . 11
2.4 Chiral Perturbation Theory . . . . . 16
2.5 The $K^+ \to \pi^+\gamma\gamma$ Branching Ratio Calculation . . . . . 21

**3 Detector Description** **30**
3.1 The Beamline . . . . . 30
3.2 Overview . . . . . 31
3.3 Beam Counters . . . . . 35
3.4 The Target . . . . . 38
3.5 Drift Chamber . . . . . 40
3.6 Range Stack . . . . . 44
3.7 Photon Vetoes . . . . . 47
3.8 Data Acquisition . . . . . 49
3.9 Ultra Thin Drift Chamber (UTC) . . . . . 51
3.9.1 Drift Chamber Principles . . . . . 52
3.9.2 Internal Design . . . . . 54
3.9.3 External Design . . . . . 57
3.9.4 Construction . . . . . 59
3.9.5 Electronics . . . . . 61
3.9.6 Calibration . . . . . 63
3.9.7 Performance . . . . . 65

**4 $K^+ \to \pi^+\gamma\gamma$ Event Selection** **66**
4.1 Introduction . . . . . 66
4.2 Online Event Selection . . . . . 69
4.2.1 Level 0 . . . . . 69
4.2.2 Level 1 . . . . . 70
4.2.3 Level 3 . . . . . 72
4.2.4 UMC . . . . . 74
4.3 Offline Event Selection . . . . . 79
4.3.1 PASS1 Analysis . . . . . 79
4.3.1.1 Event Reconstruction . . . . . 81
4.3.1.2 Photon Vetoes . . . . . 82

4.3.1.3 Charged Track Mass . . . . . 82
4.3.2 PASS2 Analysis . . . . . 84
4.3.2.1 Pion Momentum . . . . . 85
4.3.2.2 Photon Invariant Mass . . . . . 85
4.3.3 PASS3 Analysis . . . . . 86
4.3.3.1 Event Reconstruction . . . . . 86
4.3.3.2 Charged Track Mass . . . . . 88
4.3.3.3 Invariant Photon Mass . . . . . 89
4.3.3.4 Photon Vetoes . . . . . 89
4.3.3.5 Missing Momentum . . . . . 94
4.3.3.6 Opening Angle Cut . . . . . 96
4.3.3.7 $M_{\gamma\gamma}$ Mass Difference . . . . . 99
4.3.3.8 Overlapping Gamma Veto . . . . . 100
4.3.3.9 KINFIT $\chi^2$ Probability . . . . . 102
4.4 Event Selection Results . . . . . 104

**5 Background Estimation** **107**
5.1 Introduction . . . . . 107
5.2 Overlapping Gamma Background . . . . . 108
5.2.1 Method . . . . . 109
5.2.2 K$\pi$3 Background . . . . . 111
5.2.3 Radiative K$\pi$2 Background . . . . . 114
5.2.4 Cut point dependence . . . . . 115
5.2.5 PHICUT/ZCUT Correlations . . . . . 117
5.3 Non-Overlapping Gamma Background . . . . . 123
5.3.1 K$\mu$3 Background . . . . . 125
5.3.2 K$\pi$2 Background . . . . . 126
5.3.3 Radiative K$\pi$2 and K$\pi$3 Background . . . . . 128
5.3.4 Systematic error . . . . . 130
5.3.5 Background Shape . . . . . 132
5.4 Results . . . . . 132

**6 $K^+ \to \pi^+\gamma\gamma$ Acceptance** **133**
6.1 Acceptance of Online Trigger . . . . . 137
6.2 Acceptance of PASS1 Cuts . . . . . 144
6.2.1 Basic Event Reconstruction . . . . . 144
6.2.2 Stopping layer misidentification . . . . . 146
6.3 Acceptance of PASS2 Cuts . . . . . 147
6.4 Acceptance of PASS3 Cuts . . . . . 147
6.4.1 Basic Event Reconstruction . . . . . 147

6.4.2 PASS1/PASS3 Inconsistencies . . . . . 149
6.4.3 $M_{\gamma\gamma} > 200$MeV . . . . . 149
6.4.4 120 MeV < Pion mass < 165 MeV . . . . . 149
6.4.5 Photon Veto Cuts . . . . . 151
6.4.6 $M_{\gamma\gamma}$ Mass Difference . . . . . 152
6.4.7 Opening angle cut . . . . . 152
6.4.8 Overlapping Gamma Veto . . . . . 152
6.4.9 KINFIT $\chi^2$ probability . . . . . 153
6.5 Final Acceptance . . . . . 153

**7 Branching Ratio** **156**
7.1 Kaon Flux (K$\mu$2 Branching Ratio) . . . . . 156
7.2 $K\pi 2$ Branching Ratio . . . . . 159
7.3 $K^+ \to \pi^+\gamma\gamma$ Branching Ratio . . . . . 163

**8 Conclusion** **173**

**References** **175**

## List of Tables


1 The Known Fundamental Subatomic Particles . . . . . 2
2 The Eightfold Way octet of spin zero mesons. . . . . 19
3 Chamber parameters . . . . . 62
4 Potential Background Decay Modes for $\pi\gamma\gamma(2)$ . . . . . 68
5 Online Level 3 Parameters . . . . . 74
6 UMC Level 1 BV Energy Thresholds . . . . . 77
7 PASS1 Intime Parameters . . . . . 82
8 Rejection of PASS1 cuts . . . . . 85
9 Rejection of PASS2 cuts . . . . . 86
10 Photon Veto Intime Parameters . . . . . 94
11 KINFIT Variables . . . . . 103
12 Rejection of PASS3 cuts . . . . . 106
13 Signal and background estimates for various PHICUT and ZCUT cut points. . . . . 115
14 UMC $\pi\gamma\gamma$ acceptance . . . . . 118
15 Overlapping Gamma Veto Cut Rejection for UMC K$\pi$3 data. 120
16 Overlapping Gamma Veto Rejection for UMC radiative K$\pi$2 - data. . . . . 120
17 Overlapping gamma veto rejection for UMC radiative K$\pi$2 data with $P_{\pi^+} > 133$MeV/c. . . . . 121
18 Break-down of the events before overlapping gamma veto cuts are applied. . . . . 123
19 Estimated number of overlapping gamma backgrounds from the UMC study. . . . . 123
20 Acceptances Measured Using K$\mu$3 Data . . . . . 134
21 Acceptances Measured Using Level 3 Fail Pions . . . . . 137
22 Acceptances Measured Using K$\pi$2(2) Data . . . . . 139
23 Acceptances Measured Using K$\mu$2 Data . . . . . 140
24 $\pi\gamma\gamma(2)$ Spectrum Shape Normalized To All K$_l$*ive* . . . . . 142
25 $\pi\gamma\gamma(2)$ Level 0 Acceptance Values ($\cdot 10^{-2}$) . . . . . 143
26 $\pi\gamma\gamma(2)$ Online Acceptance Values (From UMC) . . . . . 143
27 Online Delayed Coincidence From K$\mu$2 Data . . . . . 144
28 $\pi\gamma\gamma(2)$ PASS1 Event Reconstruction Acceptance Values (Momentum Dependent) . . . . . 146
29 $\pi^+$ Mass Cut Acceptance Values . . . . . 149
30 Decay in Flight and Nuclear Interaction Acceptance Correction Using UMC $\check{C}$=0 Data. . . . . 151
31 $\pi\gamma\gamma(2)$ Miscellaneous Acceptance Values . . . . . 154

32 $\pi\gamma\gamma(2)$ PASS3 Acceptance Values (Momentum Dependent) . 154
33 $\pi\gamma\gamma(2)$ PASS3 Acceptance Values (Momentum Dependent) cont. . . . . 155
34 Total $\pi\gamma\gamma(2)$ Acceptance . . . . . 155
35 Online $K_t$*live* Scalers . . . . . 156
36 $K\mu 2$ Branching Ratio . . . . . 157
37 $K\mu 2$ Branching Ratio Acceptance . . . . . 158
38 $K\pi 2$ Branching Ratio Acceptance . . . . . 160
39 $K\pi 2$ Branching Ratio . . . . . 162
40 $\pi\gamma\gamma(2)$ Branching Ratios (statistical errors only) . . . . . 167
41 Fraction of $K_t$*live* With $100< P_{\pi^+} <180$MeV/c . . . . . 168
42 Background Distributions Used in the Maximum Likelihood Test . . . . . 169
43 $\pi\gamma\gamma(2)$ Final Branching Ratios Including Systematic Errors . 171
44 $\hat{c}$ values from the maximum likelihood analysis for both background shapes with and without systematic background errors. . . . . 172

## List of Figures


1 A tree level Feynman graph showing exchange of a virtual photon between two fermions and the same graph with a virtual loop on the photon line. . . . . 6
2 Gluon self interaction diagrams. . . . . 10
3 Nuclear beta decay in terms of nucleons. . . . . 11
4 Nuclear beta decay in the Fermi theory. . . . . 11
5 Fermi theory diagrams for muon decay, nuclear beta decay and $\Lambda$ beta decay. . . . . 13
6 Quark masses on a logarithmic scale, widths indicate uncertainties in the values. . . . . 18
7 Examples of loop diagrams contributing at $O(p^4)$ to $K^+ \to \pi^+\gamma\gamma$ . 24
8 The anomalous diagram contributing at $O(p^4)$ to $K^+ \to \pi^+\gamma\gamma$ . 25
9 Normalized $O(p^4)$ chiral perturbation theory predictions for the invariant photon mass distribution in $K^+ \to \pi^+\gamma\gamma$ for $\hat{c} = 0$ (solid line), $\hat{c} = 4$ (dashed line), $\hat{c} = -4$ (dotted line) and a phase space distribution (dash-dot line). . . . . 26
10 $K^+ \to \pi^+\gamma\gamma$ branching ratio prediction as a function of $\hat{c}$ at $O(p^4)$ (dashed line) and including the $O(p^6)$ unitarity correction (solid line). . . . . 27
11 $K^+ \to \pi^+\gamma\gamma$ invariant photon mass spectrum at $\hat{c} = 0$ calculated to $O(p^4)$ (dashed line) and with the inclusion of the $O(p^6)$ unitarity correction (solid line). . . . . 28
12 A schematic of the LESB 1 beamline used by E787 from 1988-1991. . . . . 30
13 Cross sectional schematic side view of the E787 detector. . . 32
14 Schematic end view of the E787 detector showing the active elements in the center plane (z=0) of the apparatus. . . . . 33
15 Isometric view of the E787 detector with the magnet sections separated. . . . . 34
16 Detailed section of figure 13 showing the beam counters. Note that the B3 counters were removed for the 1991 run. . . . . 36
17 Schematic showing the design of the Cherenkov counter and a typical light path for both pion and kaon Cherenkov light. 36
18 The layout of the beam proportional chamber . . . . . 37
19 The typical effect of kaons, pions or high energy photons on the lead glass Cherenkov counter . . . . . 38

20 Cross section of the scintillating fiber target . . . . . 39
21 A typical $K^+ \to \pi^+$ decay in the target showing ADC (top) and TDC (bottom) information. . . . . 41
22 Cross section of the drift chamber showing the 5 layers of drift cells and a typical charged track including the two possible locations each single wire hit could correspond to (crosses and squares). . . . . 42
23 View of a single drift chamber cell. . . . . 43
24 Design of a single range stack (and two barrel veto) sectors. 45
25 An example of the TD pulse shapes from either end of the $\pi^+$ stopping counter (top) and the RS counter one layer in from the stopping counter which the $\pi^+$ passed through before decaying (bottom). . . . . 46
26 The construction of one end cap module. . . . . 48
27 Schematic of the UTC showing the inside of the outer superlayer. . . . . 55
28 Schematic side view of the downstream end of the UTC and a portion of the wire layout. . . . . 58
29 Total momentum resolutions for K$\mu$2 and K$\pi$2 found using the UTC and including target energy. . . . . 65
30 The charged particle momentum spectrum of the six most probable kaon decay modes excluding Ke3 and including $\pi\nu\bar{\nu}$. 67
31 K$\pi$2 photon energy and invariant mass using a BV visible fraction of 0.308. . . . . 70
32 Total BV energy within $\pm$6.3ns of prompt for real $\pi\gamma\gamma$(2) level 0 data and UMC level 0 K$\mu$3 data. (Distribution normalized to unit height). . . . . 71
33 $Z$ distribution versus real photon energy for the most energetic and second most energetic photon clusters in the BV. . 71
34 UMC-generated photon opening angle and gap count for various triggers. . . . . 73
35 Sum of raw ADC counts over the entire BV based on level 0 monitor data. . . . . 75
36 K$\pi$2 photon energy and invariant mass from UMC data. . . 76
37 Raw ADC spectrum averaged over all sectors for the upstream and downstream end of the BV in $\pi\gamma\gamma$(2) data passing level 1. 77
38 $Z$ distribution versus photon energy for the highest and second highest energy photon clusters in the BV from UMC data. 78

39 Difference in frequency of level 3 return codes expressed as a percentage of total number of events for online or offline BV ADC banks compared to actual online return codes. . . . . 78
40 Level 3 BV energy and $M_{\gamma\gamma}$ found using the new ADC banks minus those found using the online calibrated ADC banks. . 79
41 Level 3 BV energy and $M_{\gamma\gamma}$ for K$\pi$2 events calculated using the new ADC banks and using the online calibrated ADC banks. . . . . 80
42 Typical INTIME energy/time distributions for raw $\pi\gamma\gamma(2)$ - data . . . . . 83
43 INTIME time distribution for events above 4MeV visible energy. The fit is to the equation $y = p_4 + p_1 e^{-(x-p_2)^2/2p_3^2}$ . . . 83
44 Charged track mass for A and B layer stops in $\pi\gamma\gamma(2)$ after EC and RS photon vetoes. . . . . 84
45 Total charged track momentum for events surviving PASS1. 86
46 Invariant photon mass after PASS1 and total momentum cut. 87
47 $\Delta E_{IC}$ energy difference for all PASS2 data and PASS2 pions selected using TD cuts. . . . . 88
48 $\Delta E_{TG}$ energy difference for all PASS2 data and PASS2 pions selected using TD cuts. . . . . 89
49 Mass vs RS energy for pions selected from PASS2 data using TD cuts, before and after the RS energy correction. . . . . 90
50 INTIME energy in the I-counter and veto counter. . . . . 91
51 INTIME energy in the endcap and range stack (the corresponding PASS1 photon veto cuts have not been applied). . 92
52 INTIME energy in the barrel veto (excluding the energy from the two highest energy prompt photon clusters). . . . . 93
53 Timing of excess BV energy at two different portions of the run. . . . . 93
54 Excess energy in the target relative to target pion time. . . . 94
55 Time of Pb glass hits versus delayed coincidence time. . . . 95
56 Time of Pb glass hits for 3 or more PMT's. . . . . 95
57 K$\mu$3 neutrino momentum after passing the level 1 trigger (UMC data). . . . . 96
58 Kaon momentum of $\pi\gamma\gamma(2)$ level 0 data selected using TGTRACK, $M_{\gamma\gamma}$ and TD cuts to contain a K$\pi$2 in which the $\pi^+$ had scattered in the target before stopping in the RS. . . 97

59 Missing kaon momentum in real $\pi\gamma\gamma(2)$ data (left) and UMC $\pi\gamma\gamma(2)$ data (right) after PASS1, photon veto, $P_{\pi^+}$ and $M_{\gamma\gamma}$ cuts. The solid vertical line in the left figure shows the missing momentum cut position at 86.6MeV/c. . . . . 97
60 Missing kaon momentum in $\pi\gamma\gamma(2)$ events selected to contain either muons or pions. . . . . 98
61 The $\cos(\theta_{\pi\gamma_1})$ distribution of $\pi^+\gamma\gamma$ events (generated using UMC), and the photon energy of the lower energy photon versus $\cos(\theta_{\pi\gamma_1})$. . . . . 99
62 The $\cos(\theta_{\pi\gamma_1})$ distribution for radiative K$\pi$2 events (events generated by UMC and selected using KINFIT). . . . . 100
63 The number of hit BV elements in UMC generated $\pi\gamma\gamma(2)$ - data. . . . . 101
64 $\phi_g^2$ distribution for the high (left) and low (right) energy photon. UMC was used to determine the photon energy distribution then the variables used in $\phi_g^2$ were taken from real K$\pi$2 data with photons of the same energy. The peak at low $\phi_g^2$ corresponds to photons for which all BV hits belong to one sector. . . . . 102
65 $z_{max}$ distribution for the high (left) and low (right) energy photon. UMC was used to determine the $\pi\gamma\gamma(2)$ photon energy distribution then the variables used in $z_{max}$ were taken from real K$\pi$2 data with photons of the same energy. . . . . 103
66 KINFIT stretch functions. Distributions for $\pi^+$ energy and $\pi^+$ momentum were obtained from overlapping photon events all others were from $K\pi2$ data. . . . . 105
67 The KINFIT probability for $K\pi2$ data. . . . . 107
68 KINFIT probability distribution of events which passed all cuts except for PHICUT and ZCUT. . . . . 108
69 $\pi^+$ momentum (left) and photon invariant mass (right) distributions for the events which passed all cuts except for PHICUT and ZCUT. $K\pi3$ background dominates in the region of $P_{\pi^+} < 133MeV/c$, or equivalently, in the region of $M_{\gamma\gamma} > 270MeV/c^2$. . . . . 109
70 $z_{max}$(cluster 1) vs $z_{max}$(cluster 2) for events below (left) and above (right) the $K\pi3$ threshold (133MeV/c). Events with two overlapping photons dominate below the K$\pi$3 threshold while events with a single overlapping photon dominate above the threshold. . . . . 110

71 $z_{max}$(cluster 1) vs $z_{max}$(cluster 2) for the events below the K$\pi$3 threshold which either failed (top left) or passed (top right) PHICUT. The bottom plot shows the distribution for UMC generated $K^+ \to \pi^+\gamma\gamma$ . . . . . 113
72 $\phi_g^2$(cluster 1) vs $\phi_g^2$(cluster 2) for the events above the K$\pi$3 - threshold which failed (top left) or passed (top right) ZCUT. The bottom plot shows the distribution for UMC generated $K^+ \to \pi^+\gamma\gamma$ . . . . . 116
73 The difference between the ADC and TDC based $z$ measurements in the BV ($z_{ADC} - z_{TDC}$) as a function of photon energy for real data (left) and UMC data (right). . . . . 118
74 The energy distribution of the 4th photon cluster in PASS2 data (top left) and UMC generated K$\pi$3 data (top right) and the total number of hit BV elements in real data below the K$\pi$3 threshold which failed PHICUT (bottom left) and UMC-generated K$\pi$3 (bottom right). . . . . 119
75 The real (top left) and UMC (top right) $z_{max}$ distributions for the K$\pi$3 photon cluster that had failed PHICUT. The bottom graphs show $\phi_g^2$ for a similar cluster which had failed ZCUT. 122
76 The cos($\theta_{\pi X}$)(left) and charged particle mass(right) distributions for events which had $M_{\pi^+} < 120$MeV and cos($\theta_{\pi X}$) $>$ -0.9 but passed all other Set-II cuts. . . . . 126
77 The charged particle mass distribution of events which passed all Set-II cuts except for a reversed cos($\theta_{\pi X}$) cut. . . . . 127
78 The cos($\theta_{\pi X}$) distribution of events with $M_{\pi^+} > 165$MeV and cos($\theta_{\pi X}$) $> -0.9$ which passed all other Set-II cuts. . . . . 128
79 The reconstructed charged particle mass distribution of events which passed all Set-II cuts with the photon veto removed and a reversed cos($\theta_{\pi X}$) cut. . . . . 129
80 cos($\theta_{\pi X}$) for events with $P_{\pi^+} > 133 MeV/c$, which have passed the TD cuts and all set-II cuts except for cos($\theta_{\pi X}$). Photon veto cuts were not applied. . . . . 129
81 cos($\theta_{\pi X}$) for events which passed all the set-II cuts including the $\pi^+$ mass cut (top left), with the added requirement $P_{\pi^+} >$ 133MeV/c (top right) and with the overlapping photon cuts removed (bottom). . . . . 131
82 The $\pi^+$ momentum of the non-overlapping gamma background (left) and two photon invariant mass calculated using the $\pi^+$ momentum (right). All Set-II cuts were applied except that for the cos($\theta_{\pi X}$) cut which was reversed. . . . . 132

83 Raw DC momentum in $\pi\gamma\gamma(2)$ level 0 data . . . . . 133
84 Offline level 3 based invariant photon mass in $\pi\gamma\gamma(2)$ level 0 data . . . . . 134
85 Charged track mass in K$\mu$3 decays selected from $\pi\gamma\gamma(2)$ level 0 data . . . . . 135
86 Charged track mass in level 3-fail pion sample. . . . . 136
87 Charged track mass in K$\pi$3 sample. . . . . 136
88 Total pion momentum and invariant photon mass (from GAMMAS) of the K$\pi$2(2) data sample . . . . . 138
89 Charged track momentum and mass for the K$\mu$2 sample. . . 138
90 Range stack energy versus DC momentum in $\pi\gamma\gamma(2)$ level 0 data . . . . . 145
91 Fraction failing TG-energy-difference cut as a function of TG energy (from range) for K$\pi$2(2) data and a typical UMC $\pi\gamma\gamma(2)$ TG energy distribution. . . . . 148
92 Pion decay time for PASS1 pion sample. . . . . 150
93 Acceptance of the pion mass cut vs charged track momentum for PASS1 pions. . . . . 150
94 The KINFIT probability distribution before (left) and after (right) the pion mass cut and the $M_{\gamma\gamma}$ mass difference cut. 154
95 Probability of kinematic fit for K$\pi$2(2) events after all K$\pi$2 cuts up to KINFIT. . . . . 161
96 The measured total $\pi^+$ momentum of the final event sample (solid line) and the $\hat{c}$ independent portion of the acceptance. The background (not shown) was 0.6±1.0 events per bin assuming a flat background. . . . . 163
97 The theoretical $\pi^+$ momentum distribution for various values of $\hat{c}$. . . . . 164
98 The $\pi\gamma\gamma(2)$ partial branching ratio as a function of $\hat{c}$. Only statistical errors are shown. . . . . 165
99 The KINFIT-returned invariant photon mass of the final event sample. . . . . 165
100 The KINFIT-returned invariant photon mass of UMC events using various $\hat{c}$-hat values. . . . . 166
101 $\ln\mathcal{L}$ vs $\hat{c}$ for flat or K$\pi$3-like background shapes with and without systematic error in the background estimate. . . . . 170

# 1 Introduction

Brookhaven National Labs experiment E787 officially began in 1986 as a collaboration between the University of Alberta, Princeton University, the TRi-University Meson Facility (TRIUMF) in Vancouver, Canada, and Brookhaven National Labs on Long Island, New York. The experiment became operational in 1988 and has since added KEK in Tsukuba, Japan and Osaka University to its list of collaborators.

The experiment was designed to search for the rare decay $K^+ \to \pi^+ \nu\bar{\nu}$ expected to occur with a decay probability (branching ratio) of about $10^{-10}$. However, from the beginning it was known that the same detector could be used to search for other rare kaon decays. This thesis primarily discusses the search Dr. Takashi Nakano and I undertook for the decay $K^+ \to \pi^+\gamma\gamma$, where a kaon decays directly into a pion and two photons. In the following sections I was primarily responsible for the acceptance measurements and the comparison of the final results with theory, while Dr. Nakano performed the background estimations and some of the cut tuning. Also discussed in this thesis is the construction of a new, state-of-the-art, drift chamber, which I was extensively involved with, that was installed in 1993 as part of a series of major upgrades to the E787 detector.

The decay $K^+ \to \pi^+\gamma\gamma$ had not been observed before the analysis outlined below. The previous upper limit for the branching ratio was $< 10^{-6}$ established using E787 data taken in 1989[1]. However, this limit was set by examining only the narrow portion of the possible $\pi^+$ momentum spectrum above 215 MeV/c, and assuming that the shape of the $\pi^+$ momentum spectrum was determined by simple phase space constraints. Calculations done using chiral perturbation theory, which is the leading phenomenological model used to perform calculations at energies below 1 GeV, where QCD cannot be treated perturbatively, suggested that the actual $\pi^+$ momentum spectrum was peaked at low momentum and very different from the phase space distribution. Using the chiral perturbation theory spectrum, the limit on $K^+ \to \pi^+\gamma\gamma$ from the previous E787 analysis and earlier experiments[2] was only $< 10^{-4}$, far from the predicted branching ratio of $> 4 \cdot 10^{-7}$. $K^+ \to \pi^+\gamma\gamma$ also has the feature that under chiral perturbation theory the tree level, $O(p^2)$, contribution is zero. Thus a search for $K^+ \to \pi^+\gamma\gamma$ in the momentum range below 200 MeV/c provided not only an opportunity to examine a poorly investigated portion of the decay spectrum, and a general test of chiral perturbation theory, but also a much more stringent second order test of that theory.

# 2 Theory

There are four known fundamental forces that govern the interaction between subatomic particles. In order of increasing strength these are the gravitational force, responsible for the large scale structure of the universe, the weak force, involved in solar fusion and radioactive decays, electromagnetism, which controls chemical interactions, and the strong force, which binds together atomic nuclei. On the scale of individual particles the gravitational force is so weak that it can be ignored and it is not generally considered in particle physics. The description of the other three forces constitute what is referred to as the 'standard model' of particle physics. The spin 1/2 fermions are considered to be the fundamental particles with the forces acting between them through the exchange of spin 1 vector bosons (table 1). The Higgs boson is a special case and will be mentioned later. The electromagnetic force was the first to be described theoretically and provided the mathematical template that was later used for the weak and strong forces.

Table 1: The Known Fundamental Subatomic Particles

| Fermions (leptons) | | |
|---|---|---|
| $e^{\pm}$ | $\mu^{\pm}$ | $\tau^{\pm}$ |
| $\nu_e$ | $\nu_\mu$ | $\nu_\tau$ |
| **Fermions (quarks)** | | |
| $u_i^{+2/3}$ | $c_i^{+2/3}$ | $t_i^{+2/3}$ |
| $d_i^{-1/3}$ | $s_i^{-1/3}$ | $b_i^{-1/3}$ |
| **Bosons** | | |
| Force | Carrier | |
| Electromagnetic | $\gamma$ | |
| Weak | $W^{\pm}, Z^0$ | |
| Strong | $g_j^i$ | |
| $i, j$ = red, green or blue | | |

## 2.1 Quantum Electrodynamics(QED)

Three elements stand out as being essential to theoretical particle physics; symmetries obeyed by the field equations and their implications, the Heisenberg uncertainty principle which implies the existence of virtual particles and the concept of renormalization which is needed to obtain finite mathematical

solutions.

The conservation laws obeyed by a theory can be determined by the symmetries inherent in the description of the theory. Define the Lagrangian density $\mathcal{L}$ by $L = \int d^3\vec{x}\mathcal{L}$ and assume it is of the form $\mathcal{L} = \mathcal{L}(\phi^a, \partial_\mu\phi^a)$, for some fields $\phi^a$. A transformation $\phi^a(x) \rightarrow \phi^a(x,\lambda)$ will be a symmetry if it leaves the Lagrangian intact or changes it at most by a total derivative $d\mathcal{L}/d\lambda \mid_{\lambda=0} = \partial_\mu F^\mu$ for some $F^\mu(\phi^a, \partial_\mu\phi^a)$ which vanishes on the boundary of whatever physical space we are dealing with, typically this means at infinity. This last requirement on $F$ insures that the action $S = \int d^4x\mathcal{L}$ is unchanged. By Noether's theorem[3] there will be a conserved quantity, $J^\mu$, associated with the transformation $\lambda$ given by $J^\mu = (\partial\mathcal{L}/\partial(\partial_\mu\phi^a))(d\phi^a/d\lambda) \mid_{\lambda=0} -F_\mu$. For instance the Lagrangian associated with the Dirac equation, $\mathcal{L} = \bar{\psi}(i\gamma^\mu\partial_\mu - m)\psi$, which applies to free spin 1/2 particles of mass m, is invariant under the global phase change $\psi \rightarrow e^{-i\lambda}\psi$. Noether's theorem gives $J^\mu = \bar{\psi}\gamma^\mu\psi$ which, using the Euler-Lagrange equations of motion from $\mathcal{L}$, can be shown to satisfy $\partial_\mu J^\mu = 0$ and is therefore conserved.

Modifying the Lagrangian so that it contains additional symmetries, which were not present in the basic $\mathcal{L}$, can give dynamical information about the theory. In particular, extending the global phase invariance in the Dirac equation to a local phase invariance, implies the existence of the photon and yields the QED Lagrangian. A local phase transformation is given by $\psi \rightarrow \psi' = e^{-i\lambda(x)}\psi$ where $\lambda$ is now a real function of $x$ rather than a constant and so is distinct at each point in space time. Consider the infinitesimal form of the transformation, $\delta\lambda(x)$ and Taylor expand $\psi'$.

$$\begin{aligned}
\psi' &\simeq (1 - i\delta\lambda)\psi \\
\bar{\psi}' &\simeq \bar{\psi}(1 + i\delta\lambda) \\
\mathcal{L}' &= \bar{\psi}'(i\gamma^\mu\partial_\mu - m)\psi' \\
&\simeq \mathcal{L} + \bar{\psi}i\delta\lambda(i\gamma^\mu\partial_\mu - m)\psi - \bar{\psi}(i\gamma^\mu\partial_\mu - m)i\delta\lambda\psi \\
\delta\mathcal{L} &= \mathcal{L}' - \mathcal{L} \simeq \bar{\psi}(\gamma^\mu(\partial_\mu\delta\lambda))\psi
\end{aligned}$$

This last term $\bar{\psi}(\gamma^\mu(\partial_\mu\delta\lambda))\psi$ must be eliminated if we are to have local phase invariance. This can be done by introducing a new 'gauge' field, $A_\mu(x)$, with properties specifically chosen to make $\delta\mathcal{L} = 0$. Define the covariant derivative to be $D_\mu = \partial_\mu + ieA_\mu$ and replace the partial derivative in the Dirac equation

with this covariant derivative [1].

$$\begin{aligned}\mathcal{L} &\rightarrow \bar{\psi}(i\gamma^\mu D_\mu - m)\psi \\ &= \bar{\psi}(i\gamma^\mu \partial_\mu - e\gamma^\mu A_\mu - m)\psi \\ \delta\mathcal{L} &= \bar{\psi}(\gamma^\mu(\partial_\mu \delta\lambda))\psi - \bar{\psi}e\gamma^\mu \delta A_\mu \psi\end{aligned}$$

$A_\mu$ is defined such that $\delta A_\mu = e^{-1}\partial_\mu \delta\lambda$ therefore $\delta\mathcal{L} = 0$. The new Lagrangian can also be written as $\mathcal{L} \equiv \mathcal{L}_D + \mathcal{L}_i$, where $\mathcal{L}_D$ is the normal Dirac Lagrangian and $\mathcal{L}_i = -e\bar{\psi}\gamma^\mu A_\mu \psi = -eJ^\mu A_\mu$ is an interaction term coupling the new field, with interaction strength e, to the conserved fermion current found earlier using Noether's theorem on the Dirac equation. If this $A_\mu$ is to represent a physical particle then the Lagrangian describing its free behavior should be Lorentz invariant and quadratic in $A$. Imposing simple physical requirements it can be shown[3] that $\mathcal{L}_A = -(\frac{1}{4}F_{\mu\nu}F^{\mu\nu} - \frac{\mu^2}{2}A_\mu A^\mu)$ where $F_{\mu\nu} = \partial_\mu A_\nu - \partial_\nu A_\mu$.

To make our original Lagrangian complete we must now add this free space Lagrangian for the field $A$. We therefore have $\mathcal{L} = \mathcal{L}_D + \mathcal{L}_A + \mathcal{L}_i$. Solving for the Euler-Lagrange equation for $A$ we obtain;

$$\begin{aligned}0 &= \partial_\mu \frac{\partial\mathcal{L}}{\partial(\partial_\mu A_\nu)} - \frac{\partial\mathcal{L}}{\partial A_\nu} \\ &= \partial_\mu \frac{\partial(\frac{-1}{4}F_{\mu\nu}F^{\mu\nu})}{\partial(\partial_\mu A_\nu)} + e\bar{\psi}\gamma^\nu\psi - \mu^2 A^\nu \\ &= \partial_\mu F^{\mu\nu} - e\bar{\psi}\gamma^\nu\psi + \mu^2 A^\nu \\ &= \partial_\mu F^{\mu\nu} - eJ^\nu + \mu^2 A^\nu \qquad (1)\end{aligned}$$

Referring to electromagnetism the electromagnetic tensor, $F^{\mu\nu}$, breaks down into $F^{i0} = E^i$, $F^{ij} = -\epsilon^{ijk}B^k$, where Greek indices run from 0–4, Roman indices run from 1–3 and $E, B$ are the electric and magnetic fields respectively. If we make our gauge field massless by setting $\mu = 0$ and identify $eJ^\nu$ as the current then equation 1 reduces to $\partial_\mu F^{\mu\nu} = eJ^\nu$ which is just the tensor form of Maxwell's equations. The quantum electrodynamic Lagrangian is therefore:

$$\mathcal{L}_{\text{QED}} = \frac{-1}{4}F_{\mu\nu}F^{\mu\nu} + \bar{\psi}(i\gamma^\mu\partial_\mu - m)\psi - e\bar{\psi}\gamma^\mu A_\mu\psi \qquad (2)$$

[1] Adding $A$ in this way is known as minimal coupling[3]. There are more complicated terms in $A$ that could be used and still give the correct local phase invariance but they result in theories that are not renormalizable

The requirement of local phase invariance adds the photon to the free Dirac equation and provides an interaction term between photons and fermions which also allows fermions to interact with one another through the exchange of photons. A lot of the nomenclature of particle physics results from this connection of QED with electromagnetism. The conserved quantities found by Noether's theorem are referred to as 'currents', the new fields resulting from imposing local phase invariance are referred to as 'gauge' fields and theories of this type are known as 'gauge' theories. This terminology is carried forward into both the weak and strong sectors.

First, however, there were problems with getting numerical results out of QED which had to be solved. The Heisenberg uncertainty principle states that $\Delta E \Delta t \geq \hbar$, this implies that interactions can occur which violate energy-momentum conservation as long as their duration is sufficiently short. The result is that in every calculation, even for a single free particle, must include an infinite number of virtual particles and interactions because everything possible can and will happen within the limits of the uncertainty principle. These virtual particles are not directly observable but do have an effect on the theoretically determined values. Formally a calculation is done using the scattering matrix, $S$, which relates the incident state before the interaction, $|i(t_i)>_{\text{in}}$, to the final state after the interaction,$|f(t_f)>_{\text{out}}$ with $S_{fi} = {}_{\text{out}}< f(t_f)|i(t_i)>_{\text{in}}$. In terms of the interaction time development operator, which describes how the states are related at different times we can write[3];

$$\begin{aligned} S_{fi} &= \lim_{t_i, t_f \to \mp\infty} < f(0)|u_I(t_f, t_i)|i(0) > \\ &\equiv < f(0)|\hat{S}_{fi}|i(0) > \end{aligned}$$

In practice a new quantity called the invariant amplitude is defined by, $A$, $<f|\hat{S}-1|i> \equiv (2\pi)^4 \delta^4(\sum p_f - \sum p_i) iA$. The delta function ensures overall energy-momentum conservation and $\hat{S} - 1$ is used because we are generally not interested in elastic scattering where the incident and outgoing states are identical. The invariant amplitude can be found, using a perturbation theory expansion in powers of the interaction coupling constant, with the help of Feynman diagrams which are a graphical means of keeping track of the terms in the perturbation expansion. For example figure 1 shows the simplest, or tree level, interaction of two fermions by the exchange of a single photon. However, the fermion lines or photon line can have additional interactions involving virtual particles as seen in figure 1. Each additional virtual particle results in more interaction vertices and therefore a higher overall power of the coupling, $e$, for the diagram. The laborious task of setting up the amplitude

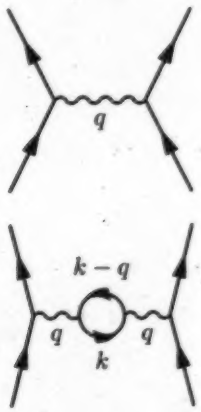


Figure 1: A tree level Feynman graph showing exchange of a virtual photon between two fermions and the same graph with a virtual loop on the photon line.

equations for each diagram has been turned into a formal process known as the Feynman rules. The rules essentially consist of inserting wave functions for each external line, which represent real particles, propagator terms for each internal line which are the free-particle Green's functions solutions (for example for fermions the Green's function, $G$, must satisfy $(i\gamma^\mu \partial x'_\mu - m)G(x', x) = \delta^4(x' - x)$), and appropriate interaction terms between them for each vertex where lines meet and therefore an interaction must occur. For simplicity calculations are normally done in momentum space. The fermion propagator[3] is then $(\gamma_\mu k^\mu - m + i\epsilon)^{-1} \equiv S_F(k)$ and the photon propagator[3] is $-g_{\mu\nu}/(q^2 + i\epsilon) \equiv D_F(q)_{\mu\nu}$, for fermions of momentum $k$ and photons of momentum $q$. The $i\epsilon$ terms are present to deal with the singularities at $q^2 = 0$ and $\gamma_\mu k^\mu - m = 0$ and it is understood that $\epsilon$ should be taken to zero at the end of the calculations.

At this point a number of complications start to arise. The mass and coupling constants that appear in equation 2 are the 'bare' values, often written as $e_0, m_0$, and do not include all of the virtual interactions that even an isolated free particle will undergo. To get out meaningful results, and make sure that the non-interacting Lagrangian, $\mathcal{L}_0$, is consistent with real measurements, the theory must be modified so that the true values appear rather than the bare quantities. Even worse, when evaluating virtual loops as shown in the second diagram of figure 1, the momentum, $k$, of the virtual

fermions is not bounded and integrals of the following form appear[2];

$$\int_0^\infty d^4k \mathrm{TR}\left(\frac{1}{\gamma_\alpha k^\alpha - m + i\epsilon} \cdot \gamma_\mu \cdot \frac{1}{\gamma_\beta (k-q)^\beta - m + i\epsilon} \cdot \gamma_\nu\right) \tag{3}$$

As $k \to \infty$ this integral diverges. These types of divergent terms are a feature of all interacting field theories[4] and lead to the third fundamental concept of particle physics: regularization and renormalization.

Both the non-physical quantities and the divergences in the theory can be addressed at the same time. The first step is to 'renormalize' the fields by scaling them by multiplicative factors so that the new fields, $\psi'$, $A'_\mu$, give the same vacuum and single particle expectation values, when no decays or observed interactions are present, as the fields do in the non-interacting theory. Then extra additive terms are added to the Lagrangian to insert the physically measured masses and coupling constants. The point of these two steps is to transform the Lagrangian into a form that can be broken into two parts, $\mathcal{L}_0$, which is the 'free' non-interacting portion of the Lagrangian now expressed entirely in terms of physical quantities, and $\mathcal{L}'$ which includes the interaction terms and a number of extra terms containing the bare quantities. For example to deal with the $m_0\bar{\psi}\psi$ term in the Dirac or QED Lagrangian an extra term would be added to change it to $m\bar{\psi}\psi - (m - m_0)\bar{\psi}\psi$, note that since $m_0$ is not determined the quantity $(m - m_0)$ is also unknown. To handle the high momentum, or 'ultraviolet', divergences mentioned earlier the theory is temporarily 'regularized' which is just some artificial means of introducing a finite high energy cutoff, $\Lambda$, with the understanding that at some point $\Lambda$ must be taken to infinity. The result will be a finite function in terms of $\Lambda$. Renormalization itself consists of adding extra counter terms, which may include the extra terms already used to insert the physical quantities, to exactly cancel the cutoff dependence. These counter terms become part of the theory and the divergent graphs resulting from the counter terms must also be taken into account. The theories of physical interest should be strictly-renormalizable, which means that a finite number of counter terms are needed and the addition of the counter terms simply redefine parameters already in the theory and don't introduce new physics. A non-renormalizable theory is one in which the counter terms lead to new divergent terms requiring yet more counter terms. In this case an infinite number of terms are needed and the theory is of no, apparent, physical value. In some cases, as with chiral perturbation theory which will be mentioned later, it is possible to get useful results from

[2]To evaluate this integral note that $(\gamma_\alpha k^\alpha - m)^{-1} = (\gamma_\alpha k^\alpha + m)/(k^2 - m^2)$.

a non-renormalizable theory but such theories are considered to be effective theories approximating some underlying more fundamental renormalizable theory.

Once renormalization has been done perturbation theory can be used with QED to obtain extremely accurate results. The expansions go in powers of the fine structure constant, $\alpha \equiv e^2/4\pi \approx 1/137$[3], and so fall off rapidly at higher orders. An example of a test of QED is finding the gyromagnetic ratio of the electron, $g$, which is a measure of the coupling of the spin of the charged electron to an external magnetic field. The calculation in QED has been done to order $\alpha^3$[3] and gives $(g-2)/2 = 0.0011596524 \pm 3$. The experimental value, measured by injecting polarised electrons into a uniform magnetic field and measuring the change in helicity of the electrons as a function of time, is $0.00115965219 \pm 1$[3]. This kind of extremely precise agreement between experiment and QED predictions is the reason that QED is often referred to as the 'best' scientific theory we have. And the reason that the same mathematical framework, and a lot of the terminology, of QED was applied to the subsequent search for theories of the strong and weak forces.

## 2.2 Quantum Chromodynamics(QCD)

The theory of the strong force, quantum chromodynamics, is the most recent of the three particle physics theories and also the most difficult to deal with mathematically. The first step toward this theory occurred in 1961 when M. Gell-Mann and Y Ne'eman[5, 6] proposed the 'eightfold way' as a means of classifying the large number of hadrons which had been discovered up to that point. The eightfold way was essentially an observation that the hadrons could be collected into either octets or decuplets based on their quantum numbers and that these groupings were representations of a symmetry group. In this case, rather than the simple U(1) group which described phase transformations of the fields in QED, the group of interest was SU(3), the set of unitary three dimensional matrices with unit determinant. In 1963 both Gell-Mann and Zweig[7] realized that all of these more complex 8 and 10 dimensional groupings could be constructed from combinations of 3 spin 1/2 fermions, the u, d and s quarks. These quarks form the fundamental 3 dimensional representation of the above SU(3) group, with the strong force being invariant to rotations amongst these three 'flavours' of quarks. Using this empirical scheme it was noted that the decuplet which contained the $\Delta$ baryon was missing one member. A search was undertaken for the predicted particle, the $\Omega^-$, which was discovered at BNL in 1964[8], thus lending sup-

port to the concept of the eightfold way. This global 'flavour' symmetry would only be exact if the three quarks had identical masses, which they do not, however their masses are similar enough that the symmetry is approximately true. This fact will be used later in the chiral perturbation theory approximation of strong interactions involving u, d and s quarks. At higher energies three additional quarks were discovered (table 1) with masses so different from one another and from the u and d quarks that this flavour symmetry, $SU(3)_f$, was not extended beyond the first three quarks.

In the mid-1960's it was realized that quarks had to carry another quantum number or it would be possible to create baryon wave functions that were symmetrical under the interchange of identical quarks, which would violate the Pauli exclusion principle for fermions[9]. This new quantum number was referred to as 'color' and it was eventually determined that three color 'charges' were needed; red, green and blue, with the strong Lagrangian obeying a new global SU(3) symmetry referred to as $SU(3)_c$ to distinguish it from flavour SU(3). QCD was created in the exact same way as QED by extending this global $SU(3)_c$ symmetry to a local symmetry. In the QED case the group involved was U(1), a one dimensional complex unitary matrix, so there were $2-1=1$ undetermined variables leading to only one independent symmetry and a single gauge field, the photon. In an SU(3) matrix there are $9 \times 2 = 18$ variables with 9 constraints from the matrix being unitary and 1 from it having unit determinant. This leaves 8 independent transformations requiring 8 gauge particles to make the symmetry local. These 8 new QCD gauge particles are referred to collectively as 'gluons'. Let $\psi_i, \lambda_j; i$=1–6,$j$=1–8, be respectively the wavefunctions of the quarks which are each 3 dimensional column vectors in color space and the Gell-Mann $3 \times 3$ matrices which are the generators of the SU(3) group. If we apply a local rotation in SU(3) of $\eta_j(x)$ we obtain: $\psi_i \rightarrow \psi_i' = \exp(i\eta_j(x)\lambda_j/2)\psi_i$ which is a direct analog of the QED transformation $\psi \rightarrow \psi' = e^{-i\lambda(x)}\psi$ listed earlier. A covariant derivative is again defined this time as $D_\mu = \partial_\mu + ig_s(\lambda_j/2)A_j^\mu(x)$ where $g_s$ is the strong coupling constant and $A_j(x)$ are the 8 gluon fields. This time when we consider an infinitesimal transformation $\delta\eta_j(x)$ and look at how the gluon fields must transform to maintain local gauge invariance we obtain an extra term: $\delta A_j^\mu = -\partial^\mu(\delta\eta_j(x)) - g_s f_{jik}\delta\eta_i A_k^\mu$. This second term appears because the generators $\lambda_j$ do not commute with each other, the $f_{ijk}$ terms are the structure constants defined by the algebra of the group where $[\lambda_i, \lambda_j] = if_{ijk}\lambda_k$. The implication of this difference is that unlike the neutral photons of QED the gluons of QCD carry color themselves and will interact with each other via the strong force. Three-gluon and four-gluon vertices occur as shown in diagram 2. Defining a field strength

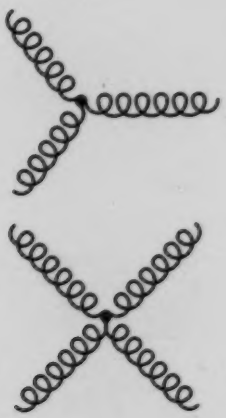

Figure 2: Gluon self interaction diagrams.

tensor, $F_j^{\mu\nu} = \partial^\mu A_j^\nu - \partial^\nu A_j^\mu - g_s f_{jik} A_i^\mu A_k^\nu$, and quark masses, $m_i$, the QCD Lagrangian becomes:

$$\mathcal{L}_{QCD} = -\frac{1}{4} F_{\mu\nu}^j F_j^{\mu\nu} + i\bar{\psi}_i \gamma^\mu D_\mu \psi_i + m_i \bar{\psi}_i \psi_i \tag{4}$$

The QCD Lagrangian has been deliberately constructed to look similar to the QED Lagrangian, however there is one major problem; the coupling $g_s$ cannot be assumed to be small, in fact since free quarks and gluons are never observed they must be strongly confined. When the renormalization procedure is applied to QCD it is found that the coupling 'constant' $g_s$ is not actually constant. During renormalization at some point it is necessary to build in the experimentally measured coupling constant, this requires the choice of some distance scale (or equivalently energy or mass scale) at which the coupling was measured. A convenient choice, as was used in QED, is the coupling at long distances which is measured in low energy experiments. Due to virtual interactions, such as vacuum polarisation in QED, this coupling is not the same at very short distances (high energy). In the case of QED this variation is not significant at any realistically achievable energies. In the case of QCD the coupling at low energy cannot be measured but at high energy the coupling strength decreases and can be determined. The coupling at other energies must then be calculated. This is the so-called 'running' coupling constant of QCD[3]. The practical effect of this is that at high energies (10's of GeV) the coupling is small enough that perturbation theory can be used to extract results from QCD while at lower energies, such

as those found in kaon and pion decays, perturbation theory breaks down and some alternative method must be used to calculate strong interactions.

## 2.3 Electroweak Theory

As with QCD the theory of weak interactions began as a phenomenological explanation of observed experimental results which was then turned into a theory using the structure of QED as a guide. Eventually the weak and electromagnetic forces were unified into a single theory, referred to as electroweak theory, which together with QCD form the 'standard model' of particle interactions. Chronologically the electroweak theory was discovered before QCD but contains a number of additional complications not present in QCD even though it can, at least, be solved perturbatively. All of the decay modes of interest to E787, including $K^+ \to \pi^+\gamma\gamma$, are weak decays.

The first known weak process was nuclear beta decay (figure 3) which

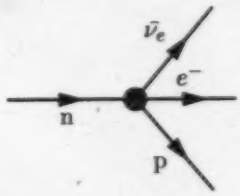


Figure 3: Nuclear beta decay in terms of nucleons.

is characterized by a long lifetime compared to electromagnetic or strong decays and changes the flavour of a quark. Specifically one of the $d$ quarks in the neutron is transformed into a u quark to change the neutron into a proton. The first attempt at a theory was by Fermi in 1934[10, 11], he considered all 4 particles to be interacting at one point (figure 4) with the $e, \nu$ pair being the equivalent of the photon in QED. He then defined weak

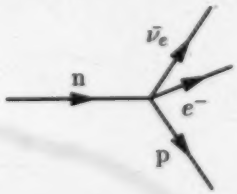


Figure 4: Nuclear beta decay in the Fermi theory.

currents, $j^{\mathrm{WK}}$, in analogy to QED's electromagnetic currents, so that the decay could be described as the interaction of two currents; one involving the hadrons the other the leptons, $<p|j_{\mu}^{\mathrm{WK}}|n><e\bar{\nu}_e|j_{\mathrm{WK}}^{\mu}|0>$. As more weak decays were recognized, especially with the discovery of the strange quark, an oddity was noticed, known as the $\tau - \theta$ puzzle, in which two particles were found to be identical with the exception of having opposite parity. In 1956 Lee and Yang[12] reviewed the available experimental data on weak interactions and predicted that the weak interaction did not conserve parity, and that the $\tau$ and $\theta$ were in fact the same particle. The following year it was experimentally proven[13] that the weak interaction violates parity and the $\tau$ and $\theta$ are now both known to be the $K^+$. Additional experimentation showed that only the left-handed helicity state of neutrinos participates in weak interactions [3]. In 1958 Feynman and Gell-Mann[14] simplified the Fermi currents to account for this by only including terms like $\bar{\psi}\gamma^{\mu}(1-\gamma^5)\psi$, the factor $\gamma^{\mu}(1-\gamma^5)$ indicating that the weak interaction involves only the difference of vector and axial vector currents, known as the V-A theory. The vector portion, $\gamma^{\mu}$, is even under parity while the axial vector component, $\gamma^{\mu}\gamma^5$, is odd therefore the combination cannot be an eigenstate of parity. Additionally the combination $(1-\gamma^5)$ acting on a Dirac spinor selects only the negative helicity component.

The next major modification to weak phenomenology came about to explain the fact that several classes of weak interactions were known each of which had a different coupling constant[15, p.359]. There were purely leptonic weak decays such as muon decay, slightly weaker strangeness-conserving ($\Delta S = 0$) hadronic decays such as $\beta$ decay and weaker still strangeness-changing ($\Delta S = 1$) hadronic decays such as $\Lambda$ decay (figure 5). In 1963 Cabibbo[16] suggested that the strength of the hadronic weak interaction was 'shared' between the $\Delta S = 0$ and $\Delta S = 1$ transitions. Introducing a single new empirical parameter, the Cabibbo angle $\theta_C$, and calling the leptonic weak coupling $g$, explained the experimental results if the $\Delta S = 0$ hadronic coupling was $g\cos\theta_C$ and the $\Delta S = 1$ coupling was $g\sin\theta_C$, with $\sin\theta_C \approx 0.23$. This is now understood as a result of the weak quark eigenstates not being the same as the quark mass eigenstates. The weak eigenstates mix quarks of different flavors. For the case above, with the u,d and s quarks, the d quark state is replaced by the mixture $d_C = d\cos\theta_C + s\sin\theta_C$ and the charge-raising quark weak current can be expressed as $j_{\mu,\mathrm{WK}}^{+} \propto g\bar{u}\gamma_{\mu}(1-\gamma_5)\bar{d}_C$. With this definition of $d_C$ there

[3] Helicity is the projection of spin along the direction of motion of the particle. As with polarised light left-handed refers to the negative helicity state.

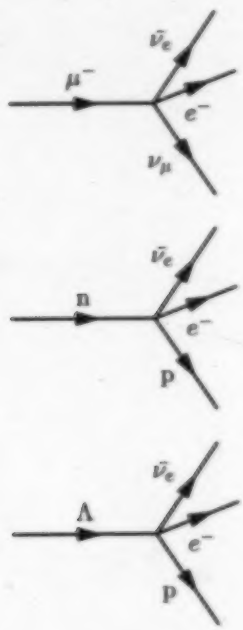


Figure 5: Fermi theory diagrams for muon decay, nuclear beta decay and Λ beta decay.

was the suggestion that weakly interacting particles (to be precise their left-handed components) could be grouped into doublets based on their weak transitions, $(e, \nu_e)$, $(\mu, \nu_\mu)$ and $(u, d_C)$, the first particle in each doublet being transformed into the second by a charge-lowering weak current and the reverse happening with a charge-raising current. This doublet structure, referred to as weak isospin, played a role later on in the development of the Glashow-Salam-Weinberg (GSW) theory of electroweak interactions.

The Fermi theory was successful up to a point but is a non-renormalizable theory which becomes increasingly more divergent at higher orders. Early attempts to follow the gauge theory approach of using a local symmetry met with complications. The (known) weak interactions were charge changing, therefore the gauge quanta would have to carry both weak and electromagnetic charge. This suggested a link between the weak force and QED. The weak isospin doublet structure suggests SU(2) as the simplest symmetry group, this would yield three vector bosons, two of which could be the

charge-raising and charge-lowering weak quanta, $W^+, W^-$, and the third neutral particle could be the photon. Such a scheme was suggested by Schwinger[17] in 1957. Unfortunately this approach gives the wrong electric charges to the members of the doublets and fails to distinguish lepton doublets, with charge (+1,0), from quark doublets with charge (+2/3,-1/3). In 1961 Glashow[18] suggested enlarging the symmetry to SU(2)×U(1), with the SU(2) portion corresponding to weak isospin and the new U(1) group to a quantity arbitrarily called weak hypercharge. The correct charges would result if the charge, Q, was defined in terms of the third component of weak isospin, $I_3$, and appropriately chosen assignments of hypercharge, Y, by the equation $Q = I_3 + Y/2$. For example if the quarks in the left-handed quark doublet, $(u, d_C)_L$, are given weak hypercharge 1/3 then the quark charges are (+2/3,-1/3) as required since $I_3$ for a doublet is (+1/2,-1/2). The right-handed fermions, which don't interact weakly, would be assigned to weak isospin singlets with $I_3 = 0$ and their hypercharge set at twice their electric charge. This is the symmetry group used in modern GSW theory.

The greatest problem with the gauge approach was that the SU(2)×U(1) symmetry, when converted to a local symmetry, yielded vector bosons that were massless just as they were in QED and QCD. The new gauge quanta were assigned the names $W^{\pm}, W^3$ and $B$. $W^{\pm}$ would have to mediate charge-changing weak interactions and, since the weak interaction was known to be short ranged, would have to be massive, while one of $W^3$ or $B$ would have to correspond to the photon and be massless. The presence of a mass term for the gauge boson breaks the gauge invariance of the Lagrangian and appears to make it a requirement of gauge theories that these particles be massless. The solution to this dilemma is the so-called Higgs mechanism[19], applied in the late 60's by Weinberg and Salam[20, 21] to the $SU(2) \times U(1)$ symmetry of Glashow. Normally the vacuum is defined as the state in which all particles have zero expectation value, $<0|P|0>= 0$ for some particle $P$. However, it is possible for there to exist fields, known as Higgs fields, $\phi$, for which $< 0|\phi|0 > \neq 0$. If these fields are weakly interacting then they can interact with the massless weak gauge quanta in such a way as to screen the weak force and give the quanta an effective mass. In GSW theory it is supposed that there exists a weak isospin doublet of complex scalar Higgs fields which may be written as[15, p.433]

$$\phi = \exp[i(\tau_i/2)\alpha_i(x)] \begin{pmatrix} 0 \\ (\sigma(x) + f)/\sqrt{2} \end{pmatrix} \qquad (5)$$

where $\tau_i$ are the three Pauli matrices appropriate to SU(2), $\alpha_i(x)$ are three real phase fields, $f$ is a real constant and $\sigma$ is a field with zero vacuum

expectation value. Any choice of $\alpha_i$ leads to an equally valid ground state for the system. In this sense there are an infinite number of possible vacua but only one is required. The choice of a unique vacuum, such as $\alpha_i = 0$, destroys the gauge symmetry and is referred to as 'spontaneous symmetry breaking' since the symmetry is not broken explicitly in the Lagrangian but rather by the vacuum. The $\alpha_i$ can also be removed by a gauge transformation on the vector bosons in the theory[15, p.433]. Either way, when the Higgs fields are added to the Lagrangian and the covariant derivative applied to make $SU(2)_L \times U(1)$ a local symmetry, mass terms appear associated with the vector bosons. This is often referred to as the gauge particles 'eating' three of the four Higgs bosons and thereby gaining mass. The $W^{\pm}$ will have a mass of $gf/2$[15, p.434], where $g$ is the coupling constant connected to $SU(2)_L$. $W^3$ and $B$ turn out to not be mass eigenstates, however with the definition $\cos\theta_w = g/\sqrt{g^2 + g'^2}$ two combinations can be created; $Z^0 = B\sin\theta_w - W^3\cos\theta_w$ with mass $gf/2\cos\theta_w$ and $A = B\cos\theta_w + W^3\sin\theta_w$[15, p.436] which corresponds to the massless photon. The remaining Higgs degree of freedom, $\sigma$, becomes a zero charge, weakly interacting scalar of undetermined mass. This Higgs scalar has yet to be observed experimentally.

One point of early contention with the GSW theory was the neutral $Z^0$ weak vector boson. It implied the existence of purely weak interactions that were not charge changing. These weak neutral currents, which include decays such as $K^+ \to \pi^+\nu\bar{\nu}$ and $K^+ \to \pi^+\gamma\gamma$, were not observed until 1973[22]. There was a particular problem with the neutral current decays of strange quarks which were highly suppressed relative to otherwise similar charge-changing strange decays. Based on GSW and the Cabibbo theory there should have been neutral currents of the form (omitting the $\gamma$ matrices)

$$j^0_{\mathrm{WK}} \propto g(\bar{u}, \bar{d_C})\tau_3 \begin{pmatrix} u \\ d_C \end{pmatrix} \tag{6}$$

containing non-zero terms like $(\bar{d}s + \bar{s}d)\cos\theta_C \sin\theta_C$. In 1970 Glashow, Iliopoulos and Maiani[23] proposed the existence of a new heavy charge $+2/3$ quark known as the charmed quark. They suggested that there was a second weak quark doublet $(c, s_C)$ in addition to the Cabibbo doublet $(u, d_C)$ with $s_C = -d\sin\theta_C + s\cos\theta_C$. The quark neutral current would then contain a second term

$$j^0_{\mathrm{WK}} \propto g(\bar{u}, \bar{d_C})\tau_3 \begin{pmatrix} u \\ d_C \end{pmatrix} + g(\bar{c}, \bar{s_C})\tau_3 \begin{pmatrix} c \\ s_C \end{pmatrix} \tag{7}$$

and all terms involving flavour changing neutral currents would cancel out. This cancellation is known as the GIM mechanism. Because the quark masses are not equal flavour-changing neutral currents do occur at higher orders. It should be noted that neutral currents are not pure $V-A$ in nature, the relevant space-time factor is instead given in terms of the parameters $c_A$ and $c_V$ by $\gamma^\mu(c_A - c_V\gamma^5)$[15, p.369].

The last major piece of the electroweak standard model is the modern extension of the GIM mechanism to three quark generations. The mixing of the quark mass eigenstates to form the weak eigenstates is done by a $3 \times 3$ unitary complex matrix, known as the Cabibbo, Kobayashi, Maskawa[24] matrix acting on the charge -1/3 quarks. It also includes a term for CP violation.

$$\begin{pmatrix} d_C \\ s_C \\ b_C \end{pmatrix} = \begin{pmatrix} V_{ud} & V_{us} & V_{ub} \\ V_{cd} & V_{cs} & V_{cb} \\ V_{td} & V_{ts} & V_{tb} \end{pmatrix} \begin{pmatrix} d \\ s \\ b \end{pmatrix}$$

The values of the matrix elements can be parameterized in a number of ways but involve only 4 independent parameters (which must be determined experimentally). The requirement that the matrix be unitary implies that $V_{ud}V_{ub}^* + V_{cd}V_{cb}^* + V_{td}V_{tb}^* = 0$. If the values of the CKM matrix elements can be measured separately then this relation can be used as a test of the theory. One of the motivations for measuring the branching ratio of $K^+ \to \pi^+\nu\bar{\nu}$ is that it can provide an extremely clean measurement of $|V_{td}|$, one of the least well known matrix elements.

## 2.4 Chiral Perturbation Theory

As was mentioned under the QCD section, perturbation theory can only be applied to QCD at very high energies. At the level of kaon decays the QCD effects cannot be calculated in the conventional way. A very accurate theoretical prediction can be made for the branching ratio of $K^+ \to \pi^+\nu\bar{\nu}$ because it can be related to a similar, easily measured, decay $K^+ \to \pi^0 e^+ \nu$[25] and because there are no long-range electromagnetic interactions involving the two neutrinos since they only interact weakly. The long range QCD effects are contained in the experimentally measured branching ratio. Such a convenient trick does not exist for $K^+ \to \pi^+\gamma\gamma$ therefore another method must be found, chiral perturbation theory (ChPT).

The principle of an effective theory is that the long range (low energy) dynamics of a system are not sensitive to the details of the short range (high energy) dynamics[50, 51]. In practice almost all physical theories are

effective theories, for example QED considerations would not be relevant in aerodynamics, and even the standard model is just an effective theory of some (hypothetical) grand unified theory. However, the full high energy theory does place certain constraints on the effective theory[26]. The most important is that the fundamental symmetries of the full theory must also be present in the effective theory. The effective theory is only valid below some energy scale characteristic of the full theory. And although a number of the degrees of freedom of the high energy theory have been removed from the effective theory it will still contain couplings that must either be calculated from the full theory or measured experimentally. A particle physics example is the Fermi theory of weak interactions. At energies well below the mass of the $W$ the electroweak theory of $SU(2)_L \times U(1)_Y$ can be replaced with the effective theory consisting of QED and the Fermi 4-point interaction. Knowledge of the details of, or even the existence of, $W$ and $Z$ exchange is not required to make calculations at those low energies although the Fermi coupling constant $G_F$ is related to both the $SU(2)_L$ coupling and the mass of the $W$, $G_F \propto g^2/M_W^2$[15, p.362].

The starting point for chiral perturbation theory is the (approximate) chiral symmetry of the QCD Lagrangian. If we define the projection operators $\Gamma_L = (1 - \gamma_5)$ and $\Gamma_R = (1 + \gamma_5)$ then acting on a Dirac wave function these will project out the left and right handed components of the wave function, $\psi_L = \Gamma_L \psi$ and $\psi_R = \Gamma_R \psi$ where $\psi = \psi_L + \psi_R$. The QCD Lagrangian (equation 4) can be written as:

$$\begin{aligned} \mathcal{L}_{QCD} &= -\frac{1}{4} F^j_{\mu\nu} F^{\mu\nu}_j + i\bar{q_L}\gamma^\mu D_\mu q_L + i\bar{q_R}\gamma^\mu D_\mu q_R \\ &- \bar{q_L} m q_R - \bar{q_R} m q_L \end{aligned} \tag{8}$$

where $q$ is the column vector of quark flavours and $m$ is the quark mass matrix. The c,t and b quarks are quite massive while the u,d and s quarks are relatively light (figure 6). The QCD Lagrangian can be decoupled into light and heavy quark components and at low energies we can ignore the heavy quark contribution[4]. If we define the quark vector, $q$, above to contain only the u,d and s quarks and set their masses to zero then the QCD Lagrangian will be invariant under the global chiral symmetry $G \equiv SU(3)_L \times SU(3)_R$ which represents independent rotations in flavour space of the quark fields $q_L, q_R$. By Noether's theorem this implies that there will be eight conserved left-handed and eight conserved right-handed currents. By convention the sum and difference of these currents is usually taken to define eight conserved vector currents and eight conserved axial-vector currents, along with their associated conserved charges. Hadrons should then appear in parity

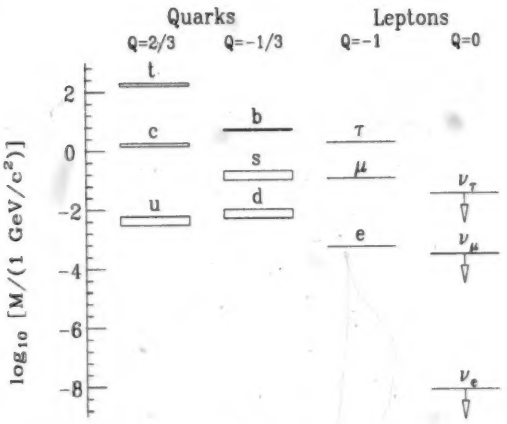


Figure 6: Quark masses on a logarithmic scale, widths indicate uncertainties in the values.

doublets, where the particles are otherwise identical but have opposite parity corresponding to the vector or axial charges. Unfortunately these parity doublets do not appear to exist in nature and even though the masses of the light quarks are not exactly zero, the chiral symmetry should be at least approximately true. The proposed solution is that the chiral symmetry is spontaneously broken from $SU(3)_L \times SU(3)_R$ to $SU(3)_{L+R}$ (or $SU(3)_V$). Note that this is a slightly different situation than the spontaneous symmetry breaking in electroweak theory since that symmetry was a local one whereas this is a global symmetry. By Goldstone's theorem[27] when a continuous global symmetry is broken there will be generated a massless boson corresponding to each broken symmetry generator. In this case eight pseudoscalar bosons since the symmetry has been reduced from $SU(3) \times SU(3)$ to only a single $SU(3)$ group. Of course no such massless bosons are observed but this is explained by the fact that the chiral symmetry is only approximate, the small quark masses, $m_d, m_u, m_s$, explicitly break the symmetry as can be seen in equation 8. This allows the Goldstone bosons to acquire

non-zero, but still relatively small, masses. These masses are considered to be a perturbation of the otherwise valid chiral symmetry. The result is that the octet of spin-zero mesons, first grouped together in the 'eightfold way' (table 2), are identified as the Goldstone bosons of the broken chiral symmetry.

Table 2: The Eightfold Way octet of spin zero mesons.

| Hypercharge, $Y$ | Strong isospin component, $I_3$ | | | | |
|---|---|---|---|---|---|
| | -1 | -1/2 | 0 | 1/2 | 1 |
| 1 | | $K^0$ | | $K^+$ | |
| 0 | $\pi^-$ | | $\eta, \pi^0$ | | $\pi^+$ |
| -1 | | $K^-$ | | $\bar{K}^0$ | |

The effective theory is created by replacing the quark and gluon interactions by interactions amongst the Goldstone bosons in the most general possible Lagrangian that still obeys the symmetry requirements of the full Lagrangian[28, 29, 30]. The convention for doing this is to define a unitary matrix, $U(\phi)$, which transforms under the chiral group, $G$, as

$$\begin{aligned} U(\phi) &\xrightarrow{G} g_R U(\phi) g_L^\dagger \\ g_{L,R} &\in SU(3)_{L,R} \end{aligned}$$

where $\phi_a$ are the eight Goldstone bosons. Defining the $3 \times 3$ matrix $\Phi$ in terms of the Goldstone bosons, $\phi$, and the Gell-Mann matrices of SU(3), $\lambda$, by

$$\Phi(x) \equiv \frac{\lambda_a \phi_a}{\sqrt{2}} = \begin{pmatrix} \frac{1}{\sqrt{2}}\pi^0 + \frac{1}{\sqrt{6}}\eta & \pi^+ & K^+ \\ \pi^- & \frac{-1}{\sqrt{2}}\pi^0 + \frac{1}{\sqrt{6}}\eta & K^0 \\ K^- & \bar{K}^0 & \frac{-2}{\sqrt{6}}\eta \end{pmatrix} \qquad (9)$$

allows $U$ to be expressed as $U(\phi) = \exp(i\sqrt{2}\Phi/f)$ for some constant $f$. The only terms which contribute to the effective Lagrangian are those that contain even numbers of derivatives of $U$, $\mathcal{L}_{\text{eff}} = \sum_n \mathcal{L}_{2n}$. Expanding in numbers of derivatives is equivalent to expanding in powers of momenta, remembering that the theory only applies to momenta below the chiral symmetry breaking scale of 1 GeV. The lowest order term, $O(p^2)$, is given by $\mathcal{L}_2 = (f^2/4)\text{TR}(\partial_\mu U^\dagger \partial^\mu U)$, in terms of the single unknown constant $f$. The

$O(p^4)$ term will contain two parts, one the direct $O(p^4)$ vertex from $\mathcal{L}_4$, the other the one loop diagram with $\mathcal{L}_2$ vertices. As with any quantum field theory, loops lead to divergences that must be removed via renormalization. In principle an effective field theory such as ChPT is non-renormalizable since an infinite number of counter-terms are needed to remove the divergences. Since the effective Lagrangian, at a given order n, contains by construction all terms that satisfy the symmetries of the full Lagrangian at that order then any order n counter-terms that need to be introduced will not add new physics but only change the coupling constant associated with that term in the theory. In this sense the effective theory is renormalizable on an order-by-order basis and retains predictive power as long as calculations are done to a finite number of orders. The price to be paid for using an effective theory is that the number of these couplings, which must be measured or calculated from the full theory, increases rapidly. In ChPT $\mathcal{L}_2$ contains one constant, $\mathcal{L}_4$ contains 10 and $\mathcal{L}_6$ contains over 140 unknowns.

Additional external fields can be added to the Lagrangian to take into account such things as electromagnetic interactions or the explicit symmetry breaking caused by non-zero quark masses. Consider scalar, pseudoscalar, vector and axial vector fields, $a, p, v_\mu$ and $a_\mu$ respectively and add a term $\bar{q}\gamma^\mu(v_\mu + \gamma_5 a_\mu)q - \bar{q}(s - i\gamma_5 p)q$ to the chiral QCD Lagrangian of equation 8. Defining the covariant derivative as $D_\mu U \equiv \partial_\mu U - i(v_\mu + a_\mu)U + iU(v_\mu - a_\mu)$ and the field $\chi \equiv 2B(s + ip)$, for constant B, then $\mathcal{L}_2$ and $\mathcal{L}_4$ can be written in the standard notation of Gasser and Leutwyler[31]:

$$\mathcal{L}_2 = \frac{1}{4}f^2(\mathrm{TR}(D_\mu U D^\mu U^\dagger) + \mathrm{TR}(\chi U^\dagger + U\chi^\dagger)) \tag{10}$$

$$\begin{aligned}\mathcal{L}_4 &= L_1\mathrm{TR}(D_\mu U^\dagger D^\mu U)^2 + L_2\mathrm{TR}(D_\mu U^\dagger D_\nu U)\mathrm{TR}(D^\mu U^\dagger D^\nu U) \\ &+ L_3\mathrm{TR}(D_\mu U^\dagger D^\mu U D_\nu U^\dagger D^\nu U) + L_4\mathrm{TR}(D_\mu U^\dagger D^\mu U)\mathrm{TR}(U^\dagger\chi + \chi^\dagger U) \\ &+ L_5\mathrm{TR}(D_\mu U^\dagger D^\mu U(U^\dagger\chi + \chi^\dagger U)) + L_6\mathrm{TR}(U^\dagger\chi + \chi^\dagger U)^2 \\ &+ L_7\mathrm{TR}(U^\dagger\chi - \chi^\dagger U)^2 + L_8\mathrm{TR}(\chi^\dagger U\chi^\dagger U + U^\dagger\chi U^\dagger\chi) \\ &- iL_9\mathrm{TR}(F_R^{\mu\nu} D_\mu U D_\nu U^\dagger + F_L^{\mu\nu} D_\mu U^\dagger D_\nu U) + L_{10}\mathrm{TR}(U^\dagger F_R^{\mu\nu} U F_{L\mu\nu}) \\ &+ H_1\mathrm{TR}(F_{R\mu\nu}F_R^{\mu\nu} + F_{L\mu\nu}F_L^{\mu\nu}) + H_2\mathrm{TR}(\chi^\dagger\chi)\end{aligned} \tag{11}$$

The $H_1$ and $H_2$ terms are used for renormalization purposes only and are not observable, and the field strength tensors are defined as

$$F_L^{\mu\nu} = \partial^\mu(v^\nu - a^\nu) - \partial^\nu(v^\mu - a^\mu) - i[(v^\mu - a^\mu), (v^\nu - a^\nu)] \tag{12}$$

$$F_R^{\mu\nu} = \partial^\mu(v^\nu + a^\nu) - \partial^\nu(v^\mu + a^\mu) - i[(v^\mu + a^\mu), (v^\nu + a^\nu)] \tag{13}$$

## 2.5 The $K^+ \to \pi^+\gamma\gamma$ Branching Ratio Calculation

The actual calculation of the $K^+ \to \pi^+\gamma\gamma$ branching ratio from ChPT requires combining the strong force effective chiral Lagrangian with an effective Lagrangian for electroweak processes. This will only be briefly outlined below.

The general procedure for adding the electroweak Lagrangian is similar to that used for the strong force. First the appropriate 'full' Lagrangian involving the quark fields is identified and its symmetries, particularly under chiral rotations, $SU(3)_L \times SU(3)_R$, are noted. Then the most general Lagrangian which satisfies these symmetries is written in terms of the Goldstone fields and the other non-quark fields required. Since the chiral scale is well below the mass of the $W$ the electroweak interaction is first described in terms of QED and the Fermi constant, $G_F$, with point-like quark interactions and no explicit reference to the $W$ or $Z$. The electromagnetic interaction can be added to the strong terms already given, equations 10 and 11, by changing the generic external vector field, $v_\mu$, to $v_\mu - eQA_\mu$, where $Q$ is the diagonal quark charge matrix $Q = \mathrm{diag}(2/3, -1/3, -1/3)$, and including a kinetic term which is lacking for external fields[32]. The weak interaction term under $SU(3)_L \times SU(3)_R$ transforms as $(8_L, 1_R) + (27_L, 1_R)$, the octet term corresponds to $\Delta I = 1/2$ transitions while the 27-plet term contains both $\Delta I = 1/2$ and $\Delta I = 3/2$ transitions[28, 30, 32, 33]. For nonleptonic weak interactions the leading term in the chiral perturbation theory effective Lagrangian is:

$$\begin{aligned} \mathcal{L}_2^{\Delta S=1} &= G_8 \mathrm{TR}[\frac{1}{2}(\lambda_6 - i\lambda_7)L_\mu L^\mu] \\ &+ G_{27}(L_{\mu 23}L_{11}^\mu + \frac{2}{3}L_{\mu 21}L_{13}^\mu) + \mathrm{H.C.} \end{aligned} \tag{14}$$

where :

$$L_\mu = if^2 U^\dagger D_\mu U \tag{15}$$

$G_8$ and $G_{27}$ are unknown coupling constants, $\lambda$ are the Gell-Mann matrices and H.C. stands for the hermitian conjugate of the explicitly stated terms. Experimentally the ratio of couplings is $G_8/G_{27} \approx 18$ and the 27-plet terms are normally ignored. The $O(p^4)$ weak Lagrangian, $\mathcal{L}_4^{\Delta S=1}$ is much more complicated, there are a total of 35 terms just in the octet component[34]. Formally it can be written as $\mathcal{L}_4^{\Delta S=1} = G_8 f^2 N_i W_i$ for coupling constants $N$ and field terms $W$. Even restricted to interactions where the only external gauge fields are photons there are still 22 terms remaining[34], fortunately each specific process generally only involves a small number of these terms.

Finally there is a term which first appears at $O(p^4)$ due to the so-called chiral anomaly. Anomalous symmetry breaking occurs when the classical equations of a theory contain a symmetry which is broken in the process of quantization. Specifically the classical, but not the quantum, theory states that axial-vector currents should be conserved[35]. A term, $\mathcal{L}_{\rm AN}$, needs to be built into the effective Lagrangian which will properly account for the anomaly and reproduce the observed results. This anomalous term does not introduce any new constants and can be written as[29]:

$$\begin{aligned}\mathcal{L}_{\rm AN} &= -\frac{N_c}{48\pi^2}\epsilon^{\mu\nu\alpha\beta}[eA_\mu \mathrm{TR}(Q\partial U_\nu U^\dagger \partial U_\alpha U^\dagger \partial U_\beta U^\dagger \\ &- Q\partial U_\nu^\dagger U \partial U_\alpha^\dagger U \partial U_\beta^\dagger U) + ie^2 F_{\mu\nu}A_\alpha T_\beta] \qquad (16)\end{aligned}$$

where

$$\begin{aligned}T_\beta &= \mathrm{TR}(Q^2\partial U_\beta U^\dagger - Q^2 \partial U_\beta^\dagger U + \frac{1}{2}QUQU^\dagger \partial U_\beta U^\dagger \\ &- \frac{1}{2}QU^\dagger QU\partial U_\beta^\dagger U) \qquad (17)\end{aligned}$$

with $N_c$ the number of quark colors. The Lagrangian to $O(p^4)$ which we are interested in can then be written as:

$$\mathcal{L}_{\rm eff} = -\frac{1}{4}F_{\mu\nu}^{\rm em}F_{\rm em}^{\mu\nu} + \mathcal{L}_2^{\rm st} + \mathcal{L}_2^{\Delta S=1} + \mathcal{L}_4^{\rm st} + \mathcal{L}_4^{\Delta S=1} + \mathcal{L}_{\rm AN} \qquad (18)$$

with the external fields $a_\mu, v_\mu$ and $p$ defined as in equation 11 set to zero and $s = \mathrm{diag}(m_u, m_d, m_s)$ to include the small explicit symmetry breaking term resulting from the non-zero quark masses. In general to perform a calculation to $O(p^4)$ several types of graphs will need to be included in addition to the tree-level graph with a $\mathcal{L}_4^{\Delta S=1}$ vertex. These are one loop diagrams with a single $\mathcal{L}_2^{\Delta S=1}$ vertex in the loop, reducible tree-level diagrams with a single $\mathcal{L}_2^{\Delta S=1}$ vertex and a single vertex from either $\mathcal{L}_4^{\rm ST}$ or $\mathcal{L}_{\rm AN}$, and one loop diagrams with a $\mathcal{L}_2^{\rm ST}$ vertex in the loop connected to a $\mathcal{L}_2^{\Delta S=1}$ vertex by a single meson line.

For the specific decay $K^+ \to \pi^+\gamma\gamma$ several simplifications can be made[33, 34, 36]. The $O(p^2)$ contribution vanishes[4] so the leading term is $O(p^4)$. The only unknown terms in $\mathcal{L}_4^{\rm ST}$ (equation 11) that appear are those involving $L_9$

[4]Equation 20 shows the general transition amplitude for $K^+ \to \pi^+\gamma\gamma$. The terms involving $A$ and $C$ have two powers of external momenta, while the terms containing $B$ and $D$ have 4 powers of external momenta. The $O(p^2)$ ChPT Lagrangian can only generate an amplitude linear in external momentum and therefore cannot satisfy equation 20. At $O(p^4)$ the Lagrangian can generate terms quadratic in external momenta and generate invariant amplitudes of type $A$ and $C$ but not $B$ or $D$.

and $L_{10}$. Similarly in $\mathcal{L}_4^{\Delta S=1}$ only the terms with $N_{14}, N_{15}$ and $N_{18}$ appear

$$\begin{aligned}\mathcal{L}_4^{\Delta S=1} &= G_8 f^2[N_{14} i\mathrm{TR}(\frac{1}{2}(\lambda_6 - i\lambda_7)\{F_L^{\mu\nu} + U^\dagger F_R^{\mu\nu} U, D_\mu U^\dagger D_\nu U\}) \\ &+ N_{15} i\mathrm{TR}(\frac{1}{2}(\lambda_6 - i\lambda_7) D_\mu U^\dagger (U F_L^{\mu\nu} U^\dagger + F_R^{\mu\nu}) D_\nu U) \\ &+ 2N_{18}\mathrm{TR}(\frac{1}{2}(\lambda_6 - i\lambda_7)(F_L^{\mu\nu} U^\dagger F_{R\mu\nu} U + U^\dagger F_{R\mu\nu} U F_L^{\mu\nu}))] \\ &+ \text{terms not in } K^+ \to \pi^+\gamma\gamma \end{aligned} \tag{19}$$

The transition amplitude, $M$, for $K^+ \to \pi^+\gamma\gamma$ , on the basis of kinematics and gauge invariance alone, can be broken down into a sum of terms involving four invariant amplitudes, $A, B, C$ and $D$, which can then be calculated theoretically[37].

$$\begin{aligned} M(K^+(p) &\to \pi^+(p')\gamma(q_1,\epsilon_1)\gamma(q_2,\epsilon_2)) \\ &= \epsilon_\mu(q_1)\epsilon_\nu(q_2)[A(y,z)\frac{q_2^\mu q_1^\nu - q_1\cdot q_2 g^{\mu\nu}}{M_K^2} + C(y,z)\varepsilon^{\mu\nu\alpha\beta}\frac{q_{1\alpha}q_{2\beta}}{M_K^2}] \\ &+ \epsilon_\mu(q_1)\epsilon_\nu(q_2)[B(y,z)M_K^{-4}(-p\cdot q_1 p\cdot q_2 g^{\mu\nu} \\ &- q_1\cdot q_2 p^\mu p^\nu + p\cdot q_1 q_2^\mu p^\nu + p\cdot q_2 p^\mu q_1^\nu)] \\ &+ \epsilon_\mu(q_1)\epsilon_\nu(q_2)[D(y,z)M_K^{-4}(\varepsilon^{\mu\nu\alpha\beta}(p\cdot q_2 q_{1\alpha} \\ &+ p\cdot q_1 q_{2\alpha})p_\beta + (p^\mu\varepsilon^{\nu\alpha\beta\gamma} + p^\nu\varepsilon^{\mu\alpha\beta\gamma})p_\alpha q_{1\beta}q_{2\gamma})] \end{aligned} \tag{20}$$

where

$$\begin{aligned} \epsilon_1,\epsilon_2 &= \text{the polarization vectors of photon 1 and 2} \\ y &= p\cdot(q_1-q_2)/M_K^2; \quad |y| \le \frac{1}{2}\sqrt{\lambda(1,z,r_\pi^2)} \\ z &= (q_1+q_2)^2/M_K^2; \quad 0 \le z \le (1-r_\pi)^2 \\ r_\pi &= M_\pi/M_K \\ \lambda(a,b,c) &= a^2+b^2+c^2-2(ab+bc+ac) \end{aligned}$$

the inequalities on $y$ and $z$ simply reflect the allowed range of those variables from energy-momentum conservation. Note that $\sqrt{z}$ is the invariant mass of the photon pair normalized to the kaon mass. At $O(p^4)$ terms $B$ and $D$ do not contribute and the other terms only depend on $z$ not $y$[33]. The photon invariant mass spectrum can then be expressed as:

$$\frac{d\Gamma}{dz}(K^+ \to \pi^+\gamma\gamma) = \frac{M_K}{2^{10}\pi^3} z^2 \sqrt{\lambda(1,z,r_\pi^2)}(|A(z)|^2 + |C(z)|^2) \tag{21}$$

Diagrams involving loops and $\Theta(p^4)$ counterterms contribute to the ampli-

tude A (figure 7)[5] while terms in the anomalous Lagrangian contribute to C (figure 8). These amplitudes have been calculated (to $O(p^4)$) with the

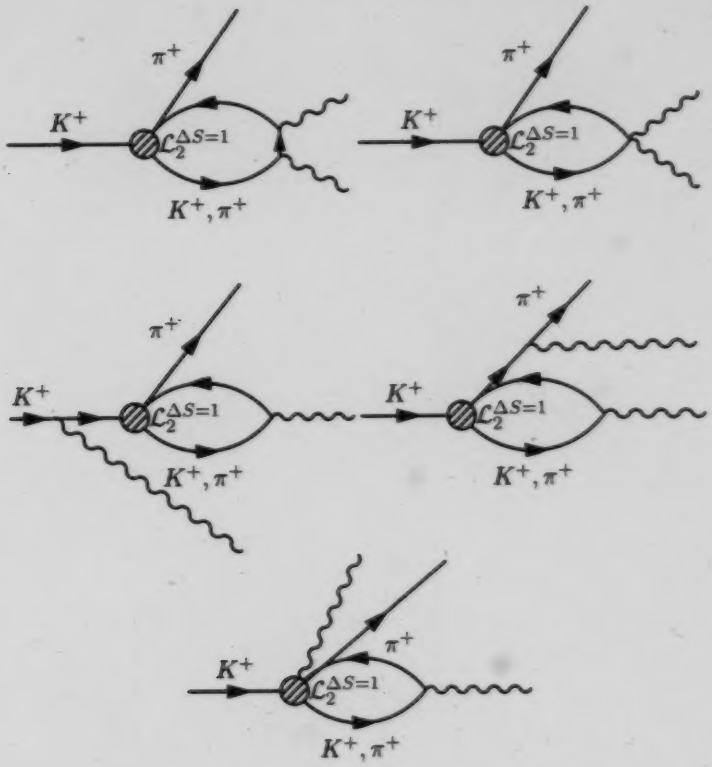


Figure 7: Examples of loop diagrams contributing at $O(p^4)$ to $K^+ \to \pi^+\gamma\gamma$ .

[5]In performing calculations for $K^+ \to \pi^+\gamma\gamma$ it is convenient to do a transformation on the pseudoscalar fields which diagonalizes their kinetic and mass terms[36, 37]. This eliminates vertices of the type $K\pi\gamma$ and requires all weak vertices to have at least three pseudoscalar fields. It also greatly simplifies the one-loop diagrams contributing to $K^+ \to \pi^+\gamma\gamma$ . The diagrams shown are in this diagonal basis.

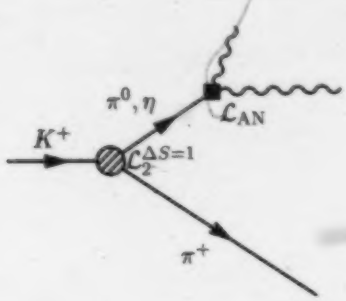


Figure 8: The anomalous diagram contributing at $O(p^4)$ to $K^+ \to \pi^+\gamma\gamma$ .

results[33]:

$$A(z) = \frac{G_8 M_K^2 \alpha}{2\pi z}[(r_\pi^2 - 1 - z)F(\frac{z}{r_\pi^2}) + (1 - r_\pi^2 - z)F(z) + \hat{c}z] \quad (22)$$

$$C(z) = \frac{G_8 M_K^2 \alpha}{\pi}[\frac{z - r_\pi^2}{z - r_\pi^2 + i r_\pi \frac{\Gamma_{\pi^0}}{M_K}} - \frac{z - \frac{2+r_\pi^2}{3}}{z - r_\eta^2}] \quad (23)$$

where

$$F(z) = \begin{cases} 1 - \frac{4}{z}\arcsin^2(\sqrt{z}/2) & z \le 4 \\ 1 + \frac{1}{z}(\ln\frac{1-\sqrt{1-4/z}}{1+\sqrt{1-4/z}} + i\pi)^2 & z > 4 \end{cases} \quad (24)$$

$$r_\eta = M_\eta / M_K \quad (25)$$

$$\hat{c} = \frac{128\pi^2}{3}[3(L_9 + L_{10}) + N_{14} - N_{15} - 2N_{18}] \quad (26)$$

the term $\Gamma_{\pi^0}$ is the rate for $\pi^0 \to \gamma\gamma$. Integrating over $z$ the decay rate is parameterized in terms of only one unknown $\hat{c}$ which only appears in the $A$ term[33]:

$$\Gamma_A(K^+ \to \pi^+\gamma\gamma) = (2.80 + 0.87\hat{c} + 0.17\hat{c}^2) \cdot 10^{-20}\text{MeV} \quad (27)$$

$$\Gamma_C(K^+ \to \pi^+\gamma\gamma) = 0.26 \cdot 10^{-20}\text{MeV} \quad (28)$$

The minimum contribution from the $A$ term, and the lower bound for the branching ratio, occurs when $\hat{c} = -2.6$ and even then the contribution from the anomalous term $C$ is still only 13% of the total rate. The value of $\hat{c}$ is in principle undetermined, but if the constants coming from the weak terms, $N_{14}, N_{15}$ and $N_{18}$, are ignored the value of $\hat{c}$ would be approximately 2 suggesting that $\hat{c}$ is probably of $O(1)$. The lower bound for the branching ratio is $4 \cdot 10^{-7}$ and is sensitive to the value of $\hat{c}$ but the most distinctive feature

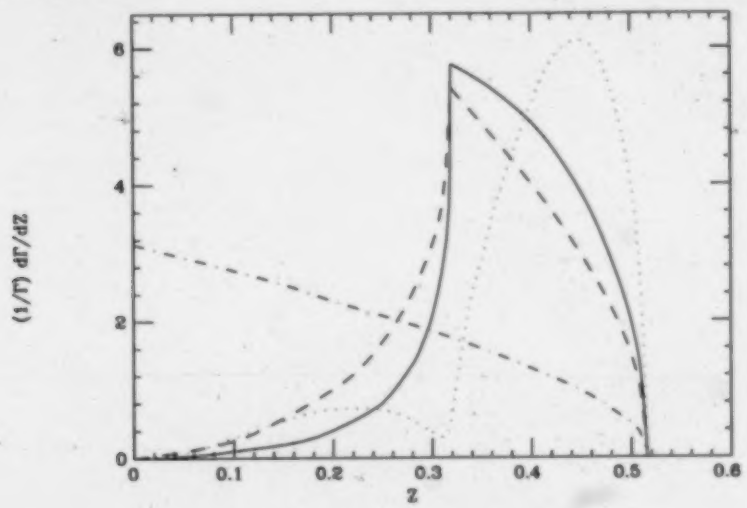


Figure 9: Normalized $O(p^4)$ chiral perturbation theory predictions for the invariant photon mass distribution in $K^+ \to \pi^+\gamma\gamma$ for $\hat{c} = 0$ (solid line), $\hat{c} = 4$ (dashed line), $\hat{c} = -4$ (dotted line) and a phase space distribution (dash-dot line).

of the ChPT prediction for $K^+ \to \pi^+\gamma\gamma$ is the shape of the two-photon invariant mass spectrum (or equivalently the $\pi^+$ momentum spectrum) which varies significantly as a function of $\hat{c}$ and is completely different than what would be expected if the spectrum were determined just on the basis of phase space (figure 9). In the analysis of the experimental data the main emphasis was therefore on the shape of the distribution rather than the absolute branching ratio although both were used.

Another reason for the emphasis on spectrum shape is that the branching ratio observed at CERN for the decay $K_L^0 \to \pi^0\gamma\gamma$ is approximately a factor of two to three higher than that predicted by ChPT even though the spectrum shape is in reasonable agreement with theory[38]. This has prompted investigations into the $O(p^6)$ contributions of ChPT to non-leptonic radiative kaon decays, which seem to effect the overall branching ratio much more than the shape. The analysis in this thesis has been done using $O(p^4)$ chiral perturbation theory, however, there have now been attempts to extend the theoretical predictions for $K^+ \to \pi^+\gamma\gamma$ to include an $O(p^6)$ unitarity correction

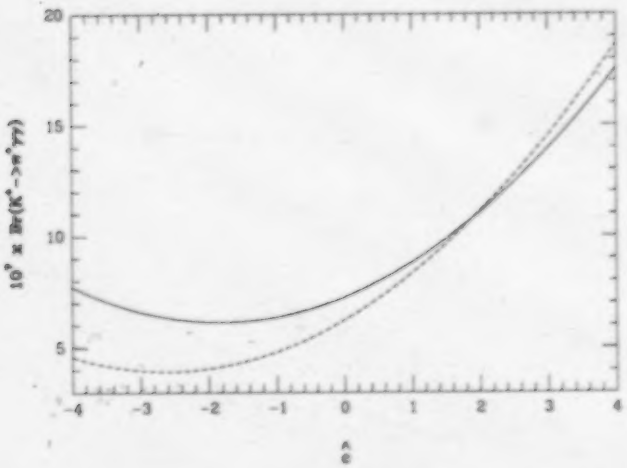


Figure 10: $K^+ \to \pi^+\gamma\gamma$ branching ratio prediction as a function of $\hat{c}$ at $O(p^4)$ (dashed line) and including the $O(p^6)$ unitarity correction (solid line).

(the full $\mathcal{L}_6$ contains far too many unknown constants to make a full $O(p^6)$ correction possible). The unitarity correction is based on the fact that the dominant $O(p^4)$ contribution to $K^+ \to \pi^+\gamma\gamma$ comes from the loop diagrams (figure 7) involving $K^+ \to \pi^+\pi^+\pi^-$. However, the $O(p^4)$ $K^+ \to \pi^+\gamma\gamma$ term comes from the $O(p^2)$ $K^+ \to \pi^+\pi^+\pi^-$ amplitude which is not in full agreement with the experimentally measured $K^+ \to \pi^+\pi^+\pi^-$ result[39]. The $O(p^4)$ correction to $K^+ \to \pi^+\pi^+\pi^-$ is in good agreement with experiment and when this is applied to the loop diagram in $K^+ \to \pi^+\gamma\gamma$ it results in an $O(p^6)$ $K^+ \to \pi^+\gamma\gamma$ term. The overall effect of this correction is that the predicted $K^+ \to \pi^+\gamma\gamma$ branching ratio, at a given value of $\hat{c}$, increases by up to 30-40% (figure 10)[39] but the shape of the invariant photon mass spectrum, while altered (figure 11), is not changed enough to make a significant difference with the experimental resolution available. Therefore the spectrum shape is a more reliable means of estimating $\hat{c}$ than the branching ratio because it is both more sensitive to changes in $\hat{c}$ and less sensitive to theoretical uncertainties.

One last topic that should be mentioned are models to predict the values of the weak coupling constants $N_i$. Two models are frequently men-

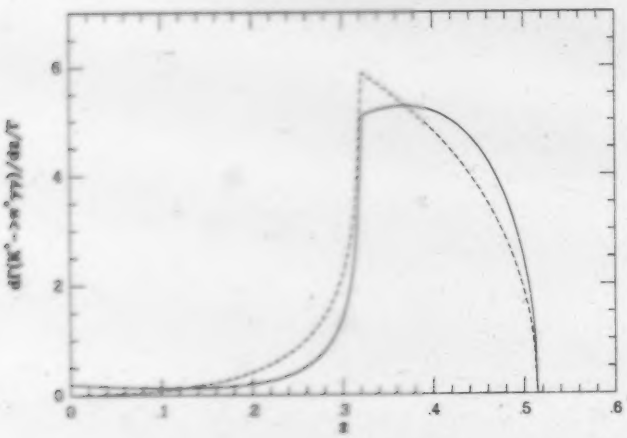


Figure 11: $K^+ \to \pi^+\gamma\gamma$ invariant photon mass spectrum at $\hat{c} = 0$ calculated to $O(p^4)$ (dashed line) and with the inclusion of the $O(p^6)$ unitarity correction (solid line).

tioned in the literature, the factorization model (FM) and the weak deformation model (WDM)[39, 40, 41, for both models]. Both models assume that the strong effective Lagrangian, $\mathcal{L}_{ST}$, determines the structure of the weak Lagrangian, $\mathcal{L}_{\Delta S=1}$, so that the unknown weak constants, $N_i$, can be expressed in terms of the more easily measured strong constants, $L_i$. The factorization model starts with the same effective weak Hamiltonian that was used to find $\mathcal{L}_{\Delta S=1}$ with the heavy quarks and $W, Z$ already integrated out and the weak vertices written as four-quark point interactions, $\mathcal{H}_{\text{eff}}^{\Delta S=1} = (G_F\sqrt{2})V_{ud}V_{us}^*C_i(\mu^2)Q_i + \text{H.C.}$, where $C_i$ are Wilson coefficients, $\mu$ is the QCD renormalization scale, and $Q_i$ are four-quark operators. The assumption is made that each $Q_i$ can be factorized as products of two left-handed quark currents. Under chiral perturbation theory the quark currents are identified via;

$$\overline{q_{iL}}\gamma^\mu(1-\gamma_5)q_{jL} \quad \leftrightarrow \quad \frac{\delta S}{\delta l_{\mu,ij}} \tag{29}$$

where $i, j$ are flavour indices, $q_L$ are left-handed quark fields and $S$ is the strong effective chiral action in terms of $U$ and external fields $l_\mu, r_\mu, s, p$ (see

equations 10, 11 noting that $l_\mu = v_\mu - a_\mu$ and $r_\mu = v_\mu + a_\mu$). The action $S$ of course decomposes in the same manner as $\mathcal{L}_{\rm ST}$ so the currents can be written as $J^1_\mu \equiv \delta S_2/\delta l^\mu = -i(f^2/2)U^\dagger D_\mu U$, $J^3_\mu \equiv \delta S_4/\delta l^\mu$, etc. At $O(p^2)$ the FM gives the usual $\mathcal{L}_2^{\Delta S=1}$ while at $O(p^4)$ it gives the weak Lagrangian as $\mathcal{L}_{\rm 4FM}^{\Delta S=1} = 4k_f G_8 {\rm TR}[(1/2)(\lambda_6 - i\lambda_7)\{J^1_\mu, J^{\mu 3}\}] + {\rm H.C.}$ for an undetermined constant $k_f$. The weak coupling constants relevant to $K^+ \to \pi^+\gamma\gamma$ are given by;

$$N_{14}^{FM} = 2k_f(-L_9 - L_{10} - 2H_1) \quad (30)$$

$$N_{15}^{FM} = 2k_f(-2L_9) \quad (31)$$

$$N_{18}^{FM} = 2k_f(L_{10} - H_1) \quad (32)$$

The value of $k_f$ is expected to be of $O(1)$ but is not determined by the model, the choice $k_f = 1$ is referred to as the naive factorization model and results in $\hat{c} = -2.3$.

The origin of the weak deformation model is best explained in an alternative notation often used in ChPT. A new matrix, $u$, is defined as the square root of the matrix, $U$, such that $U = uu$. Then defining $u_\mu \equiv iu^\dagger D_\mu U u^\dagger$ the strong Lagrangian, $\mathcal{L}_2^{\rm ST}$, (equation 10) can be written as

$$\mathcal{L}_2^{\rm ST} = \frac{f^2}{4}{\rm TR}(u_\mu u^\mu) + {\rm TR}(u^\dagger \chi u^\dagger + u\chi^\dagger u) \quad (33)$$

The weak deformation model is inspired by the observation that the octet portion of the weak Lagrangian, $\mathcal{L}_2^{\Delta S=1}$ (equation 14), can be obtained from the first term in equation 33 with the replacement

$$u_\mu \to u_\mu + G_8 f^2\{u_\mu, u\lambda_6 u^\dagger\} - (2G_8 f^2/3){\rm TR}(u_\mu u\lambda_6 u^\dagger) \quad (34)$$

The assumption is made that not just $\mathcal{L}_2^{\Delta S=1}$ but the entire weak octet Lagrangian can be obtained, term by term, from the strong ChPT Lagrangian using the 'deformation' on $u_\mu$ in equation 34 and an additional deformation given by

$$\Gamma_\mu \to \Gamma_\mu + \frac{1}{2}iG_8 f^2\{u_\mu, u\lambda_6 u^\dagger\} - \frac{1}{3}iG_8 f^2 {\rm TR}(u_\mu u\lambda_6 u^\dagger) \quad (35)$$

$$\Gamma_\mu \equiv \frac{1}{2}(u^\dagger(\partial_\mu - ir_\mu)u + u(\partial_\mu - il_\mu)u^\dagger) \quad (36)$$

If $\mathcal{L}_4^{\rm ST}$ (equation 11) is written in terms of $u$ and $\Gamma$ and the deformations in equations 34 and 36 applied to obtain $\mathcal{L}_4^{\Delta S=1}$ then the weak coupling constants, $N_i$, will be related to the strong coupling constants, $L_i, H_i$, in a similar manner to the factorization model. In fact to $O(p^4)$ the weak deformation model is equivalent to the factorization model with $k_f = 1/2$ thus giving a prediction of $\hat{c} = 0$ for $K^+ \to \pi^+\gamma\gamma$ .

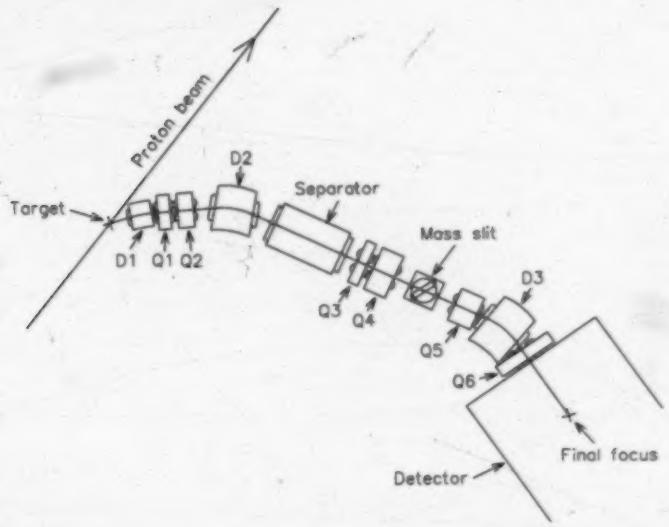


Figure 12: A schematic of the LESB 1 beamline used by E787 from 1988-1991.

# 3 Detector Description

The E787 detector first became operational in 1988 with incremental improvements being made every year up to 1991. After 1991 a series of major upgrades were made to the detector, the beam line and the readout electronics. One of these upgrades, the ultra-thin drift chamber (UTC), is described here, but from the standpoint of the $K^+ \to \pi^+\gamma\gamma$ data analysis only the detector at the time the data was taken, 1991, is relevant.

## 3.1 The Beamline

The AGS at Brookhaven produced a proton beam with energy around 28GeV. Kaons were produced when the protons hit a platinum target, however to separate the kaons from the large number of other particles produced and to ensure that the resulting kaon beam was well collimated and of known energy required a separate beamline designed for the E787 experiment. The LESB 1 (Low Energy Separated Beam) beamline is shown in figure 12 and consisted first of a dipole, D1, which selected low momentum positive particles emerging at roughly 10.5 degrees from the production target. After

passing through two focusing quadrupoles, Q1 and Q2, the particles then entered the main dipole, D2, which bent the beam and thereby restricted the momentum range of the particles which entered the next beamline element. The electrostatic separator after D2 used magnetic and electric fields at right angles to each other tuned so that a kaon with the mean momentum selected by D2 would not be deflected. The beam was then focussed by two more quadrupoles, Q3 and Q4, and passed through the mass slit which was simply a collimator with adjustable aperture. The net effect of D2 and the electrostatic separator was to disperse the incoming particle beam in two dimensions based on the momentum and velocity of the particles. By selecting a particular portion of this two dimensional region the mass slit, as its name implies, tended to select particles of a particular mass. The beam went through two more quadrupoles and another dipole before entering the detector, these last elements were primarily for focusing the beam.

The total length of the beamline was 14.2m and approximately 90% of the kaons which entered at D1 decayed before reaching the detector. Despite this the ratio of pions to kaons was only 2:1 *at* the detector. The proton beam from the AGS had a 'spill' length of about 1.6 seconds and the kaons tended to be uniformly spread out over that period of time which helped prevent pile-up in the detector target. In 1991 the typical number of kaons which stopped in the E787 target per spill was about 300000.

## 3.2 Overview

Although E787 was a fixed target experiment the detector design[42] was very similar to a collider detector in terms of symmetry since the incoming kaons were stopped and decayed at rest. Since the two main decay modes of positive kaons are $K^+ \to \mu^+\nu$ and $K^+ \to \pi^+\pi^0$ the detector needed to have extremely good pion/muon differentiation and nearly $4\pi$ sr photon detection. It was this last feature in particular that made it possible to observe $K^+ \to \pi^+\gamma\gamma$ decays. Figure 13 shows the side view of the detector while figure 14 shows an end view of the active components and figure 15 show an expanded view with scale.

All of the active components of the detector were contained within a large solenoid which maintained a 1T field through the volume of the detector and also acted as the support structure for the several tons of lead and plastic that made up the detector subsystems. The magnet was 3.3m long by 5m in diameter with an internal usable volume of 2.22m by 2.96m (figure 13). By enclosing the detector entirely within the magnet there was no concern that parts of the magnet might interfere with photon detection although it

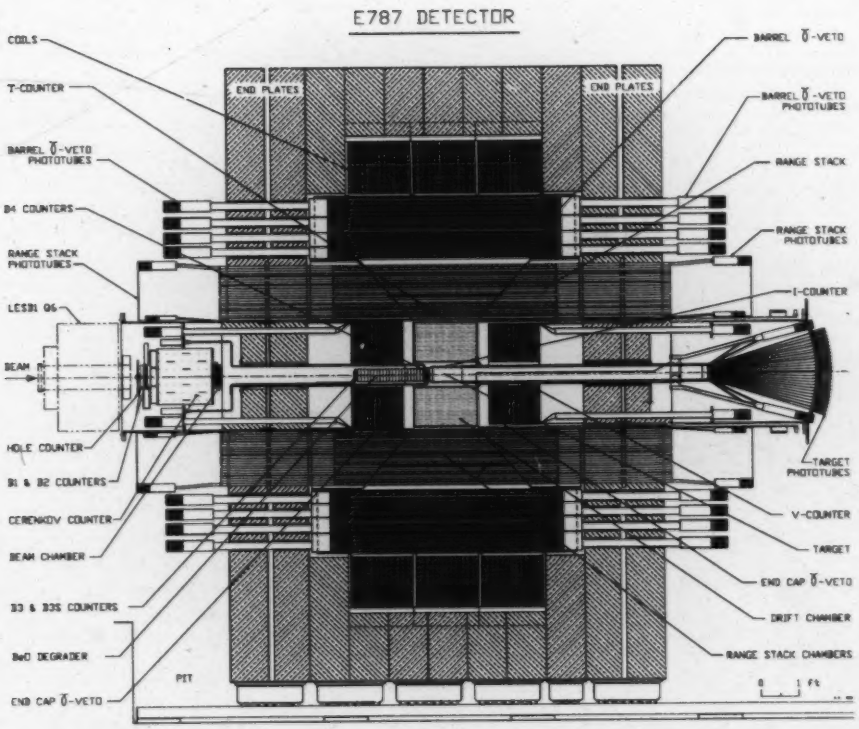


Figure 13: Cross sectional schematic side view of the E787 detector.

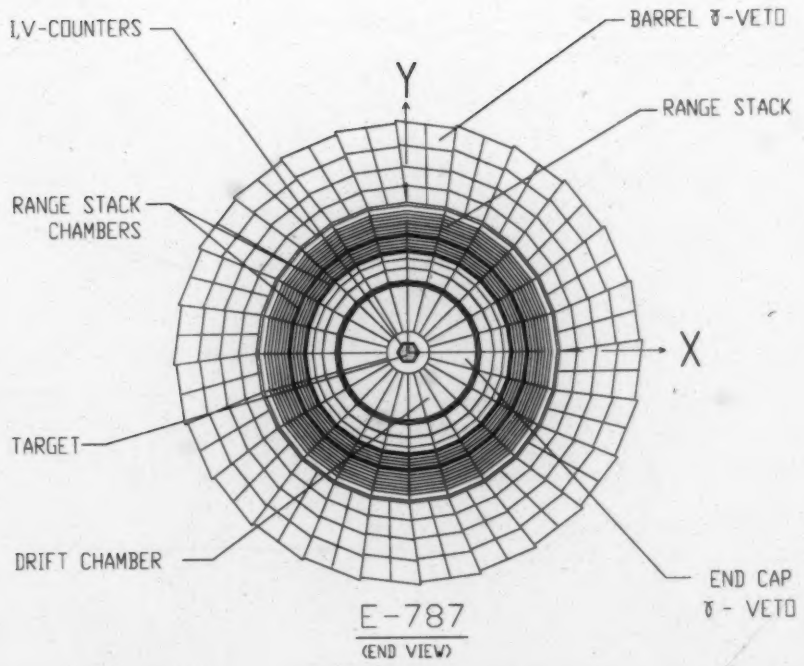


**Figure 14: Schematic end view of the E787 detector showing the active elements in the center plane (z=0) of the apparatus.**

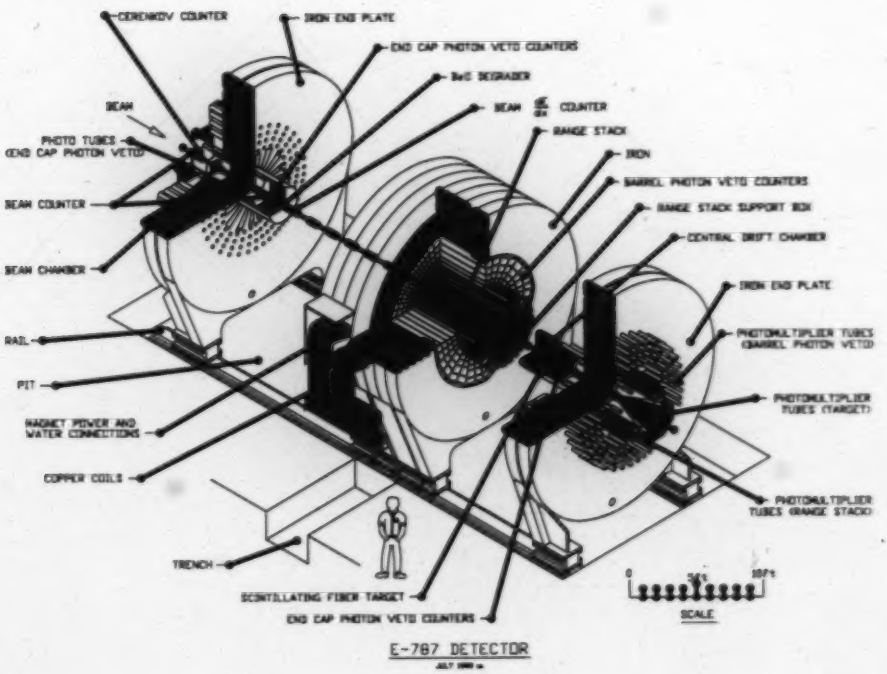


Figure 15: Isometric view of the E787 detector with the magnet sections separated.

did require that a lot of the metal in the end plates be removed to provide exits for light guides so that the photomultiplier tubes (PMTs) could be located outside of the main magnetic field (all PMTs were also individually shielded against fringe fields which were in the range of $2 \cdot 10^{-3}$T). The magnet could be separated into 3 sections as shown in figure 15. The magnet coils drew about 1.1MW of power and were water cooled to maintain the internal temperature of the magnet at about 30 degrees C. Dry nitrogen gas was flowed into the interior of the magnet to keep the humidity levels low around the detector.

## 3.3 Beam Counters

Going through the apparatus component-by-component from the standpoint of an incoming kaon, the first items encountered were a series of beam counters. These were primarily used for beam tuning, flux monitoring and to ensure that the incoming particle was a kaon, as opposed to a pion. The incoming kaons had a nominal momentum of 750-800MeV/c and first passed through two 3mm thick multi-finger scintillator hodoscopes, known as B1 and B2 (figure 13 and 16), multiple segments were used to decrease the instantaneous rate seen by each photomultiplier and the two counters overlapped in such a way that any gaps in the first counter were covered by the second. The rate information from these counters was stored in the beam scaler records recorded with each beam spill. Their main function was for use in beam tuning. This was also true of the 'hole counter' (figure 16), which was another 3mm thick pair of scintillation counters located 7.5mm above and below the detector axis which monitored the edges of the beam profile, although the hole counter was also used in the $K^+ \to \pi^+\nu\bar{\nu}$ analysis to look for extra particles entering the detector at the same time as the desired event.

Next was a Cherenkov counter used to differentiate between kaons and pions and one of the key components in the trigger logic of all of the analysis triggers. The Cherenkov counter consisted of a lucite radiator 25.4mm thick, a series of mirrors and two rings of photomultiplier tubes fed by Winston cones (figure 17). At 800MeV/c momentum kaons passing through the radiator produced light which left the surface of the lucite and was reflected by the parabolic mirrors into a ring of 10 Winston cones (in this case the cones were hollow with aluminized inner surfaces) each of which was connected to a 50mm PMT. However, at the same momentum a pion produced a light cone in the lucite that was totally internally reflected within the radiator until it encountered the conical mirrors at either end where the light was

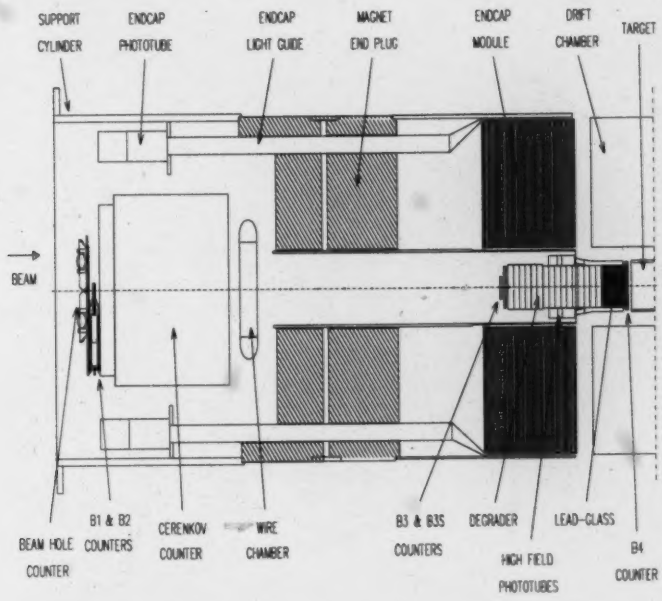


Figure 16: Detailed section of figure 13 showing the beam counters. Note that the B3 counters were removed for the 1991 run.

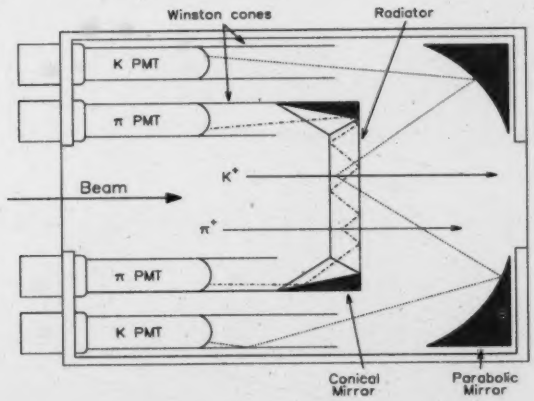


Figure 17: Schematic showing the design of the Cherenkov counter and a typical light path for both pion and kaon Cherenkov light.

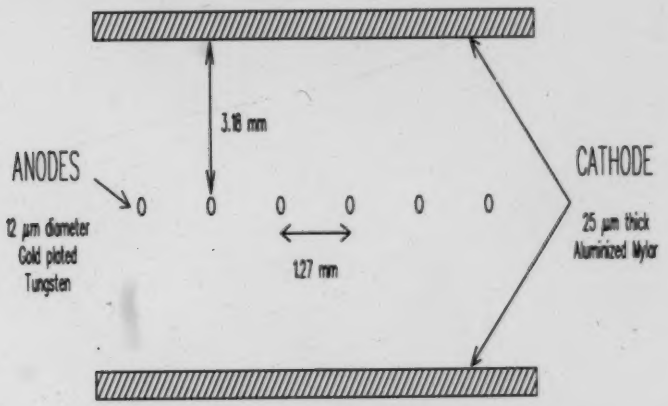


Figure 18: The layout of the beam proportional chamber

reflected into a second ring of 10 PMTs. By requiring multiple PMTs to fire in either the kaon or pion rings the effects of random noise or light leaking into the wrong ring were greatly reduced. The typical number of PMTs to define either a kaon or a pion was 6.

After the Cherenkov counter was a multiwire proportional chamber which consisted of three planes of 12$\mu$m gold plated tungsten sense wires between 25$\mu$m aluminized mylar cathode planes (figure 18). This chamber was used for determining the beam profile and in the $K^+ \to \pi^+\nu\bar{\nu}$ analysis it was used to look for a second particle in coincidence with the incident kaon which could indicate that a beam pion had given a false $K^+ \to \pi^+\nu\bar{\nu}$ trigger. Because $K^+ \to \pi^+\gamma\gamma$ was not sensitive to these pion scatter events the beam chambers were not used in this analysis.

Up to this point the incident particle had not lost very much of its momentum. It then entered a beryllium oxide degrader approximately 43cm long where the kaon lost most of its energy. BeO was used because it has a high density but low atomic number which minimized the amount of multiple scattering. Note that originally 53cm of BeO were used but that in 1991 the last 10cm were removed so that a lead glass Cherenkov counter could be added (this is shown in figure 16 but not in the full detector views). This lead glass counter served three different functions. It completed the reduction of kaon momentum necessary for the kaon to stop in the target. It also served as a pion Cherenkov counter, using PMT tubes capable of operating within a high magnetic field, to make sure that the incident particle was not a pion (kaons leaving the degrader would not have enough energy to

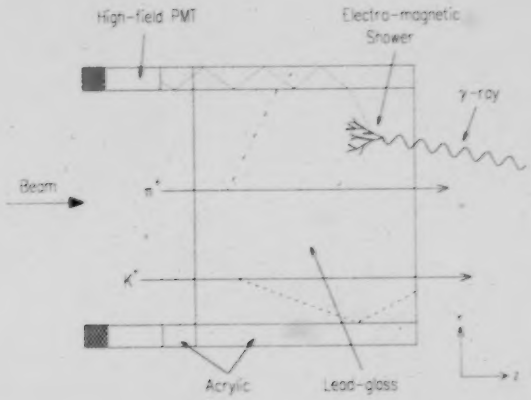


Figure 19: The typical effect of kaons, pions or high energy photons on the lead glass Cherenkov counter

produce Cherenkov radiation). Finally it served as part of the photon veto system, helping to plug what would otherwise have been the beam hole, with photons that converted in the lead glass resulting in a signal in the high field PMTs (figure 19). As with the first Cherenkov counter its use as a pion or photon veto was based on phototube multiplicity. For $K^+ \to \pi^+\gamma\gamma$ the pion detecting ability of the lead glass Cherenkov was not needed but it was used as a photon veto, details of which will be given in the event selection section (section 4.3.3.4).

Finally the last beam counter, B4 (figure 16), immediately before the target was a pair of 6mm thick multi-finger scintillators similar to B1 and B2. Timing in this counter was used along with the kaon Cherenkov as part of the trigger logic for identifying an incoming kaon. dE/dx and hit multiplicity could also be used to spot multiple particles passing through B4.

Of these counters only the lead glass Cherenkov was used in the offline $K^+ \to \pi^+\gamma\gamma$ analysis. The kaon Cherenkov and B4 counter entered as part of the level 0 trigger, which will be discussed in more detail in section 4.2.1.

## 3.4 The Target

The first of the major detector subsystems was the target. In the trigger an incoming kaon was defined as a coincidence between the B4 counters, the kaon Cherenkov, $C_K$, and the target. The target, of course, was not one

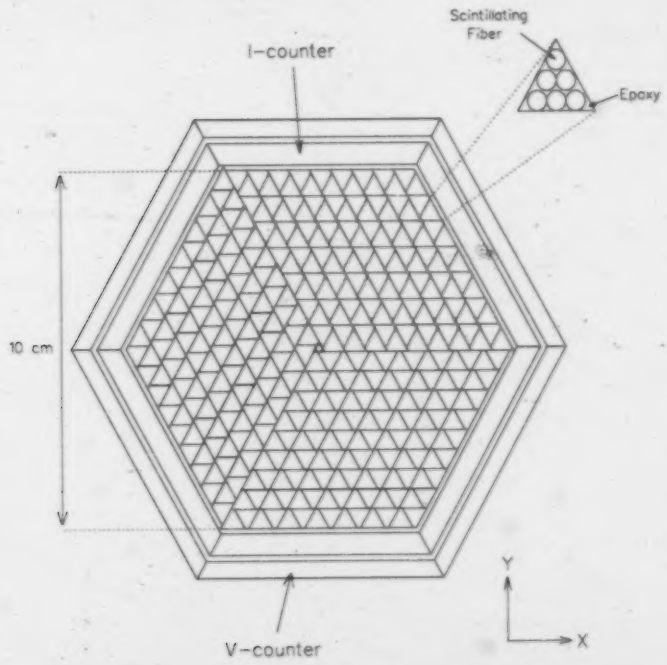


Figure 20: Cross section of the scintillating fiber target

active element but actually a hexagonal bundle 10cm across composed of 2269 2mm diameter scintillating fibers 3.12m long. The 2m of fiber within the detector (figure 13), were epoxyed into 378 triangles of 6 fibers each (figure 20) with a single fiber running down the center of the target. Each triangle was read out, at the downstream end of the detector where the fibers fan out, by a 1cm PMT. The lengths of all the fibers, and the flat upstream face of each fiber, were aluminized to improve their light collection efficiency and prevent crosstalk between fibers. With this packing 75% of the target was active with the inactive portion primarily consisting of the epoxy used to create the triangular bundles. To make the response of the overall target as uniform as possible the fibers within each triangle where matched for light output and the quantum efficiency of the PMTs was matched to the output of the triangles.

A typical kaon entering the target traveled several centimeters along the axis of the target passing though only a small number of triangles but, due

to the long path length and high dE/dx as the kaon slowed down, leaving a fairly large amount of energy in each triangle, typically over 5MeV. The kaon came to rest then, after a few nanoseconds, decayed into a pion which then exited the target. For the pion to enter the fiducial volume of the detector and satisfy the online triggers, it had to travel generally perpendicular to the fibers and be minimum ionizing leaving a track of hit triangles with low energy, typically less then 2MeV per triangle (figure 21). In the offline analysis the pattern of hit fibers was analyzed using both energy and timing information to identify the cluster of hits associated with the kaon (and therefore the position of the stopping vertex in the x-y plane), the track of pion hits leading away from the kaon cluster and any disconnected hits which could indicate a photon conversion or an extra particle in the detector. By looking for a time delay between the pion track and the kaon cluster it could be verified that the kaon was at rest before it decayed.

One problem with the target design was that the entire length of the fibers was active but only stops in the first 20cm of the target were of interest. To deal with this two layers of scintillator surrounded the target, the I counters (IC) and V counters (VC) (figure 20). The 6 I counters were 24cm long to define the fiducial region of the target and 6.4mm thick, the time difference between the IC hit and the kaon Cherenkov hit was used in the trigger to try and ensure that the kaon stopped before it decayed. The V counters overlapped the ICs by 6mm then extend an additional 195cm down the length of the scintillating fibers to veto events where the kaon had stopped downstream of the fiducial target volume.

## 3.5 Drift Chamber

Surrounding the target, and the reason the entire detector was contained within a 5m diameter solenoid, was one of the most important subsystems, the drift chamber (figure 13). The active volume of the chamber was 51cm long and 34cm in depth and provided the momentum information on the charged decay products of the kaon decay as well as directional tracking in xy and z. This tracking information was used to refine the position of the decay vertex and correct the path length of the charged track through the target and other detector components for the tracks dip angle (the angle of the track to the longitudinal, or z, axis of the detector).

The drift chamber consisted of 5 concentric layers (figure 22) of drift cells. Each cell consisted of two cathode wire planes of 19 Be-Cu wires strung 2.54mm apart from each other (note that cathode planes were shared by adjacent cells) and a central anode wire plane composed of 8 20$\mu$m gold

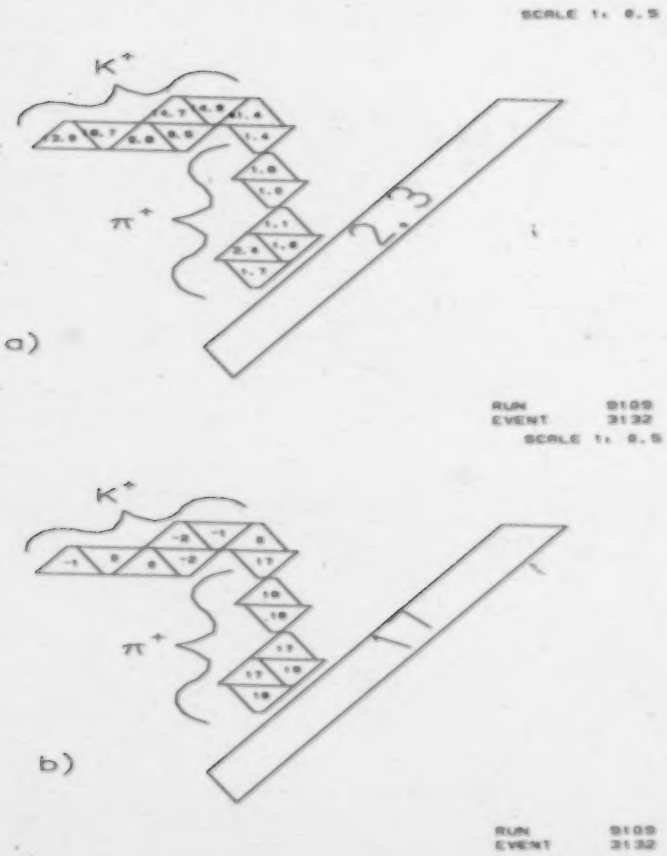


Figure 21: A typical $K^+ \to \pi^+$ decay in the target showing ADC (top) and TDC (bottom) information.

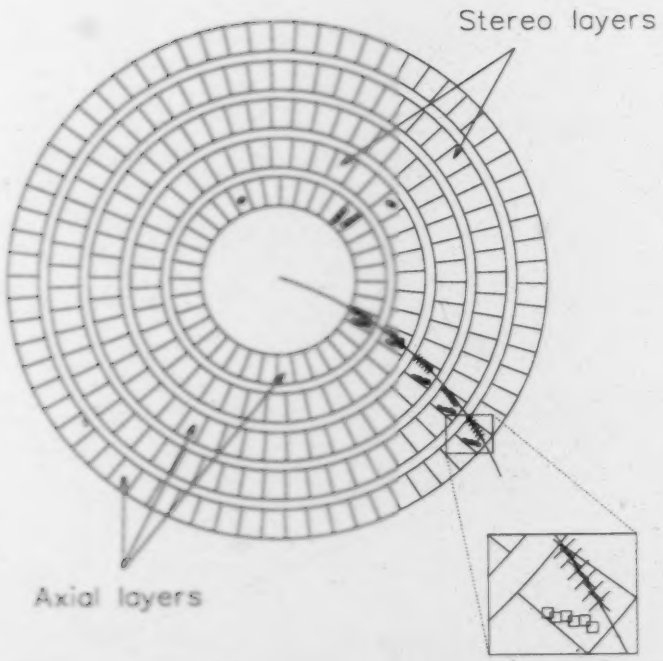


Figure 22: Cross section of the drift chamber showing the 5 layers of drift cells and a typical charged track including the two possible locations each single wire hit could correspond to (crosses and squares).

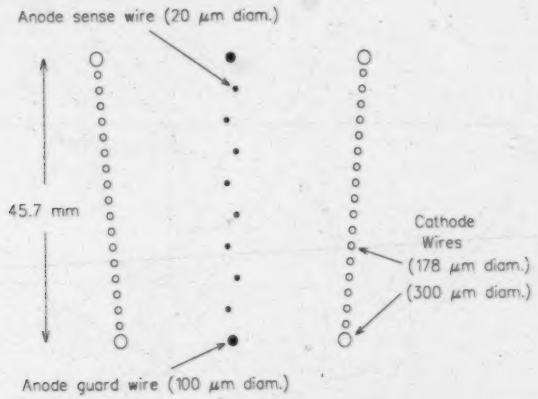


Figure 23: View of a single drift chamber cell.

plated tungsten wires 5.08mm apart from each other with two larger diameter Be-Cu guard wires at either end of the anode wires (figure 23). Because of the fundamental left-right ambiguity in determining which side of the anode plane the charged track actually passed through, the anode wires were staggered by $\pm 254\mu$m from the centerline of the cell. The number of cells per layer was 36, 40, 50, 60 and 70 going from the inner to outer layer. This means that the width of the individual cells varied from layer to layer between 24 and 34mm. To provide a $z$ measurement the wires in layers 2 and 4 were offset by one cell at the downstream end relative to the upstream end, i.e. the wires in these two layers were not parallel to the axis of the chamber but instead were offset by 3.1 and 4.0 degrees. To eliminate the variation in electric field which would have resulted due to the radial dependence of the anode/cathode spacing the high voltage to the cathodes was applied through a compensating resistor chain. It should be noted that to avoid the distortions in the electric field near the edges of the cells only the center 6 anode wires in each cell were read out. The chamber used a 50-50 mixture of argon and ethane with a small amount of ethanol. The drift velocity of electrons in this gas was about $50\mu$m/ns and was fairly insensitive to changes in temperature and pressure avoiding the need to monitor and adjust for those variables.

Although the momentum measurement of the drift chamber was in principle independent of the other detector subsystems, in practice the variable that was desired was normally the momentum of the charged particle at the moment the kaon decayed, i.e. the momentum at birth, and so the measured

momentum had to be adjusted for energy lost in the target and the inner carbon fiber wall of the drift chamber.

## 3.6 Range Stack

The range stack was a series of 21 concentric layers of scintillator surrounding the drift chamber and extending much further in both the upstream and downstream directions (figure 13). It was a requirement in the trigger that the charged track from the kaon decay enter the range stack. In most cases the charged particle would also stop in the range stack and its decay could be observed using high speed digitizers. Figure 24 shows one of the 24 azimuthal sectors the range stack was divided into (figure 14). The innermost layer, known as the 'T' counter, was 52cm long and 6.35mm thick, all the other layers were 1.8m long and 19.05mm thick although it should be noted that for readout purposes some of the inner layers were multiplexed as shown in figure 24 (4 layers formed the A counter, 3 the B counter and 2 the C counter). All of the analysis triggers required a coincidence between the T and A counters in one sector in addition to the beam counter requirements. The main event timing was taken from the time of the range stack hits, this was the so called 'prompt' time and referred either to the time of the T·A coincidence or a more refined time found offline by considering all of the range stack counters hit by the charged track. In addition to the scintillator there were two layers of proportional chambers (figure 24) located in the range stack which provided $xyz$ information to refine the tracking of the charged particle through the range stack. In the case of the $K^+ \to \pi^+\gamma\gamma$ trigger the low momentum of the $\pi^+$ prevented it from ever reaching even the inner of these wire chambers and so they were not used.

Light guides at either end of each range stack (RS) layer transmitted the scintillation light to PMTs located outside of the main magnet. In addition to the conventional readout electronics each RS PMT was also connected to a transient digitizer, or TD, channel which sampled the pulse height of the analog signal from the tube every 2ns from approximately 3$\mu$s before the prompt time to 6$\mu$s after prompt. This high sampling speed made it possible to observe the decay chain of whatever charged particle had stopped in that RS counter. Specifically, a $\pi^+$ decays as $\pi^+ \to \mu^+ + \nu$ with a lifetime of about 26ns, while a $\mu^+$ will decay by $\mu^+ \to e^+ + 2\nu$ with a lifetime of 2.2$\mu$s. The kaon decay modes of interest were generally of the form $K^+ \to \pi^+ + \cdots$ so a means was needed of rejecting events where the kaon had decayed by $K^+ \to \mu^+ + \cdots$. The muon produced by the pion decay had 4MeV of kinetic energy which was deposited locally due to the short range of such a

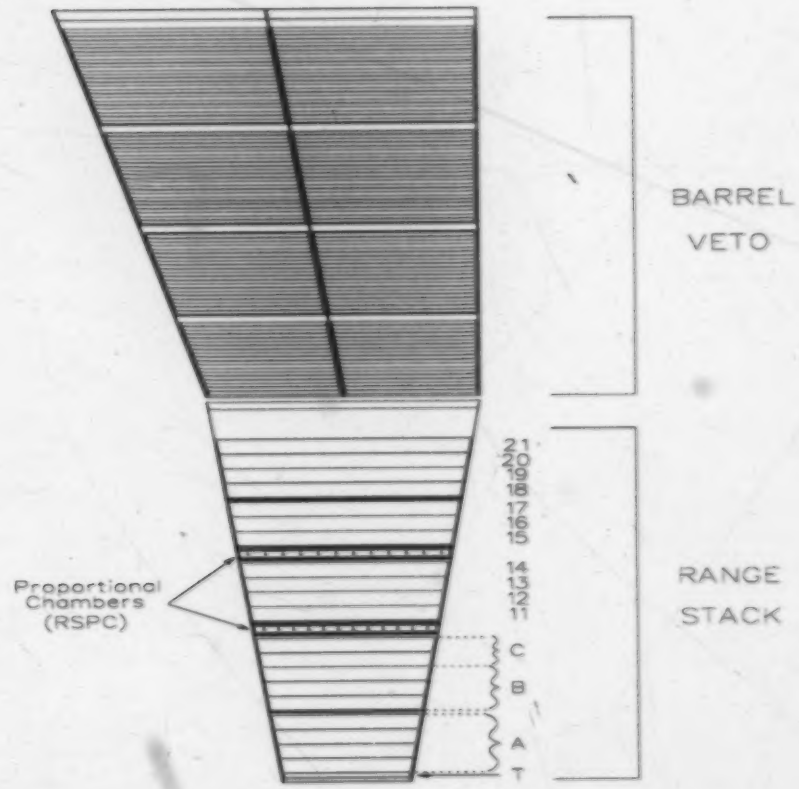


Figure 24: Design of a single range stack (and two barrel veto) sectors.

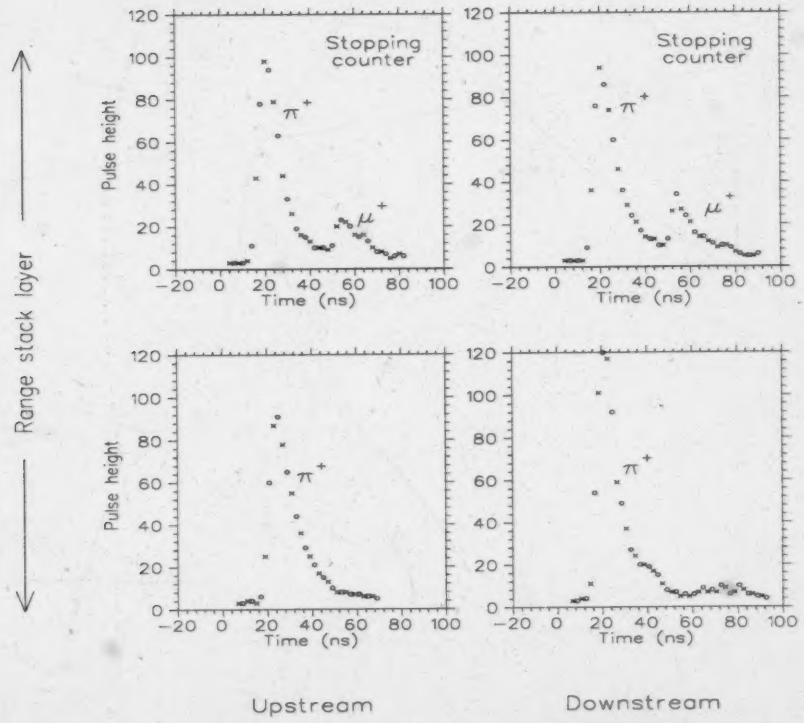


Figure 25: An example of the TD pulse shapes from either end of the $\pi^+$ stopping counter (top) and the RS counter one layer in from the stopping counter which the $\pi^+$ passed through before decaying (bottom).

low energy muon, thus the stopped pion differed from the stopped muon by this extra 4MeV pulse riding on the tail of the original pion pulse. Fitting the data observed by the TDs with either a single (muon) pulse hypothesis or a double (pion) pulse hypothesis (figure 25) allowed one to select pions with a high rejection rate (approximately 50) for muons. However, because the pion lifetime was short the decay pulse tended to appear in the tail of the stopping signal rather than as a detached pulse and in some cases would not produce enough of a distortion in the pulse shape for the event to be recognized as a double pulse and instead the event was rejected as a muon. This acceptance loss became worse as the size of the stopping pulse increased and the relative size of the 4MeV decay pulse to the overall

pulse area decreased. The $K^+ \to \pi^+\gamma\gamma$ trigger only accepted stops in the A and B layers of the RS which, because they were multiplexed and therefore thicker, tended to have larger amounts of energy deposited in the stopping counter. So even though the TDs could have been used to obtain a factor of 50 rejection for muons it was decided not to incur the pion acceptance loss which ranged up to 60% in A layer. The TD cuts were still usable in selecting events for background studies, acceptance measurements and verifying that there were no muons in the final event sample.

## 3.7 Photon Vetoes

The remaining active components of the detector were used for photon detection. The end caps (EC) filled the region on either side of the drift chamber between the range stack and the target/beam axis, while the barrel veto (BV) surrounded the outside of the range stack (figure 13). Both were composed of alternating layers of scintillator and lead to ensure that the photons would convert within them. It is this almost $4\pi$sr photon coverage which made it possible to use the E787 detector for studying photon dominated decays such as $K^+ \to \pi^+\gamma\gamma$ .

Because the decay photons were expected to originate in the target the end caps were arranged with the lead/scintillator layers perpendicular to the axis of the detector. Each end cap was composed of 24 azimuthal modules with 66 5mm thick scintillator layers alternating with 1mm thick lead sheets to give a total of 12.4 radiation lengths of material. Because the light guides leading to the PMTs had to run parallel to the axis of the detector the scintillator was not read out directly but had a sheet of wavelength shifter which covered the wider end of all 33 scintillator layers (figure 26). Each of the 24 petals was then enclosed in a stainless steel can with the wavelength shifter being connected via a light guide to a PMT outside of the magnet. In the $K^+ \to \pi^+\gamma\gamma$ analysis it was decided that the energy and spatial resolutions of the ECs were not good enough to use them for actually measuring $K^+ \to \pi^+\gamma\gamma$ photons, instead the events were vetoed both online and offline if significant prompt energy was observed in either end cap.

The barrel veto was the system exclusively used to detect and measure the $K^+ \to \pi^+\gamma\gamma$ photons. The barrel was segmented into 48 azimuthal modules and 4 radial layers. One of the important features of the BV was that the modules were tilted to make sure that the inactive edges of the azimuthal modules did not point back toward the target (figures 14 and 24). This helped to make sure that photons could not escape through the 'cracks' formed where barrel veto modules met. The four radial layers were

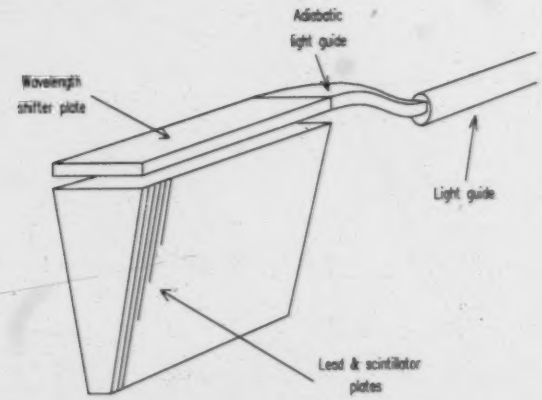


Figure 26: The construction of one end cap module.

composed of 16, 18, 20 and 21 5mm thick scintillator sheets alternating with 1mm lead as was the case in the end caps. The total thickness of the BV was 14.3 radiation lengths. The active section of the BV was 1.9m long and was read out at both ends using light guides and PMTs. Because they were read out at both ends it was also possible to use end-to-end timing and energy to estimate the z position at which the photon had converted.

Accurate $z$ position information was required in the barrel veto to look for events with overlapping photons, and to produce the best possible invariant photon mass, $M_{\gamma\gamma}$. It was also important to eliminate counter-to-counter variations which might interfere with the overlapping photon cuts. There were two independent ways to measure the $z$ position, using either timing or energy, which resulted in four constants needing to be measured for every counter.

$$z_t = \frac{c}{2}(t_1 - t_2) + z_{0_t} \tag{37}$$

$$z_a = \frac{a}{2}\ln\frac{E_1}{E_2} + z_{0_a} \tag{38}$$

$c$ = The speed of light in that counter.

$t_1, t_2$ = The TDC time at either end of the BV counter.

$z_{0_t}$ = A constant offset that includes such factors as TDC pedestals.

$a$ = The attenuation length of light in that counter.

$E_1, E_2$ = The pedestal subtracted ADC energy at either end of the BV.

$z_{0_a}$ = A constant offset including such factors as multiplicative ADC energy calibrations.

Using cosmic ray data taken with the main magnetic field turned off an iterative calibration was done on several of the detector subsystems. First the drift chamber was calibrated for use with cosmic rays, then using the drift chamber tracks the range stack chambers were calibrated. Next using both the drift chamber and range stack chamber results the range stack attenuation lengths and speed-of-light values were measured. And finally using all of the available $z$ information from these three subsystems the barrel veto itself was done. Cosmic data was used to obtain speed-of-light and attenuation length values for each BV counter (a typical result being around 15cm/ns and 100cm respectively).

Cosmics provided the best available means of measuring the speed of light and attenuation lengths in the BV, however, they didn't necessarily provide the best means of measuring the $z$ offsets for real data. In terms of the ADC and TDC calibration values at either end of a BV module the $z$ offsets were given by:

$$z_{0_t} = \frac{c}{2}(t_{0_1} - t_{0_2}) \tag{39}$$

$$z_{0_a} = \frac{a}{2}\ln\frac{E_{0_2}}{E_{0_1}} \tag{40}$$

$t_{0_i}$ = The additive TDC calibration constant for end i of the BV module.

$E_{0_i}$ = The multiplictive ADC calibration constant for end i of the BV module.

The offsets were thus sensitive to the timing and energy calibration at either end of each BV module and may have differed for cosmics and other monitor triggers. To measure the offsets the photons from $K^+ \to \pi^+\pi^0$ data were used, with the speed-of-light and attenuation lengths found using cosmics, and the knowledge that the two photons had to reconstruct to a $\pi^0$ and the entire event to a stationary $K^+$.

## 3.8 Data Acquisition

A very brief overview of the data acquisition and online triggering will be helpful in understanding the $K^+ \to \pi^+\gamma\gamma$ analysis later on. Most detector systems were instrumented with both TDC's and ADC's with the exception

of the range stack which used TD's instead of TDC's. If an event was going to be kept the data from the various crates of electronics was first assembled together then passed to one of the ACP nodes, these were simple CPUs capable of running short programs. After the ACP farm the event data was written onto the data acquisition workstation and finally onto 8mm magnetic tape.

The online event selection did not make use of the TDC or ADC information with the exception of event selection done in the ACP nodes. Instead energy information from either individual counters or sums of different counters was applied by passing the input signal through a discriminator, if the signal was above some set threshold then a logic pulse was produced by the discriminator with a preset duration. Timing information between counters generally took the form of first passing the signal through a discriminator set at a threshold high enough to ensure that the counter was hit, then requiring a coincidence between the discriminated signals from the various counters.

Events of various types were selected by applying different logical triggers to the data. The triggers were categorized into different levels primarily on the basis of how quickly the decision could be made whether the event passed or failed the trigger. For example the level 0 triggers for K$\mu$2(1) and K$\pi$2(1) were:

$$K^+ \to \mu^+\nu \;:\; \mathrm{K_T}\cdot(\mathrm{T}\cdot\mathrm{A})\cdot\mathrm{B_{\bar{C}T}}\cdot(19_{\mathrm{CT}}+20_{\mathrm{CT}}+21_{\mathrm{CT}})$$
$$K^+ \to \pi^+\pi^0 \;:\; \mathrm{K_T}\cdot(\mathrm{T}\cdot\mathrm{A})\cdot\mathrm{B_{CT}}\cdot\overline{(19_{\mathrm{CT}}+20_{\mathrm{CT}}+21_{\mathrm{CT}})}$$

With the following definitions:

| | | |
|---|---|---|
| $\mathrm{K_T}$ | $\equiv$ | $\hat{\mathrm{C}}_{\mathrm{K}}\cdot\mathrm{B4}\cdot\mathrm{TG}\cdot\mathrm{spill}$ |
| $\hat{\mathrm{C}}_{\mathrm{K}}$ | $\equiv$ | A hit in the kaon Čerenkov counter |
| B4 | $\equiv$ | A B4 hodoscope hit |
| TG | $\equiv$ | Target energy |
| spill | $\equiv$ | The spill gate provided by the AGS |
| $(\mathrm{T}\cdot\mathrm{A})$ | $\equiv$ | A coincidence in the inner two layers of one RS sector |
| $\mathrm{X_{CT}}$ | $\equiv$ | A hit in RS layer X in the T · A sector or the two sectors counter clockwise of the T · A |

CT refers to 'charged track' and was used to take into account the curvature of a positive charged track in the field of the main magnet. There were

no additional trigger levels for K$\mu$2(1) or K$\pi$2(1), however a subset of the K$\pi$2(1) trigger, called K$\pi$2(2), was defined which had both a level 1 and level 2 trigger. The level 1 K$\pi$2(2) trigger grouped the 24 range stack sectors into 6 hextants, determined which hextant the $\pi^+$ stopped in, and required that there be less than 10 MeV of energy in each of the other hextants excluding the hextants on either side of the stopping hextant. This was the level 1 hextant cut which was applied to most of the actual physics triggers. In the case of K$\pi$2(2) there was also a level 2 cut which used the RS stopping sector and layer and looked for evidence in the TD's of a $\pi^+ \to \mu^+$ decay in that counter. The most complex and slowest trigger level was level 3 which was used only for the $K^+ \to \pi^+\gamma\gamma$ analysis and took place in the ACP nodes.

It was also common in the triggers that were intended to be used for actual physics analysis for a small fraction of the events at each trigger level to be written to tape regardless of whether or not they passed the higher trigger levels. This data was used to monitor the higher level triggers and also for measuring the acceptance of both online and offline cuts. So, for example, in the case of $K^+ \to \pi^+\gamma\gamma$ there was level 0 monitor data, which consisted of events that had passed level 0 but not had the level 1 or level 3 triggers applied, and level 3 failure data, which had passed both level 0 and level 1 but failed level 3. There was no level 2 trigger for $K^+ \to \pi^+\gamma\gamma$ .

## 3.9 Ultra Thin Drift Chamber (UTC)

As was mentioned earlier a number of major upgrades were performed on the E787 detector between the 1991 and 1994 runs, one of these was replacing the existing drift (jet) chamber with a new chamber of roughly the same dimensions but completely different, and state of the art, design. Although this new chamber was not used in the $K^+ \to \pi^+\gamma\gamma$ analysis, I was extensively involved in its prototyping, construction, installation and testing and have included it here in the detector description because the design of the chamber is itself quite interesting.

There were two primary goals to the detector upgrades, one was to allow the detector to handle much higher incident kaon rates and, more importantly, to improve the rejection of backgrounds for the $K^+ \to \pi^+\nu\bar{\nu}$ analysis. Since the drift chamber provides the only momentum measurement of the charged kaon decay product and the best tracking information on the path of this charged particle a large improvement was demanded of the new chamber. At the same time the drift chamber is one of the first components exposed to photons from potential $K^+ \to \pi^+\nu\bar{\nu}$ backgrounds, such as K$\pi$2, so the inactive mass of the chamber that might absorb, and therefore hide,

photons had to be reduced as much as possible.

### 3.9.1 Drift Chamber Principles

All drift chambers operate on the same basic principle of tracking the path of a charged particle passing through a gas. Unless it undergoes a nuclear interaction, a high energy charged particle will deposit energy in the material it passes through by ionizing random molecules along its path. If a constant electric field exists in the region of the ionization the ion pairs will drift along predictable paths toward either the cathode(s) or the anode(s). In principle, knowing the time, $t_0$, that the charged particle went through the gas volume, the time, $t_a$, that the first ionization electron reached the anode and its drift velocity, $w(t)$, the location of the point of closest approach between the track and the anode can be found. This assumes that an ion pair was produced at the point of closest approach, that this electron was the first to reach the anode and that the velocity of the charged particle is much higher than the drift velocity of the electrons in the gas, generally these assumptions are valid.

In practice a drift chamber generally contains a large number of anodes so that multiple hits are recorded for each track, the space-time relation, $\bar{x}(t_a - t_0) = \int_{t_0}^{t_a} w(t)dt$, giving the point of closest approach of the track for a particular anode is found directly by minimizing the chi-square of the track fit for a large number of events, rather than by directly measuring $w(t)$. Also the calculated track position relative to the anode for a particular drift time is generally not unique due to symmetries of the electric field around the anode wires. For example in the jet chamber there were two locations, one of the left hand side and one on the right hand side of the anode plane, which would result in the same drift time. This is the so called left-right ambiguity. For the UTC, where the electric fields are roughly cylindrical, the drift time corresponds to an ionization source somewhere on a circle of a given radius around the anode. Finally, to make a drift chamber practical the electric field strength around the anodes should be sufficiently high so that it operates in proportional mode not ionization mode. In other words once the electron is near the anode the mean energy it acquires between collisions should be higher than the ionization potential of the gas molecules. The electron will then produce additional ion pairs which will in turn produce more ionization until an avalanche of electrons reaches the anode. The typical gain due to this type of cascade, in proportional mode, is about $10^5$. Care must be taken to keep the electric field strength near the anode and cathode below the level where electron emission occurs at the surface of the cathode or

spontaneous ionization occurs at the anode. It is also necessary to keep the chamber from going into a Geiger mode where an avalanche anywhere along the anode results in additional avalanches along the length of the anode, and the resulting pulse on the anode wire becomes non-localized and of fixed amplitude regardless of the number of ion pairs coming from the track. The positive ions have been ignored in the above discussion due to their low drift velocity and the fact that field strengths at the cathodes are by design too low for them to produce an avalanche.

At this point it is possible to determine the path of the charged particle, however, if the entire chamber is placed in a constant magnetic field the trajectory of the charged particle will become a helix with radius, $R$, and pitch angle, $\theta$ (also referred to as the dip angle). The momentum of the charged particle perpendicular to the magnetic field can be determined by measuring the radius of curvature of its track[2, p. 146].

$$P\cos\theta = 0.3qBR \tag{41}$$

where

$P$ = The particle momentum in MeV/c

$\pi - \theta$ = The angle of the track relative to the B field axis

$q$ = The particle charge in units of the electron charge

$B$ = The magnetic field in kG

$R$ = The radius of curvature of the track in cm

If the pitch angle, $\theta$, can also be measured then the total momentum of the charged particle is known. It should be noted that the presence of the magnetic field also changes the trajectories of the drifting electrons and therefore the space-time relation for the drift cells must be remeasured.

A number of factors contribute to the error in the momentum measurement. The two most significant are the overall effect of the individual position measurement errors and multiple scattering of the charged track as it passes through the drift chamber gas. An approximation to the error in the curvature, $k = 1/R$, caused by the position measurement errors for 10 or more measurement points is given by[2, p. 147];

$$\delta k_m \approx \frac{\delta x}{(L\cos\theta)^2}\sqrt{\frac{720}{N+4}} \tag{42}$$

$N$ = The number of position measurements

$L$ = The total track length

$\delta x$ = The error in the individual position measurements

perpendicular to the track

The error due to multiple scattering in the chamber is given by[2, p. 147];

$$\delta k_s = \frac{0.016q}{LP\beta\cos^2\theta}\sqrt{\frac{L}{X_0\rho}} \tag{43}$$

$\beta$ = $v/c$ = The speed of the charged track

$X_0$ = The radiation length of material along path L

$\rho$ = The density of the scattering medium

$P$ = The momentum of the charged particle in GeV

These errors must be added in quadrature to give the total error, $\delta k = \sqrt{(\delta k_s)^2 + (\delta k_m)^2}$. It can be seen that increasing the length, $L$, of the track in the chamber reduces both errors while reducing the 'thickness', $X_0\rho$, of the chamber reduces multiple scattering. These were two of the goals of the UTC.

### 3.9.2 Internal Design

The design that was chosen consisted of 5 concentric cylindrical 'superlayers' separated by foils with only three of the layers being active (figure 27). The foils were 25$\mu$m thick Upilex [6] coated with first a 1200Å thick layer of copper then 300Å of nickel. A strip pattern was etched[49] onto the surface of the foils by removing a 1mm wide line of metal every 8mm. The foils were arranged so that the strips made an angle of about 45 degrees to the wires. Each active superlayer consisted of 7 concentric layers of wires, with each layer being either all cathodes or cathodes alternating with anodes, to give a simple box geometry to the drift cells (figure 27).

As noted above one of the things which limited the momentum resolution of the original chamber was multiple Coulomb scattering of the charged particle by the wires and the drift chamber gas. The UTC incorporated several features which reduced the amount of mass within the chamber. The three active superlayers used the same drift chamber gas as the jet chamber, essentially 50-50 argon-ethane, but the two inactive superlayers used nitrogen which resulted in a lower cross sectional mass then a chamber entirely filled with the argon ethane mix. Helium could also have been used

[6] This material was essentially identical to the product with the better known tradename of Kapton

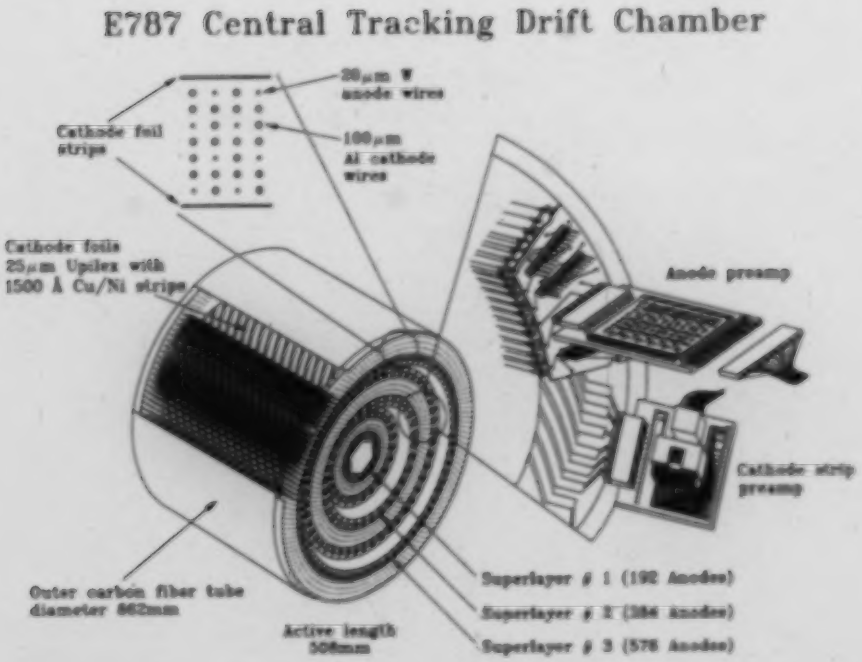


Figure 27: Schematic of the UTC showing the inside of the outer superlayer.

but helium leakage out of the chamber might have proved a threat to nearby phototubes[7] and the relative benefit over nitrogen was not large.

Superlayers 2 and 4, the inactive layers, of course contained no wires, but the use of grounded metal coated foils also eliminated the need for a layer of cathode wires in the drift cells closest to the foils. During construction the foils were tensioned with roughly a 40 gram load per centimeter of foil circumference. During operation a pressure difference equivalent to 2cm of water was maintained between each pair of superlayers with the pressure being the highest in the innermost layer and decreasing toward the outer layer. This effectively inflated the superlayers thus stabilizing their shape while at the same time not causing the foils to protrude too close to the wires due to the foil pretensioning and the low elasticity of Kapton. By holding the shape of the foils in this way very thin foils could be used and no support structure was needed within the chamber other than the inner and outer walls.

The use of a stripe pattern on the foils oriented at roughly 45 degrees to the wires meant that an avalanche on an anode adjacent to the foils would result in a measurable induced voltage pulse on the nearest strips which could be used to provide $z$ information and eliminated the need for stereo wires as were used in the jet chamber(section 3.5). This meant that all of the wires could be axial and the simple box-like cell geometry meant that fewer wires were needed. In fact the use of foils, inactive regions and a simple cell type resulted in the UTC using only 4032 wires whereas the jet chamber had needed a total of 7424 wires. The anode wires were the same in both chambers, namely 20$\mu$m tungsten plated with gold, however the cathodes were completely different. The jet chamber used a beryllium-copper alloy with a gold plating and a variety of wire diameters; 100$\mu$m, 178$\mu$m and 300$\mu$m. The UTC uses only 100$\mu$m aluminum cathode wires. Like all the wires these aluminum cathode wires were gold plated with a very thin coating of zinc being needed on the aluminum before the gold would adhere. Producing aluminum wires of sufficient quality took several months of interaction with the manufacturer with us performing extensive examinations of the wires, using both optical and scanning electron microscopes, as well as surface composition testing and elasticity and breakage tests.

The net effect, in terms of the cross sectional thickness of the chamber and considering only the interior of the chamber not the inner and outer support walls, was that the UTC has a thickness of about $2 \cdot 10^{-3}$ radiation

[7]Helium can diffuse through the glass casings of photomultiplier tubes where it will pollute the vacuum maintained within the tube resulting in loss of gain and resolution.

lengths whereas the jet chamber was $8.4 \cdot 10^{-3}$ radiation lengths thick. The old chamber was dominated by the wire contribution ($6.4 \cdot 10^{-3}$ radiation lengths for the wires and $2.0 \cdot 10^{-3}$ for the argon-ethane) while the new chamber is dominated by the drift chamber gas ($1.05 \cdot 10^{-3}$ radiation lengths from the argon-ethane, $0.37 \cdot 10^{-3}$ from the foils, $0.20 \cdot 10^{-3}$ from the wires and the remainder from the nitrogen). The UTC is also 5% larger in radius because, while both chambers have the same outer diameter, the inner diameter of the UTC is 7.85cm while that of the jet chamber is 9.5cm. This difference in radius, along with the more efficient cell geometry, means that tracks in the UTC are about 15% longer than in the jet chamber. The combination of these two factors result in the UTC having twice the momentum resolution of the chamber it replaced.

### 3.9.3 External Design

So far only the active volume of the chamber has been discussed, the support structure of the chamber also plays a role since energy lost by charged particles or photons in the supports will not be observed. The original chamber used flat 9.5mm thick aluminum endplates with carbon fiber cylinders forming the inner and outer walls of the chamber (80 and 94mg/cm$^2$ thick respectively) and providing the mechanical strength needed to support the 880kg load created by the wires. Because the jet chamber endplates were Al and therefore conductive it was necessary to install non-conductive feedthroughs to support the wires and make sure they were not shorted to the endplates. In the UTC not only was the number of wires reduced but the tension on the Al wires was lower then that used on the Be-Cu wires of the jet chamber so the total load on the endplates due to wire tension was only 360kg rather then 880kg. This allowed the use of plastic endplates reducing the photon absorption cross section in the $z$ direction. Two types of plastic were used for the endplates, the innermost superlayer used 12mm thick Ultem, while the other two active superlayers used 12mm thick Noryl. Both of these plastics can be machined but Noryl was not strong enough to support the higher linear loading on the inner superlayer. The two inactive gas volumes, superlayers 2 and 4, where closed at either end by 4mm thick aluminum brackets whose primary function was to connect together the active layers. The aluminum brackets extended the chamber both radially and in length (figure 28). By using different lengths for the three active superlayers the solid angle coverage of the drift chamber relative to the target was kept constant but the total mass of the chamber was reduced since the inner layers were shorter then the length needed for the outer layer.

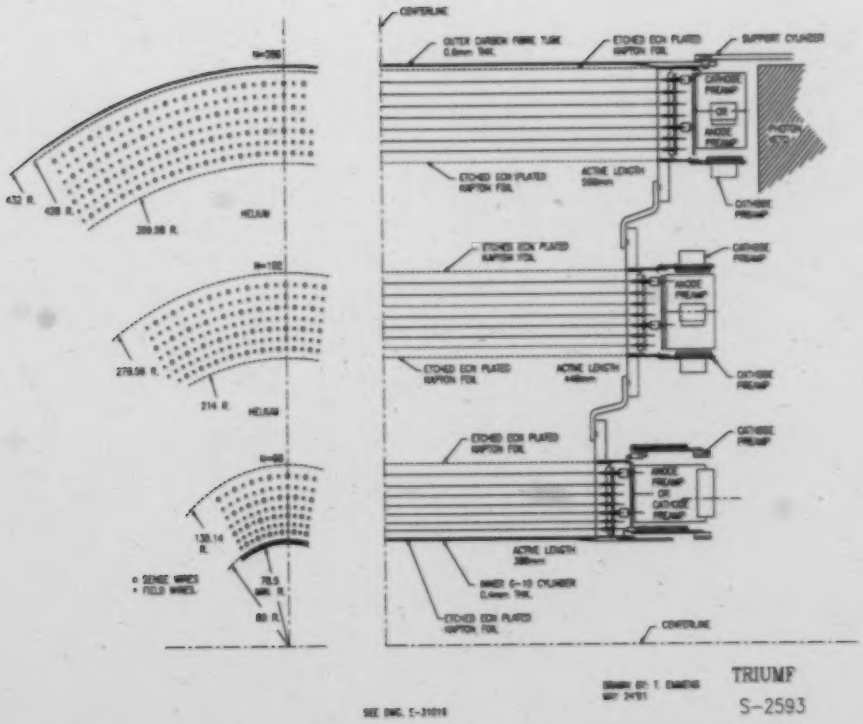


Figure 28: Schematic side view of the downstream end of the UTC and a portion of the wire layout.

As with the jet chamber the inner and outer cylindrical shells provided all of the structural support between the endplates, in fact the outer wall of the UTC is a carbon fiber shell identical in size and design to that used in the jet chamber. The inner shell of the UTC was a cylinder of G10 1mm thick, copper plated on its inner face to help provide RF shielding. An aluminum flange was epoxyed to either end of this cylinder for use as a guide when the target was installed into the detector.

### 3.9.4 Construction

Starting from the inner G10 cylinder, and remembering that all of the data and high voltage connections leading to the outside of the detector were located on the downstream end of the chamber, the actual construction went as follows. The first foil was directly glued to the outer, non-copper plated, face of the cylinder (which was the innermost surface of superlayer 1). A thin copper plated G10 ring with traces etched on its surface, was epoxyed to the foil at the downstream end and a connection made using silver epoxy between the strips on the foil and the copper traces on the G10. A similar G10 ring was used to read out all six of the foils. At the upstream end of the inner G10 cylinder another thin G10 ring, without a copper plating, was epoxyed to the foil as a spacer. The Ultem endplates were then epoxyed and screwed to the inner cylinder, with an O-ring providing the gas seal between the G10 rings and the endplates. Because the endplates were plastic and therefore nonconductive, the wire feedthroughs used in the jet chamber were not needed, instead the endplates were predrilled so that the wires could be installed using gold plated copper crimp pins.

The stringing procedure for all layers consisted of first mounting compression and expansion rods at several points around the outside of the endplates to lock the endplates at the point they were expected to be in once all the wire and foil load was applied so that when all the wires and foils were installed and the rods removed the position of the endplates would not change. To speed up stringing, the crimp pins in the upstream endplate were already inserted before the endplate was installed. The chamber was mounted vertically with the upstream endplate upwards. The wire was fed through a crimp pin at the upstream end (quite a feat with barely visible 20$\mu$m wires) then lowered the length of the chamber through the correct hole in the downstream endplate where another crimp pin was slipped over the wire and inserted into the endplate. A weight was hung from the wire to apply the correct tension (either 40g or 100g) and the pins crimped at first the top (upstream endplate) then bottom (downstream endplate). After

stringing and at several stages during the construction of the chamber the wire tensions were remeasured by applying an alternating current though the wire in the presence of a magnetic field and determing what frequency current would produce a standing vibration in the wire. Overall the tensions were quite stable and less then 1% of the wires needed to be replaced.

The foils were originally flat sheets that needed to be formed into cylinders. This was done by cutting the foils to the correct size along the strip direction so that no strips were broken, lining up the two cut edges to be bonded and then gluing a 1cm wide piece of 12.5$\mu$m Kapton over the length of the splice. Foil 1 was done on a mandrel of the correct diameter the rest were made on an adjustable table. The preamplifier cards connected to the chamber used 6 channels each so the number of strips in each foil layer was chosen to be a multiple of 6. The angle of the strips with respect to the wires was fine tuned to give the correct radius on the finished foil which meant that the angle varied from foil to foil but was around 45 degrees. Except for foils 1 and 6, which were directly bonded to the inner and outer support tubes, the foils were epoxyed to Noryl mounting rings which were then attached to the endplates. These foil rings had holes in them for chamber elongation and tensioning rods, these rods were used to fix the separation and position of the foil mounting rings before the foil was installed on them. The separation between the rings was calculated to take into account the expected stretching of the foil under the desired final load of 40g/cm of circumference. The upstream endplates were slightly larger in radius then the downstream so that the foil support rings sat on the face of the endplate within the chamber, using an O-ring for a gas seal, while at the downstream end the foil was larger in diameter then the endplate. This made it possible, once the tension rods were removed to slide the upstream foil support ring and the foil over the downstream endplate. The upstream foil ring was backed off slightly from the upstream endplate so that once the downstream end of the foil was attached the act of tightening the screws on the upstream end would stretch and tension the foil the desired amount. The downstream foil ring was mounted then the various rods removed while the upstream ring was screwed to the upstream endplate. After this the rods were reinstalled to stabilize the superlayer during construction. Finally the aluminum support rings were bolted on to extend the chamber to the next active superlayer.

The above foil/endplate/stringing procedure was repeated until the outer cylinder was ready to be installed. Foil 6 was not bonded directly to the carbon fiber cylinder but instead had a spacing of 4mm of Rohacell, a closed cell Styrofoam, between it and the outer shell. The entire carbon fiber shell

along with foil 6 was slid over the otherwise completed chamber and bolted to the outer endplates with radial screws. All of the tension and elongation rods were removed and plugs installed to seal the holes in the foil support rings and the chamber was finished. Table 3 summarizes many of the physical details of the chamber.

It should be mentioned that the chamber, with all of its separate radial sections, was extremely difficult to assemble. Additionally the endplates, being made of plastic, tended to warp and creep slightly over time once a load was applied to them. It was found to be impossible to keep some of the intermediate foils free of wrinkles during installation although once the layers were inflated these creases were not large enough to effect the chamber operation. A great deal of effort was placed into trying to keep the alignment between layers and ends correct. Fortunately, the absolute rotation of each superlayer with respect to the others is not important as long as the layers are parallel and concentric. Calibrating out offsets and rotations was part of the process needed to set up the track finding software once data was available using the chamber.

### 3.9.5 Electronics

At the upstream end of the chamber printed circuit cards were installed for high voltage distribution to the anodes. Each anode layer was operated at a separate voltage with the layer divided into two independent sections so that if there was a failure somewhere in an anode layer only 1/2 of the wires in that layer would be disabled. The actual high voltage entered from the downstream end and was fed through one anode wire per independent section to the voltage distribution cards. To limit the current that each anode wire might be exposed to the main anode wire was connected to the cards through a 100k$\Omega$ resistor and the other anodes through 1M$\Omega$ resistors. The incoming high voltage went through two different sets of filters after leaving the power supply, one just outside of the detector and another at the downstream endplates.

The downstream end of the chamber used a more complex arrangement of printed circuit boards. First were copper plated cards which connected together and grounded all of the cathode wires. The copper plating helped provide an RF shield over that end of the chamber since the plastic endplates provided no such protection. These cathode grounding cards had holes in them above all of the anode pins. Over top of these cards came a second layer of cards which connected only to the anode wires. These cards carried the high voltage connection and filters for the one anode per half anode layer

Table 3: Chamber parameters

| | |
|---|---|
| Sense wires | 1152 cells in 12 layers, grouped in 3 superlayers |
| | Number of cells per layer in a superlayer: 48, 96, 144 |
| | 20 $\mu$m diameter gold-plated tungsten (tension: 40 g) |
| Cathode wires | 100 $\mu$m gold-plated aluminum (tension: 100 g) |
| Foils | Number of layers: 6 |
| | Number of strips per foil: 48, 72, 108, 144, 180, 216 |
| | Active length in $z$ (cm): 38.8, 38.8, 44.8, 44.8, 50.8, 50.8 |
| | 25 $\mu$m Kapton plus 1200Å copper, 300Å nickel |
| | (tension: 40 g/cm) |
| Inner cylinder | Inner radius: 7.85 cm, Length: 38.8 cm |
| | 0.038cm thick G10 |
| Outer cylinder | Outer radius: 43.31 cm, Length: 50.8 cm |
| | 4 layers preimpregnated carbon fiber |
| | Thickness: 0.1 cm (effective thickness 82.5 mg/cm$^2$) |
| Outer cylinder spacer | Inner radius: 42.81 cm |
| | 0.4 cm thick Rohacell (effective thickness 24 mg/cm$^2$) |
| End plates | 1.20 cm thick ULTEM (inner superlayer) |
| | 1.20 cm thick NORYL (middle and outer superlayers) |
| | 0.40 cm thick aluminum (intermediate support) |
| Gas | Active volume: argon-ethane-ethanol (49.6%:49.6%:0.8%) |
| | Inactive regions: nitrogen |
| | Gain: $8 \times 10^4$ |
| | Drift velocity: 5cm/$\mu$s |
| Voltages | Anodes: –2 kV |
| | Cathodes: ground |
| Surface fields | Anodes: 260 kV/cm |
| | Cathodes: $< 15$ kV/cm |
| | Foils: $< 1$ kV/cm |

which transfered high voltage to the distribution cards mentioned above. They also AC coupled every anode through a small high voltage capacitor to 12 pin connectors soldered onto the cards. To these connectors where plugged custom made preamplifier cards each of which serviced 6 anodes. Similar preamplifiers were connected to the foils using 12 pin connectors on the small G10 foil readout rings mentioned earlier, with the foils being grounded through the amplifiers. The anode preamplifiers had a gain of 5mV/$\mu$A and the cathode preamplifiers 10mV/$\mu$A. The preamplified signals were carried by thin 50 ohm coaxial cables about 4m long to the outside of the chamber and from there on heavier 30m long coaxial cables to the counting house where they were plugged into rack mounted 'postamplifiers' which provided another factor of 10 gain on the anodes and 25 on the foils. The custom postamp boards also split and discriminated the signal so that a discriminator output could be send to LeCroy 1879 TDCs for timing while an analog signal was send to LeCroy 1881 ADCs to measure total charge.

### 3.9.6 Calibration

Two pieces of information are essential for using data from the chamber: the actual time taken for the ionization electrons to drift to the anode, and the space-time relation needed to convert that time into a distance from the anode. The start signal to the TDCs is provided by the time of the T·A which defines a charged track having entered the range stack. The lowest time that a wire can register a hit corresponds to a drift distance of zero, i. e. the charged track passing through or almost through the wire. Fitting the leading edge of the time distribution for a large number of hits for each wire gives this TDC pedestal which must be subtracted from the measured time to get the correct drift time. Note that this procedure assumes that the tracks originate in the target and proceed outward, for cosmic data, where the track enters the detector from the outside different pedestals must be measured.

Once the timing pedestals are known the space-time relation must be found. The drift paths which electrons follow within the drift chamber cells are intrinsically non-uniform because the cathodes form a square around the anode rather than a cylinder. This is even worse for anodes where one end of the cell is formed by the foil. The introduction of a magnetic field then twists all of the drift lines due to the Lorentz force on the charged ions so that the drift path isn't even radial. Finding the time-distance relation was an iterative process. The initial starting point was a uniform relation using simply the known drift velocity of electrons in Ar-ethane. For each

superlayer the tracks of K$\mu$2 data with no magnetic field were fit using this simple space-time equation. The residuals of the fits as a function of drift time were used to refine the relation which was then used in the next round of track fitting. This was repeated, with a separate time-distance relation in each anode layer, until the result converged. The same iterative procedure was then used on data taken with the standard magnetic field strength, with tracks being fit to the entire chamber not just one superlayer. The space-time relations were parameterized as 6th order polynomials and in the presence of the magnetic field it was no longer sufficient to have one relation per anode layer but instead the angle which the track went through the cell became important. The cells were divided into 6 azimuthal segments and a separate relation found for each of the six regions.

The above relations define positions in the xy plane. The $z$ positions were determined separately by using the ADC pulse heights on the foil strips. ADC and TDC pedestals were first determined for each strip to determine the values which had to be subtracted from either the energy or time to yield the true value. Then only strips with a pedestal subtracted ADC value of at least three times the root mean square (RMS) of the pedestal distribution were accepted. Typically an anode hit in the adjacent wire layer would induce charge on several strips. The $z$ position was taken as the ADC weighted mean of the intersections between the hit anode wire(s) and adjacent hit strips. The innermost and outermost foils were capacitively coupled to the inner copper-plated G10 cylinder and outer carbon fiber cylinder and consequently had the lowest signal-to-noise ratios and worst z resolutions.

It was also necessary to do a few alignment corrections to check the orientation of the chamber. Tracks were fit separately for each superlayer and extrapolated into the other superlayers to check for possible azimuthal rotation of superlayers relative to one another or possible xy translations of the axis of the superlayers relative to one another. The three cylindrical superlayers were concentric to within 90$\mu$m of each other with relative rotations of 0.3-0.7 milliradians. The global rotation of the UTC in the xy plane relative to the rest of the detector was done by comparing tracks in the UTC to tracks extrapolated from the upgraded equivalent of the range stack chambers (the position of which was well known from mechanical constraints on their installation). A similar procedure was used to check for rotations of the foils relative to one another and then globally align them to the detector by using the well known location of the edges of some of the scintillators. One last calibration had to be made on the foils since the angle of the strips on each foil, relative to the UTC axis, was determined

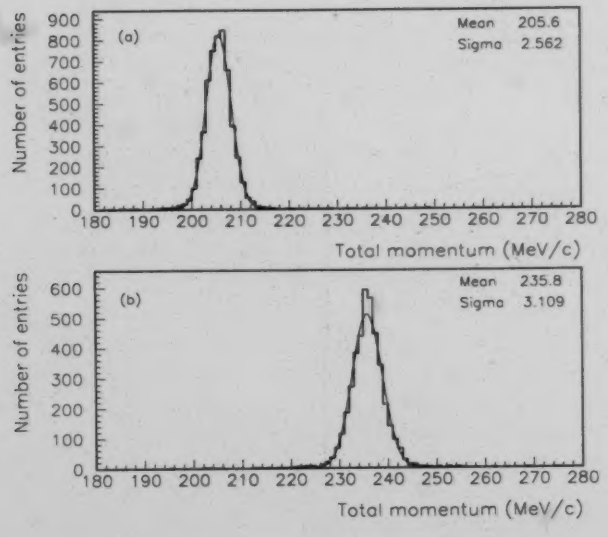


Figure 29: Total momentum resolutions for K$\mu$2 and K$\pi$2 found using the UTC and including target energy.

by construction constraints and not exactly known a priori. This was done for each foil by looking for, and removing, a $z$ dependence in the average $z$ residuals of the track fits.

### 3.9.7 Performance

For K$\mu$2 and K$\pi$2 events the total momentum resolution, including target energy corrections, was about 1.3% (figure 29). This compares to roughly 2.6% at the K$\pi$2 peak for the previous drift chamber. However, the target was also replaced with an improved version and this affects the overall momentum resolution. Removing the estimated target contribution for both the circa 1991 detector and the current UTC/target combinations gives an intrinsic resolution, for K$\pi$2, of approximately 2% for the jet chamber and 0.9% for the UTC. This resolution is consistent with the expected chamber resolution and meets the design goal of having twice the momentum resolution of the previous chamber.

# 4 $K^+ \to \pi^+\gamma\gamma$ Event Selection

## 4.1 Introduction

The basic equation used to measure any branching ratio is

$$BR(X \to Y) = \frac{N_{events} - N_{background}}{Acc \cdot N_X} \tag{44}$$

where $N_{events}$ is the total number of events in the final sample, $N_{background}$ is the number of those events which are background rather than true $X \to Y$ decays and $Acc$ is the acceptance (to be defined shortly) of the cuts used to select the final sample. The quantity $(N_{events} - N_{background})/Acc$ is the total number of $X \to Y$ decays which occurred in the $N_X$ $X$ decays observed. It is therefore necessary to accurately measure the background, acceptance and total number of decaying particles. The first step is to chose a set of cuts which will distinguish the decay of interest from all the other decay modes which may be occurring in the detector.

The K$\pi$2 decay, $K^+ \to \pi^+\pi^0; \pi^0 \to \gamma\gamma$, is superficially the decay most similar to $K^+ \to \pi^+\gamma\gamma$. Both have a $\pi^+$ and two photons in their final state, but the K$\pi$2 decay is a two body decay and since the kaon decays at rest the $\pi^+$, to conserve momentum, can only have a fixed momentum of 205MeV/c, this is the so-called K$\pi$2 peak. On the other hand the $K^+ \to \pi^+\gamma\gamma$ decay goes to a $\pi^+$ and two photons without the intermediate, on mass shell, $\pi^0$ state and so the $\pi^+$ in that case can have a momentum ranging anywhere from zero up to the maximum allowed by energy conservation of 227MeV/c. Because 21.16% of $K^+$ decay via K$\pi$2 it is necessary to exclude the $\pi^+$ momentum region around 205MeV/c from any search for $K^+ \to \pi^+\gamma\gamma$. This was done by creating two separate triggers referred to as, $\pi\gamma\gamma(1)$ and $\pi\gamma\gamma(2)$. The $\pi\gamma\gamma(1)$ trigger searched the momentum region above the K$\pi$2 peak while the $\pi\gamma\gamma(2)$ trigger examined the region below the peak.

The $\pi\gamma\gamma(1)$ trigger was one of the first E787 triggers installed. Using data taken in 1989 an upper limit of $10^{-6}$ was set on the $K^+ \to \pi^+\gamma\gamma$ branching ratio[1]. However, because the full $\pi^+$ momentum range was not accessible some assumption had to be made about the shape of the $\pi^+$ momentum spectrum. The standard assumption is a phase space distribution, where there is no fundamental restriction on the momentum of the $\pi^+$ and the probability of the pion having a particular momentum is simply determined by the available phase space of the decay products. This assumption was used in the $\pi\gamma\gamma(1)$ analysis. Chiral perturbation theory has now predicted

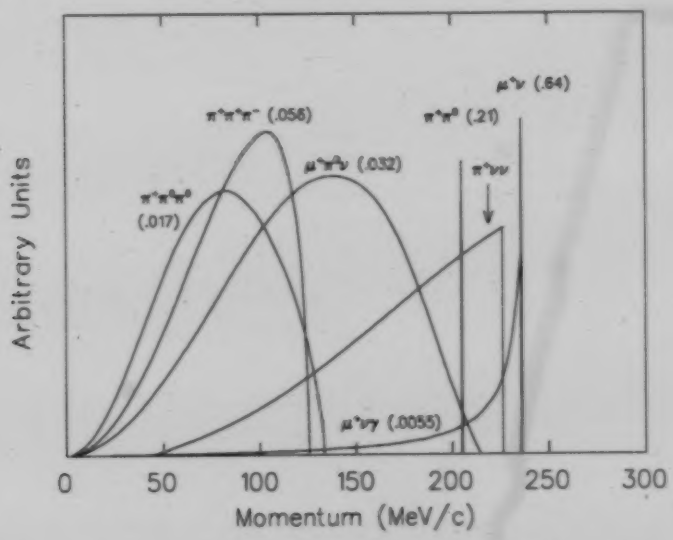


Figure 30: The charged particle momentum spectrum of the six most probable kaon decay modes excluding Ke3 and including $\pi\nu\bar{\nu}$.

that the spectrum will be strongly peaked below the K$\pi$2 peak with an extremely low probability of any events having a high enough momentum to satisfy the $\pi\gamma\gamma(1)$ trigger. Therefore, in 1990 the $\pi\gamma\gamma(2)$ trigger was tested and in 1991 a full data run taken with the trigger turned on. This trigger examined a $\pi^+$ momentum between 100–180MeV/c, the region below 100MeV/c was not reachable using the E787 detector due to the requirement that the pion reach A layer in the range stack.

Unfortunately the region below the K$\pi$2 peak was subject to more potential background modes than above the peak (figure 30). The possible kaon decay modes with 2 or more photons and a branching ratio large enough to make them backgrounds are listed in table 4 along with the abbreviation used to identify them. K$\pi$2$\gamma$ and Ke3$\gamma$ are radiative modes of the simpler K$\pi$2 and Ke3 decays. The primary goal of the data analysis was to reduce these backgrounds modes to a level below that of the real $K^+ \to \pi^+\gamma\gamma$ signal. In practice the electron in Ke3 and Ke3$\gamma$ tended to shower like a photon and was unlikely to end up looking like a pion, so these two decays were not a significant background. The other decays will be discussed in more detail in the background estimate section below (section

Table 4: Potential Background Decay Modes for $\pi\gamma\gamma(2)$

| Abbreviation | Decay Mode | Branching Ratio |
|---|---|---|
| K$\pi$2 | $K^+ \to \pi^+\pi^0$ | 0.2116 |
| Ke3 | $K^+ \to e^+\nu_e\pi^0$ | 0.0482 |
| K$\mu$3 | $K^+ \to \mu^+\nu_\mu\pi^0$ | 0.0318 |
| K$\pi$3 | $K^+ \to \pi^+\pi^0\pi^0$ | 0.0173 |
| K$\pi$2$\gamma$ | $K^+ \to \pi^+\pi^0\gamma$ | 0.0003 |
| Ke3$\gamma$ | $K^+ \to e^+\nu_e\pi^0\gamma$ | 0.0003 |

5).

Once a final set of cuts had been determined which reduced the background to a manageable level while still leaving some signal events, it was necessary to measure what fraction of the real $K^+ \to \pi^+\gamma\gamma$ events were removed by these cuts. The acceptance of a cut was defined as the ratio of desired events after application of the cut to before the cut, i. e. the fraction of events the cut left behind. The rejection of a cut was the reciprocal of its acceptance. It was generally desirable to measure the acceptance of each cut using real data but very often this was impossible simply because there was not normally a clean sample of the decay of interest that could be used for this purpose. Because of this a monte carlo simulation of the detector, referred to as UMC, was used. This computer simulation contained as much of the real detector composition and physics as possible in the attempt to make an event generated via UMC look virtually identical to a real event, with the advantage of course, of knowing exactly what kind of decay you were looking at. In addition to estimating acceptances, events produced by UMC were also very useful for examining the differences one could expect between $\pi\gamma\gamma(2)$ events and the various backgrounds.

The total number of decaying kaons, corresponding to $N_X$ in equation 44, was not simply the number of $K_T$. First an adjustment had to be made for the 'dead time' of the electronic readout system, if a $K_T$ occurred while the data from a previous event was being read out the detector would not be 'live' to record the new event. Therefore an alternative quantity, $K_T live$, was used instead of $K_T$. Then an adjustment had to be made to take into account the fact that not all $K_T live$ counts were actually due to kaons which had stopped and decayed at rest. This adjustment was known as the kaon stopping fraction, $f_s$, and is discussed more in section 7.

## 4.2 Online Event Selection

There were three distinct levels to the $\pi\gamma\gamma(2)$ trigger. Level 0 used discriminator levels and timing coincidences for speed and was similar to most other level 0 triggers. Level 1 used a majority logic unit and a custom made trigger board to look for correlations between different parts of the BV. Level 3 used a simplified Fortran routine running in the ACP nodes to do an even more detailed analysis of BV activity[8]

### 4.2.1 Level 0

In 1991 the level 0 $\pi\gamma\gamma(2)$ trigger was:

$$K_T \cdot IC \cdot DC \cdot (T \cdot A) \cdot \overline{(C_{CT} + \cdots + 21_{CT})} \cdot \overline{(ECM + ECP)} \cdot E_{BV}$$

With the following definitions:

| | | |
|---|---|---|
| IC | $\equiv$ | An I counter hit |
| DC | $\equiv$ | Delayed coincidence between the IC and $\hat{C}_K$ |
| $\overline{(C_{CT} + \cdots + 21_{CT})}$ | $\equiv$ | Charged track does not extend past B layer |
| $\overline{(ECM + ECP)}$ | $\equiv$ | Veto on upstream(M) or downstream(P) EC energy |
| $E_{BV}$ | $\equiv$ | BV energy requirement |

The online delayed coincidence requirement was roughly equivalent to a 1.5–2.0ns delay between the time of the incoming kaon and the outgoing charged track. The barrel veto energy requirement was based on a sum of all energy in the BV being above some threshold. To determine the actual energy corresponding to this hardware threshold the visible fraction in the BV first had to be measured. The 'visible fraction' was a multiplicative calibration needed to account for the fact that most of the energy deposition in the BV was in the lead layers and therefore was not visible to the active scintillator layers. In the barrel veto and elsewhere the term 'visible energy' refers to the observed energy before applying any 'visible fraction' corrections. $K\pi2$'s were extracted from $\pi\gamma\gamma(2)$ level 0 monitor data by requiring a pion momentum between 190 and 215 MeV/c and only two photon clusters in the barrel veto with energy above 30MeV each. Fitting the total BV energy and invariant mass of the photon pair and requiring them to match a $\pi^0$ from $K\pi2$ ($E_{BV}$ = 245.6MeV, $M_{\gamma\gamma}$ =135.0MeV) resulted in a visible fraction of 0.308 (figure 31). Looking at the leading edge of the BV energy

[8]By convention a 'level 2' trigger was one which used the RS TD's online. Since this wasn't done in $\pi\gamma\gamma(2)$ there was no level 2 trigger and the next level was level 3.

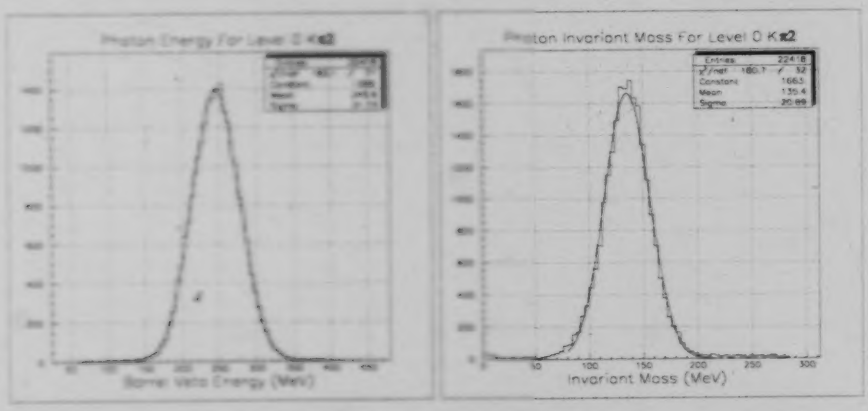


Figure 31: Kπ2 photon energy and invariant mass using a BV visible fraction of 0.308.

distribution for all level 0 $\pi\gamma\gamma(2)$ monitors showed that the level 0 threshold was about 190MeV (figure 32). The low energy tail of this distribution was the result of using a more narrow time window than was used online which in some events resulted in a lower energy sum.

### 4.2.2 Level 1

The online level 1 trigger consisted of the hextant cut, to look for energy in the range stack outside of the stopping hextant (see section 3.8), and a search for photons in the barrel veto. Pairs of adjacent barrel veto sectors were grouped together to reduce the number of sectors from 48 to 24. The energy in all 4 layers of each of these super-sectors was summed separately for the upstream and downstream ends and put through a discriminator with a threshold equivalent to about 50MeV of actual energy per end. The output of these discriminators was ORed for either end of a given super-sector. Because the ends were discriminated separately then ORed there was a bias against events stopping at the center of the BV. Assuming an attenuation length of 100cm a photon at the edge of the BV could fire one discriminator with half the energy required by a photon at the center of the BV. This effect was particularly clear when the photons in the BV were sorted by energy and their $z$ positions compared (figure 33). The high energy photon cluster fires a level 1 discriminator regardless of its $z$ position while the lower energy photon shows a strong $z$ dependence.

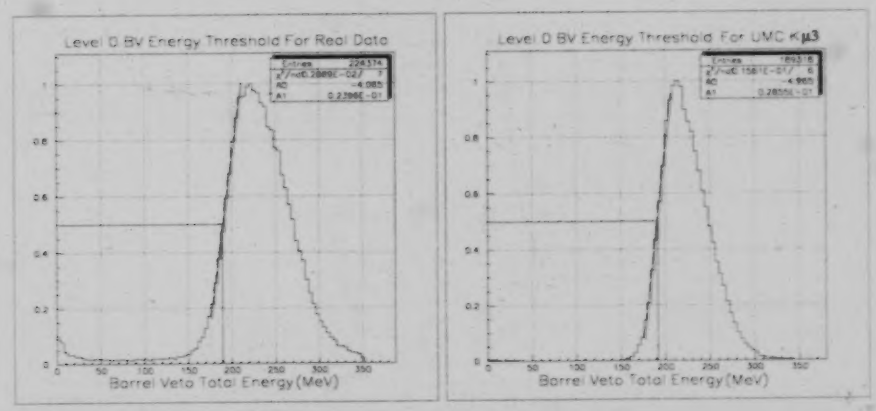
Level 0 BV Energy Threshold For Real Data
Barrel Veto Total Energy (MeV)
Level 0 BV Energy Threshold For UMC Kμ3
Barrel Veto Total Energy (MeV)

**Figure 32: Total BV energy within ±6.3ns of prompt for real $\pi\gamma\gamma(2)$ level 0 data and UMC level 0 K$\mu$3 data. (Distribution normalized to unit height).**

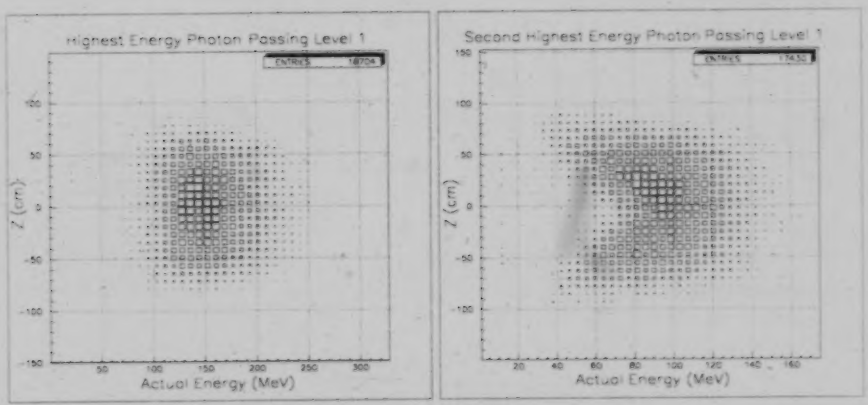


**Figure 33: $Z$ distribution versus real photon energy for the most energetic and second most energetic photon clusters in the BV.**

The result of the above OR was fed into a LeCroy majority logic unit to count the number of photon clusters. A photon cluster was defined as one or more adjacent hit super-sectors with empty super-sectors on either side of it, this allowed photon showers to span barrel veto sectors without being counted as more than one photon. To pass the trigger exactly two photon clusters had to be identified by the majority logic unit. A second set of discriminated outputs was sent to a custom made board which counted the gap between the two photon clusters. This was done by starting between super-sector 1 and 24 and counting the number of sectors in both directions before a hit super-sector was encountered. The gap count was the number of empty super-sectors separating the hit sectors, if a count greater than 11 was returned, i. e. both photons were on the far side of the BV from the starting point, then 22 minus the sector count was used as the correct size of the gap. The trigger required a gap of at least 6 empty super-sectors which corresponded to a opening angle of 90 degrees between the photons. This gap cut was designed to remove $\pi^0$ from K$\pi$2 and K$\mu$3 (figure 34).

### 4.2.3 Level 3

The level 3 trigger performed a limited analysis of the barrel veto in the ACP nodes. Using only BV ADC information, and ADC calibration files determined during the course of the run, a more detailed study was made of the photon clusters than was possible in the level 1 hardware. Using a visible fraction of 0.338 the energy in each of the 48 BV sectors was summed for all four BV layers and if above 2MeV that sector was considered to contain a photon cluster. Clusters in adjacent sectors were then summed to form so called super-clusters. If two super-clusters with at least 30MeV each were found then the energy weighted position coordinates of each super-cluster were measured and the invariant mass of the pair determined.

$$
\begin{aligned}
r_{SC} &= \sum_{mod} \frac{r_{mod} E_{mod}}{E_{total}} \\
\phi_{SC} &= \sum_{mod} \frac{\phi_{mod} E_{mod}}{E_{total}} \\
z_{SC} &= \sum_{mod} \frac{0.5(l_{attn})_{mod} \ln(E_2/E_1)_{mod} E_{mod}}{E_{total}} \\
M_{\gamma\gamma} &= \sqrt{2E_{SC1}E_{SC2}(1-\cos\theta_{\gamma\gamma})}
\end{aligned}
$$

$mod$ = module number

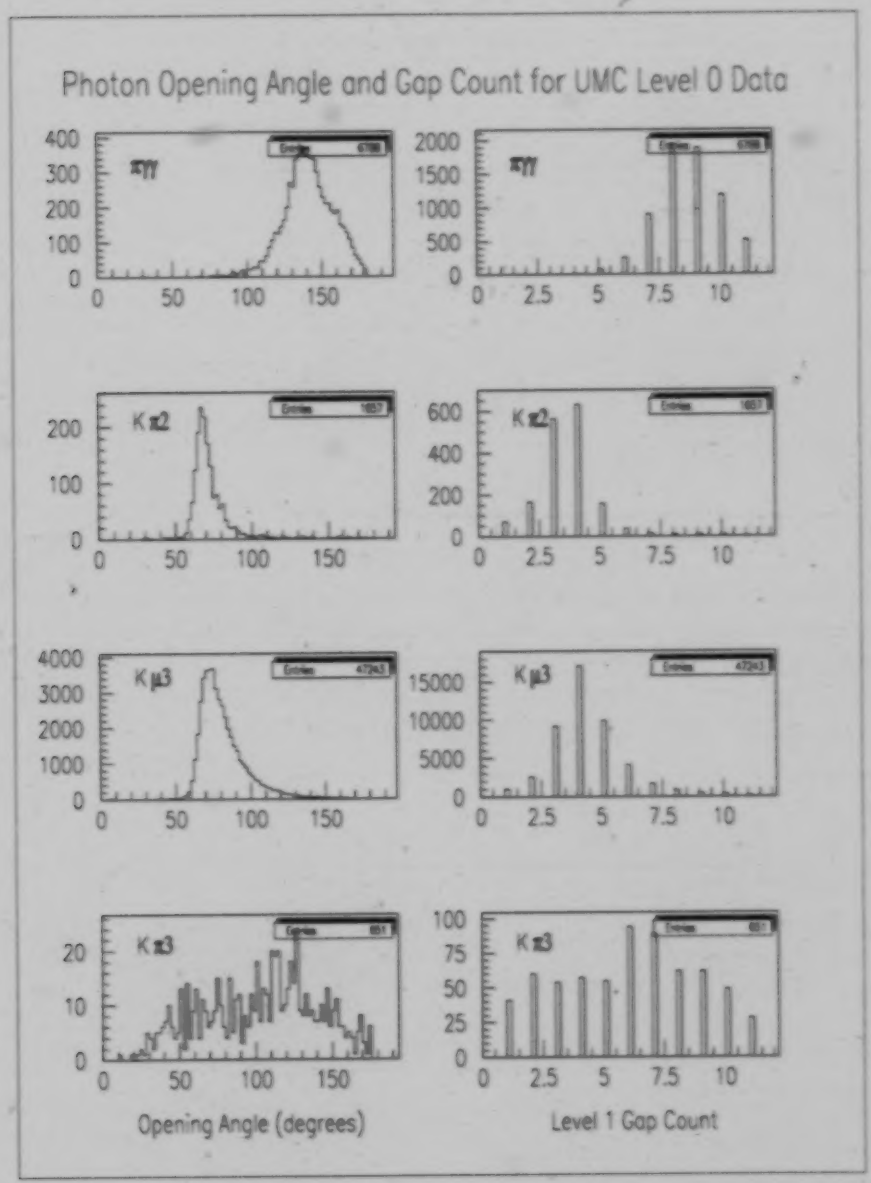


**Figure 34: UMC-generated photon opening angle and gap count for various triggers.**

$r_{mod}$ = Radius of BV module
$\phi_{mod}$ = $\phi$ of BV module
$E_{mod}$ = Calibrated energy of BV module
$E_{total}$ = Total energy of all modules used in cluster
$(E_1)_{mod}, (E_2)_{mod}$ = Energy at either end of BV module
$(l_{attn})_{mod}$ = Attenuation length of BV module
$E_{SC1}, E_{SC2}$ = Energy of the two super – clusters
$\theta_{\gamma\gamma}$ = Opening angle between the two super – clusters

To pass level 3 exactly two 30MeV super-clusters had to be found and the total energy in the barrel veto had to be between 100 and 600 MeV with the photon invariant mass being between 190 and 600 MeV (table 5). However, the energy and mass requirements were waived if the opening angle between the pair of photons was less than 15 degrees (equivalent to two BV sectors). Additionally, 1 in 10 events which failed level 3 was written to tape as monitor data.

Table 5: Online Level 3 Parameters

| | |
|---|---|
| Visible fraction | 0.338 |
| Attenuation length, $l_{attn}$ | 118.15cm |
| Cluster energy threshold | 2MeV |
| Super-cluster energy threshold | 30MeV |
| Number of super-clusters found | 2 |
| Minimum BV energy | 100MeV |
| Maximum BV energy | 600MeV |
| Minimum invariant mass, $M_{\gamma\gamma}$ | 190MeV |
| Maximum invariant mass, $M_{\gamma\gamma}$ | 600MeV |

### 4.2.4 UMC

In the monte carlo simulation of the online trigger a few points are worth noting. The visible fraction used in the barrel veto was 0.29, which differed slightly from the value used in online level 3 or the final analysis and had to be taken into account when analyzing UMC data. The energy deposited at either end of a barrel veto module was determined assuming a speed of light of 15.0cm/ns and an attenuation length of 100.0cm. Before applying the level 0 and level 1 energy thresholds this single end energy was multiplied by the ADC-count-to-MeV calibration used with the real data. This

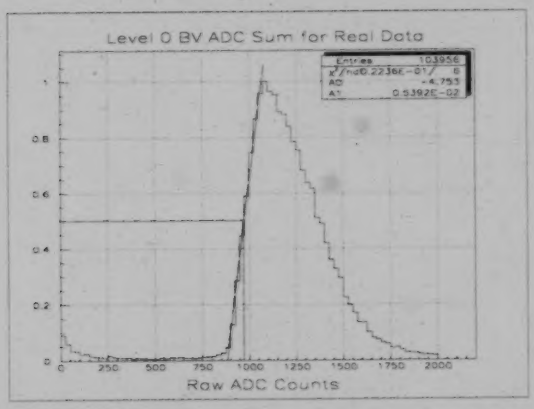


Figure 35: Sum of raw ADC counts over the entire BV based on level 0 monitor data.

helped reproduce the fact that the online energy calibrations were not exactly uniform from one module to the next. The level 0 BV energy sum was formed by summing these single end values for all counters and dividing by 2. To pass level 0 a sum of $> 960$ counts was demanded which is close to the actual raw ADC count measured using level 0 trigger data from all runs (figure 35). Measuring the resulting BV energy using the same INTIME [9] routine as for real data (figure 32) showed that UMC gave almost exactly the same value for the threshold with only a slightly sharper leading edge. Note that the width of the two energy distributions in figure 32 can not be directly compared since this UMC result is only for K$\mu$3 while the real data covers all possible backgrounds.

Measuring the $\pi^0$ energy and invariant mass using UMC-generated K$\pi$2(1) data (figure 36) with the same selection cuts that were applied to the real data in figure 31 shows that the distributions are similar with UMC having a slightly better resolution then the real data.

For level 1 the single end energy was again converted to ADC counts and summed to form 24 super-sectors. Looking at real data there were differences in the threshold at the upstream and downstream end of the BV (figure 37) and sector and end dependent thresholds were used in UMC

[9] INTIME sorted the hits in different detector subsystems and summed up the energy of any hits that were within a time window given to the routine. Its main use was to look for photon conversions that happened at the same time as the charged track in the range stack.

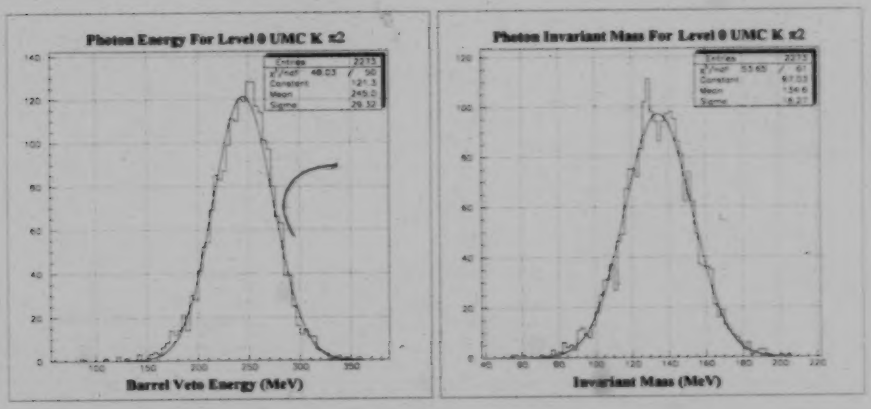


Figure 36: K$\pi$2 photon energy and invariant mass from UMC data.

(table 6). The discriminated results from either end were ORed and a gap count performed exactly as described in the real trigger. Comparing the level 1 $z$ vs energy distributions in figure 33 to the same distributions found using K$\pi$2(1) UMC data (figure 38) it can be seen that UMC is correctly reproducing the real behavior of the trigger.

The level 3 trigger was done in software in the ACP nodes and was reproduced simply by running the same code on the UMC data. The offline level 3 cut was not exactly identical to the online cut due to differences in calibration files. The offline calibration files were more accurate than the online and are a better reflection of the accuracy of the UMC calibrations. Therefore looking at how well the offline level 3 trigger reproduces the online result gives some indication of how well UMC will do.

The prescaled online level 3 failures had both the level 3 failure code and the calibrated online BV banks written with them which made it possible to reconstruct the online results and compare them to the offline values. Figure 39 shows the difference between the frequency of level 3 offline return codes of each type, calculated either using the online or new BV banks, and the frequency of that return code online. The numbers are normalized to show a percentage of the total number of events. The agreement with level 3 using the offline calibration seems no worse than that with the calibrated banks written online. The offline and online return codes agree 98% of the time, with only 0.7% of the events which failed online passing offline. Selecting K$\pi$2 events using 195MeV/c$< P_{\pi^+} <$215MeV/c and comparing the total BV energy and the photon invariant mass for both the online and offline BV

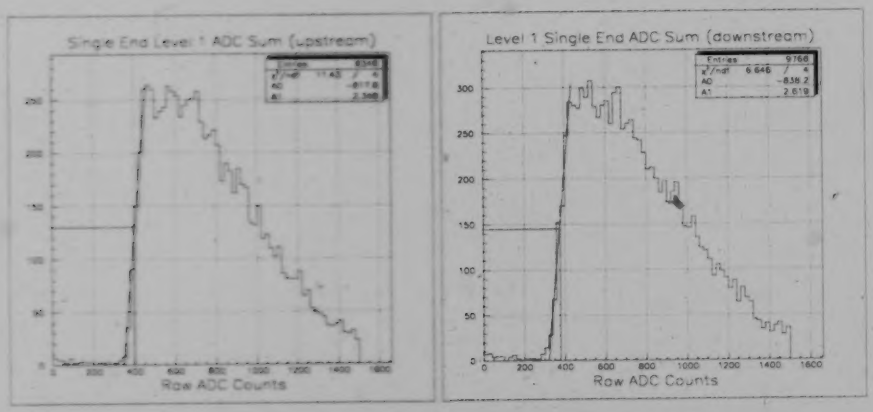


**Figure 37: Raw ADC spectrum averaged over all sectors for the upstream and downstream end of the BV in $\pi\gamma\gamma(2)$ data passing level 1.**

**Table 6: UMC Level 1 BV Energy Thresholds**

| Super-sector | End 1 | End 2 | Super-sector | End 1 | End 2 |
|---|---|---|---|---|---|
| 1 | 400 | 340 | 13 | 380 | 360 |
| 2 | 380 | 360 | 14 | 420 | 360 |
| 3 | 380 | 360 | 15 | 400 | 360 |
| 4 | 440 | 420 | 16 | 460 | 400 |
| 5 | 440 | 400 | 17 | 400 | 400 |
| 6 | 380 | 360 | 18 | 400 | 400 |
| 7 | 440 | 400 | 19 | 440 | 440 |
| 8 | 440 | 400 | 20 | 380 | 420 |
| 9 | 360 | 360 | 21 | 400 | 380 |
| 10 | 380 | 360 | 22 | 440 | 380 |
| 11 | 360 | 340 | 23 | 440 | 420 |
| 12 | 380 | 380 | 24 | 440 | 420 |

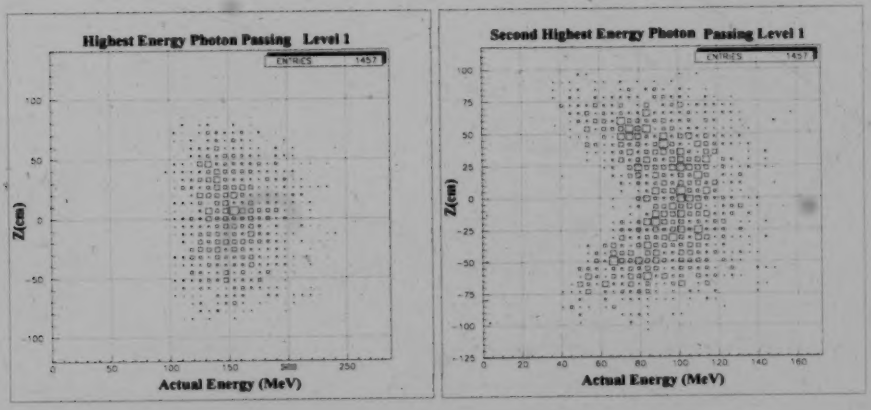


Figure 38: $Z$ distribution versus photon energy for the highest and second highest energy photon clusters in the BV from UMC data.

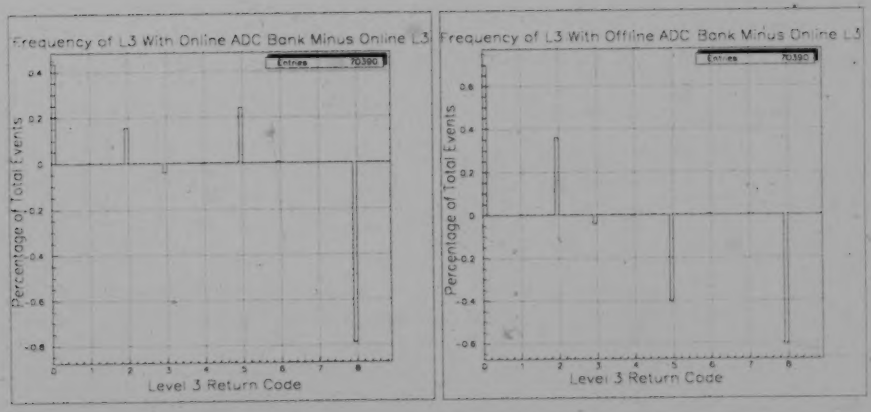
Frequency of L3 With Online ADC Bank Minus Online L3
Percentage of Total Events
Level 3 Return Code
Frequency of L3 With Offline ADC Bank Minus Online L3
Percentage of Total Events
Level 3 Return Code

Figure 39: Difference in frequency of level 3 return codes expressed as a percentage of total number of events for online or offline BV ADC banks compared to actual online return codes.

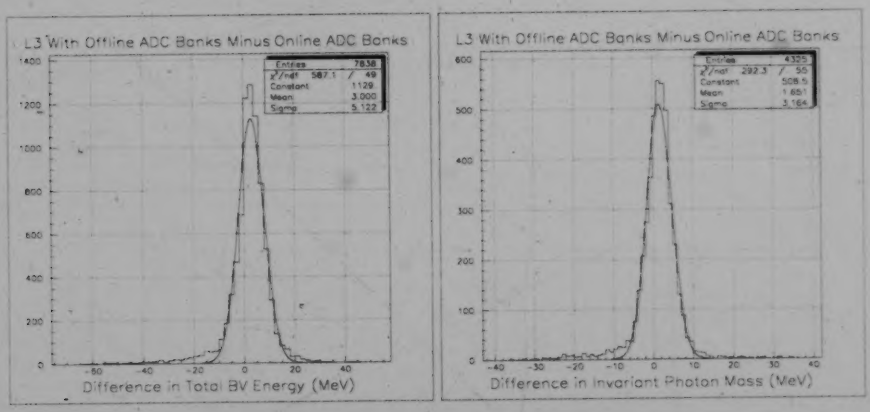
L3 With Offline ADC Banks Minus Online ADC Banks
Difference in Total BV Energy (MeV)
L3 With Offline ADC Banks Minus Online ADC Banks
Difference in Invariant Photon Mass (MeV)

Figure 40: Level 3 BV energy and $M_{\gamma\gamma}$ found using the new ADC banks minus those found using the online calibrated ADC banks.

ADC banks shows that the online result has a small high $M_{\gamma\gamma}$ tail but a slightly lower mean photon mass (figure 40). The acceptances measured using the offline level 3 should be reasonably close to true online values. Also because the energy and mass are close to the correct K$\pi$2 values the visible fraction used in the level 3 simulator must be set to 0.29 when using UMC data (figure 41).

## 4.3 Offline Event Selection

The offline analysis was broken down into a series of 'passes' for logistical reasons. PASS0 didn't apply any cuts to the data it simply skimmed all of the $K^+ \to \pi^+\gamma\gamma$ triggers from the original $\approx$ 300 8mm data tapes written online. PASS1 was a set of loose, minimum bias, cuts applied early on to reduce the volume of data without imposing cuts that would be sensitive to later refinements of detector calibrations. The goal of PASS2 was to reduce the number of PASS1 events so that they would fit on a single 8mm tape making the main analysis, PASS3, more convenient.

### 4.3.1 PASS1 Analysis

Skimming out all $\pi\gamma\gamma(2)$ triggers between run 9348 and 10141 (tape NI2508-NI2799) resulted in a total of 2,726,738 events spread over 30 8mm tapes. Since a large rejection was not needed to reduce this to a manageable size

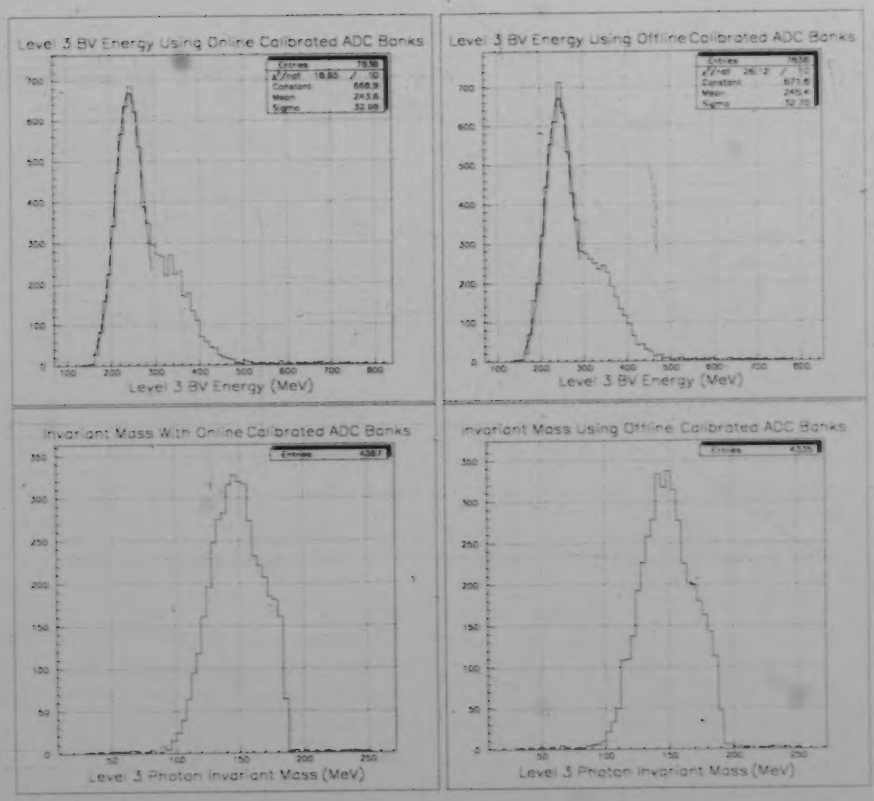
Level 3 BV Energy Using Online Calibrated ADC Banks
Level 3 BV Energy (MeV)
Level 3 BV Energy Using Offline Calibrated ADC Banks
Level 3 BV Energy (MeV)
Invariant Mass With Online Calibrated ADC Banks
Level 3 Photon Invariant Mass (MeV)
Invariant Mass Using Offline Calibrated ADC Banks
Level 3 Photon Invariant Mass (MeV)

**Figure 41: Level 3 BV energy and $M_{\gamma\gamma}$ for K$\pi$2 events calculated using the new ADC banks and using the online calibrated ADC banks.**

it was decided that the best strategy for PASS1 was to use the smallest number of safe and effective cuts that would result in a reasonable overall rejection. The cuts are described below and their rejections given in table 8. The rejection of a cut was defined as the inverse of the fraction of events passing the cut. After PASS1 there were 373912 surviving events.

#### 4.3.1.1 Event Reconstruction

Event reconstruction cuts were mainly designed to ensure that the event was understandable to the offline analysis code, but they also rejected some background events in which photons had converted before reaching the barrel veto.

- Target reconstruction. TARBNK[10] was used to require that a kaon module had been identified and at least one IC was hit, but did not demand that a pion cluster be found. In terms of software this cut was expressed as the requirement that the TARBNK variable iqual be less than 3. The cut was sometimes referred to in that manner to distinguish it from the PASS3 cut which required iqual<2.
- Drift chamber tracking. Exactly one drift chamber track had to be found. The tracking parameters adopted are in reference [44].
- Drift chamber track charge. The drift chamber track found above had to be positive.
- IC range routine. The IC routine ICRNGE[11] was used to verify that there was a hit IC corresponding to the DC track.
- Range stack tracking. Exactly one RS track was required.

[10]TARBNK examined the timing and energy of any hit fibers in the target and sorted them into either kaon, pion or disconnected clusters. The kaon traveled along the length of the fibers and tended to deposit a large amount of energy in a small number of fibers. The pion clusters started at one of the kaon clusters and had only a couple of MeV per fiber because the pions tended to travel perpendicular to the fibers and had a high momentum so they were minimum ionizing. Disconnected clusters could have any energy and weren't associated with the pion or kaon clusters, they were either accidental hits that occurred at roughly the same time as the entry or decay of the kaon, or photons from the kaon decay that converted in the target.

[11]ICRNGE tracked the DC track back into the IC's and checked if the expected IC, or if the DC track was near the edge of an IC then the adjacent IC, had been hit. It also used the DC information to determine the expected path length of the track in the IC (or ICs) and the energy it should have deposited there.

- Track time. Verified that TRKTIM[12] did find a T·A time, almost no events should have failed this since range stack tracking had already succeeded.
- Stopping layer misidentification. Although the online trigger required the event to stop in either layer A or B, it was observed that the offline stopping counter was occasionally deeper than layer B. These events were rejected.

#### 4.3.1.2 Photon Vetoes

PASS1 photon vetoes were restricted to the end cap and range stack. The range stack veto included all RS counters which were not part of the charged track identified during the event reconstruction. For both subsystems a cut point of 4MeV visible INTIME energy was chosen (figure 42). The INTIME timing windows were set by fitting the time of the largest hit in each subsystem to a Gaussian plus flat background (figure 43). The EC fit was quite good, but the RS showed a large non-Gaussian tail at positive time. The windows used in PASS1 were arbitrarily chosen to be two standard deviations about the mean of the time spectrum (table 7).

Table 7: PASS1 Intime Parameters

| Subsystem | Threshold (MeV) | Time Offset (ns) | Time Window (ns) |
|---|---|---|---|
| End cap | 4 | 0.53 | ±3.46 |
| Range stack | 4 | 0.42 | ±1.56 |

#### 4.3.1.3 Charged Track Mass

The mass of the charged particle was reconstructed using the drift chamber momentum and the range stack energy ($M_{\pi^+} = (P_{DC}^2 - E_{RS}^2)/2E_{RS}$). However, due to nuclear interactions and misalignment of the range stack light guides[13] there was very often unseen energy in the range stack result-

[12]TRKTIM looked at the range stack counters hit by the charged track and determined the time of the track, it required that there be hits in, at least, the T and A layers.

[13]The four layers of scintillator that made up the A layer were separated from each other but were read out at either end by a single light guide. It was discovered that the thickness of the light guides was slightly less than the combined thickness of the four scintillator layers. This meant that a fraction of the light from either the inner or outer (or possible both) scintillator layer was not collected. This effect was only relevant for events where the charged track stopped in the A layer where it could result in a small underestimation of the charged-track energy.

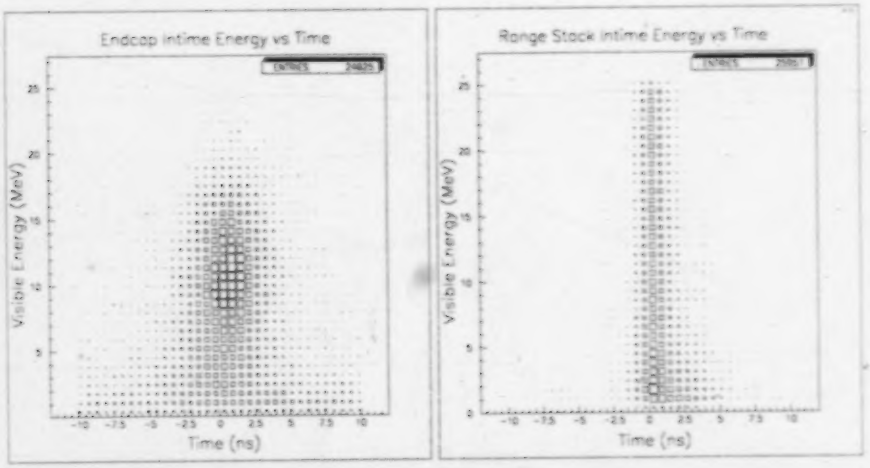


**Figure 42: Typical INTIME energy/time distributions for raw $\pi\gamma\gamma(2)$ data**

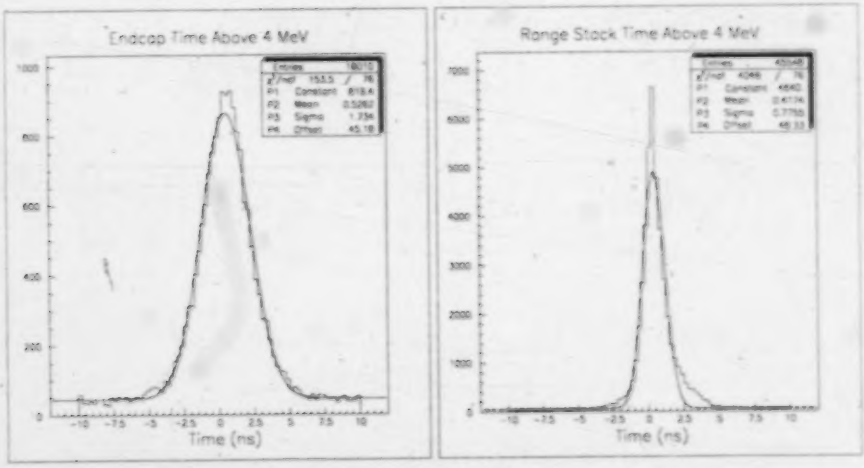


**Figure 43: INTIME time distribution for events above 4MeV visible energy. The fit is to the equation $y = p_4 + p_1 e^{-(x-p_2)^2/2p_3^2}$**

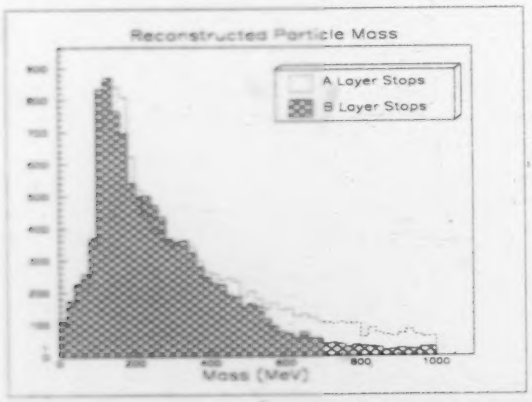


Figure 44: Charged track mass for A and B layer stops in $\pi\gamma\gamma(2)$ after EC and RS photon vetoes.

ing in extremely high masses (figure 44). The mass was required to be less than 300MeV, which mainly eliminated $K\pi 2$ decays, since there was a large background of $K\pi 2$ events where the $\pi^+$ had inelastically interacted in the RS. It should be noted that the charged particle was assumed to be a pion for the purposes of unsaturating the RS stopping counter[14], subtracting the $\pi \to \mu$ decay energy and correcting for energy loss in the outer drift chamber wall[15]. For muons this increased their measured mass by a few MeV.

### 4.3.2 PASS2 Analysis

The PASS2 cuts were simply used to reduce the data remaining after PASS1 to a size that would fit on a single 8mm tape. Only two cuts were used, charged track momentum and photon invariant mass. At this time all events from runs 9474-9485 were also rejected because an incorrect version of CFM, the calibration database, had been loaded into the ACPs online thus compro-

[14]Since the $dE/dx$ of a charged particle is velocity dependent the particle tends to deposit a large amount of energy in a small volume as it comes to rest. This can saturate the light generating capacity of the scintillator and result in an underestimate of the deposited energy. A correction was applied which required that the type of charged particle be known.

[15]Energy loss in non-active portions of the detector, such as the drift chamber carbon fibre walls, was estimated using the path-length of the charged track in the material and the $dE/dx$ of the particle. To determine the $dE/dx$ an assumption had to be made about the type of particle involved.

Table 8: Rejection of PASS1 cuts

| Cut Description | Pass | Rejection |
|---|---|---|
| Total Events | 2726738 | |
| Target Reconstruction (ierr=0, iqual<3) | 2696718 | 1.011 |
| DC Tracking (exactly 1 track) | 2317582 | 1.164 |
| Positive Charged Track | 2202240 | 1.052 |
| IC Reconstruction | 2144985 | 1.027 |
| RS Tracking (exactly 1 track) | 2096010 | 1.023 |
| Track Time (TRKTIM succeeds) | 2095985 | 1.000 |
| Stopping Layer | 1971441 | 1.063 |
| EC and RS Photon Vetoes | 664813 | 2.965 |
| Charged Track Mass < 300MeV | 373912 | 1.778 |
| Total PASS1 Rejection | 7.292 | |

mising the level 3 trigger. The cuts are described below and their rejections given in table 9. After PASS2 there remained 130991 events.

#### 4.3.2.1 Pion Momentum

After the PASS1 analysis there was still considerable K$\pi$2 contamination. Most of these events had pions which nuclear interacted in the range stack thus stopping in layer A or B but still had the expected $\pi^+$ momentum of 205 MeV/c (figure 45). To remove this background only events with a charged track momentum of less than 180MeV/c were accepted. Note that this charged track momentum was corrected for energy lost before reaching the DC using target range and assuming the charged particle to be a $\pi^+$.

#### 4.3.2.2 Photon Invariant Mass

In the online level 3 code photons in the barrel veto were combined in pairs to create the highest possible invariant mass. This mass was then required to be at least 190 MeV (section 4.2.3). However, the online code did not use TDC information in finding the barrel veto photons and used barrel veto energy calibration files which were not as accurate as those determined after the 1991 run was finished. The GAMMAS routine[16] was used to search for photon clusters in the barrel veto counting only elements with a visible energy of at least 0.5 MeV and within $\pm$6.3ns of the charged track time. The

[16]GAMMAS used information from the INTIME routine to sort the BV hits into possible photon conversions.

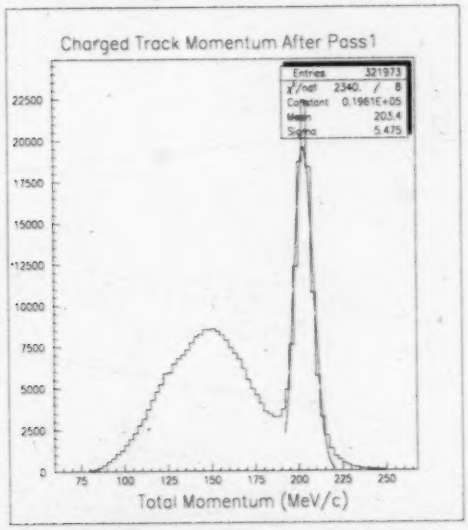


Figure 45: Total charged track momentum for events surviving PASS1.

Table 9: Rejection of PASS2 cuts

| Cut Description | Total | Pass | Rejection |
|---|---|---|---|
| Charged track momentum ($P_{\pi^+}$ <180MeV/c) | 334289 | 202301 | 1.652 |
| Photon invariant mass ($M_{\gamma\gamma}$ >190MeV) | 202301 | 130991 | 1.544 |
| Total PASS2 Rejection | 334289 | 130991 | 2.552 |

two most energetic clusters were used to determine the photon invariant mass using a visible fraction of 0.31 and the BV speed-of-light/attenuation length calibration files which were mentioned earlier (section 3.7). The on-line requirement of $M_{\gamma\gamma}$ >190MeV was applied again using this new mass measurement. Figure 46 shows that a significant fraction of the events re-constructed to zero mass due to a missing or very low energy second photon cluster.

### 4.3.3 PASS3 Analysis

#### 4.3.3.1 Event Reconstruction

To take into account minor changes in the analysis and calibrations the reconstruction cuts of PASS1 were re-applied in PASS3 with some additional

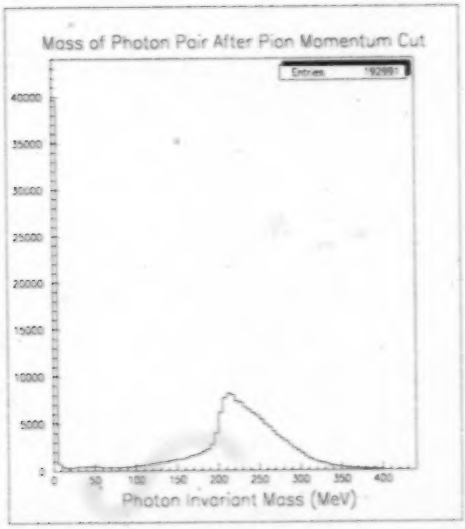


Figure 46: Invariant photon mass after PASS1 and total momentum cut.

conditions.

- Target reconstruction now required that a pion cluster be found, i.e. target quality return code $< 2$.
- DC tracking code ifail_code(i_dc) was required to be 0. PASS1 cut on the basis of exactly one drift chamber track being identified by the tracking routines but this did not eliminate tracks which failed the $z$ fitting, and returned ifail_code(i_dc) = 15 or 17, as long as there was a good $xy$ track. The number of these events after PASS1 was 6459/334289 (1.93%).
- The TRKTIM return code was required to be $\geq 0$ in PASS1, however return code 0 also indicated a failure to find a track time, so the cut was tightened to $> 0$. There were a total of 18067/334289 (5.40%) such events after PASS1. Almost all of these were eliminated incidentally by the $M_{\gamma\gamma}$ >190MeV cut in PASS2.

Two new reconstruction cuts were defined based on the difference in the IC and TG between the actual energy deposited and the energy expected based on charged track length.

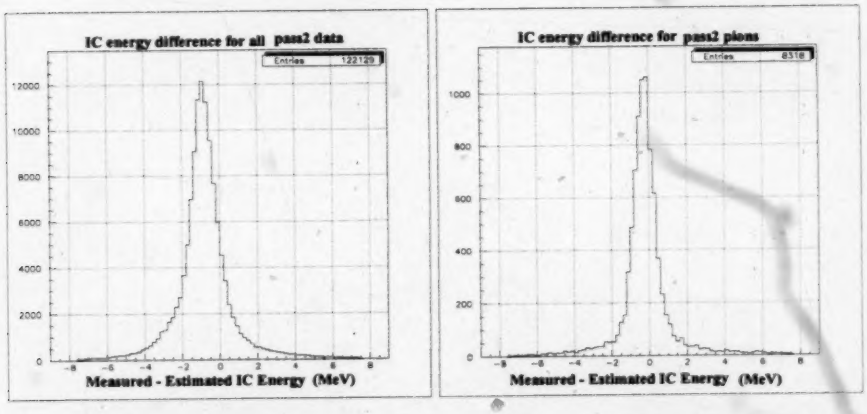
IC energy difference for all pass2 data
Entries 122129
Measured - Estimated IC Energy (MeV)
IC energy difference for pass2 pions
Entries 8318
Measured - Estimated IC Energy (MeV)

Figure 47: $\Delta E_{IC}$ energy difference for all PASS2 data and PASS2 pions selected using TD cuts.

- |IC energy - expected IC energy|<2.5MeV. This compared the measured IC energy to the expected IC energy returned by ICRNGE (figure 47).
- |TG energy - expected TG energy + 1.47MeV|<5MeV. The measured target energy was compared to the TG energy expected based on the target range (figure 48). The 1.47MeV was an empirical correction to the measured TG energy used to bring it in line with the range based estimate for good pions.

#### 4.3.3.2 Charged Track Mass

A cut was applied to the charged track mass requiring 120MeV<$M_{\pi^+}$ <165MeV to exclude K$\mu$3 muons as well as pions which had interacted in the RS.

However, an empirical correction was first applied to the measured RS energy because it was noted that the measured particle mass for pions tended to be too high in RS layers A and B and showed an energy dependence (figure 49). This corresponded to a few MeV (on the order of 4) of missing energy, possibly due to problems such as the misaligned light guides. If $E_r$ is the measured RS energy after subtraction of the $\pi \to \mu$ decay energy then $E_{RS} = 0.0005E_r^2 + 0.83E_r + 7.7$. Figure 49 shows the mass versus RS energy distribution before and after the correction. Note that this correction was only valid for $\pi\gamma\gamma(2)$ triggers and was not used for events which stopped

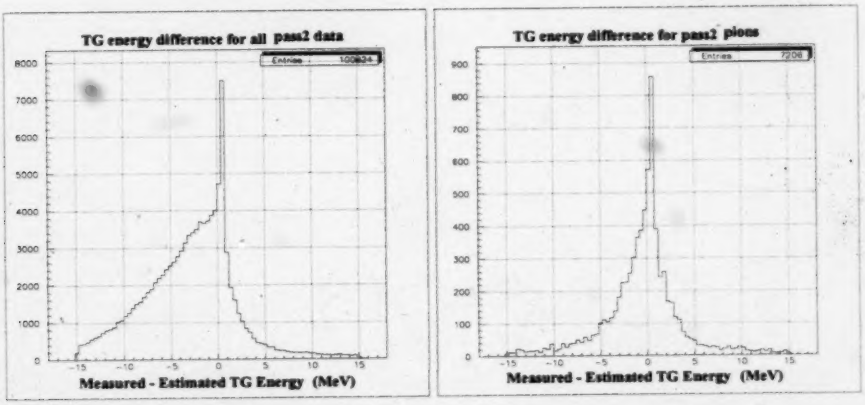
TG energy difference for all pass2 data
Measured - Estimated TG Energy (MeV)
TG energy difference for pass2 pions
Measured - Estimated TG Energy (MeV)

Figure 48: $\Delta E_{TG}$ energy difference for all PASS2 data and PASS2 pions selected using TD cuts.

deeper in the RS such as K$\mu$2 or K$\pi$2 .

#### 4.3.3.3 Invariant Photon Mass

In PASS2 a cut was applied requiring $M_{\gamma\gamma}$ >190MeV, this was increased in PASS3 to $M_{\gamma\gamma}$ >200MeV.

#### 4.3.3.4 Photon Vetoes

To eliminate events containing extra photons, such as K$\pi$3 and radiative K$\pi$2, the photon vetoes on the EC and RS were tightened and vetoing done on the target, lead glass, IC and VC as well as a search for extra energy outside of the two photon clusters expected in the BV.

Events were selected which had survived PASS2 and the timing spectrum of each subsystem was fit to a Gaussian plus flat background (figure 50). For the EC and RS the corresponding PASS1 photon veto cut was not applied so that the full spectrum of hits could be plotted (figure 51). The INTIME windows were set at approximately the times where the prompt peak sank to the level of the flat background (table 10). The peak at +6ns in the barrel veto time distribution (figure 52) is an artifact due to the removal of the counters associated with the two highest energy photon clusters within 6.3ns of the prompt time. This results in a slight suppression of the number of events between ±6.3ns relative to the tails. The bump in the BV spectrum

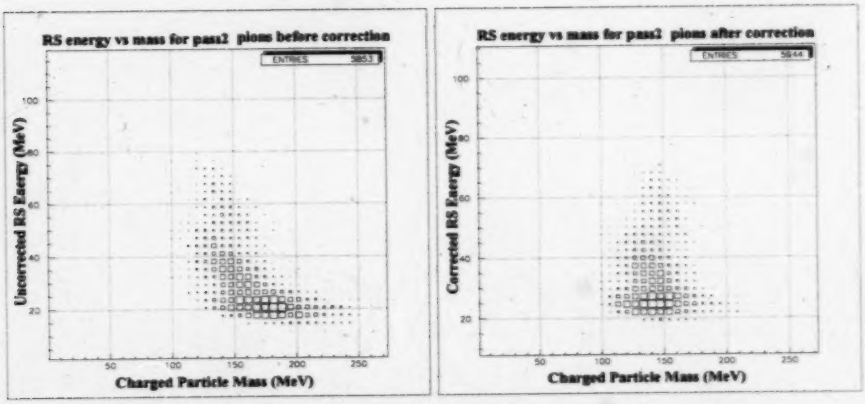
RS energy vs mass for pass2 pions before correction
ENTRIES 5853
Uncorrected RS Energy (MeV)
Charged Particle Mass (MeV)
RS energy vs mass for pass2 pions after correction
ENTRIES 5844
Corrected RS Energy (MeV)
Charged Particle Mass (MeV)

Figure 49: Mass vs RS energy for pions selected from PASS2 data using TD cuts, before and after the RS energy correction.

at -7.5ns is mainly caused by an 8ns bifurcation in the TDC time of some of the BV modules up to about run 9485[17]. This bifurcation is clear if two different portions of the 1991 run are considered without exclusion of the prompt counters and with some of the cuts removed to improve statistics (see figure 53). However, it did not pose a problem in the final analysis and did not have to be specifically removed.

Excess target energy was not found by INTIME but by looking for target clusters with energy above 0.3MeV identified by TARBNK but not associated with the stopping kaon or the pion track. The time shown in figure 54 is an energy weighted mean time of all the disconnected clusters which were within ±16ns of the pion time [18].

In the lead glass counter there was no absolute energy measurement, instead the energy deposited was considered proportional to the number of photomultiplier tubes above some hardware signal threshold. The time of any hits was recorded versus the number of PMT's fired. The incoming kaon often produced enough light to leave a signal at the one or two tube level as can be seen by the diagonal band on the left side of the graphs in figure 55 where the time of the Pb glass hit was the same as that of the incoming

[17]This was a hardware problem which persisted for a small part of the run before it was corrected. A block of TDC's reading out part of the BV had a random jitter which would shift the time read out by all of those TDC's by 8ns.

[18]Pion time was defined as either the time of the pion cluster or the RS time adjusted for possible RS-TG time offsets if no target pion cluster was found.

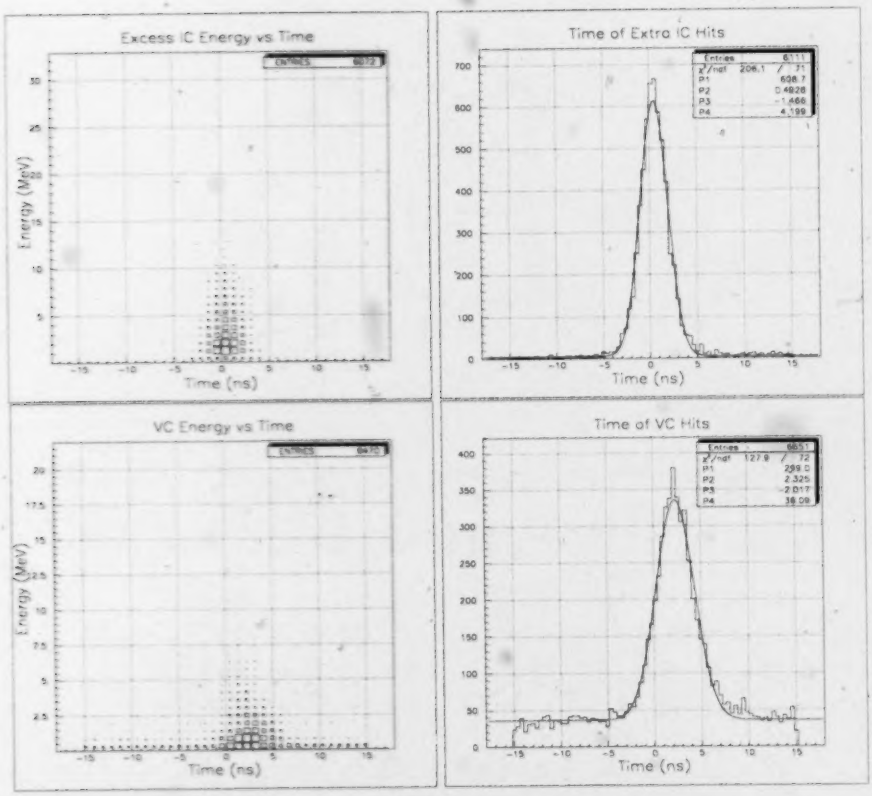


**Figure 50: INTIME energy in the I-counter and veto counter.**

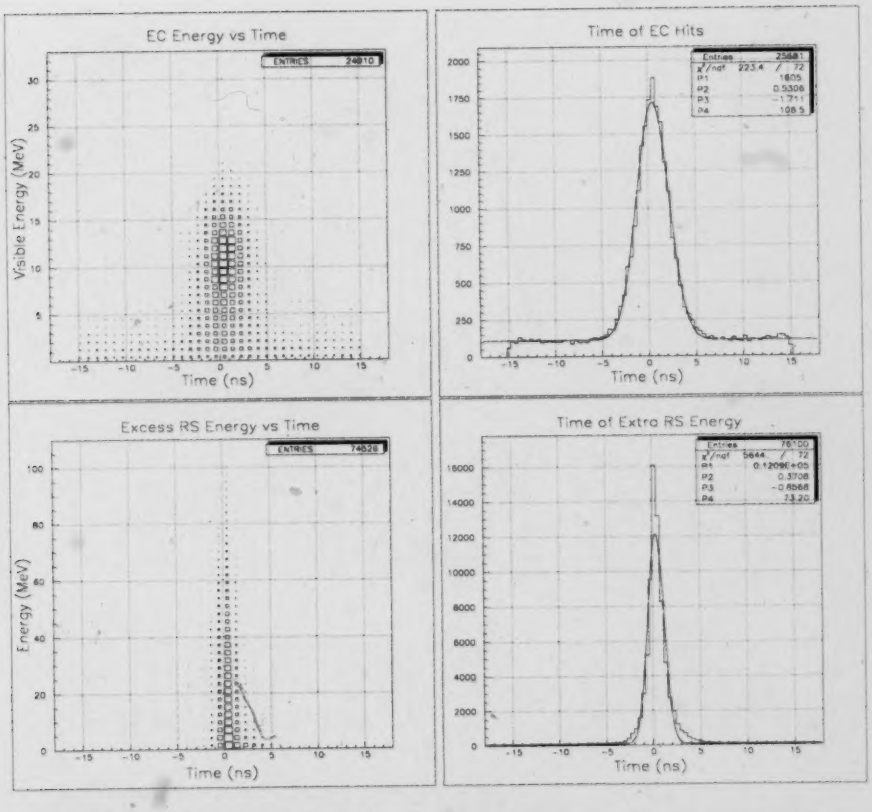


**Figure 51: INTIME energy in the endcap and range stack (the corresponding PASS1 photon veto cuts have not been applied).**

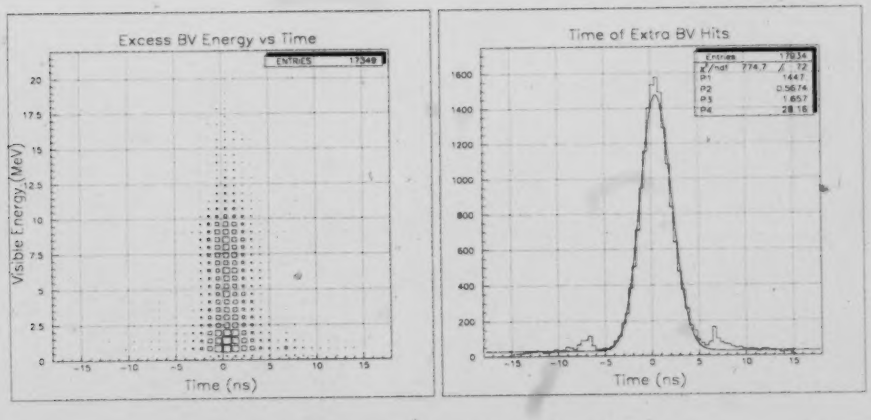


**Figure 52: INTIME energy in the barrel veto (excluding the energy from the two highest energy prompt photon clusters).**

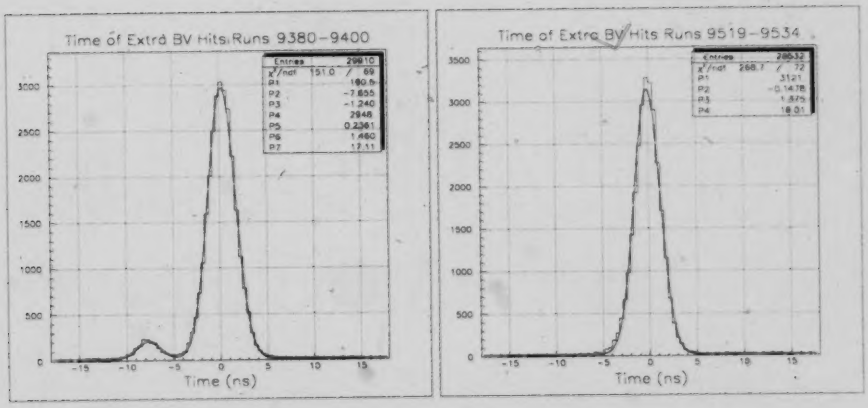


**Figure 53: Timing of excess BV energy at two different portions of the run.**

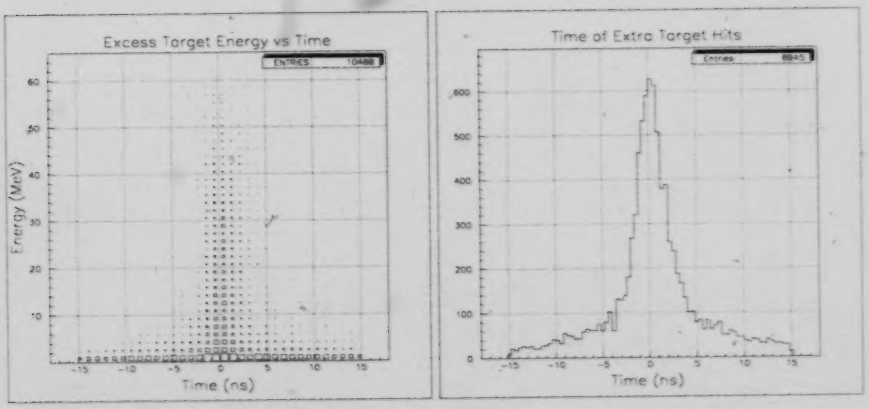


Figure 54: Excess energy in the target relative to target pion time.

kaon. For three or more PMT's the time closest to the prompt pion time was used for photon vetoing (figure 56).

Table 10: Photon Veto Intime Parameters

| Subsystem | | Threshold (MeV) | Time Offset (ns) | Window (ns) |
|---|---|---|---|---|
| I counter | IC | 1 | 0.5 | ±5.0 |
| Veto counter | VC | 1 | 2.0 | ±5.0 |
| End cap | EC | 1(visible) | 0.0 | ±5.0 |
| Range stack | RS | 4 | 0.75 | ±5.25 |
| Barrel veto | BV | 2(visible) | 0.0 | ±6.3 |
| Target | TG | 3 | 0.0 | ±6.0 |
| Pb Glass | PG | 3 PMT's | 0.0 | ±5.0 |

#### 4.3.3.5 Missing Momentum

In a true $\pi\gamma\gamma(2)$ event all three decay products of the kaon were stopped and measured so it should have been possible to reconstruct the original kaon mass, momentum and energy. Since the kaons were presumed stopped in the target before they decayed, the total momentum of the pion and two photons should have reconstructed to zero. This was not true for several of the potential background modes, foremost of which were $K\hat{\mu}3$ in which the neutrino carries away a considerable amount of momentum (figure 57), $K\pi 2$ events in which the pion scattered before entering the drift chamber and thus had

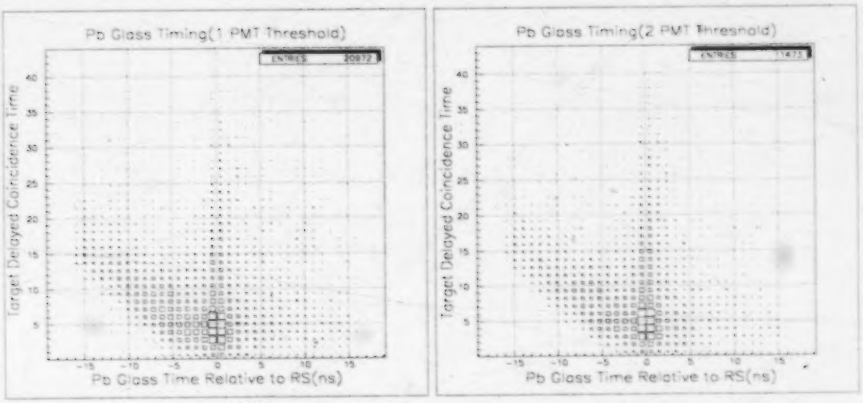
Pb Glass Timing(1 PMT Threshold)
Target Delayed Coincidence Time
Pb Glass Time Relative to RS(ns)
Pb Glass Timing(2 PMT Threshold)
Target Delayed Coincidence Time
Pb Glass Time Relative to RS(ns)

**Figure 55: Time of Pb glass hits versus delayed coincidence time.**

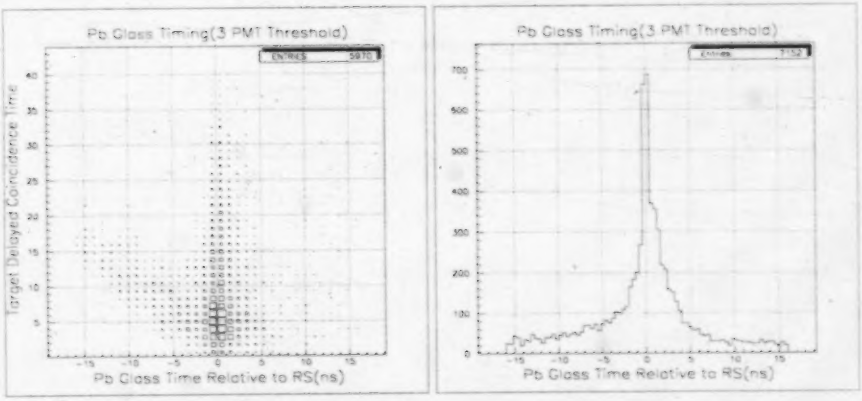
Pb Glass Timing(3 PMT Threshold)
Target Delayed Coincidence Time
Pb Glass Time Relative to RS(ns)
Pb Glass Timing(3 PMT Threshold)
Pb Glass Time Relative to RS(ns)

**Figure 56: Time of Pb glass hits for 3 or more PMT's.**

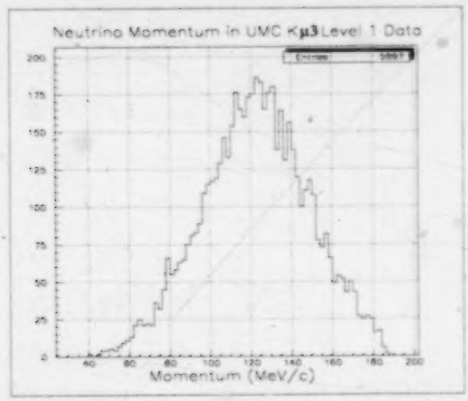


Figure 57: K$\mu$3 neutrino momentum after passing the level 1 trigger (UMC data).

a momentum low enough to pass the K$\pi$2 peak cut of $P_{\pi^+}$ <180MeV/c (figure 58) and K$\pi$3's in which a photon had been missed or absorbed. To determine the momentum of the entire event the kaon decay vertex was located by extrapolating the charged particle track to the position of the kaon stopping fibers identified by the target routine. The energy and centroid position of the two photon clusters in the barrel veto were combined with the momentum vector of the charged particle track and the decay vertex to yield the magnitude of the 'kaon' momentum, i. e. the vector sum of the momentum of the $\pi^+$ and the two photons which was the momentum that the original kaon would have had to have, at the time it decayed, to conserve momentum conservation. A cut was placed requiring the excess momentum to be less than 86.6MeV/c ($P_{K^+}{}^2 < 7500$) (figure 59). Figure 60 shows this momentum, $P_{K^+}$, for $\pi\gamma\gamma(2)$ PASS1 events which had been selected using TD cuts and mass constraints to have a charged track that was either a muon or a pion. There is a good separation between the muon containing events (K$\mu$3 ) with their missing neutrino and the pion events (K$\pi$3 , K$\pi$2 , $\pi\gamma\gamma(2)$) which deposit all their energy in the detector.

#### 4.3.3.6 Opening Angle Cut

There were two different opening angles that were considered in the $\pi\gamma\gamma(2)$ analysis. One was the opening angle between the two photons, $\theta_{\gamma\gamma}$, used in the online cuts, the other was the angle, $\theta_{\pi\gamma_1}$, between the more energetic

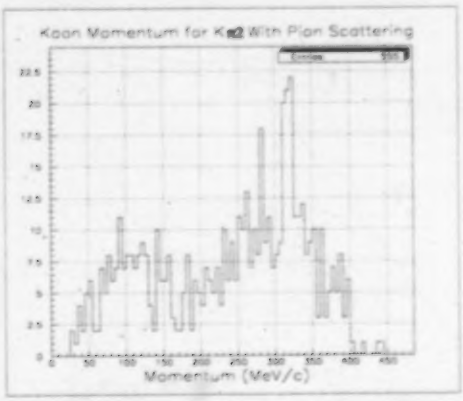


**Figure 58: Kaon momentum of $\pi\gamma\gamma(2)$ level 0 data selected using TGTRACK, $M_{\gamma\gamma}$ and TD cuts to contain a K$\pi$2 in which the $\pi^+$ had scattered in the target before stopping in the RS.**

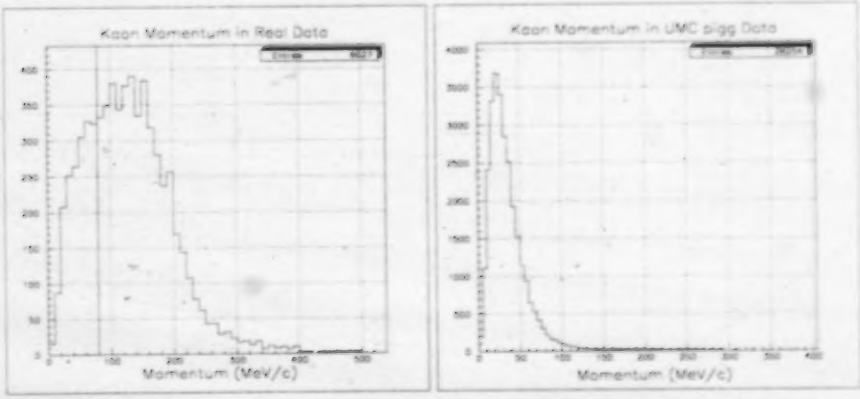


**Figure 59: Missing kaon momentum in real $\pi\gamma\gamma(2)$ data (left) and UMC $\pi\gamma\gamma(2)$ data (right) after PASS1, photon veto, $P_{\pi^+}$ and $M_{\gamma\gamma}$ cuts. The solid vertical line in the left figure shows the missing momentum cut position at 86.6MeV/c.**

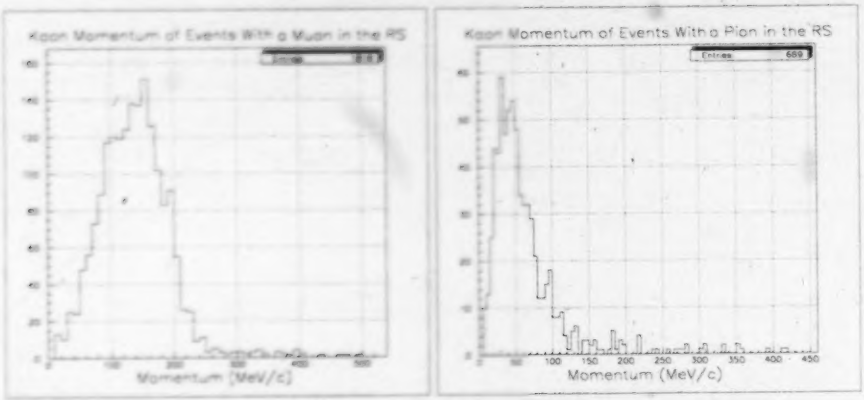
Kaon Momentum of Events With a Muon in the RS
Momentum (MeV/c)
Kaon Momentum of Events With a Pion in the RS
Entries 689
Momentum (MeV/c)

Figure 60: Missing kaon momentum in $\pi\gamma\gamma(2)$ events selected to contain either muons or pions.

of the two photons and the charged particle defined by;

$$cos(\theta_{\pi\gamma_1}) = \frac{\mathbf{P}_{\gamma_1} \cdot \mathbf{P}_{\pi^+}}{|\mathbf{P}_{\gamma_1}||\mathbf{P}_{\pi^+}|}$$

where $\mathbf{P}_{\gamma_1}$ and $\mathbf{P}_{\pi^+}$ are the momentum 3-vectors of the high energy photon and the charged particle. These two cuts were to some extent related. Since the $\pi^+$ was required in the analysis to have a momentum of at least 100MeV/c a large opening angle between the two photons, $\theta_{\gamma\gamma}$, implied that one of the photons would have a low energy while the higher energy photon would have to travel in the opposite direction from the $\pi^+$ to conserve overall momentum. Figure 61 shows UMC generated $K^+ \to \pi^+\gamma\gamma$ distributions of $\cos(\theta_{\pi\gamma_1})$ and the energy of the lower energy photon versus $\cos(\theta_{\pi\gamma_1})$. Looking at the equation for the invariant photon mass;

$$M_{\gamma\gamma} = \sqrt{2(1 - \cos(\theta_{\gamma\gamma}))E_{\gamma_1}E_{\gamma_2}},$$

it can be seen that for large $\theta_{\gamma\gamma}$ the term $2(1 - cos(\theta_{\gamma\gamma})) \approx 4$ and the resolution of the invariant mass was dominated by the least accurate of the two energy measurements. Since the resolution of the energy measurements was proportional to $1/\sqrt{E}$, events with large $\theta_{\gamma\gamma}$, or equivalently $\cos(\theta_{\pi\gamma_1})$ near -1, had the least accurately determined values for $M_{\gamma\gamma}$ .

Additionally, the main contribution to one of the most dangerous background modes, radiative K$\pi$2, came from internal bremsstrahlung where

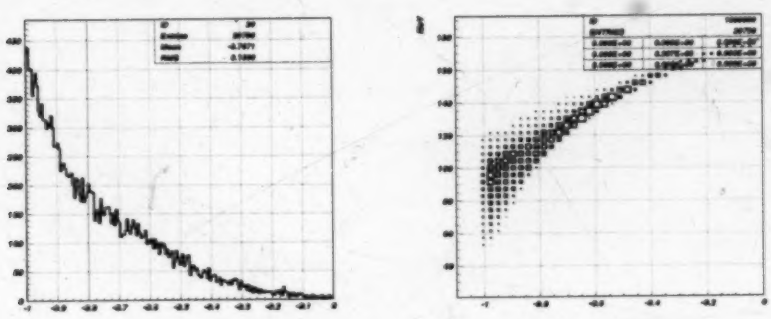

Figure 61: The $\cos(\theta_{\pi\gamma_1})$ distribution of $\pi^+\gamma\gamma$ events (generated using UMC), and the photon energy of the lower energy photon versus $\cos(\theta_{\pi\gamma_1})$.

the third photon was radiated by the $\pi^+$ line and tended to travel in the same direction as the $\pi^+$. To satisfy the two photon requirement in the analysis, one of the $\pi^0$ photons would have had to overlap with this internal bremsstrahlung photon requiring the other, higher energy, $\pi^0$ photon to travel in the opposite direction from the $\pi^+$ (figure 62).

To eliminate these two classes of events a cut was applied requiring $\cos(\theta_{\pi\gamma_1}) > -0.8$.

#### 4.3.3.7 $M_{\gamma\gamma}$ Mass Difference

For $K^+ \to \pi^+\gamma\gamma$, there is a relation between the $\pi^+$ momentum ($P_{\pi^+}$) and the invariant mass of the two photons:

$$\mathrm{M_{\gamma\gamma}(P_{\pi^+}) = \sqrt{M^2_{K^+} - 2M_{K^+}\sqrt{M^2_{\pi^+} + P^2_{\pi^+}} + M^2_{\pi^+}}}.$$

A cut to check the above relation was applied requiring:

$$\mathrm{M_{\gamma\gamma}(\gamma\gamma) - M_{\gamma\gamma}(P_{\pi^+}) > -30MeV},$$

where $M_{\gamma\gamma}(\gamma\gamma)$ is the invariant mass calculated from the energies and directions of the two photons. Since we are searching for $K^+ \to \pi^+\gamma\gamma$ whose $\pi^+$ momentum is below the K$\pi$2 peak, $M_{\gamma\gamma}(P_{\pi^+})$ is always larger than $M_{\pi^0}$. Therefore, this cut was effective in eliminating background events from K$\mu$3,

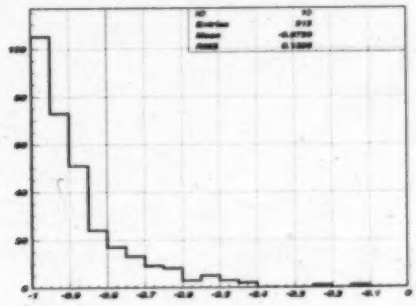

Figure 62: The $\cos(\theta_{\pi\gamma_1})$ distribution for radiative K$\pi$2 events (events generated by UMC and selected using KINFIT).

K$\pi$2 and radiative K$\pi$2 where the third photon was missed, all of which would tend to have negative values for $M_{\gamma\gamma}(\gamma\gamma) - M_{\gamma\gamma}(P_{\pi^+})$.

#### 4.3.3.8 Overlapping Gamma Veto

K$\pi$3 and radiative K$\pi$2 could be mistaken for $\pi\gamma\gamma$ events if the photons overlapped in the barrel veto and the number of photons was miscounted as being only two. Fortunately, it was extremely unlikely for two overlapping photons to be travelling in exactly the same direction, so they tended to affect a larger volume of the BV than a single photon of the the same total energy.

The overlapping gamma veto cut consisted of three different cuts. NGCUT, a cut on the total number of BV elements in a photon cluster. PHICUT, a cut on the azimuthal dispersion of the hit elements in the cluster. And ZCUT, a cut on the extent of the cluster in the longitudinal direction.

Defining NG as the number of hit BV elements in a particular photon cluster then NGCUT rejected events if $NG > 7$ in either the low or high energy photon cluster (figure 63 shows the typical number of elements hit for UMC generated $K^+ \to \pi^+\gamma\gamma$ events).

PHICUT defined the energy weighted azimuthal dispersion of a photon

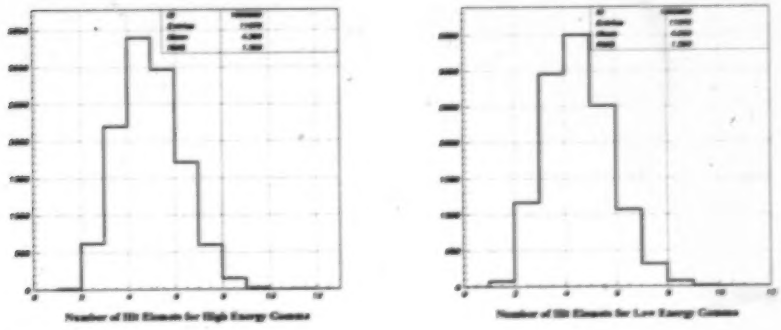

Figure 63: The number of hit BV elements in UMC generated $\pi\gamma\gamma(2)$ data.

cluster, $\phi_g^2$,as;

$$\phi_g^2 = \frac{(\sum_{i=1}^{NG} E_i \times \phi_i^2) - (\sum_{i=1}^{NG} E_i \times \phi_i)^2}{\sum_{i=1}^{NG} E_i} \tag{45}$$

where $E_i$ and $\phi_i$ are the energy deposited and azimuthal angle of the i-th hit BV module in the cluster. Clearly as the number of hit elements in the cluster, NG, increases the value of $\phi_g^2$ will tend to increase. To remove this dependence an empirical correction was applied;

$$\phi_g^2 \to \frac{6.0 \times \phi_g^2}{-0.08571 \times (\mathrm{NG})^2 + 1.617 \times \mathrm{NG} + 0.2087}$$

The correction was designed so that the PHICUT requirement of $\phi_g^2 < 0.06$, applied to photon clusters in the energy range $100 < E_\gamma < 200$MeV, would have a 90% acceptance for each separate value of NG when 2<NG<8 (figure 64).

ZCUT defined the $z$ position of the hit in each struck BV module by taking a weighted mean of the $z$ measurement given by the end-to-end energy difference and the end-to-end time difference (as defined in section 3.7). A variable $z_{max}$ was defined as the maximum fluctuation of the measurement in a cluster:

$$z_{max} \;=\; \mathrm{MAX} \mid z_i - z_j \mid ; i, j = 1 \cdots \mathrm{NG}.$$

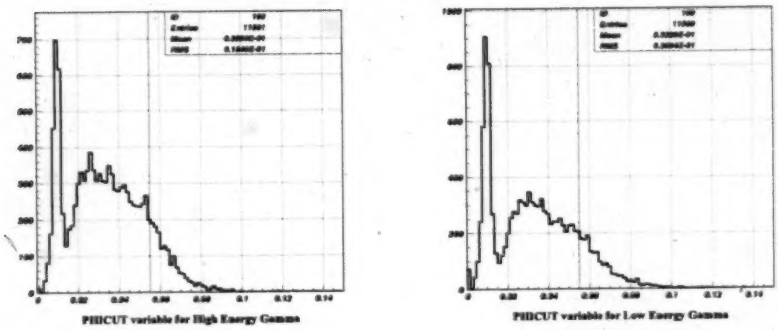


Figure 64: $\phi_g^2$ distribution for the high (left) and low (right) energy photon. UMC was used to determine the photon energy distribution then the variables used in $\phi_g^2$ were taken from real K$\pi$2 data with photons of the same energy. The peak at low $\phi_g^2$ corresponds to photons for which all BV hits belong to one sector.

As with $\phi_g^2$ there is a clear dependence on the value of NG so again an empirical correction was applied;

$$z_{max} \to \frac{4.0 \times z_{max}}{-0.04946 \times (\mathrm{NG})^2 + 1.274 \times \mathrm{NG} + 0.5419}$$

where $z_{max}$ was measured in units of 15cm (the distance travelled in 1ns by light in the BV based on an average speed-of-light of 15cm/ns). This correction was again designed so that the ZCUT condition of $z_{max} < 4$, applied to clusters with $100 < E_\gamma < 200$MeV, would give a 90% acceptance for each value of NG in the range $2 < \mathrm{NG} < 8$ (figure 65).

#### 4.3.3.9 KINFIT $\chi^2$ Probability

A constrained fit was done on the kinematics of the pion and the two photons assuming a $K^+ \to \pi^+\gamma\gamma$ decay. The constraints required were 4-momentum conservation for the kaon and an on-shell $\pi^+$:

$$\begin{aligned} \sqrt{P_\pi^2 + m_\pi^2} &= T_\pi + m_\pi \\ T_\pi + m_\pi + P_{\gamma_1} + P_{\gamma_2} &= m_K \\ P_\pi \sin(\theta_\pi) + P_{\gamma_1} \sin(\theta_{\gamma_1}) + P_{\gamma_2} \sin(\theta_{\gamma_2}) &= 0 \end{aligned}$$

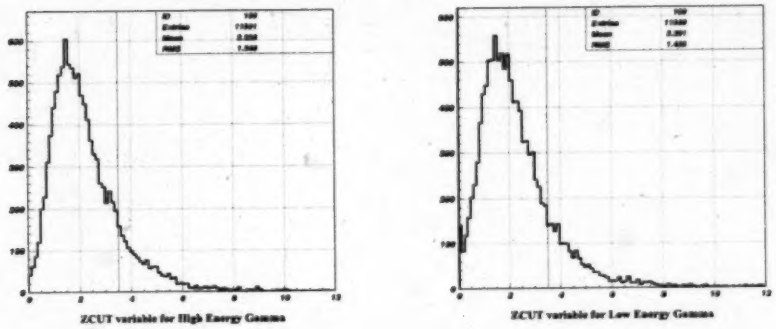


Figure 65: $z_{max}$ distribution for the high (left) and low (right) energy photon. UMC was used to determine the $\pi\gamma\gamma(2)$ photon energy distribution then the variables used in $z_{max}$ were taken from real K$\pi$2 data with photons of the same energy.

Table 11: KINFIT Variables

| | Pion | $\gamma$ (high energy) | $\gamma$ (low energy) |
|---|---|---|---|
| momentum | $P_\pi$ | $P_{\gamma 1}$ | $P_{\gamma 2}$ |
| azimuthal angle | $\phi_\pi$ | $\phi_{\gamma 1}$ | $\phi_{\gamma 2}$ |
| dip angle | $\theta_\pi$ | $\theta_{\gamma 1}$ | $\theta_{\gamma 2}$ |
| kinetic energy | $T_\pi$ | - | - |

$$P_\pi \cos(\phi_\pi)\cos(\theta_\pi) + P_{\gamma_1}\cos(\phi_{\gamma_1})\cos(\theta_{\gamma_1}) + P_{\gamma_2}\cos(\phi_{\gamma_2})\cos(\theta_{\gamma_2}) = 0$$
$$P_\pi \sin(\phi_\pi)\cos(\theta_\pi) + P_{\gamma_1}\sin(\phi_{\gamma_1})\cos(\theta_{\gamma_1}) + P_{\gamma_2}\sin(\phi_{\gamma_2})\cos(\theta_{\gamma_2}) = 0$$

The measured variables appearing in the constraints are listed in table 11. Fitting was performed to minimize a $\chi^2$ given by:

$$\chi^2 = \sum_{i=1}^{10} \left(\frac{X^i_{meas} - X^i_{fit}}{\sigma^i_{meas}}\right)^2,$$

where $X^i_{meas}(i = 1 \cdots 10)$ are the measured variables, $X^i_{fit}$ are the fitted values, and $\sigma^i_{meas}$ are the standard deviations of $X^i_{meas}$ which were given by

$$\sigma(\phi_\pi) = 0.010$$

$$\sigma(\phi_{\gamma_1}) = \sigma(\phi_{\gamma_2}) = 0.045$$

$$\sigma(\theta_\pi) = 0.035 \times |cos(\theta_\pi)|$$

$$\sigma(\theta_{\gamma_1}) = 0.075 \times |cos(\theta_{\gamma_1})|$$

$$\sigma(\theta_{\gamma_2}) = 0.075 \times |cos(\theta_{\gamma_2})|$$

$$\sigma(P_\pi) = \sqrt{0.932 \times 10^{-8} P_\pi^4 + 1.51 \times 10^{-4} P_\pi^2}$$

$$\sigma(P_{\gamma 1}) = 1.63 \times \sqrt{P_{\gamma 1}}$$

$$\sigma(P_{\gamma 2}) = 1.63 \times \sqrt{P_{\gamma 2}}$$

$$\sigma(T_\pi) = 0.351 \times \sqrt{T_\pi}$$

To determine the standard deviations, initial values were calculated from the photon energy and position resolutions of K$\pi$2, from the $\pi^+$ energy and momentum resolutions of K$\pi$2, and from the $\pi^+$ mass resolution of K$\pi$2 and K$\pi$3. Then the standard deviations were fine-tuned to make the stretch functions defined below follow a normal Gaussian distribution (figure 66):

$$s_i \equiv \frac{X^i_{meas} - X^i_{fit}}{\sqrt{{\sigma^i_{meas}}^2 - {\sigma^i_{fit}}^2}},$$

If the standard deviations were well determined the probability distribution of the data would be flat (figure 67). Events were rejected if:

$$Prob(\chi^2) < 0.1$$

## 4.4 Event Selection Results

The net result of the online event selection cuts was to reduce the $1.01 \cdot 10^{11}$ stopped kaons examined by the trigger to only $2.7 \cdot 10^6$ events recorded to tape. The offline selection cuts further reduced this number to the 31 candidate events mentioned in table 12. All of these events were consistent with $K^+ \to \pi^+\gamma\gamma$ but a detailed study of other decay modes was required to determine how many of these 31 events may in fact have been simply background.

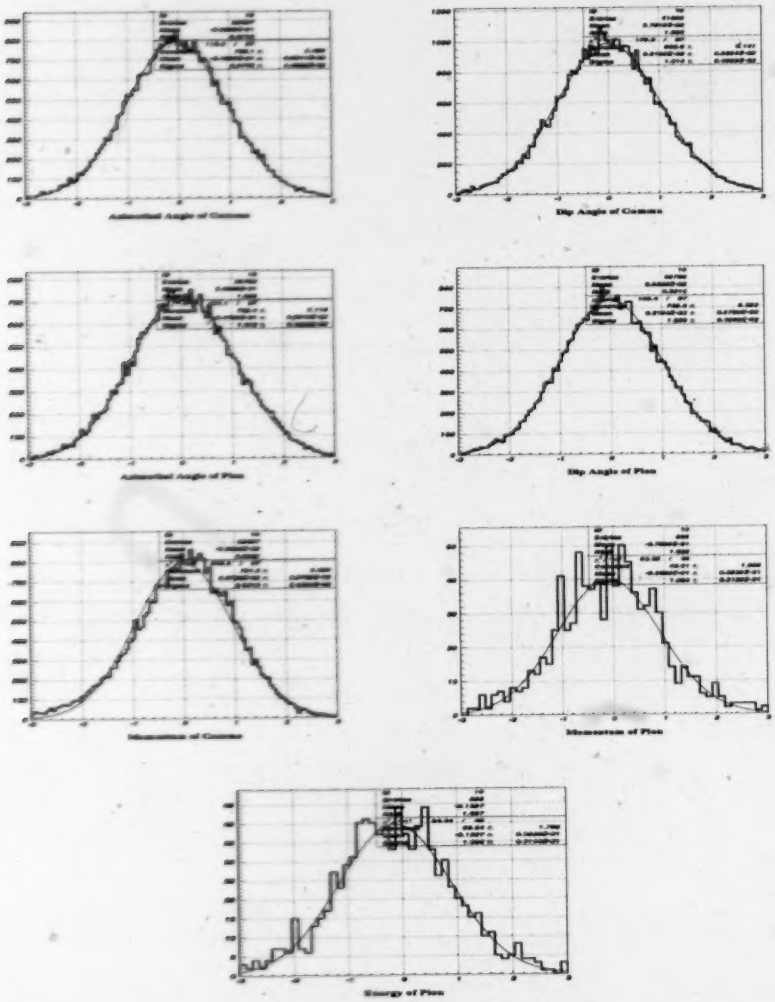

Figure 66: KINFIT stretch functions. Distributions for $\pi^+$ energy and $\pi^+$ momentum were obtained from overlapping photon events all others were from $K\pi 2$ data.

Table 12: Rejection of PASS3 cuts

| Cut Description | Cut Name | Pass | Rejection |
|---|---|---|---|
| After PASS2 | | 130991 | |
| Target Reconstruction | TG iqual<2 | 129123 | 1.0145 |
| Exactly 1 DC Track | DC xy track | 127678 | 1.0113 |
| DC Failure Code = 0 | DC $z$ track | 124265 | 1.0275 |
| Positive Charged Track | DC charge | 124242 | 1.0002 |
| Exactly 1 RS Track | RS track | 124220 | 1.0002 |
| Track Time Found | TRKTIM | 124205 | 1.0001 |
| IC Reconstruction, IC code≠1 | IC recon. | 124136 | 1.0006 |
| $\lvert E_{IC} - E_{IC}(est.)\rvert < 2.5$MeV | $\Delta E_{IC}$ | 107254 | 1.1574 |
| $\lvert E_{TG} - E_{TG}(est.) + 1.47\rvert < 5$MeV | $\Delta E_{TG}$ | 65885 | 1.6279 |
| 120<$M_{\pi^+}$ <165MeV | $M_{\pi^+}$ | 23656 | 2.7851 |
| IC Photon Veto | IC $\gamma$ veto | 20124 | 1.1755 |
| VC Photon Veto | VC $\gamma$ veto | 19229 | 1.0465 |
| EC Photon Veto | EC $\gamma$ veto | 15641 | 1.2294 |
| RS Photon Veto | RS $\gamma$ veto | 13774 | 1.1355 |
| TG Photon Veto | TG $\gamma$ veto | 11899 | 1.1576 |
| Pb Glass Photon Veto | C2 $\gamma$ veto | 10993 | 1.0824 |
| BV Photon Veto | BV $\gamma$ veto | 6551 | 1.6781 |
| 100≤$P_{\pi^+}$ <180MeV/c | | 6425 | 1.0196 |
| $M_{\gamma\gamma}$ >200MeV | | 5895 | 1.0899 |
| Missing Momentum < 86.6MeV/c | | 2727 | 2.1617 |
| $\pi^+$ $\gamma_1$ Opening Angle | $\cos\theta_{\pi\gamma_1}$ | 994 | 2.7435 |
| $M_{\gamma\gamma} - M_{\gamma\gamma}$ $(est.) > -30$MeV | $\Delta M_{\gamma\gamma}$ | 770 | 1.2909 |
| #BV Elements < 8/photon | $N_{BV}/\gamma$ | 655 | 1.1756 |
| Overlapping Photon Veto | $\gamma$ overlap | 47 | 13.9362 |
| KINFIT Probability>0.1 | KINFIT | 31 | 1.5161 |

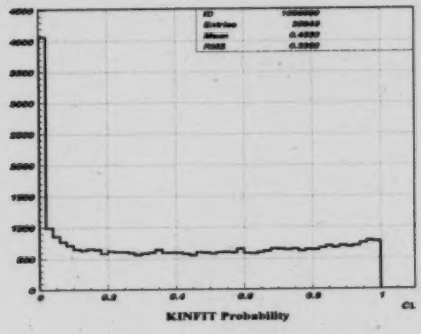


Figure 67: The KINFIT probability for $K\pi 2$ data.

# 5 Background Estimation

## 5.1 Introduction

As was mentioned in section 4.1 there are six decay modes with two or more photons which have branching ratios large enough to make them potential backgrounds (table 4). These were grouped into two general categories: events with 3 or more photons that fooled the event selection cuts because some of the photons overlapped each other in the barrel veto, and events which did not contain overlapping photons but instead passed due to event reconstruction inaccuracies. Due to the low electron rest mass and the tendency of high energy electrons to undergo electromagnetic showers, Ke3 and Ke3$\gamma$ were not significant backgrounds[19]. This left K$\pi$3 and K$\pi 2\gamma$ as the only possible overlapping decay modes. All of the decays could have potentially contributed to the non-overlapping background.

[19] Additionally any Ke3 background would be included in the K$\mu$3 background estimate.

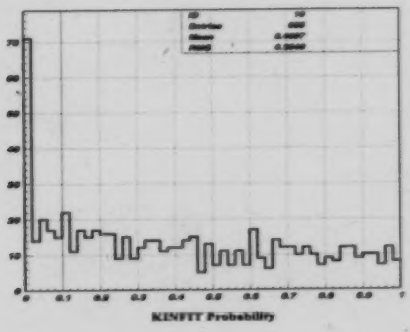


Figure 68: KINFIT probability distribution of events which passed all cuts except for PHICUT and ZCUT.

## 5.2 Overlapping Gamma Background

If the photons from K$\pi$3 or radiative K$\pi$2 overlapped[20] and were reconstructed as two photon clusters it was possible for the event to pass all other cuts including the kinematical fitting, as can be seen in figure 68 which shows the KINFIT probability of the $\pi\gamma\gamma(2)$ data set after applying all cuts except the overlapping photon cuts.

To estimate this background all cuts, except for PHICUT and ZCUT, were applied. This included the cut on the number of hit BV elements, $NG < 8$, which was added to remove a possible correlation between PHICUT and ZCUT when the number of hit elements was large. Figure 69 shows the $\pi^+$ momentum and the two photon invariant mass distribution of the 518 surviving events with a solid vertical line to indicate the position of the K$\pi$3 endpoint in $P_{\pi^+}$ and $M_{\gamma\gamma}$.

The number of potential overlapping photons was different for the K$\pi$3 background, which had two extra photons, and the radiative K$\pi$2 background, which had only one extra photon. Therefore the overall rejection of the overlapping photon cuts was expected to be different for the two background

[20]The term overlap always refers to two photons in the BV being contiguous so that they were resolved as a single photon cluster by the GAMMAS routine. At this point it is understood that exactly two photon clusters are present in the BV. One overlapping or two overlapping photon events refer to whether or not one or both of the photon clusters were actually the result of overlapping photons.

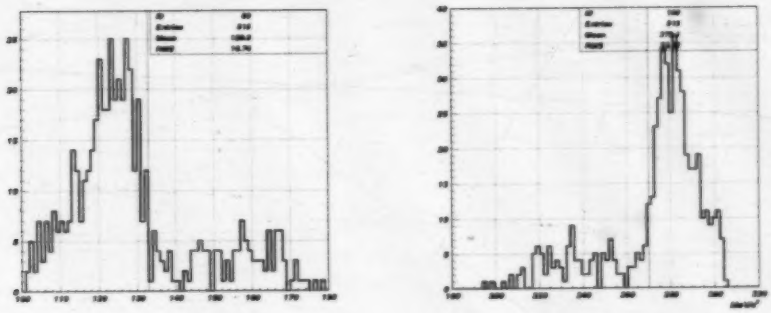

Figure 69: $\pi^+$ momentum (left) and photon invariant mass (right) distributions for the events which passed all cuts except for PHICUT and ZCUT. $K\pi 3$ background dominates in the region of $P_{\pi^+} < 133 MeV/c$, or equivalently, in the region of $M_{\gamma\gamma} > 270 MeV/c^2$.

types. To separate them the background was estimated both above and below the K$\pi$3 threshold ($P_{\pi^+}$ $\leq$133 MeV/c) (figure 70).

### 5.2.1 Method

Events were categorized according to the pass/fail conditions of the overlapping photon cuts:

$\phi z$ : passed both cuts.
$\phi \bar{z}$ : passed PHICUT, failed ZCUT.
$\bar{\phi} z$ : failed PHICUT, passed ZCUT.
$\bar{\phi} \bar{z}$ : failed both cuts.

Assuming that the rejection of the overlapping cuts were independent and letting $N$, $S$, and $B$ denote the total number of events, the number of signal events, and the number of background events, then:

$$\begin{aligned} N_{\phi z} &= S_{\phi z} + B_{\phi z} \\ N_{\phi \bar{z}} &= S_{\phi \bar{z}} + B_{\phi \bar{z}} \\ N_{\bar{\phi} z} &= S_{\bar{\phi} z} + B_{\bar{\phi} z} \\ N_{\bar{\phi} \bar{z}} &= S_{\bar{\phi} \bar{z}} + B_{\bar{\phi} \bar{z}} \end{aligned}$$

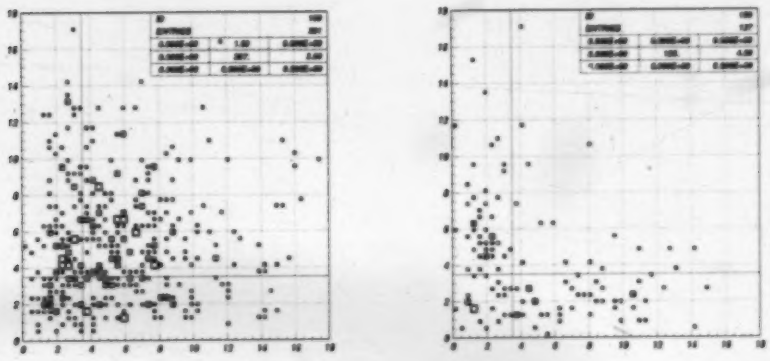

Figure 70: $z_{max}$(cluster 1) vs $z_{max}$(cluster 2) for events below (left) and above (right) the $K\pi 3$ threshold (133MeV/c). Events with two overlapping photons dominate below the K$\pi$3 threshold while events with a single overlapping photon dominate above the threshold.

$$\frac{B_{\phi z}}{B_{\phi \bar{z}}} = \frac{B_{\bar{\phi} z}}{B_{\bar{\phi}\bar{z}}}$$
$$\frac{B_{\phi z}}{B_{\bar{\phi} z}} = \frac{B_{\phi \bar{z}}}{B_{\bar{\phi}\bar{z}}}$$

The following acceptances were defined:

$$a_{\phi \bar{z}} \equiv \frac{S_{\phi \bar{z}}}{S_{\phi z}}, \quad a_{\bar{\phi} z} \equiv \frac{S_{\bar{\phi} z}}{S_{\phi z}}, \quad a_{\bar{\phi}\bar{z}} \equiv \frac{S_{\bar{\phi}\bar{z}}}{S_{\phi z}}$$

If we let $x = S_{\phi z}$, then x can be expressed in terms of the $N$'s and $a$'s by:

$$\begin{aligned} N_{\phi z} &= x + B_{\phi z} \\ &= x + \frac{(N_{\bar{\phi} z} - a_{\bar{\phi} z} x)(N_{\phi \bar{z}} - a_{\phi \bar{z}} x)}{N_{\bar{\phi}\bar{z}} - a_{\bar{\phi}\bar{z}} x} \end{aligned}$$

which gives the following quadratic equation in $x$:

$$\begin{aligned} &(a_{\phi \bar{z}} a_{\bar{\phi} z} - a_{\bar{\phi}\bar{z}})x^2 + N_{\phi \bar{z}} N_{\bar{\phi} z} - N_{\phi z} N_{\bar{\phi}\bar{z}} \\ &+(N_{\bar{\phi}\bar{z}} - a_{\phi \bar{z}} N_{\phi \bar{z}} - a_{\bar{\phi} z} N_{\bar{\phi} z} + a_{\bar{\phi}\bar{z}} N_{\phi z})x = 0 \end{aligned} \qquad (46)$$

At the standard cut points, $z_{max}(1) < 3.5$, $z_{max}(2) < 3.5$, $\phi_g^2(1) < 0.055$ and $\phi_g^2(2) < 0.055$, the following acceptances were measured using the data set which will be mentioned in section 6.4.8, where UMC was used to generate the photon energy spectrum and real K$\pi$2 data provided the values of the cut variables at each given photon energy:

$$a_{\phi z} = 0.3908 \pm 0.0096$$
$$a_{\bar{\phi} z} = 0.3967 \pm 0.0096$$
$$a_{\bar{\phi}\bar{z}} = 0.1320 \pm 0.0050$$

Inserting these acceptances and the values for $N_{\phi z}$, $N_{\phi\bar{z}}$, $N_{\bar{\phi} z}$, and $N_{\bar{\phi}\bar{z}}$, into equation 46 two solutions for $x$ would be found of which only the positive one was a physically valid result for $S_{\phi z}$.

### 5.2.2 K$\pi$3 Background

UMC indicated that K$\pi$3 with two overlapping photons would dominate the overlapping background. The one-overlapping/one-missing photon background was estimated to be an order of magnitude less than the two overlapping background, due to the excellent $4\pi$ photon detection coverage of the detector, although this estimate contained a large statistical uncertainty. Therefore, it was first assumed that all the K$\pi$3 background events had two overlapping photons and then a correction was made for the possible effect of one overlapping events.

391 of the 518 events which passed all non-overlapping cuts were below the K$\pi$3 threshold. The number of events in each category was:

$$N_{\phi z} = 20, \quad N_{\phi\bar{z}} = 29, \quad N_{\bar{\phi} z} = 34, \quad N_{\bar{\phi}\bar{z}} = 308.$$

Using equation 46 this gave the real number of signal ($K^+ \to \pi^+\gamma\gamma$) events as:

$$S_{\phi z} = 18.08 \pm 4.82$$

where the error is statistical and only includes the uncertainties in the $N$ values which are much large than those in the $a$'s. Therefore the number of background events was $B_{\phi z} = N_{\phi z} - S_{\phi z} = 1.92 \pm 1.80$.

If there was contamination by single overlapping photon events from either K$\pi$3 or radiative K$\pi$2, the background would have been underestimated

because the rejection of ZCUT for the one overlapping photon events was, of course, less than the rejection for events with two overlapping photons. The correct number of background events which passed the overlapping gamma vetoes should then have been:

$$B_{\phi_2} = \frac{(1-p)B_\phi}{R_{2ovlp}} + \frac{pB_\phi}{R_{1ovlp}},$$

where $B_\phi$ is the number of background events which passed PHICUT, $p$ is the fraction of one overlapping photon events in $B_\phi$, and $R_{1ovlp}$ and $R_{2ovlp}$ are the ZCUT rejections for one overlapping events and two overlapping events respectively.

To determine $p$ the following variables were examined for the events which either passed or failed PHICUT:

$N_2$ = Number of events where both photons fail ZCUT
$N_1$ = Number of events where only one photon fails ZCUT
$N_0$ = Number of events where both photons pass ZCUT

The values were $N_2 = 168$, $N_1 = 140$ and $N_0 = 29$ for the events which failed PHICUT and $N_2 = 14$, $N_1 = 20$ and $N_0 = 20$ for the events which passed PHICUT. Figure 71 shows the ZCUT variables for the events which passed or failed PHICUT and shows a clear enhancement of the fraction of events in the signal region for the events which passed PHICUT.

The acceptance of ZCUT is given in table 31 (section 6.4) as 0.719, so the expected acceptance loss would cause $(1-0.719)/0.719 \times 18.08 = 7$ of the events in $N_1 + N_2$, after PHICUT was applied, to be real $\pi\gamma\gamma$ events. The 0.719 value was the product of the acceptance of ZCUT on both the first and second photon clusters so taking the acceptance of ZCUT on a single cluster to be $\sqrt{0.719} = 0.848$ implied that 6 of the 7 events contributed to $N_1$ while 1 contributed to $N_2$. The corrected ratio of $N1/N2$ for the events which passed PHICUT was therefore $(20-6)/(14-1) = 1.08 \pm 0.38$ which was consistent, within error, with the ratio for the events which failed PHICUT $N1/N2 = 140/168 = 0.83 \pm 0.09$. This suggested that the fraction of one overlap events, $p$, in the data sample was small.

The known rejection of the photon vetoes was additional reason to believe that $p$ was small. The photon veto acceptance for events which failed PHICUT was measured to be $337/500 = 0.67 \pm 0.05$, and the acceptance for events which passed PHICUT was $54/89 = 0.56 \pm 0.09$. If it was assumed that the decrease in photon veto acceptance was due entirely to contamination by one-photon-missing K$\pi$3 events in the latter sample, then the

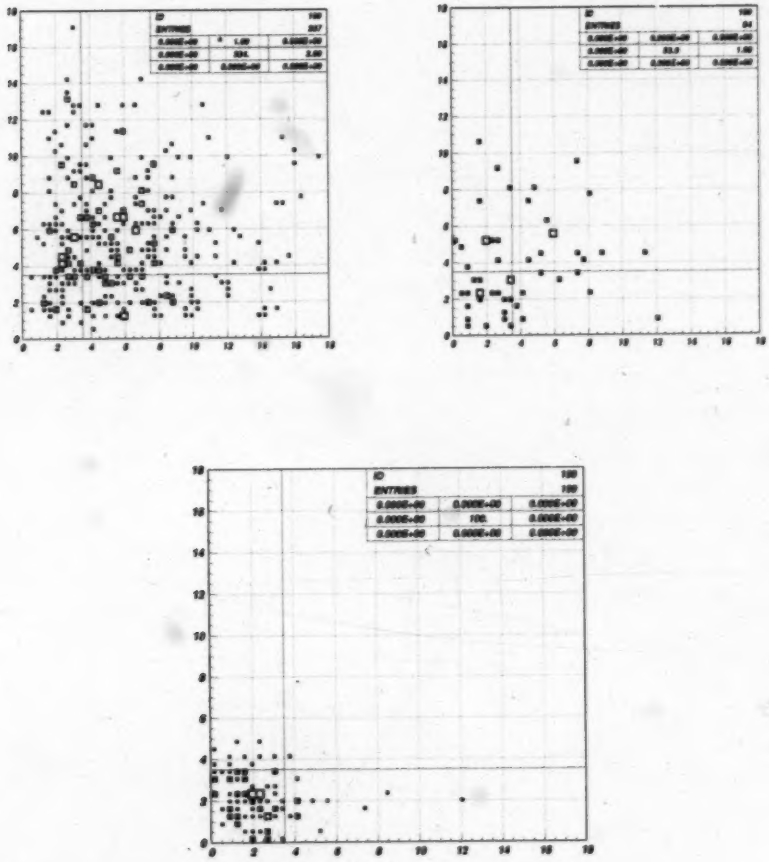

Figure 71: $z_{max}$(cluster 1) vs $z_{max}$(cluster 2) for the events below the K$\pi$3 threshold which either failed (top left) or passed (top right) PHICUT. The bottom plot shows the distribution for UMC generated $K^+ \to \pi^+\gamma\gamma$ .

number of one-photon missing events present before the photon vetoes were applied should have been roughly $89 - 54/0.67 = 8.4$. The minimum photon energy in K$\pi$3, when $P_{\pi^+} > 100$MeV/c, is 30MeV. The overall single photon inefficiency for photons in the energy range $20 < E_\gamma < 40$MeV was known to be 0.07[43]. Therefore it was expected that at most approximately $8.4 \times 0.07 = 0.6$ one-photon-missing K$\pi$3 events were in the sample which passed PHICUT.

To estimate the systematic error in the K$\pi$3 background measurement the worst case scenario was chosen which meant assuming that there was no contribution to $N_1$ from the real $\pi\gamma\gamma$ events. Adjusting for the mixing between events in the three groups caused by the finite acceptance and rejection of ZCUT the value of $p$ was approximately 0.232. Then using $B_\phi = 34$, $R_{2ovlp} = 15.1$ and $R_{1ovlp} = \sqrt{(15.1)} = 3.89$, the background would have been:

$$B_{\phi z} = \frac{(1 - 0.232) \times 34}{15.1} + \frac{0.232 \times 34}{3.89} = 3.76$$

Therefore the systematic error in $S_{\phi z}$ was taken to be $1.92 - 3.76 = -1.84$.

### 5.2.3 Radiative K$\pi$2 Background

127 events out of the 518 which passed all cuts, other than the overlapping photon cuts, were above the K$\pi$3 threshold. They were a mix of radiative K$\pi$2 with one overlapping photon, true $\pi\gamma\gamma$ signal, and backgrounds with no overlapping photons which will be dealt with in the next section. For the purposes of the radiative K$\pi$2 background estimate, no distinction was made (or required) between the non-overlapping backgrounds and the real signal.

Using equation 46 and the procedure of section 5.2.1 the following values were obtained:

$$N_{\phi z} = 11, \quad N_{\phi \bar{z}} = 29, \quad N_{\bar{\phi} z} = 11, \quad N_{\bar{\phi}\bar{z}} = 76,$$

$$S_{\phi z} = 8.36 \pm 4.30$$

and

$$B_{\phi z} = 2.64 \pm 2.74.$$

The errors listed are statistical as in the K$\pi$3 case. Figure 72 shows the PHICUT variables for events which passed or failed ZCUT. The $\pi\gamma\gamma$ signal region was enhanced after application of ZCUT and contamination by two overlapping photon events was not seen.

### 5.2.4 Cut point dependence

At the standard cut points of $z_{max} = 3.5$ and $\phi_g^2 = 0.055$, the size of the $\pi\gamma\gamma$ signal was $18.08 + 8.36 = 26.64$ with a statistical uncertainty of $\sqrt{(4.82^2 + 4.30^2)} = 6.46$. Since the combined acceptance of the overlapping $z$ and $\phi$ cuts was 0.521 (table 31) the total number of $\pi\gamma\gamma$ events that should have been present before application of the overlapping cuts was

$$\begin{aligned} S_{total} &\equiv S_{\phi z} + S_{\bar{\phi} z} + S_{\phi \bar{z}} + S_{\bar{\phi}\bar{z}} \\ &= 50.75 \pm 12.40. \end{aligned}$$

If there were no systematic effects in the background and acceptance estimates then the value of $S_{total}$ should not have depended on the exact cut points used. This was tested for a variety of different cut positions and the dependence of $S_{total}$, along with the acceptance at each cut point, are summarized in table 13.

Table 13: Signal and background estimates for various PHICUT and ZCUT cut points.

| $z$ cut point | $\phi$ cut point | $N_{\phi z}$ | $S_{\phi z}$ | $B_{\phi z}$ | $S_{total}$ | Acc. |
|---|---|---|---|---|---|---|
| 2.5 | 0.040 | 11 | 10.88 | 0.12 | 61.82 | 0.176 |
| 2.5 | 0.055 | 18 | 17.18 | 0.82 | 54.71 | 0.314 |
| 3.5 | 0.040 | 16 | 15.37 | 0.63 | 52.46 | 0.293 |
| 3.5 | 0.055 | 31 | 26.44 | 4.56 | 50.75 | 0.521 |
| 3.5 | 0.070 | 49 | 36.62 | 12.38 | 54.17 | 0.676 |
| 5.0 | 0.055 | 44 | 28.24 | 15.76 | 42.98 | 0.657 |
| 5.0 | 0.070 | 79 | 35.66 | 43.34 | 42.10 | 0.847 |

The observed variation in $S_{total}$ was consistent with statistical fluctuations. For example, at $z_{max} = 2.5$ and $\phi_g^2 = 0.040$, the acceptance was 33.8% of the acceptance at the standard cut point. If we assume that $S_{\phi z}$ at the standard cut point was correct then the expected $S_{\phi z}$ at $z_{max} = 2.5$ and $\phi_g^2 = 0.040$ would have been 9.0 with a statistical uncertainty of $\sqrt{26.64 \times 0.338 \times (1 - 0.338)} = 2.4$, which is within error of the value shown in table 13 of $S_{\phi z} = 10.88$.

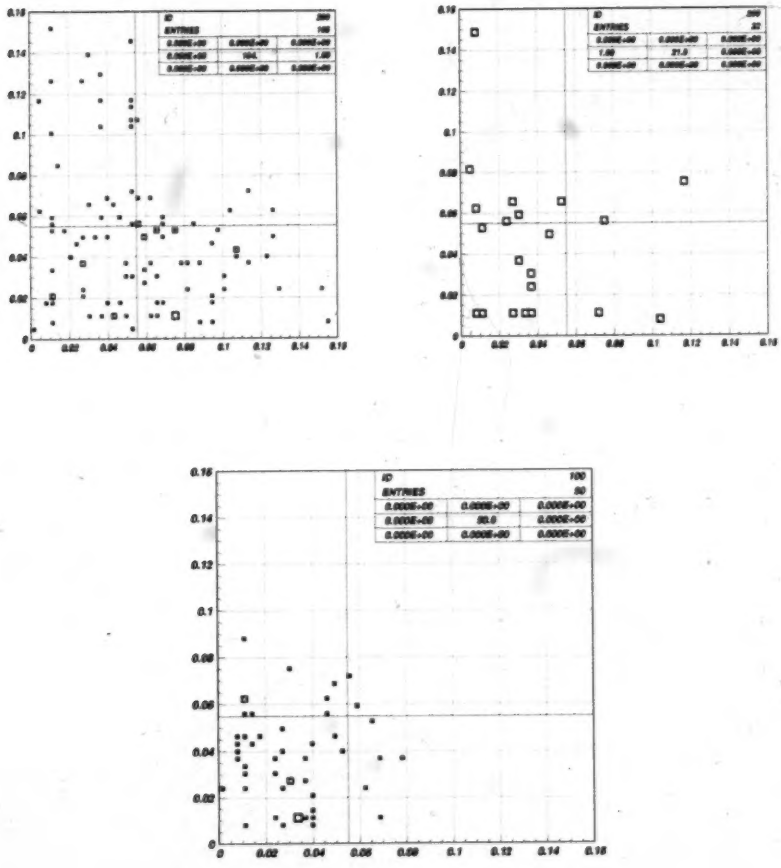

Figure 72: $\phi_g^2$(cluster 1) vs $\phi_g^2$(cluster 2) for the events above the K$\pi$3 - threshold which failed (top left) or passed (top right) ZCUT. The bottom plot shows the distribution for UMC generated $K^+ \to \pi^+\gamma\gamma$ .

However, to estimate the systematic error the extreme values in table 13 were used. It was assumed that the smallest value of $S_{total}$, at $z_{max} = 5.0$ and $\phi_g^2 = 0.070$, was due to a systematic over estimation of the background level. And that the value of $S_{total}$ at $z_{max} = 2.5$ and $\phi_g^2 = 0.040$ was correct. Then the expected $B_{\phi z}$ at $z_{max} = 5.0$ and $\phi_g^2 = 0.070$ should have been $79 - 0.847 \times 61.82 = 26.64$ which differs by 39% from the value shown in table 13. At the standard cut point, a 39% systematic error in the background estimate would correspond to an error in $S_{\phi z}$ of +1.78 events.

### 5.2.5 PHICUT/ZCUT Correlations

An important assumption in the above background estimates was that the two overlapping photon cuts, PHICUT and ZCUT, were independent of one another. If this assumption was not true then the overlapping photon background estimate would either be too high or too low depending on how the cuts were correlated. Examination of the cut point dependence (section 5.2.4) did not show a strong correlation between the two cuts. However, a more detailed study was carried out using UMC.

Sufficient quantities of both K$\pi$3 and radiative K$\pi$2 UMC events were generated to ensure that both the UMC and real $\pi\gamma\gamma(2)$ data samples were approximately the same size after applying all cuts up to the overlapping photon cuts.

To reproduce in UMC the measured BV $z$ resolutions, both the energy and timing of the BV hits were smeared. The energy was smeared according to Poisson statistics with the number of photo-electrons per MeV equal to 9. The timing was smeared by:

$$T' = T + G \times \frac{c}{E}, \tag{47}$$

where $G$ is a Gaussian distributed random number, $E$ is the energy in MeV, and $c$ is a constant. The value of $c$ (in this case 1.5) was chosen to give the correct $Z_{\mathrm{ADC}}$-$Z_{\mathrm{TDC}}$ energy dependent resolution (figure 73). The minimum UMC energy at which a BV TDC would fire was set to 0.3 MeV to reproduce the edge of the energy spectrum observed in real data (figure 74). Figure 74 also shows that there was good agreement between UMC and real data on the total number of hit BV elements in the K$\pi$3 events. To check the validity of the energy and time smearing, $\pi\gamma\gamma$ events were generated and the acceptance of the overlapping photon cuts was measured at various cut points. Table 14 shows the acceptances measured purely using UMC and those obtained using the data set which combined UMC-generated $\pi\gamma\gamma$

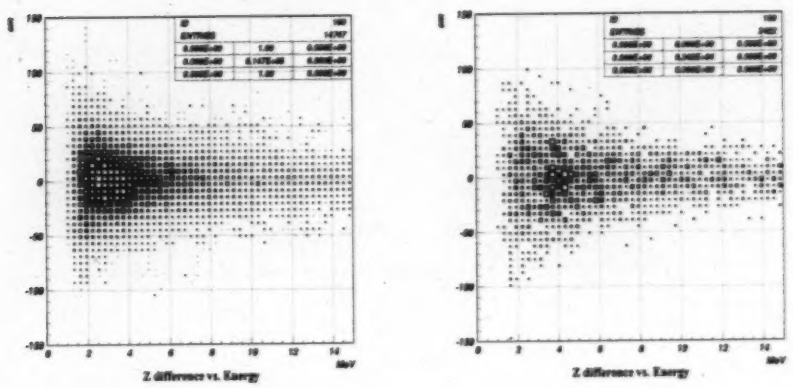

Figure 73: The difference between the ADC and TDC based $z$ measurements in the BV ($z_{ADC} - z_{TDC}$) as a function of photon energy for real data (left) and UMC data (right).

photon energy distributions with overlapping variables measured from real K$\pi$2 data (section 6.4.8).

Table 14: UMC $\pi\gamma\gamma$ acceptance

| $z$ cut point | $\phi$ cut point | UMC acceptance | UMC + K$\pi$2 |
|---|---|---|---|
| 2.5 | 0.040 | 0.189 ± 0.0145 | 0.176 |
| 2.5 | 0.055 | 0.340 ± 0.0176 | 0.314 |
| 3.5 | 0.040 | 0.284 ± 0.0167 | 0.293 |
| 3.5 | 0.055 | 0.515 ± 0.0186 | 0.521 |
| 3.5 | 0.070 | 0.631 ± 0.0179 | 0.676 |
| 5.0 | 0.055 | 0.632 ± 0.0179 | 0.657 |
| 5.0 | 0.070 | 0.795 ± 0.0150 | 0.847 |

All cuts were applied to the UMC K$\pi$3 and radiative K$\pi$2 data sets except for the overlapping photon cuts and the pion mass cut. The pion mass cut was removed in order to increase the number of surviving events and was not correlated with the overlapping photon veto cuts. After the cuts there were 235 radiative K$\pi$2 and 554 K$\pi$3 UMC events remaining. PHICUT and ZCUT were applied separately to the UMC events and their rejections mea-

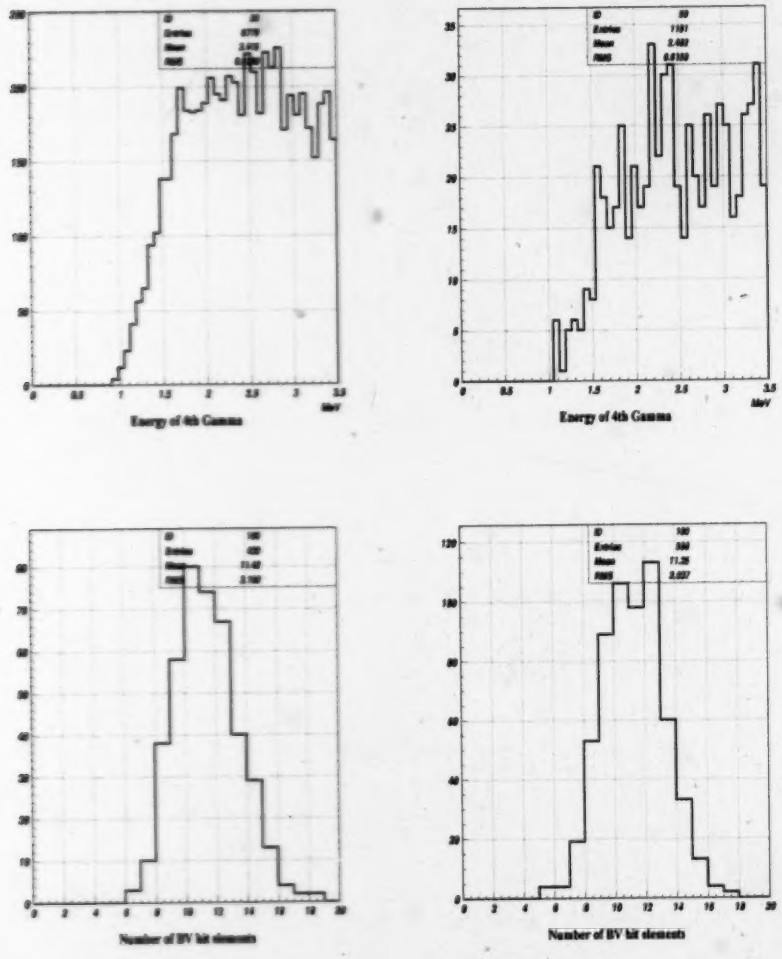


Figure 74: The energy distribution of the 4th photon cluster in PASS2 data (top left) and UMC generated K$\pi$3 data (top right) and the total number of hit BV elements in real data below the K$\pi$3 threshold which failed PHICUT (bottom left) and UMC-generated K$\pi$3 (bottom right).

Table 15: Overlapping Gamma Veto Cut Rejection for UMC K$\pi$3 data.

| Cut Point | | Rejection | | Events Surviving | |
|---|---|---|---|---|---|
| Z | $\phi$ | Zcut | Phicut | Estimated | Real |
| 2.5 | 0.040 | 36.9 | 34.6 | 0.4 | 0 |
| 2.5 | 0.055 | 36.9 | 12.6 | 1.2 | 0 |
| 3.5 | 0.040 | 13.5 | 34.6 | 1.2 | 0 |
| 3.5 | 0.055 | 13.5 | 12.6 | 3.3 | 2 |
| 3.5 | 0.070 | 13.5 | 3.0 | 14 | 19 |
| 5.0 | 0.055 | 5.1 | 12.6 | 8.7 | 9 |
| 5.0 | 0.070 | 5.1 | 3.0 | 37 | 42 |

sured. Then both cuts were applied and the number of surviving events noted. If no correlation was present between PHICUT and ZCUT then the number of surviving events would have been the same (within error) as the initial number of events divided by the product of the PHICUT and ZCUT rejections. Tables 15 and 16 show the results of these measurements for K$\pi$3 and radiative K$\pi$2, no strong correlation was seen between the overlapping variables for either data set.

Table 16: Overlapping Gamma Veto Rejection for UMC radiative K$\pi$2 data.

| Cut Point | | Rejection | | Events Surviving | |
|---|---|---|---|---|---|
| Z | $\phi$ | Zcut | Phicut | Estimated | Real |
| 2.5 | 0.040 | 11.8 | 7.8 | 2.6 | 4 |
| 2.5 | 0.055 | 11.8 | 3.8 | 5.3 | 6 |
| 3.5 | 0.040 | 5.9 | 7.8 | 5.1 | 8 |
| 3.5 | 0.055 | 5.9 | 3.8 | 11 | 13 |
| 3.5 | 0.070 | 5.9 | 1.9 | 22 | 23 |
| 5.0 | 0.055 | 2.7 | 3.8 | 23 | 27 |
| 5.0 | 0.070 | 2.7 | 1.9 | 46 | 51 |

In the background study a cut was applied at $P_{\pi^+} = 133\text{MeV/c}$ to separate the K$\pi$3 background from the radiative K$\pi$2 background. To make sure that this momentum cut hadn't somehow induced a correlation between the overlapping photon cuts in the case of radiative K$\pi$2, the above correlation analysis was repeated on the radiative K$\pi$2 sample considering only events with $P_{\pi^+} > 133\text{MeV/c}$. A total of 190 events satisfied the momentum re-

quirement and the results are in table 17. Again there was no apparent correlation between PHICUT and ZCUT.

Table 17: Overlapping gamma veto rejection for UMC radiative K$\pi$2 data with $P_{\pi^+} > 133$MeV/c.

| Cut Point | | Rejection | | Events Surviving | |
|---|---|---|---|---|---|
| Z | $\phi$ | Zcut | Phicut | Estimated | Real |
| 2.5 | 0.040 | 12.7 | 8.6 | 1.7 | 3 |
| 2.5 | 0.055 | 12.7 | 4.2 | 3.6 | 5 |
| 3.5 | 0.040 | 6.3 | 8.6 | 3.5 | 6 |
| 3.5 | 0.055 | 6.3 | 4.2 | 7.1 | 9 |
| 3.5 | 0.070 | 6.3 | 2.0 | 15 | 15 |
| 5.0 | 0.055 | 2.9 | 4.2 | 16 | 19 |
| 5.0 | 0.070 | 2.9 | 2.0 | 33 | 35 |

A comparison was made between the $z_{max}$ and $\phi_g^2$ distributions produced by UMC and those from real data. A K$\pi$3 sample was prepared by applying all cuts except the overlapping photon cuts, requiring $P_{\pi^+} < 133$MeV/c and inverting either PHICUT or ZCUT on one of the photon clusters. This was done with both real data and UMC K$\pi$3 data. Figure 75 shows the real and UMC distributions of the variable, PHICUT or ZCUT, which wasn't inverted, for the same photon cluster that had failed either PHICUT or ZCUT. The real and UMC curves are consistent with one another.

UMC was used to estimate the K$\pi$3 and radiative K$\pi$2 background levels by first using the momentum spectra measured with UMC, for both the radiative K$\pi$2 and K$\pi$3 events, to measure the ratio of events above and below 133 MeV/c momentum[21]. With these ratios the final real data sample, before the overlapping photon veto cuts were applied, was broken into three physical processes: radiative K$\pi$2 , K$\pi$3 and events with only two photons, in the two momentum regions about the 133 MeV/c cut. These values are listed in table 18[22].

Then the PHICUT and ZCUT rejections measured using UMC were applied to the K$\pi$3 and radiative K$\pi$2 categories to estimate the number

[21]The momentum dependence of the pion mass cut has been corrected for at this point (section 6.4.4).

[22]The number of K$\pi$3 and radiative K$\pi$2 events were consistent (to within 10%) with the known branching ratios[2] and the measured UMC acceptances if it was assumed that the ratio of the real acceptance to the UMC acceptance for these decay modes was the same as the ratio for $\pi\gamma\gamma(2)$ events.

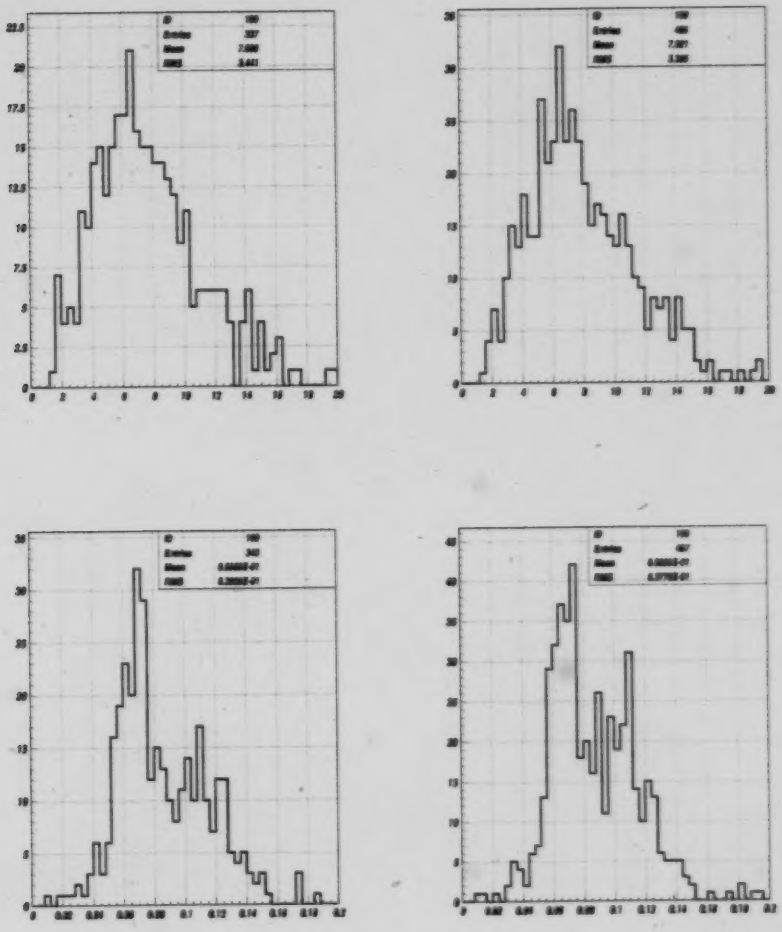

Figure 75: The real (top left) and UMC (top right) $z_{max}$ distributions for the K$\pi$3 photon cluster that had failed PHICUT. The bottom graphs show $\phi_g^2$ for a similar cluster which had failed ZCUT.

of background events which would be present after the overlapping photon veto cuts were applied. For K$\pi$3 a rejection of $544/2 = 272$ was used for both momentum regions. For radiative K$\pi$2 rejections of $190/9 = 21.1$ and $45/4 = 11.3$ were used for $P_{\pi^+} > 133$MeV/c and $P_{\pi^+} < 133$MeV/c, respectively. The results are given in table 19. The number of background events was slightly higher than the numbers calculated in sections 5.2.2 and 5.2.3 but was within statistical error. The non-UMC values were used with the difference between them and the UMC numbers treated as the systematic error in the K$\pi$3 and radiative K$\pi$2 background estimates.

Table 18: Break-down of the events before overlapping gamma veto cuts are applied.

| Momentum range | Radiative K$\pi$2 | K$\pi$3 | no overlapping | Total |
|---|---|---|---|---|
| $P_{\pi^+} > 133$MeV/c | 91.9 | 19.0 | 16.1 | 127 |
| $P_{\pi^+} < 133$MeV/c | 20.6 | 325.7 | 34.7 | 381 |

Table 19: Estimated number of overlapping gamma backgrounds from the UMC study.

| Momentum range | Radiative K$\pi$2 | K$\pi$3 | Total | Real Data Analysis |
|---|---|---|---|---|
| $P_{\pi^+} > 133$MeV/c | 4.35 | 0.07 | 4.42 | $2.64 \pm 2.74$ |
| $P_{\pi^+} < 133$MeV/c | 1.83 | 1.24 | 3.07 | $1.92 \pm 1.80$ |

## 5.3 Non-Overlapping Gamma Background

The background which didn't involve overlapping photons potentially involved four decay modes: K$\mu$3, K$\pi$2, radiative K$\pi$2 and K$\pi$3. Normally, none of these would have satisfied the combined requirements of overall energy-momentum conservation, a $\pi^+$ momentum below 180MeV/c and a charged particle with energy and momentum consistent with a pion. Radiative K$\pi$2 and K$\pi$3 would have had to have either one or two photons escape without being detected and still manage to satisfy total energy-momentum conservation. K$\mu$3 and K$\pi$2 both had two photons that originated from a $\pi^0$ and so would have had a photon invariant mass that was too low. Additionally the muon in K$\mu$3 would have had to be misidentified as a pion and the energy carried away by the neutrino compensated by some other effect. The pion in K$\pi$2 would have to lose energy before entering the DC to satisfy the $\pi^+$ momentum cut.

The following cuts were effective in reducing the non-overlapping background.

- The KINFIT cut on the kinematic constrained fit, $Prob(\chi^2) > 0.1$.
- The charged particle mass cut, $120 < M_{\pi^+} < 165\text{MeV}$.
- The cut on the difference between the measured photon invariant mass and that calculated based on the $\pi^+$ momentum, $M_{\gamma\gamma}(\gamma\gamma) - M_{\gamma\gamma}(P_{\pi^+}) > -30\text{MeV}$.
- And the opening angle cut between the high energy photon and the charged particle, $\mathbf{P}_{\gamma_1} \cdot \mathbf{P}_{\pi^+} / (|\mathbf{P}_{\gamma_1}||\mathbf{P}_{\pi^+}|) > -0.8$.

From the standpoint of performing a background study the above set of cuts, referred to as 'set-I', had a major flaw: the cuts were strongly correlated with one another so it was not possible to select a data sample by inverting one cut and using that sample to measure the rejections of the other cuts. Therefore, for the background study only, a new set of less correlated cuts, set-II, was defined.

The set-II cuts consisted of the charged particle mass cut and invariant photon mass cuts from set-I along with three new cuts. An opening angle cut which was defined by

$$\frac{\mathbf{P}_{\gamma 1} \cdot (\mathbf{P}_{\gamma 1} + \mathbf{P}_{\gamma 2})}{|\mathbf{P}_{\gamma 1}||\mathbf{P}_{\gamma 1} + \mathbf{P}_{\gamma 2}|} < 0.8,$$

where $\mathbf{P}_{\gamma 1}$ and $\mathbf{P}_{\gamma 2}$ are the momenta of the high and low energy photon and the cut now does not depend on the $\pi^+$ momentum. Part of the energy-momentum conservation requirement referred to as the 'magnitude' cut and defined as $Prob(\chi^2_{magn.}) > 0.1$, with $\chi^2_{magn.}$ calculated, using UMC resolutions, by:

$$\chi^2_{\text{magn.}} = \frac{(|\mathbf{P_X}| - |\mathbf{P}_{\pi^+}|)^2}{(21.0\text{MeV/c})^2} + \frac{(\mathrm{M}_{\gamma\gamma} - \mathrm{M_X})^2}{(28.5\text{MeV})^2}$$

where

$$\mathrm{M_X} = \sqrt{\mathrm{M}^2_{\mathrm{K}^+} + \mathrm{M}^2_{\pi^+} - 2\mathrm{M}_{\mathrm{K}^+}\sqrt{\mathrm{M}^2_{\pi^+} + \mathrm{P}^2_{\pi^+}}},$$

and X denotes a virtual particle, with momentum, $\mathbf{P}_X$, and mass, $M_X$, which decays into two photons . And finally a 'direction' cut defined by

$$\frac{\mathbf{P}_\pi \cdot \mathbf{P_X}}{|\mathbf{P}_\pi||\mathbf{P_X}|} = \cos(\theta_{\pi\mathrm{X}}) < -0.9.$$

The acceptance of the direction cut for UMC events which passed the Set-I cuts was 97 %.

The general procedure for the background estimates was to remove or reverse one or two of either the set-II or PASS3 cuts to enhance a particular background. Then the direction cut, $\cos(\theta_{\pi X}) < -0.9$, was inverted and the distribution above -0.9 was fit by a Gaussian. The number of events in the region $\cos(\theta_{\pi X}) < -0.9$ was estimated by extrapolating the Gaussian and determining the area under the curve in that region. And the number of expected background events was found by dividing this estimated number of events by the rejection of the cut(s) which had been removed or reversed in the first step.

### 5.3.1 K$\mu$3 Background

To enhance the K$\mu$3 background, the $\pi^+$ mass cut was reversed requiring $(P_{DC}^2 - E_{RS}^2)/2E_{RS} = M_\pi < 120$MeV and the invariant photon mass cut was removed. Figure 76 shows the $\cos(\theta_{\pi X})$ distribution of the 83 events in this sample. The number of events in the region of $\cos(\theta_{\pi X}) < -0.9$ was calculated to be $2.01 \pm 0.44$.

The rejection of the invariant photon mass cut was estimated by simply applying this cut to the above background sample. The number of events surviving was 40, and the rejection of the cut was estimated to be $83/40 = 2.08 \pm 0.40$.

To estimate the rejection of the $\pi^+$ mass cut the mass distribution was fit by a Gaussian (figure 76) and a Gaussian tail used in the region of $120 < M_\pi < 165$MeV. The estimated rejection was $7.86 \pm 2.56$ based on the ratio of the area in the tail to the full area of the Gaussian.

The number of events, 2.01, with $\cos(\theta_{\pi X}) < -0.9$ was found with the condition $M_{\pi^+} <$120MeV already applied. To estimate the total background this number had to be scaled up to include the entire $M_{\pi^+}$ mass spectrum using the Gaussian in figure 76. In practice, because the estimated number of K$\mu$3 events with $M_{\pi^+} >$165MeV was approximately zero, applying this increase then the mass cut rejection was equivalent to using the original number and subtracting 1 from the rejection. Therefore the estimated K$\mu$3 background was:
$(2.01 \pm 0.44)/((7.86 \pm 2.56) - 1)/(2.08 \pm 0.40) = 0.14 \pm 0.07$.

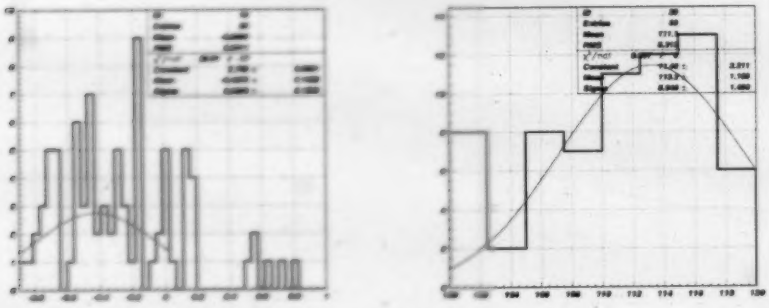

Figure 76: The $\cos(\theta_{\pi X})$(left) and charged particle mass(right) distributions for events which had $M_{\pi^+} < 120$MeV and $\cos(\theta_{\pi X})$ >-0.9 but passed all other Set-II cuts.

### 5.3.2 K$\pi$2 Background

K$\pi$2 was unique amongst the backgrounds in that, being a two body decay, it was impossible for the $\pi^+$ from K$\pi$2 to have a momentum in the accepted range of 100–180MeV/c. To pass the momentum cut the $\pi^+$ had to either scatter in the target and lose energy or have had its momentum mismeasured. In both cases the majority of pions would still have had too high a momentum to stop in RS layers A or B without nuclear interacting in the RS. It was seen earlier in section 4.3.2.1 that a large number of K$\pi$2 events survived up to PASS2 because of RS interactions (figure 45).

As with the K$\mu$3 background the two photons from the $\pi^0$ had to be mismeasured so that they reconstructed to an object with an invariant mass much higher than that of a $\pi^0$ . Finally the entire event had to reconstruct to a kaon which had decayed at rest. When K$\pi$2 events were selected with a $\pi^+$ which had scattered in the target it was found, not surprisingly, that the missing momentum was generally even higher than that seen in K$\mu$3 events (figure 57 and 58 in section 4.3.3.5).

As was done with K$\mu$3 , to estimate the K$\pi$2 background the $\cos(\theta_{\pi X})$ cut was reversed and all other normal and set-II cuts were applied with the exception of the $M_{\pi^+}$ cut. The mass distribution (figure 77 shows the distribution with $M_{\pi^+} > 120$MeV and the right hand graph of figure 76 shows the distribution for $M_{\pi^+} < 120$MeV) shows no peak at the $\pi^+$ mass

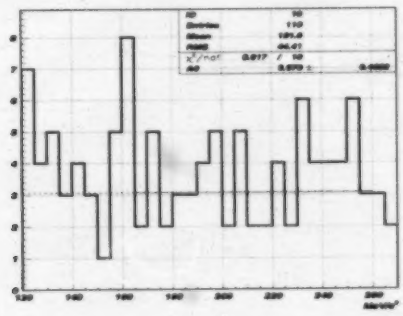

Figure 77: The charged particle mass distribution of events which passed all Set-II cuts except for a reversed $\cos(\theta_{\pi X})$ cut.

and is consistent with a combination of muons which stopped normally and pions which interacted in the RS resulting in unobserved RS energy and a high reconstructed charged particle mass.

To enhance the K$\pi$2 background and eliminate the muons, the $\pi^+$ mass cut was reversed requiring $M_{\pi^+} > 165$MeV. The $\cos(\theta_{\pi X})$ distribution of these 79 events (figure 78) was fit with a Gaussian and the number of events in the signal region, $\cos(\theta_{\pi X}) < -0.9$, was calculated to be $1.02 \pm 0.18$.

The rejection of the $M_{\pi^+}$ mass cut was estimated using two different methods. In the first method the $\pi^+$ mass distribution was assumed to be flat below $M_\pi = 220$MeV and the events in the range $165 < M_\pi < 220$MeV were used to estimate the mean height of the distribution (figure 77). This gave 30.7 events with $120 < M_\pi < 165$MeV and a rejection of $(30.7 + 79)/30.7 = 3.57 \pm 0.72$. In the second method it was assumed that all of the events with $M_{\pi^+} < 120$MeV were K$\mu$3 and that all events with $M_{\pi^+} > 120$MeV which weren't K$\mu$3 were K$\pi$2 . The estimated number of K$\mu$3 events with $120 < M_{\pi^+} < 165$MeV was $40/(7.86 - 1) = 5.83$ (section 5.3.1). Therefore the $\pi^+$ mass rejection for K$\pi$2 was $(40 + 79 - 5.83)/(40 - 5.83) = 3.31 \pm 0.60$.

The results of both methods were consistent with each other. The rejection from the second method was used in the background estimate and gave the size of the K$\pi$2 background as $(1.02 \pm 0.18)/((3.31 \pm 0.60) - 1) = 0.44 \pm 0.11$.

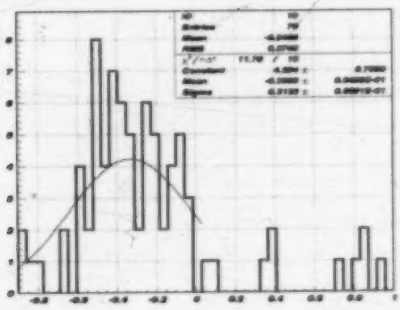

Figure 78: The $\cos(\theta_{\pi X})$ distribution of events with $M_{\pi^+} > 165$MeV and $\cos(\theta_{\pi X}) > -0.9$ which passed all other Set-II cuts.

### 5.3.3 Radiative K$\pi$2 and K$\pi$3 Background

K$\pi 2\gamma$ and K$\pi$3 events with missing photons could have contributed to the non-overlapping background and would have tended to reconstruct to the correct $\pi^+$ mass in the RS unlike normal K$\pi$2 .

After applying the set-II cuts, with an inverted $\cos(\theta_{\pi X})$ requirement, there was no pion mass peak even if the photon veto cuts were removed (figures 77 and 79). A total of 40 of these events satisfied $120 < M_{\pi^+} < 165$MeV with 7 having $\pi^+$ momentum below 133MeV/c and 33 with momentum above 133MeV/c. In the momentum region $P_{\pi^+} > 133$MeV/c only 2 out of the 33 events passed the TD cuts while the acceptance of the TD cuts for radiative K$\pi$2 events with overlapping photons was measured to be about 50%. Turning off the photon vetoes resulted in 130 events of which only 9 passed the TD cuts (figure 80). This suggested that radiative K$\pi$2 events were not a significant contribution to the non-overlapping background. Note that if the $\cos(\theta_{\pi X})$ distribution of the K$\pi 2\gamma$ background was similar to that of the standard K$\pi$2 background then the relative enhancement of the $M_{\pi^+}$ spectrum in the $120 < M_\pi < 165$MeV region would have reduced the rejection of the K$\pi$2 $\pi^+$ mass cut, effectively sweeping these K$\pi 2\gamma$ events into the already measured K$\pi$2 background value.

For the K$\pi$3 background there were only 7 events with $P_{\pi^+} < 133$MeV/c and removing the photon vetoes only increased this number to 39. The known single photon inefficiency of the detector for photons with energy

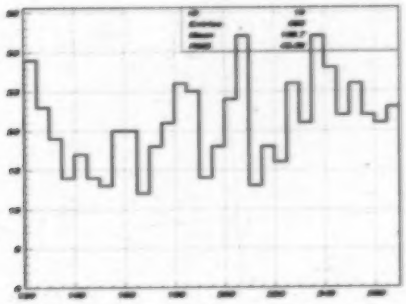

Figure 79: The reconstructed charged particle mass distribution of events which passed all Set-II cuts with the photon veto removed and a reversed $\cos(\theta_{\pi X})$ cut.

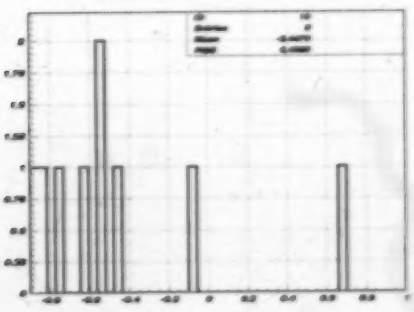

Figure 80: $\cos(\theta_{\pi X})$ for events with $P_{\pi^+} > 133 MeV/c$, which have passed the TD cuts and all set-II cuts except for $\cos(\theta_{\pi X})$. Photon veto cuts were not applied.

20< $E_\gamma$ <40MeV was 0.07[43]. Therefore the number of K$\pi$3 background with two missing photons and $\cos(\theta_{\pi X}) > -0.9$ was expected to be about 0.2. There was no reason to expect a large number of K$\pi$3 events with $\cos(\theta_{\pi X}) < -0.9$ therefore the K$\pi$3 background with two missing photons was considered to be negligible.

### 5.3.4 Systematic error

In the above background estimates it was assumed that $\cos(\theta_{\pi X})$ was independent of the charged particle mass. To check this the $\cos(\theta_{\pi X})$ distribution in figure 78, which required $M_{\pi^+}$ >165MeV, was compared with the distribution from events that had passed all cuts including the pion mass cut (figure 81). The two distributions were consistent with one another except that the latter had a peak at very low $\cos(\theta_{\pi X})$. This peak was found to consist mainly of events with $P_{\pi^+} < 133$MeV/c (figure 81) and was greatly enhanced if the overlapping photon cuts were removed (figure 81) but was only slightly increased if the photon veto cuts were removed. It was concluded that this peak was due to contamination from K$\pi$3 events with overlapping photons and that $\cos(\theta_{\pi X})$ was independent of the pion mass cut for purposes of the non-overlapping background estimate.

The rejection of the $\cos(\theta_{\pi X}) < -0.9$ cut for K$\mu$3 was approximately 2.01/83 (section 5.3.1) which was smaller than the rejection for K$\pi$2 which was roughly 1.02/79 (section 5.3.2). Because of this the assumption that the number of K$\mu$3 with $120 < M_{\pi^+} < 165$MeV could be found using the Gaussian of figure 76, which determined the ratio of K$\mu$3 to K$\pi$2 used in the background estimate, may have introduced a systematic error. There were 40 events which passed all the cuts except for the $\cos(\theta_{\pi X})$ cut. If it was assumed they were all K$\mu$3 background then the estimated number of background events would have been $40 \times 2.01/83 = 0.97$ while if it was assumed they were all K$\pi$2 then the background would have been $40 \times 1.02/79 = 0.52$. The number actually used was 0.58 events (0.14 K$\mu$3 + 0.44 K$\pi$2 ).

A systematic error might have occurred if the overall acceptance of set-I and set-II differed greatly. For example if the acceptance of the set-II cuts was lower than the set-I cuts then the background may have been underestimated because background events were removed simply due to the greater acceptance loss of set-II. The $K^+ \to \pi^+\gamma\gamma$ acceptance of set-II after set-I was applied was 82%, while that of set-I after set-II was applied was 83%, with most of the difference being caused by the opening angle cuts. In the extreme case where the background rejection of set-II after applying

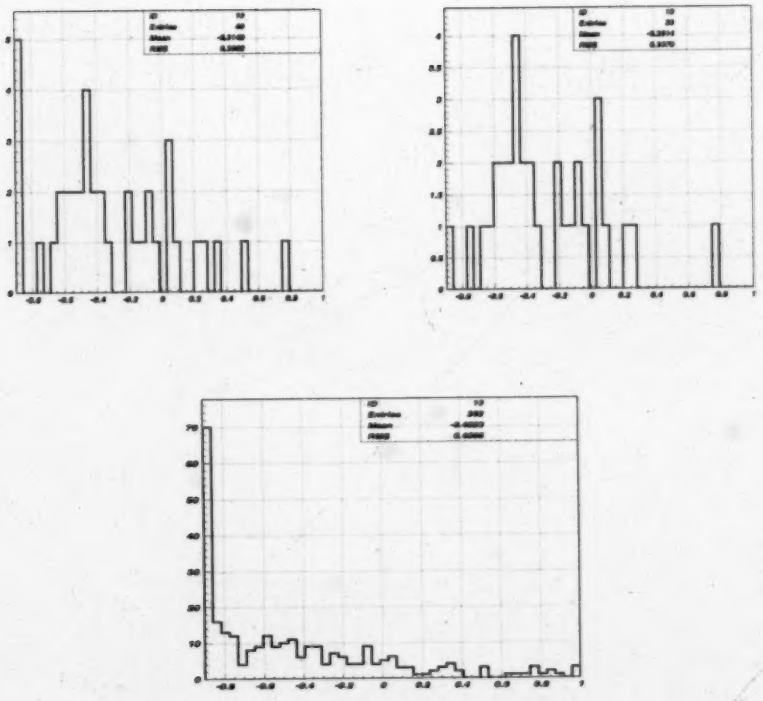

Figure 81: $\cos(\theta_{\pi X})$ for events which passed all the set-II cuts including the $\pi^+$ mass cut (top left), with the added requirement $P_{\pi^+} > 133\text{MeV/c}$ (top right) and with the overlapping photon cuts removed (bottom).

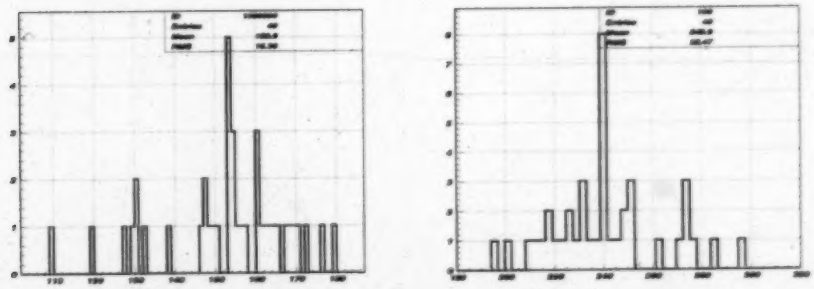

Figure 82: The $\pi^+$ momentum of the non-overlapping gamma background (left) and two photon invariant mass calculated using the $\pi^+$ momentum (right). All Set-II cuts were applied except that for the $\cos(\theta_{\pi X})$ cut which was reversed.

set-I was the inverse of the corresponding $K^+ \to \pi^+\gamma\gamma$ signal acceptance, the background would have been underestimated by 22%, which would have increased the background estimate of 0.58 events (0.14 K$\mu$3 + 0.44 K$\pi$2 ) by $0.58 \times 0.22 = 0.13$ events.

### 5.3.5 Background Shape

To get some idea of the shape of the non-overlapping background spectrum the $\pi^+$ momentum was plotted for those events which had passed all standard cuts not in set-I or set-II and all set-II cuts except for the $\cos(\theta_{\pi X})$ cut which was inverted. The majority of the events are between 145 and 170 MeV/c (figure 82).

## 5.4 Results

The conclusion reached from the background studies was that the overlapping background resulting from K$\pi$3 and radiative K$\pi$2 decays was $1.92 \pm 1.80$ in the region $P_{\pi^+} < 133$MeV/c and $2.64 \pm 2.74$ in the region $P_{\pi^+} > 133$MeV/c. The non-overlapping background from K$\mu$3 and K$\pi$2 was $0.58 \pm 0.13$. K$\pi$3 and radiative K$\pi$2 were not found to contribute significantly to the non-overlapping background. The errors listed on these values are statistical. Possible systematic errors on the values were checked but were not large enough to have a significant impact on the overall $K^+ \to \pi^+\gamma\gamma$ result and so were not included.

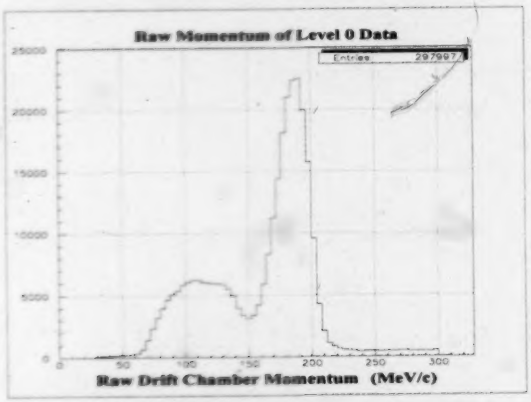


Figure 83: Raw DC momentum in $\pi\gamma\gamma(2)$ level 0 data

# 6 $K^+ \to \pi^+\gamma\gamma$ Acceptance

The event selection cuts fell into two general categories, depending on whether or not there was a momentum dependence in the acceptance. For the momentum independent cuts a single number was measured, for the momentum dependent cuts the charged track momentum was broken into 8 bins 10MeV/c wide spanning 100–180MeV/c. Events with momentum below 100MeV/c were rejected since few such events reached the RS making acceptance measurements unreliable in that momentum region.

To measure the acceptances a variety of different data sources were used. From $\pi\gamma\gamma(2)$-data samples were chosen to emphasize K$\mu$3, K$\pi$3 or events containing pions in the RS. From the monitor triggers K$\mu$2 or K$\pi$2(2) were chosen. Finally, UMC data had to be used in cases where these other processes were too dissimilar from $\pi\gamma\gamma(2)$ or were contaminated in such a way that they could not be used to measure particular acceptances.

Examining the raw DC momentum of the level 0 $\pi\gamma\gamma(2)$ data (figure 83) showed two distinct regions. Above 150MeV/c were primarily K$\pi$2 peak events which had nuclear interacted in the RS and stopped layers A or B, while the low momentum region contained scattered K$\pi$2 and K$\pi$3 but mainly consisted of K$\mu$3. K$\mu$3 were selected by requiring $P_{DC}$ <140MeV/c, a level 1 hextant cut pass and that the offline version of the level 3 trigger return an invariant photon mass of 128.9±18.4MeV (figure 84). The results are shown in table 20.

The purity of the sample can be seen by examining the mass spectrum of

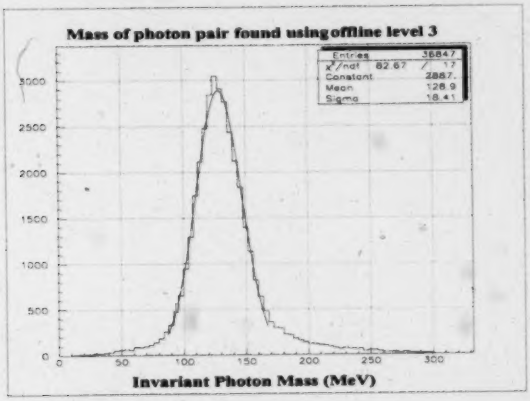


Figure 84: Offline level 3 based invariant photon mass in $\pi\gamma\gamma(2)$ level 0 data

Table 20: Acceptances Measured Using K$\mu$3 Data

| Cut Description | Pass | Acceptance |
|---|---|---|
| $\pi\gamma\gamma(2)$ level 0 data | 328779 | - |
| Level 1 Hextant | 227435 | - |
| $P_{DC}$ <140MeV/c | 66016 | - |
| 110.5MeV<$M_{\gamma\gamma}$ (level 3)<147.3MeV | 22909 | - |
| TG iqual<3 | 22671 | **0.990±0.001** |
| TG iqual<2 | 22225 | - |
| DC xy track | 19817 | - |
| DC charge | 19404 | - |
| DC $z$ track | 18711 | **0.964±0.001** |
| IC reconstruction | 18084 | - |
| RS track | 17893 | **0.989±0.001** |
| TRKTIM | 17760 | **0.993±0.001** |

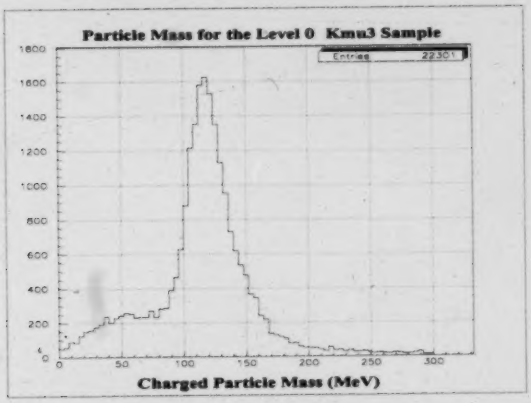


Figure 85: Charged track mass in K$\mu$3 decays selected from $\pi\gamma\gamma(2)$ level 0 data

the surviving events since the only muons came from K$\mu$3 decays. Note that the muon mass peak was shifted upwards since the RS energy was always corrected for $\pi \to \mu$ decay energy (figure 85).

A data set containing pions in the RS was selected from data failing the online level 3 trigger using FITPI [23] with $12ns < t_\mu < 80ns$. A loose cut on the charged track mass, $0 < M_{\pi^+} < 250$MeV, and the pion momentum, $P_{\pi^+} < 180$MeV/c, were also applied (figure 86). Table 21 lists the acceptances found using this data set. A similar set of cuts was used on PASS1 data to select a sample biased toward K$\pi$3, with the removal of the $M_{\pi^+}$ cut, tightening the $P_{\pi^+}$ cut to the K$\pi$3 cutoff of 133MeV/c and requiring that there be at least one overlapping photon in the BV (figure 87).

K$\pi$2(2) (see section 3.8) were chosen from both the monitor triggers and two special runs. For the reconstruction cuts the acceptance of both sets of K$\pi$2(2) data were consistent so they were combined to improve the event statistics. To most closely match the $\pi\gamma\gamma(2)$ trigger K$\pi$2(2) were selected by requiring a BV energy >190MeV [24], applying the level 0 EC and level

[23] FITPI fit the TD information from the stopping range stack counter assuming first one pulse then two pulses. Based on the quality and details of these fits it was decided whether or not FITPI 'passed', in other words found evidence for a second pulse from a $\pi^+ \to \mu^+$ decay. Some of the useful results returned from the fitting were the chisq of the single pulse fit, $\chi_\mu$, and the time of the second pulse (if one was found), $t_\mu$.

[24] INTIME energy measured between -16 and +18ns of prompt and divided by the visible fraction to simulate level 0.

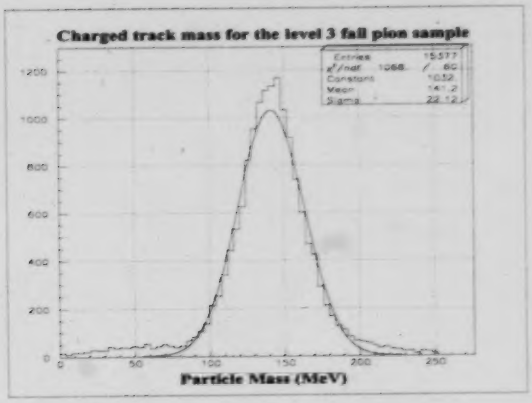


Figure 86: Charged track mass in level 3-fail pion sample.

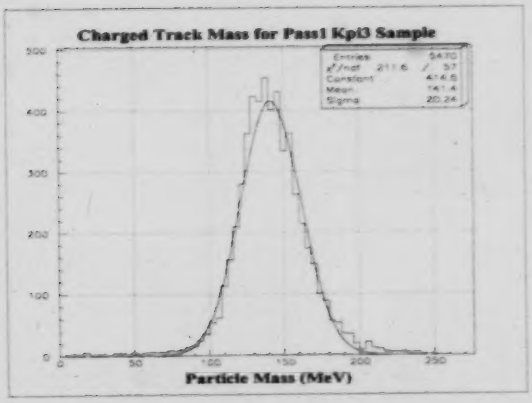


Figure 87: Charged track mass in K$\pi$3 sample.

Table 21: Acceptances Measured Using Level 3 Fail Pions

| Cut Description | Pass | Acceptance |
|---|---|---|
| Level 3 failures | 573556 | - |
| FITPI succeeds | 46493 | - |
| 12< $t_\mu$ <80ns | 25923 | - |
| $P_{\pi^+}$ <180MeV/c | 15857 | - |
| 0<$M_{\pi^+}$ <250MeV/c | 15377 | - |
| TG iqual<2 | 14742 | - |
| DC xy track | 13248 | - |
| DC $z$ track | 12718 | 0.960±0.002 |
| DC charge | 12630 | - |
| IC reconstruction | 11955 | - |
| RS track | 11946 | - |
| TRKTIM | 11850 | 0.992±0.001 |
| Remove $M_{\pi^+}$ cut | 12076 | - |
| $\Delta E_{IC}$ | 10903 | - |
| $\Delta E_{TG}$ | 7826 | - |
| $M_{\pi^+}$ (PASS1)<300MeV | 7726 | **0.987±0.001** |

1 hextant cuts and requiring that offline level 3 find exactly two photon clusters (table 22). This produced a relatively clean sample of K$\pi$2 (figure 88).

K$\mu$2 were chosen from monitor data with online delayed coincidence applied, stopping layer less than layer 21 and two sigma cuts on momentum and mass (223.6 < $P_{\pi^+}$ < 248.8MeV/c, 80.2 < $M_{\pi^+}$ < 124.4MeV) (figure 89 and table 23). Note that the charged track mass used for K$\mu$2 did not have the empirical RS energy correction applied to it that was used for $\pi\gamma\gamma(2)$ (section 4.3.3.2). To keep the K$\mu$2 sample in line with the $\pi\gamma\gamma(2)$ trigger the level 0 EC and level 1 hextant bits were also checked and the offline level 3 simulator had to find 0 photon clusters in the BV.

## 6.1 Acceptance of Online Trigger

The acceptance of the trigger was primarily estimated using UMC data with corrections applied for accidentals and the online delayed coincidence cut. Data was generated using a range of different values of $\hat{c}$ from -5 to +9. To look at the momentum dependence of the online cuts, the data was sorted into 10MeV/c momentum bins based on the $\pi^+$ momentum at birth. To give

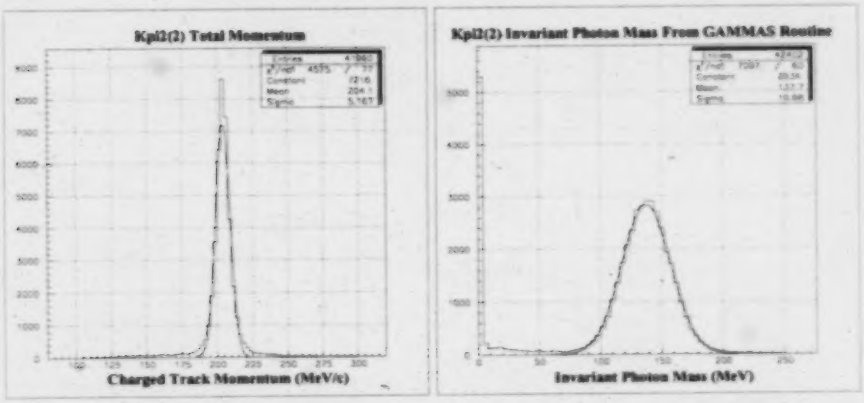
Kpi2(2) Total Momentum
Charged Track Momentum (MeV/c)
Kpi2(2) Invariant Photon Mass From GAMMAS Routine
Invariant Photon Mass (MeV)

Figure 88: Total pion momentum and invariant photon mass (from GAMMAS) of the K$\pi$2(2) data sample

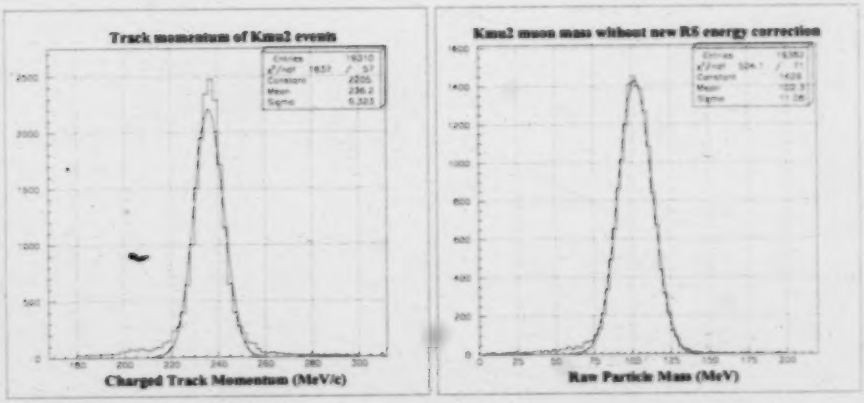
Track momentum of Kmu2 events
Charged Track Momentum (MeV/c)
Kmu2 muon mass without new R5 energy correction
Raw Particle Mass (MeV)

Figure 89: Charged track momentum and mass for the K$\mu$2 sample.

Table 22: Acceptances Measured Using K$\pi$2(2) Data

| Cut Description | Pass | Acceptance |
|---|---|---|
| K$\pi$2(2) triggers | 212285 | - |
| $E_{BV}$(level 0)>190MeV | 98990 | - |
| Level 0 EC Veto | 77875 | - |
| Level 1 Hextant | 77875 | - |
| Level 3 Exactly 2 Photons | 42459 | - |
| TG iqual<3 | 42056 | 0.991±0.0005 |
| TG iqual<2 | 41896 | **0.9962±0.0003** |
| DC xy track | 39621 | - |
| DC $z$ track | 39480 | - |
| DC charge | 39402 | - |
| IC reconstruction | 38772 | **0.984±0.001** |
| RS track | 38704 | - |
| TRKTIM | 38701 | - |
| $\Delta E_{IC}$ | 37529 | **0.970±0.001** |
| $\Delta E_{TG}$ | 33219 | 0.885±0.002 |
| IC $\gamma$ veto | 32536 | **0.979±0.001** |
| VC $\gamma$ veto | 32253 | **0.991±0.001** |
| EC $\gamma$ veto | 28955 | **0.898±0.002** |
| RS $\gamma$ veto | 26450 | - |
| TG $\gamma$ veto | 24841 | **0.939±0.001** |
| Pb glass $\gamma$ veto | 24090 | **0.970±0.001** |
| BV $\gamma$ veto | 21562 | **0.895±0.002** |

Table 23: Acceptances Measured Using K$\mu$2 Data

| Cut Description | Pass | Acceptance |
|---|---|---|
| K$\mu$2 triggers | - | - |
| Level 0 delco | - | - |
| RS layer<15 | 19933 | - |
| 222.8<$P_{\pi^+}$ <249.4MeV/c | 16521 | - |
| 79.3<$M_{\pi^+}$ <125.5MeV | 11106 | - |
| Level 0 EC Veto | 9974 | **0.898±0.003** |
| Level 1 Hextant | 9660 | **0.969±0.002** |
| Level 3 Exactly 0 Photons | 9295 | **0.962±0.002** |
| TG iqual<2 | 9261 | - |
| DC xy track | 8696 | - |
| DC $z$ track | 8680 | - |
| DC charge | 8679 | - |
| IC reconstruction | 8628 | - |
| RS track | 8614 | - |
| TRKTIM | 8612 | - |
| $\Delta E_{IC}$ | 8401 | - |
| $\Delta E_{TG}$ | 7427 | - |
| IC $\gamma$ veto | 7344 | 0.989±0.001 |
| VC $\gamma$ veto | 7278 | 0.991±0.001 |
| EC $\gamma$ veto | 6562 | 0.902±0.003 |
| RS $\gamma$ veto | 6455 | **0.984±0.002** |
| RS geometrical correction for $\pi\gamma\gamma(2)$ | | **0.968** |
| TG $\gamma$ veto | 6069 | 0.940±0.003 |
| Pb glass $\gamma$ veto | 5884 | 0.970±0.002 |
| BV $\gamma$ veto | 5884 | - |

the spectrum shape this was done separately for each value of $\hat{c}$, before any cuts were applied, and the result normalized to the total number of $K_{\ell}live$[25] generated (table 24). This gave the fraction of decays, for a particular $\hat{c}$, that were in each momentum bin. All other cuts, including the level 0 trigger, were dependent only on the momentum of the $\pi^+$ and showed very little variation with $\hat{c}$. Therefore the only $\hat{c}$ dependence entered through table 24 and all acceptances will be listed in a $\hat{c}$ independent form.

In the acceptances measured using UMC, the online, DC tracking and DC track charge cuts all were binned based on the true $\pi^+$ momentum at birth (tables 25, 26 and 28), all other acceptances were binned using the measured DC momentum corrected for target range as was used in the real data.

The acceptance of the level 1 hextant cut could be directly checked using the hextant bits set online in K$\pi$2(1) monitor data. K$\pi$2 was the background most superficially similar to $\pi\gamma\gamma(2)$ in that it contained a $\pi^+$ and two photons. The K$\pi$2(2) sample used elsewhere in the acceptance measurements, although much cleaner, had the hextant cut applied online and could not be used here. Selecting K$\pi$2(1) triggers with the TD cuts and applying a loose photon invariant mass requirement, $100 < M_{\gamma\gamma} < 170$MeV, to ensure that the photons stopped in the BV, yielded a hextant cut acceptance of $0.711 \pm 0.009$, consistent with the high $\pi^+$ momentum end of the UMC result.

The level 0 EC veto, the level 1 hextant cut and the requirement that there be only two photon clusters in level 3 were all subject to accidental vetoing[26]. The accidental rate was measured using K$\mu$2 monitor data selected as mentioned above using layer, mass and momentum cuts. The level 0 EC veto bit and hextant bit were directly checked in the trigger bank written online, while the level 3 code was run offline to see if it found one or more photon clusters. The results are given in table 23.

Finally the acceptance of the online delayed coincidence had to be measured using real data. This was done by applying a tight set of cuts to K$\mu$2(1) monitor data to extract the cleanest possible K$\mu$2 signal. The cuts consisted of basic event reconstruction, one standard deviation cuts around

[25] $K_{\ell}$ was defined earlier in the description of the online trigger logic and was presumed to indicate a kaon had entered the target. The 'live' qualifier simply means a $K_{\ell}$ when data acquisition was able to accept the event. There was some dead time associated with reading out any trigger and if another $K_{\ell}$ was signalled during that time then data acquisition was not 'live' to deal with it.

[26] If another particle 'accidentally' deposited energy in the detector at the same time as a real event this extra energy would not be distinguishable from a photon and the event might be rejected.

Table 24: $\pi\gamma\gamma(2)$ Spectrum Shape Normalized To All $K_\ell live$

| $P_{\pi^+}$ | Spectrum Shape From UMC ($\cdot 10^{-2}$) | | | |
|---|---|---|---|---|
| (MeV/c) | $\hat{c}$=-5 | $\hat{c}$=-4 | $\hat{c}$=-3 | $\hat{c}$=-2 |
| 100-110 | 8.666± 0.027 | 9.721± 0.030 | 11.278± 0.034 | 12.491± 0.023 |
| 110-120 | 5.492± 0.022 | 6.810± 0.026 | 9.223± 0.031 | 11.836± 0.023 |
| 120-130 | 1.641± 0.012 | 2.491± 0.016 | 4.897± 0.023 | 8.167± 0.019 |
| 130-140 | 2.042± 0.014 | 1.151± 0.011 | 0.993± 0.011 | 1.936± 0.010 |
| 140-150 | 2.963± 0.016 | 1.751± 0.013 | 0.900± 0.010 | 0.958± 0.007 |
| 150-160 | 3.352± 0.017 | 2.120± 0.015 | 1.027± 0.011 | 0.647± 0.006 |
| 160-170 | 3.235± 0.017 | 2.198± 0.015 | 1.109± 0.011 | 0.496± 0.005 |
| 170-180 | 2.860± 0.016 | 1.983± 0.014 | 1.026± 0.011 | 0.407± 0.005 |
| (MeV/c) | $\hat{c}$=-1 | $\hat{c}$=-0.5 | $\hat{c}$=0 | $\hat{c}$=+0.5 |
| 100-110 | 12.959± 0.038 | 12.957± 0.036 | 12.715± 0.024 | 12.409± 0.053 |
| 110-120 | 13.574± 0.039 | 13.971± 0.037 | 14.166± 0.025 | 14.312± 0.057 |
| 120-130 | 11.025± 0.036 | 11.990± 0.035 | 12.601± 0.024 | 12.955± 0.054 |
| 130-140 | 3.658± 0.021 | 4.469± 0.022 | 5.224± 0.016 | 5.849± 0.038 |
| 140-150 | 1.870± 0.015 | 2.495± 0.017 | 3.094± 0.013 | 3.657± 0.030 |
| 150-160 | 1.104± 0.012 | 1.524± 0.013 | 1.974± 0.010 | 2.487± 0.025 |
| 160-170 | 0.669± 0.009 | 0.964± 0.011 | 1.296± 0.008 | 1.645± 0.021 |
| 170-180 | 0.403± 0.007 | 0.588± 0.008 | 0.803± 0.006 | 1.056± 0.017 |
| (MeV/c) | $\hat{c}$=+1 | $\hat{c}$=+2 | $\hat{c}$=+3 | $\hat{c}$=+4 |
| 100-110 | 12.299± 0.035 | 11.762± 0.033 | 11.337± 0.034 | 10.930± 0.032 |
| 110-120 | 14.030± 0.038 | 13.606± 0.035 | 13.075± 0.036 | 12.667± 0.034 |
| 120-130 | 13.117± 0.036 | 13.146± 0.034 | 12.890± 0.036 | 12.552± 0.034 |
| 130-140 | 6.342± 0.026 | 7.081± 0.026 | 7.541± 0.029 | 7.785± 0.027 |
| 140-150 | 4.107± 0.021 | 4.907± 0.022 | 5.437± 0.025 | 5.731± 0.024 |
| 150-160 | 2.871± 0.018 | 3.520± 0.019 | 4.050± 0.021 | 4.401± 0.021 |
| 160-170 | 1.956± 0.015 | 2.529± 0.016 | 2.998± 0.018 | 3.342± 0.018 |
| 170-180 | 1.316± 0.012 | 1.743± 0.013 | 2.109± 0.016 | 2.368± 0.016 |
| (MeV/c) | $\hat{c}$=+5 | $\hat{c}$=+7 | $\hat{c}$=+9 | |
| 100-110 | 10.645± 0.033 | 10.230± 0.033 | 9.864± 0.032 | |
| 110-120 | 12.180± 0.035 | 11.646± 0.035 | 11.148± 0.034 | |
| 120-130 | 12.291± 0.035 | 11.715± 0.035 | 11.297± 0.034 | |
| 130-140 | 7.987± 0.029 | 8.049± 0.029 | 8.173± 0.030 | |
| 140-150 | 6.046± 0.026 | 6.403± 0.026 | 6.648± 0.027 | |
| 150-160 | 4.709± 0.023 | 5.052± 0.024 | 5.351± 0.024 | |
| 160-170 | 3.565± 0.020 | 3.982± 0.021 | 4.172± 0.022 | |
| 170-180 | 2.598± 0.017 | 2.912± 0.018 | 3.130± 0.019 | |

Table 25: $\pi\gamma\gamma(2)$ Level 0 Acceptance Values ($\cdot 10^{-2}$)

| Momentum | Cut Description |
|---|---|
| (MeV/c) | Level 0 |
| 100-110 | 2.171±0.045 |
| 110-120 | 3.671±0.059 |
| 120-130 | 5.323±0.090 |
| 130-140 | 7.203±0.155 |
| 140-150 | 8.196±0.185 |
| 150-160 | 8.333±0.212 |
| 160-170 | 7.826±0.237 |
| 170-180 | 6.177±0.248 |

Table 26: $\pi\gamma\gamma(2)$ Online Acceptance Values (From UMC)

| Momentum | Cut Description | | | |
|---|---|---|---|---|
| Range | Level 1 | Level 1 | Level 1 | Level 3 |
| (MeV/c) | Hextant | 2 Photons | Gap count | Pass |
| 100-110 | 0.693±0.003 | 0.624±0.004 | 0.986±0.001 | 0.963±0.002 |
| 110-120 | 0.681±0.003 | 0.682±0.003 | 0.992±0.001 | 0.973±0.001 |
| 120-130 | 0.675±0.002 | 0.701±0.003 | 0.995±0.001 | 0.975±0.001 |
| 130-140 | 0.684±0.003 | 0.684±0.004 | 0.996±0.001 | 0.969±0.002 |
| 140-150 | 0.688±0.004 | 0.652±0.005 | 0.997±0.001 | 0.961±0.002 |
| 150-160 | 0.702±0.004 | 0.599±0.005 | 0.991±0.001 | 0.934±0.003 |
| 160-170 | 0.718±0.005 | 0.564±0.006 | 0.943±0.004 | 0.884±0.006 |
| 170-180 | 0.712±0.006 | 0.529±0.008 | 0.756±0.010 | 0.776±0.011 |

the measured muon momentum, energy and range, TD cuts (to make sure the event was consistent with a muon) and photon vetoes (table 27[27]). To make sure that application of the TG iqual and TG photon veto cuts didn't bias this result the acceptance was also measured without the two TG cuts. There was no significant difference in acceptance.

Table 27: Online Delayed Coincidence From K$\mu$2 Data

| Cut Description | Events |
|---|---|
| K$\mu$2(1) triggers | 143436 |
| TG iqual<2 | 141231 |
| DC xy track | 124230 |
| DC $z$ track | 123439 |
| DC charge | 122425 |
| RS track | 121308 |
| Photon veto (all) | 75066 |
| $\chi_\mu < 2$ from FITPI | 69328 |
| EV5 finds a $\mu \to e$ decay | 58859 |
| $\lvert P_{\pi^+} - 236.5\rvert < 6.2$MeV/c | 38547 |
| $\lvert R_\pi - 52.3\rvert < 2.9$cm | 23958 |
| $\lvert E_\pi - 144.7\rvert < 4.2$MeV | 14386 |
| Online delayed coincidence | 11775 |
| $t_{TG}(\pi) - t_{TG}(K) > 2ns$ | 10869 |
| Online delayed coincidence | **0.819±0.003** |
| $t_{TG}(\pi) - t_{TG}(K) > 2ns$ | 0.923±0.002 |

## 6.2 Acceptance of PASS1 Cuts

A number of the PASS1 cuts were tightened at PASS3. Including the target reconstruction, TRKTIM and the EC and RS photon vetoes as well as the $M_{\pi^+}$ mass cut. These tightened cuts will be dealt with under the PASS3 section.

### 6.2.1 Basic Event Reconstruction

Whenever possible the acceptance of each reconstruction cut was measured using two different data samples. The details of each acceptance measure-

[27] $t_{TG}(\pi) - t_{TG}(K) > 2ns$ was the offline delayed coincidence which used target timing to require a greater then 2ns time difference between the kaon stopping and decaying. EV5 was a TD based routine which searched for a $\mu \to e$ transition in the RS.

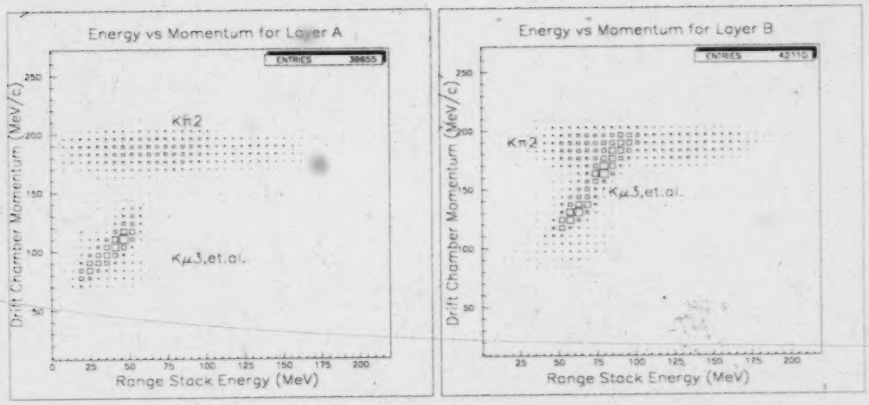


Figure 90: Range stack energy versus DC momentum in $\pi\gamma\gamma(2)$ level 0 data

ment are given below:

- Drift chamber tracking (exactly one track found). Target reconstruction had to succeed but no additional requirement was placed on the K$\pi$2(2) sample. For K$\mu$3 one RS track with <60MeV RS energy was also required in place of the DC momentum cut to reduce the amount of K$\pi$2 contamination (figure 90). For K$\pi$2(2) the DC tracking acceptance was 0.946$\pm$0.001, for K$\mu$3 0.908$\pm$0.002, for level 3 pions 0.899$\pm$0.002 and for a K$\pi$3 sample selected using TD cuts and low RS energy, 0.891$\pm$0.005. These data sets have progressively lower average charged track momentum and show a momentum dependence in the DC reconstruction. The momentum spectrum of $\pi\gamma\gamma(2)$ fell around that of the K$\pi$3 and level 3 pion samples and UMC gave an overall DC track reconstruction acceptance consistent with those data samples. Therefore, the UMC generated values were used since it is impossible to accurately measure the momentum dependence of the DC tracking efficiency for real data. With the UMC data the momentum at birth of the $\pi^+$ was used for binning the acceptance values rather than the DC measured momentum. Also, since the acceptance was primarily dependent only on the particle momentum, not the value of $\hat{c}$, only one set of numbers was needed.

- Drift chamber charge (the track found is positive). Events which have had a TD cut in the RS applied (K$\pi$2(2) and pion samples) are biased

Table 28: $\pi\gamma\gamma(2)$ PASS1 Event Reconstruction Acceptance Values (Momentum Dependent)

| Momentum | Cut Description | |
|---|---|---|
| Range | DC xy track | DC charge |
| (MeV/c) | UMC | UMC |
| 100-110 | 0.860±0.006 | 0.966±0.003 |
| 110-120 | 0.879±0.004 | 0.972±0.002 |
| 120-130 | 0.884±0.003 | 0.967±0.002 |
| 130-140 | 0.903±0.004 | 0.956±0.003 |
| 140-150 | 0.920±0.004 | 0.949±0.004 |
| 150-160 | 0.931±0.005 | 0.916±0.005 |
| 160-170 | 0.945±0.005 | 0.875±0.008 |
| 170-180 | 0.948±0.008 | 0.790±0.016 |

since the TD cut selects positive pions. The K$\mu$3 value (0.979±0.001) was close to the overall value from UMC, but UMC showed a momentum dependence in the track charge because a larger fraction of high momentum tracks are due to photon conversions not real pions. The DC charge acceptance was measured using UMC data binned based on $\pi^+$ momentum at birth and was essentially constant except at high momentum.

- IC range routine succeeds (return code $\neq 1$). This cut extrapolated the DC track back to the IC and so was sensitive to scattered K$\pi$2 contamination in the $\pi\gamma\gamma(2)$-based samples. K$\pi$2(2) data was used instead.
- Range stack tracking (exactly one track found). Because of the TD cut built into the pion samples they could not be used to measure the RS tracking acceptance. Instead only K$\mu$3 data was used. In the momentum range of interest there was not a significant momentum dependence in the RS tracking.

### 6.2.2 Stopping layer misidentification

Although the online trigger required the event to stop in either layer A or B, it was observed that the offline stopping counter was occasionally deeper than layer B. This was checked using $\pi\gamma\gamma(2)$ UMC data for different values of $\hat{c}$ and had an acceptance very close to 1.

## 6.3 Acceptance of PASS2 Cuts

The $M_{\gamma\gamma}$ cut at 190MeV in PASS2 was tightened to 200MeV in PASS3 and will be measured there. The charged track momentum < 180 MeV/c cut had to be measured using UMC data and was $\hat{c}$ dependent but was implicitly measured in the level 0 trigger acceptance measurements since they restricted the $\pi^+$ momentum to be between 100 and 180MeV/c.

## 6.4 Acceptance of PASS3 Cuts

### 6.4.1 Basic Event Reconstruction

This covers both PASS1 cuts tightened in PASS3 and new cuts applied only at PASS3. Unless otherwise mentioned the results are given in tables 20, 21, 22 and 23.

- Target reconstruction (ierr=0, iqual<2). The acceptance was broken into two parts, the first required iqual<3 and the second iqual≠2. Iqual=2 corresponded to no pion module being found in the target and had to be considered separately because low momentum events were more likely to reach the RS and survive the trigger if they stopped near the edge of the target.

  For iqual<3 no additional requirements were made other than the event selection listed above. Requiring that there be one positive DC and RS track made no difference in the acceptance for either K$\mu$3 or K$\pi$2(2) . The value from K$\pi$2(2) was consistent with that from K$\mu$3 .

  The acceptance loss for iqual≠2 (after requiring iqual<3) was fairly small but was momentum dependent since low momentum pions were more likely to reach the RS if they decayed at the edge of the target. Using K$\pi$2(2) monitor data the acceptance of this cut for high momentum $\pi^+$ was 0.9962±0.0003. The level 3-fail pion sample contained a sufficient number of K$\pi$2 with target scatters to skew the results. However if the K$\pi$3 portion of this sample was selected by requiring 3 photons with at least 30MeV energy each in the BV then a low momentum pion sample could be selected without biasing the target analysis. This resulted in an iqual≠2 acceptance in the 110<$P_{\pi^+}$ <125MeV/c region of 0.9963±0.0013. Below 110MeV/c there was evidence that the expected momentum dependence appears but the difference was not significant above 100MeV/c.

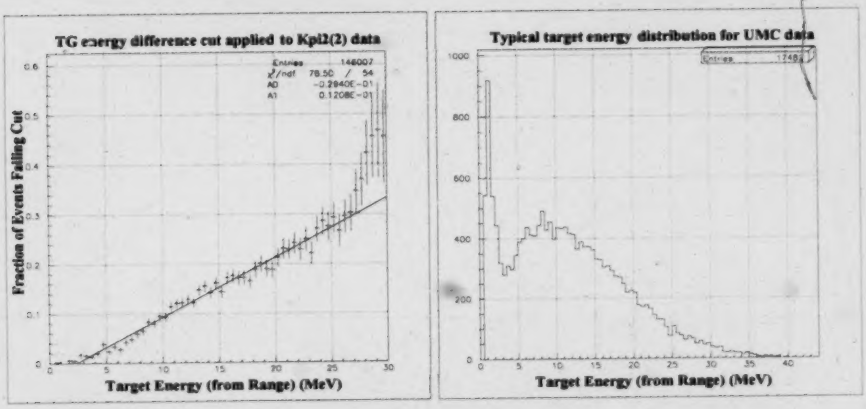
TG energy difference cut applied to Kpi2(2) data
Fraction of Events Failing Cut
Target Energy (from Range) (MeV)
Typical target energy distribution for UMC data
Target Energy (from Range) (MeV)

Figure 91: Fraction failing TG-energy-difference cut as a function of TG energy (from range) for K$\pi$2(2) data and a typical UMC $\pi\gamma\gamma(2)$ TG energy distribution.

- Drift chamber tracking failure code (icfail_dc=0). K$\mu$3 and level 3 fail pions gave a similar result of about 0.96.
- TRKTIM (a RS track time was found). As expected the TRKTIM acceptance, after a RS track had been found, was close to one making the data sample used to measure it less critical. The K$\mu$3 result was used in this case and was consistent with the result from the level-3-fail pion sample.
- IC energy difference (|actual energy - estimated energy|<2.5MeV). As with the previous IC cut and the TG energy difference below, scattered K$\pi$2 contamination was again a problem. K$\pi$2(2) was used with an acceptance of $0.970 \pm 0.001$ which was similar to the UMC result of approximately $0.957 \pm 0.003$.
- TG energy difference (|actual energy + 1.47MeV - estimated energy| <5MeV). K$\pi$2(2) data was used which was also consistent with the result from K$\mu$2. However, there was a strong dependence on the target range which was measured using K$\pi$2(2) (figure 91). The target range distribution was found for each of the 8 $\pi^+$ momentum bins using UMC data and the acceptance determined by integrating the measured acceptance over these UMC range distributions (table 32).

### 6.4.2 PASS1/PASS3 Inconsistencies

It can be seen from table 12 that additional events are being cut by cuts that were already applied at PASS1 or PASS2. This resulted from minor updates to several routines which were linked into the PASS3 code but were not present in PASS1 or PASS2. There was also a small change made in the RS time offsets, and the BV time window for forming photon clusters, between PASS2 and PASS3. After applying the PASS3 cuts to a K$\mu$3 sample the PASS1 and PASS2 cuts had acceptances in excess of 99.9% except for the DC tracking requirement which had an acceptance of 0.989±0.001. An acceptance correction was made only for that cut (table 31).

### 6.4.3 $M_{\gamma\gamma} > 200$MeV

As with $P_{\pi^+}$ <180MeV/c this cut could only be measured using UMC. It was also, of course, momentum dependent since $M_{\gamma\gamma}$ was directly correlated to $P_{\pi^+}$ (table 32).

### 6.4.4 120 MeV < Pion mass < 165 MeV

A large high mass tail existed on the reconstructed charged track mass due to unseen energy being deposited in the RS. A cut at 300MeV removed the worst examples of these events at PASS1, and has already been included in the data used for this measurement.

To reduce the number of K$\pi$2 with interactions or scatters, a pion sample was chosen from PASS1 data with all of the above reconstruction cuts, TD cuts as in the level 3 fail sample and a requirement of at least one overlapping photon in the BV. This resulted in a sample that was mainly K$\pi$3 with some radiative or scattered K$\pi$2. Fitting the pion decay time returned by FITPI for these events results in a lifetime of 26.5±0.7ns compared to the actual pion lifetime of 26.0ns (figure 92). The resolution of the mass measurement was layer dependent which translated to a step in the acceptance at a momentum of about 150MeV/c (figure 93). The acceptance was broken into the regions 100-150MeV/c and 150-180MeV/c (table 29).

Table 29: $\pi^+$ Mass Cut Acceptance Values

| Cut Description | Source | Acceptance |
|---|---|---|
| $\pi^+$ mass ($P_{\pi^+}$ ≤150MeV/c) | PASS1 pions | 0.735±0.006 |
| $\pi^+$ mass ($P_{\pi^+}$ >150MeV/c) | PASS1 pions | 0.777±0.016 |

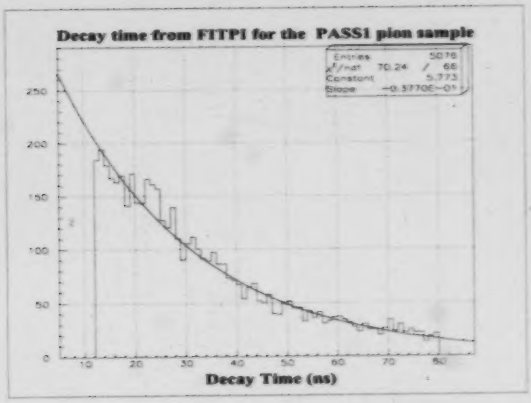


Figure 92: Pion decay time for PASS1 pion sample.

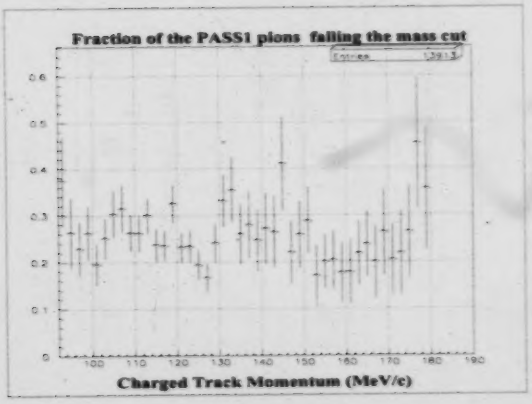


Figure 93: Acceptance of the pion mass cut vs charged track momentum for PASS1 pions.

The above data sample had already had the PASS1 mass cut of 300MeV on the uncorrected charged track mass applied to it. This introduced another acceptance factor which was measured by applying a similar set of K$\pi$3 selection cuts to data which had failed level 3 and then applying the PASS1 mass cut (table 21).

Because TD fitting was performed this sample only addressed pions which did not decay in flight and only lost energy due to elastic collisions or light collection inefficiencies such as misaligned light guides. To account for pions which decayed in flight or nuclear interacted in the RS the acceptance of the mass cut in UMC $\hat{C}$=0 data was examined as a function of the pion ifate code, i. e. the code indicating whether the pion had decayed in flight (code 2), nuclear interacted (code 3) or come to a stop normally before decaying (code 1) (table 30). [28]

Table 30: Decay in Flight and Nuclear Interaction Acceptance Correction Using UMC $\hat{C}$=0 Data.

| Ifate | Before mass cut | After mass cut | Acceptance ($A$) |
|---|---|---|---|
| 1 | 15653 | 13737 | 0.8776±0.0026 |
| 1,2 | 16700 | 14019 | 0.8395±0.0028 |
| 1,3 | 15764 | 13752 | 0.8724±0.0027 |
| Nuclear interaction correction ($A_{1,3}/A_1$) | | | 0.994±0.005 |
| Decay in flight correction ($A_{1,2}/A_1$) | | | 0.957±0.004 |

### 6.4.5 Photon Veto Cuts

All of the photon veto cuts were essentially independent of $\pi^+$ momentum except for the RS cut. The acceptance for the EC and RS photon vetoes that were applied at PASS1 are included in the acceptances listed here for the EC and RS. Accidentals in the IC, VC, EC, TG and lead glass Cherenkov where measured using both K$\pi$2(2) and K$\mu$2 data. The results were consistent except for the IC where the K$\pi$2(2) sample had a slightly lower acceptance than the K$\mu$2 value (tables 22 and 23). The K$\pi$2(2) result was used because the presence of a pion and two photons made it the decay more similar to $\pi\gamma\gamma(2)$ . The BV was sensitive to the presence of the photons in $\pi\gamma\gamma(2)$ and was studied using K$\pi$2(2) (table 22). Finally the RS photon veto was sensitive to the energy contained in the $\pi\gamma\gamma(2)$ photons and its acceptance was

[28] As usual all cuts which came in sequence before the mass cut were also applied to this sample to minimize systematic errors due to correlations between cuts.

measured as a function of $\pi^+$ momentum using UMC (table 32). With the number of UMC events generated for each $\hat{c}$ there was no statistically significant dependence between $\hat{c}$ and the RS gamma veto acceptance. The acceptance was then corrected for the purely accidental rate using K$\mu$2 and taking into account the fact that more of the RS was available for vetoing in $\pi\gamma\gamma(2)$ then for K$\mu$2 due to the shorter charged track length (table 23).

### 6.4.6 $M_{\gamma\gamma}$ Mass Difference

The acceptance of the $M_{\gamma\gamma}$ mass difference cut was estimated using UMC data (table 33). It depended on the $\pi^+$ momentum because the resolution of $M_{\gamma\gamma}$ was roughly proportional to $\sqrt{M_{\gamma\gamma}}$ which was in turn inversely proportional to $P_{\pi^+}$. Moreover, the $M_{\gamma\gamma} > 200$MeV cut removed the events which would have been rejected by the $M_{\gamma\gamma}$ mass difference cut at high $\pi^+$ momentum.

### 6.4.7 Opening angle cut

The acceptance of the opening angle cut was estimated using UMC data (table 33). Since the minimum opening angle between the $\pi^+$ and the high energy gamma increased as the $\pi^+$ momentum increased, the cut was momentum dependent. However, this dependence was weak in the region of $\pi^+$ momentum less than 160 MeV/c.

### 6.4.8 Overlapping Gamma Veto

The photons in real K$\pi$2 data were sorted by energy and the three values relevant to the overlapping cuts; the number of hit elements, the azimuthal dispersion and the $z$ fluctuation, were tabulated as a function of cluster energy. UMC was used to generate $\pi\gamma\gamma$ data and all of the cuts up to the overlapping cuts were applied. The acceptance of the overlapping cuts was measured by replacing the UMC determined overlapping veto variables for each photon cluster with those from the K$\pi$2 data set with the same cluster energy (table 31). Thus for this acceptance measurement UMC was used only to obtain the photon energy spectrum for $\pi\gamma\gamma$. This was done because in the monte carlo the BV modules all had exactly the same attenuation length, speed of light, and $z$ offsets which, of course, was not true of the real detector.

### 6.4.9 KINFIT $\chi^2$ probability

If the standard deviations of the measurements were correct then the cut Prob($\chi^2$) > 0.1 would have had a 90% acceptance. However, this cut was correlated with the pion mass cut and the $M_{\gamma\gamma}$ mass difference cut which both rejected events with a high $\chi^2$. To estimate this effect the acceptance of the $\chi^2$ probability cut, before and after the pion mass cut and the $M_{\gamma\gamma}$ mass difference cut, was measured using UMC data.

First the probability distributions before and after the cuts were fit by a straight line

$$y = ax + b$$

where x is the probability and y is the number of counts. The fit region was $x = [0.1, 1.0]$ because there was a peak near zero in the data before the cuts, mainly due to $\pi^+$ nuclear interactions and missed photon energy. Next the acceptance loss was calculated by measuring the ratio of the area under the fit curve in the region rejected by the KINFIT cut, $x = [0.0, 0.1]$, to the total area under the curve for the complete range $x = [0.0, 1.0]$. In other words;

$$1 - Acc = (a/2 \times (0.1)^2 + b \times 0.1)/(a/2 + b).$$

The acceptance loss decreased from 0.0838 before the $M_{\pi^+}$ and $M_{\gamma\gamma}$ cuts to 0.0491 after these cuts were applied. The KINFIT acceptance loss for real data was estimated by assuming a flat distribution for the KINFIT probability and applying this acceptance ratio, i. e. :

$$1 - Acc = 0.1 \times 0.0491/0.0838 = 0.0586.$$

This gave 0.9414 for the KINFIT acceptance with a statistical and fitting error of $\pm$ 0.001 (figure 94).

The momentum dependence of this cut was not examined because the acceptance of the KINFIT probability cut was high, and any momentum dependence would not introduce a significant systematic error.

## 6.5 Final Acceptance

Tables 20, 21, 22, and 23 show the details of the acceptances measured using different event samples. Values used for $\pi\gamma\gamma(2)$ are in bold face. The final $\pi\gamma\gamma(2)$ acceptance was found by multiplying all of the bold entries in these tables with the data in tables 25, 26, 27, 28, 29, 30, 31, 32 and 33 for each particular momentum bin. The results are listed in table 34 and are

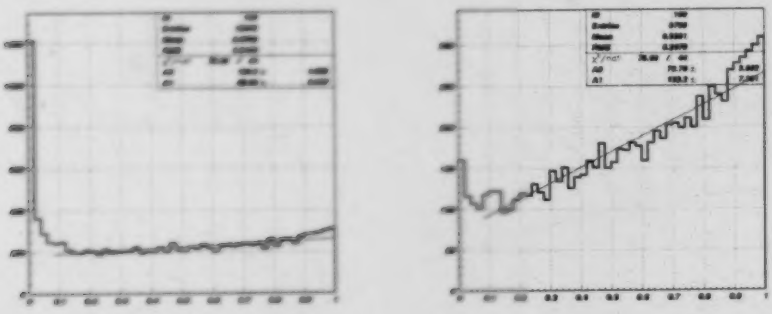

Figure 94: The KINFIT probability distribution before (left) and after (right) the pion mass cut and the $M_{\gamma\gamma}$ mass difference cut.

Table 31: $\pi\gamma\gamma(2)$ Miscellaneous Acceptance Values

| Cut Description | Source | Acceptance |
|---|---|---|
| Stopping layer | UMC | 0.998±0.001 |
| PASS1 correction | K$\mu$3 | 0.989±0.001 |
| $N_{BV}/\gamma$ | UMC | 0.978±0.001 |
| $\gamma$ overlap ($\phi$) | K$\pi$2 | 0.725±0.004 |
| $\gamma$ overlap ($z$) | K$\pi$2 | 0.719±0.005 |
| KINFIT | UMC | 0.941±0.001 |

Table 32: $\pi\gamma\gamma(2)$ PASS3 Acceptance Values (Momentum Dependent)

| Momentum | Cut Description | | |
|---|---|---|---|
| Range | $\Delta E_{TC}$ | $M_{\gamma\gamma}$ >200MeV | RS $\gamma$ veto |
| (MeV/c) | K$\pi$2(2) /UMC | UMC | UMC |
| 100-110 | 0.946±0.004 | 0.966±0.003 | 0.829±0.007 |
| 110-120 | 0.913±0.003 | 0.972±0.002 | 0.850±0.005 |
| 120-130 | 0.884±0.004 | 0.967±0.002 | 0.858±0.004 |
| 130-140 | 0.858±0.006 | 0.956±0.003 | 0.872±0.005 |
| 140-150 | 0.851±0.007 | 0.949±0.004 | 0.894±0.005 |
| 150-160 | 0.852±0.008 | 0.916±0.005 | 0.907±0.006 |
| 160-170 | 0.847±0.010 | 0.875±0.008 | 0.918±0.008 |
| 170-180 | 0.828±0.014 | 0.790±0.016 | 0.931±0.012 |

Table 33: $\pi\gamma\gamma(2)$ PASS3 Acceptance Values (Momentum Dependent) cont.

| Momentum | Cut Description | |
|---|---|---|
| Range | $\cos\theta_{\pi\gamma_1}$ | $\Delta M_{\gamma\gamma}$ |
| (MeV/c) | UMC | UMC |
| 100-110 | 0.500±0.009 | 0.811±0.011 |
| 110-120 | 0.481±0.007 | 0.831±0.007 |
| 120-130 | 0.476±0.006 | 0.846±0.007 |
| 130-140 | 0.470±0.007 | 0.865±0.007 |
| 140-150 | 0.453±0.008 | 0.871±0.008 |
| 150-160 | 0.450±0.010 | 0.932±0.008 |
| 160-170 | 0.407±0.013 | 0.997±0.002 |
| 170-180 | 0.342±0.020 | 1.000 |

Table 34: Total $\pi\gamma\gamma(2)$ Acceptance

| Momentum | Acceptance of All Cuts |
|---|---|
| (MeV/c) | $(\cdot 10^{-3})$ |
| 100-110 | 0.309±0.012 |
| 110-120 | 0.587±0.018 |
| 120-130 | 0.864±0.025 |
| 130-140 | 1.162±0.040 |
| 140-150 | 1.257±0.047 |
| 150-160 | 1.291±0.060 |
| 160-170 | 0.993±0.055 |
| 170-180 | 0.388±0.033 |

effectively theory independent. Note that the $f_s$ factor mentioned later in the branching ratio section is not included in the acceptance at this point so that the values in table 34 would have to be multiplied by this factor to find the *true* experimental acceptance.

# 7 Branching Ratio

## 7.1 Kaon Flux (K$\mu$2 Branching Ratio)

Three different scalers recorded the number of $K_{\ell}live$ online. However, the the final sum of these three records was not identical (table 35). For consistency with the K$\mu$2 and K$\pi$2 branching ratio measurements below, scaler one was used with an error equal to the difference between the first and second scalers. Scaler three was considered to be incorrect.

Table 35: Online $K_{\ell}live$ Scalers

| | $K_{\ell}live \cdot 10^{11}$ |
|---|---|
| Scaler 1 | 1.0111 |
| Scaler 2 | 1.0107 |
| Scaler 3 | 1.0000 |
| Value used | 1.0111±0.0004 |

An adjustment was necessary to the flux because not all $K_{\ell}live$ counts correspond to actual stopped kaons, this is the so called $f_s$ ratio. This ratio was determined be measuring the branching ratio of a well known and easy to measure decay mode, such as K$\mu$2, and determining what normalization was required to reconcile the measured value with the known branching ratio. To measure $f_s$ K$\mu$2(1) monitor triggers spanning roughly the same set of runs as the $\pi\gamma\gamma(2)$ data were used [29]. The K$\mu$2 selection cuts are shown in table 36. Muon energy and range were not used because doing so would require a cut to eliminate muons which passed through the entire RS and stopped in the BV. The acceptance of this cut would have to be measured using UMC and would be dependent on the effective thickness of the RS, a quantity which there is reason to believe may not be well determined in UMC[45]. For the same reason the BV photon veto was not used. The number of $K_{\ell}live$ listed in table 36 was not directly measured from the monitor data because the scaler records were dropped from this data stream at PASS0. Instead the ratio of unprescaled K$\mu$2(1) level 0 triggers to $K_{\ell}live$ was measured for the applicable set of runs using the scalers attached to the $\pi\gamma\gamma(2)$ data; $1.8494619 \cdot 10^{10}/9.181544 \cdot 10^{10} = 0.20143$. Using this ratio and the online K$\mu$2 prescale of 131072 implies that to produce the 143436 K$\mu$2(1) triggers required $K_{\ell}live = 143436 \cdot 131072/0.20143 = 9.3334 \cdot 10^{10}$. Note that the value obtained directly from $\pi\gamma\gamma(2)$ data was $9.181544 \cdot 10^{10}$. The calculated

[29] The exact runs were 9380-10116 for K$\mu$2(1) and 9348-10141 for $\pi\gamma\gamma(2)$, with both excluding runs 9474-9485.

Table 36: K$\mu$2 Branching Ratio

| Cut Description | Pass |
|---|---|
| $K_t live$ | $(9.33 \pm 0.15) \cdot 10^{10}$ |
| K$\mu$2 triggers | 143436 |
| Level 0 delayed coincidence | 95626 |
| EC photon veto | 78725 |
| TG photon veto | 71193 |
| RS photon veto | 63925 |
| TG iqual<2 | 63168 |
| Offline delayed coincidence | 55244 |
| DC xy track | 51914 |
| DC $z$ track | 51694 |
| DC charge | 51554 |
| RS track | 51332 |
| TRKTIM | 51289 |
| $P_{\pi^+}$ 236.7±6.0 MeV/c | 34610 |
| K$\mu$2 acceptance | 0.128±0.002 |
| K$\mu$2 prescale | 131072 |
| Real K$\mu$2 branching ratio | 0.6315±0.0019 |
| Kaon stopping fraction, $f_s$ | **0.598±0.014** |

Table 37: K$\mu$2 Branching Ratio Acceptance

| Cut Description | Pass | Acceptance | Pass | Acceptance |
|---|---|---|---|---|
| | Prescaled K$\mu$2 | | UMC | |
| K$_t$*live* | Not Available | | 47530 | - |
| K$\mu$2 triggers | Not Available | | 18323 | **0.3855±0.0022** |
| Level 0 delco | Not Available | | - | - |
| Online RS layer<15 | 20360 | - | - | - |
| EC photon veto | 16777 | - | 18323 | - |
| TG photon veto | 15100 | - | 18300 | - |
| RS photon veto | 13912 | - | 17547 | - |
| TG iqual<2 | 13757 | **0.9889±0.009** | 17469 | 0.9955±0.0005 |
| Offline delco | 12556 | - | 13722 | - |
| DC xy track | 11807 | **0.940±0.002** | 13374 | 0.975±0.001 |
| DC $z$ track | 11754 | **0.9955±0.0006** | 13373 | 0.9999±0.0001 |
| DC charge | 11719 | **0.9970±0.0005** | 13364 | 0.9993±0.0002 |
| RS track | 11672 | **0.9960±0.0006** | 13357 | 0.9995±0.0002 |
| TRKTIM | 11664 | **0.9993±0.0002** | 13357 | 1.0 |
| $P_{\pi^+}$ $\pm 1\sigma$ | 7812 | **0.670±0.004** | 9124 | 0.683±0.004 |
| Before photon vetoes | 20360 | - | - | - |
| TD cuts | 17039 | - | - | - |
| EC $\gamma$ veto | 14215 | **0.834±0.003** | - | - |
| TG $\gamma$ veto | 12846 | **0.904±0.002** | - | - |
| RS $\gamma$ veto | 12196 | **0.949±0.002** | - | - |
| Level 0 delco | see text | **0.819±0.003** | - | - |
| Offline delco | see text | **0.923±0.002** | - | - |
| Total K$\mu$2 acceptance | | 0.128±0.002 | | |

value was adopted with an error equal to the difference between the two numbers.

The acceptances of the various cuts are listed in table 37. UMC was only used to determine the acceptance of the level 0 trigger. The online and offline delayed coincidence acceptances are dealt with in section 6.1. The real data in table 37 was skimmed from the full data set using online delayed coincidence and online RS layer < 15 (hardware layer 21, the outermost layer of the RS).

Since $f_s$ was measured by normalizing to a branching ratio, it could have various systematic effects rolled into it and so was somewhat analysis

dependent. However, the number obtained, $f_s = 0.598 \pm 0.014$, was similar to that of several previous analyses, such as $0.59 \pm 0.02$[45], $0.584 \pm 0.011$[46] and $0.591 \pm 0.012$[47].

## 7.2 $K\pi 2$ Branching Ratio

Once $f_s$ was known it was possible to unambiguously measure the K$\pi$2 branching ratio. This was done not to obtain the best possible K$\pi$2 branching ratio measurement but rather as a test for systematic errors in the $\pi\gamma\gamma(2)$ analysis. All the $\pi\gamma\gamma(2)$ cuts which weren't specifically designed to cut K$\pi$2 were applied to K$\pi$2(1) monitor data. Any acceptances used in the $\pi\gamma\gamma(2)$ analysis which could be expected to be reasonably accurate for K$\pi$2 were directly copied. Acceptances which were measured using UMC in the $\pi\gamma\gamma(2)$ analysis were remeasured using UMC and the same general technique for K$\pi$2(1). There were a few values that had to be remeasured using K$\pi$2(2) data specifically for this K$\pi$2 branching ratio measurement. Table 38 shows the various acceptances, with the numbers actually used to determine the total acceptance in bold face.

Most of the acceptances in table 38 are self explanatory with the following exceptions: $\Delta E_{TG}$, $M_{\pi^+}$, nuclear interactions and decays in flight, kinematic fitting and the overlapping photon cuts. In the $\pi\gamma\gamma(2)$ analysis the acceptance for the target energy difference cut, $\Delta E_{TG}$, was measured using K$\pi$2(2) data adjusted for the $\pi\gamma\gamma(2)$ target energy spectrum from UMC. Clearly for K$\pi$2 no additional adjustment was needed and the acceptance was measured directly using K$\pi$2(2) triggers (table 22). The $M_{\pi^+}$ mass cut was measured using K$\pi$2(2) data which had passed all cuts up to the mass cut as well as TD cuts. Note that in this measurement and also the result for the kinematic fit below it was necessary to use RS energy which did not have the empirical correction used in $\pi\gamma\gamma(2)$ (see section 4.3.3.2). The nuclear interaction and decay in flight acceptance values were corrections applied to the $M_{\pi^+}$ cut since that cut used the TDs for event selection. The same method that was shown for $\pi\gamma\gamma(2)$ data in table 30 was used here to compare the acceptance for UMC events that either did or did not interact or decay in flight. For the kinematic fitting, the same technique was used as in section 6.4.9 but with K$\pi$2(1) UMC data rather than $\pi\gamma\gamma(2)$ UMC data. The technique used to adjust the overlapping photon variables to remove the dependence on the number of BV elements struck (section 4.3.3.8) was only applicable to photons above 100MeV. For K$\pi$2 this meant only the higher energy photon, therefore the overlapping photon cuts were only applied to $\gamma_1$. The acceptance was measured using K$\pi$2(2) data which had all other

Table 38: K$\pi$2 Branching Ratio Acceptance

| Cut Description | Pass | Acceptance | Pass | Acceptance |
|---|---|---|---|---|
| | Data | | UMC | |
| $K_t live$ | $(1.447\pm0.001)\cdot10^{11}$ | | 95171 | - |
| K$\pi$2(1) triggers | 166726 | - | 34656 | **0.364±0.002** |
| Level 0 EC veto | - | - | 24616 | **0.710±0.002** |
| Correction to EC veto | Table 23 | **0.898±0.003** | - | - |
| Level 0 delco | Table 27 | **0.819±0.003** | - | - |
| Level 1 hextant | - | - | 7832 | **0.318±0.003** |
| Correction to hextant | Table 23 | **0.969±0.002** | - | - |
| Level 3 two photons | - | - | 3416 | **0.436±0.006** |
| Correction to level 3 | Table 23 | **0.962±0.002** | - | - |
| TG iqual<2 | Table 22 | **0.986±0.001** | 3393 | 0.993±0.001 |
| DC xy track | - | - | 3231 | **0.952±0.004** |
| DC charge | - | - | 3223 | **0.998±0.001** |
| DC $z$ track | Table 20 | **0.964±0.001** | 3221 | 0.9994±0.0004 |
| IC reconstruction | Table 22 | **0.984±0.001** | 3197 | 0.992±0.002 |
| RS tracking | Table 20 | **0.989±0.001** | 3188 | 0.997±0.001 |
| TRKTIM | Table 20 | **0.993±0.001** | 3188 | 1.0 |
| $\Delta E_{IC}$ | Table 22 | **0.970±0.001** | 3126 | 0.981±0.002 |
| $\Delta E_{TG}$ | K$\pi$2(2) | **0.885±0.002** | 3000 | 0.960±0.004 |
| $M_{\pi^+}$ | K$\pi$2(2) | **0.856±0.002** | 2322 | 0.774±0.008 |
| Nuclear inter. | UMC | **0.947±0.007** | - | - |
| Decay in flight | UMC | **0.942±0.006** | - | - |
| IC $\gamma$ veto | Table 22 | **0.979±0.001** | 2280 | 0.982±0.003 |
| VC $\gamma$ veto | Table 22 | **0.991±0.001** | 2258 | 0.990±0.002 |
| EC $\gamma$ veto | Table 22 | **0.898±0.002** | 2246 | 0.995±0.002 |
| RS $\gamma$ veto | - | - | 2054 | **0.915±0.006** |
| RS correction | Table 23 | **0.957±0.002** | - | - |
| TG $\gamma$ veto | Table 22 | **0.939±0.001** | 2045 | 0.996±0.001 |
| Pb glass $\gamma$ veto | Table 22 | **0.970±0.001** | 2045 | 1.0 |
| BV $\gamma$ veto | Table 22 | **0.895±0.002** | 1892 | 0.925±0.006 |
| $\Delta M_{\gamma\gamma}$ | - | - | 1645 | **0.869±0.008** |
| KINFIT | UMC | **0.933±0.013** | 1476 | 0.897±0.007 |
| BV elements in $\gamma_1$ <8 | K$\pi$2(2) | **0.984±0.001** | 1402 | 0.950±0.006 |
| Overlapping $\gamma$, $\phi_1$ | K$\pi$2(2) | **0.869±0.003** | 1280 | - |
| Overlapping $\gamma$, $z_1$ | K$\pi$2(2) | **0.814±0.004** | 1187 | - |
| Total K$\pi$2 acceptance | $(4.93\pm0.14)\cdot10^{-3}$ | | | |

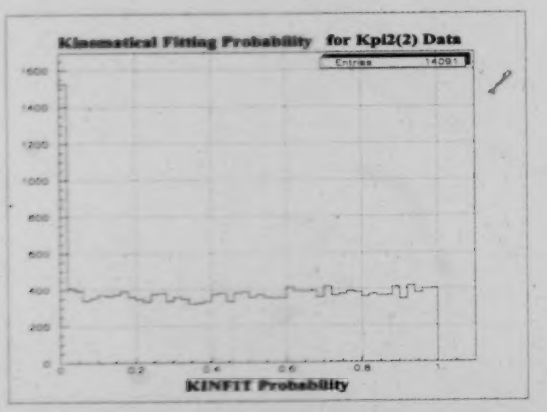


Figure 95: Probability of kinematic fit for K$\pi$2(2) events after all K$\pi$2 cuts up to KINFIT.

cuts applied to it.

The K$_t$*live* flux, $1.447 \cdot 10^{11}$, was obtained from scalers associated with the 1991 $\pi\nu\bar{\nu}$ analysis[48]. As was done with the K$\mu$2 scaler data a comparison was made between the ratio of unprescaled K$\pi$2(1) triggers per K$_t$*live* recorded in the scaler records and the number of K$\pi$2(1) events and kaon flux used in the branching ratio measurement. In this case the values were consistent so no additional adjustment was made to the K$_t$*live* count.

The measured K$\pi$2 branching ratio is shown in table 39. The resulting value was approximately 11% below the known K$\pi$2 branching ratio or 2.3 standard deviations based on the statistical error associated with the measured branching ratio. However, simply from Poisson statistics the $\pi\gamma\gamma(2)$ branching ratio will have a statistical error of at least 18%, which dominates any systematic error caused by the acceptance measurements. Therefore a systematic error on the order of 10% was acceptable. It should be noted that if the direct UMC value was used for the acceptance of the kinematic fitting instead of assuming a 90% acceptance and using UMC to correct for the correlation of the $M_{\pi^+}$ and $\Delta M_{\gamma\gamma}$ cuts, then the measured K$\pi$2 branching ratio would be within 1.5 standard deviations of the true value. If the KINFIT acceptance was measured using K$\pi$2(2) data, then due to a spike around probability zero (figure 95) the acceptance was 0.847$\pm$0.003 making the K$\pi$2 branching ratio 0.208$\pm$0.011 which is completely consistent with the true branching ratio.

Table 39: K$\pi$2 Branching Ratio

| Cut Description | Pass |
|---|---|
| $K_t live$ | $(1.447 \pm 0.001) \cdot 10^{11}$ |
| K$\pi$2(1) triggers | 166726 |
| Level 0 EC veto | 109294 |
| Level 0 delco | 64475 |
| Level 1 hextant | 39553 |
| Level 3 two photons | 5023 |
| TG iqual<2 | 4961 |
| DC xy track | 4467 |
| DC charge | 4421 |
| DC $z$ track | 4397 |
| IC reconstruction | 4319 |
| RS track | 4309 |
| TRKTIM | 4301 |
| $\Delta E_{IC}$ | 4100 |
| $\Delta E_{TG}$ | 3479 |
| $M_{\pi+}$ | 2155 |
| IC $\gamma$ veto | 2091 |
| VC $\gamma$ veto | 2073 |
| EC $\gamma$ veto | 1832 |
| RS $\gamma$ veto | 1621 |
| TG $\gamma$ veto | 1522 |
| Pb glass $\gamma$ veto | 1480 |
| BV $\gamma$ veto | 1328 |
| $\Delta M_{\gamma\gamma}$ | 1108 |
| KINFIT | 923 |
| BV elements in $\gamma_1$ <8 | 906 |
| Overlapping photons, $\phi_1$ | 775 |
| Overlapping photons, $z_1$ | 614 |
| K$\pi$2 acceptance | $(4.93\pm0.14)\cdot10^{-3}$ |
| K$\pi$2 prescale | 131072 |
| Kaon stopping fraction, $f_s$ | 0.598±0.014 |
| Measured K$\pi$2 branching ratio | 0.189±0.010 |
| Real K$\pi$2 branching ratio | 0.2117±0.0016 |

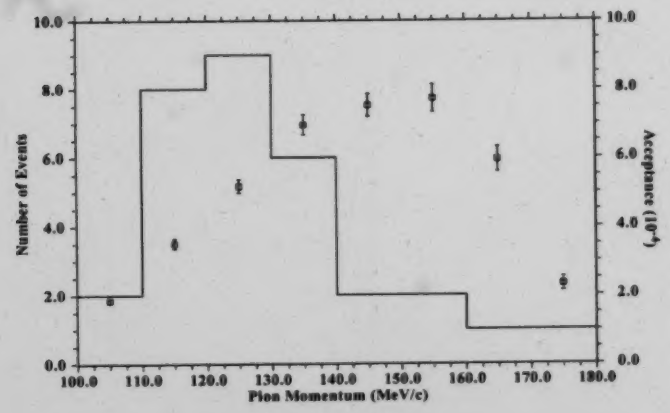


Figure 96: The measured total $\pi^+$ momentum of the final event sample (solid line) and the $\hat{c}$ independent portion of the acceptance. The background (not shown) was 0.6±1.0 events per bin assuming a flat background.

## 7.3 $K^+ \to \pi^+\gamma\gamma$ Branching Ratio

Figure 96 shows the $\pi^+$ momentum of the final 31 events which survived event selection (table 12), based on the actual measured momentum as well as the $\hat{c}$ independent portion of the acceptance in each bin ($f_s$ times table 34). The fit momentum returned from KINFIT shifts a couple of events slightly downward at the high momentum end of the spectrum but is essentially identical. Figure 97 shows the theoretical $\pi^+$ momentum distribution for various values of $\hat{c}$.

The effective acceptance for a particular $\hat{c}$ and momentum bin was found by multiplying $f_s$ by the appropriate values in table 24 and table 34. Summing the acceptances from all 8 momentum bins then gave the total acceptance for that value of $\hat{c}$. Table 40 shows both the final branching ratio as a function of $\hat{c}$ based on the measured effective acceptance and the value predicted by chiral perturbation theory. The final number of events was taken to be 31±5.57 with a background subtraction of 5.14±3.28 (section 5.4).

There was a strong dependence of the branching ratio on $\hat{c}$. A partial

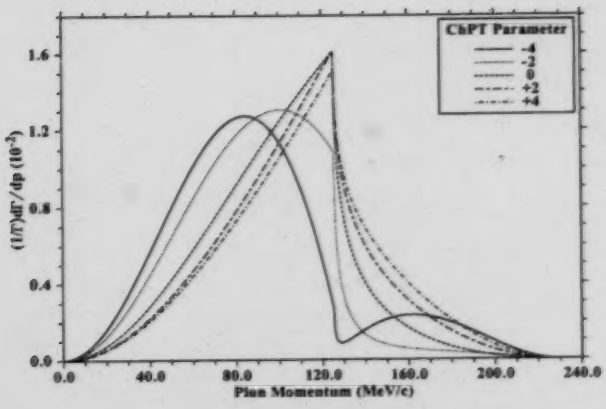


Figure 97: The theoretical $\pi^+$ momentum distribution for various values of $\hat{c}$.

branching ratio in the momentum region 100< $P_{\pi^+}$ <180MeV/c, $BR(K^+ \to \pi^+\gamma\gamma, 100 < \pi^+ < 180\text{MeV/c})$, was calculated by rescaling the kaon flux to only include decays with a $\pi^+$ in that momentum range. In practice this was done by adjusting the level 0 acceptance measured using UMC by the ratio of the number of events with 100< $P_{\pi^+}$ <180MeV/c to the total number of events (table 41). The result was much less dependent on $\hat{c}$, as shown in table 40 and figure 98, and indicated that most of the $\hat{c}$ driven variation in branching ratio was the result of the difference in spectrum shape. This shape difference and the magnitude of the branching ratio were used to determine which values of $\hat{c}$ were supported by the data.

After the kinematic constrained fit, there was a one-to-one relation between the $\pi^+$ momentum and the invariant mass of the two photons, $M_{\gamma\gamma}$. Figure 99 shows the $M_{\gamma\gamma}$ spectrum of the final event sample and figure 100 the $M_{\gamma\gamma}$ spectra of several ChPT predictions. The observed spectrum favoured non-negative values for $\hat{c}$.

To make this more quantitative, the method of maximum likelihood was used to determine the value of $\hat{c}$ which best matched the observed data. The

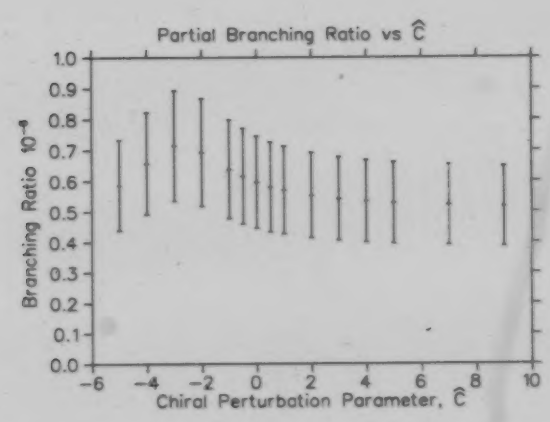


Figure 98: The $\pi\gamma\gamma(2)$ partial branching ratio as a function of $\hat{c}$. Only statistical errors are shown.

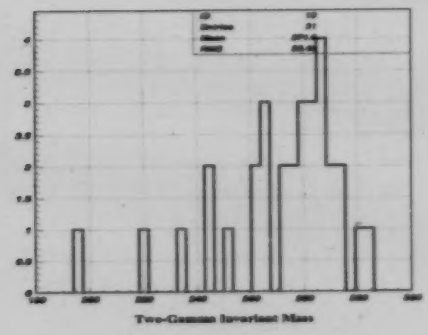

Figure 99: The KINFIT-returned invariant photon mass of the final event sample.

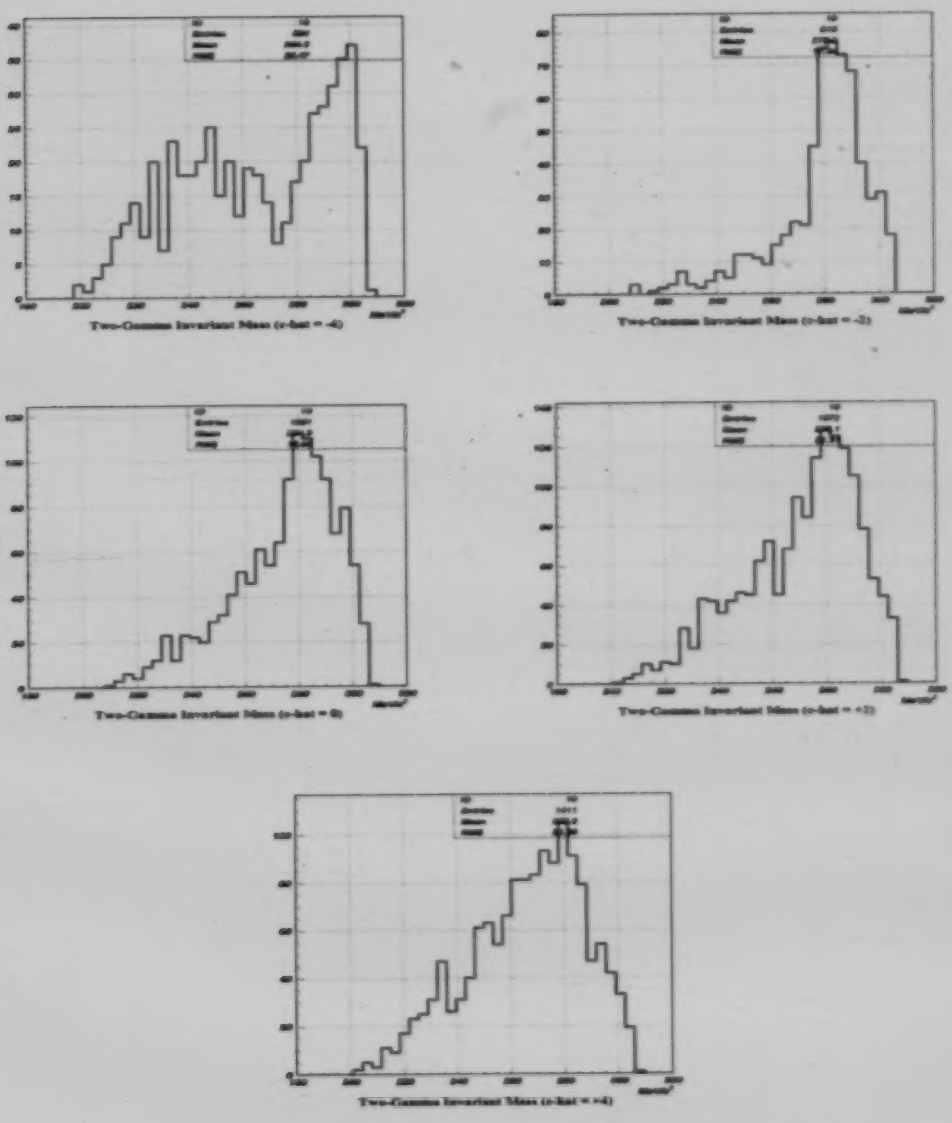

Figure 100: The KINFIT-returned invariant photon mass of UMC events using various ĉ-hat values.

Table 40: $\pi\gamma\gamma(2)$ Branching Ratios (statistical errors only)

| | Branching Ratio-$10^{-8}$ | | |
|---|---|---|---|
| $\hat{C}$ | Measured | Predicted | Partial |
| -5 | 1.938±0.487 | 0.56 | 0.586±0.147 |
| -4 | 2.326±0.585 | 0.43 | 0.657±0.165 |
| -3 | 2.344±0.589 | 0.37 | 0.714±0.179 |
| -2 | 1.875±0.471 | 0.38 | 0.693±0.174 |
| -1 | 1.409±0.354 | 0.44 | 0.638±0.160 |
| -0.5 | 1.256±0.316 | 0.50 | 0.615±0.155 |
| 0 | 1.148±0.289 | 0.58 | 0.596±0.150 |
| +0.5 | 1.067±0.268 | 0.67 | 0.580±0.146 |
| +1 | 1.017±0.256 | 0.77 | 0.570±0.143 |
| +2 | 0.948±0.238 | 1.03 | 0.553±0.139 |
| +3 | 0.911±0.229 | 1.36 | 0.542±0.136 |
| +4 | 0.894±0.225 | 1.74 | 0.534±0.134 |
| +5 | 0.881±0.221 | 2.20 | 0.528±0.133 |
| +7 | 0.870±0.219 | 3.29 | 0.522±0.131 |
| +9 | 0.864±0.217 | 4.64 | 0.517±0.130 |

likelihood, $\mathcal{L}$, of making a set of $n$ independent measurements is defined as:

$$\mathcal{L}(\alpha) = \prod_{i=1}^{n} p(x_i, \alpha) \tag{48}$$

$\alpha$ = An unknown set of parameters

$x_i$ = The measured quantities

$f(x_i, \alpha)$ = The probability of making measurement $x_i$ for given $\alpha$.

Maximizing $\mathcal{L}$ as a function of $\alpha$, or alternately maximizing the logarithm of $\mathcal{L}$, should yield the value(s) of $\alpha$ which best match the experimental data.

Using the total branching ratios given in table 40, the measured kaon flux in table 35, $f_s$ and the total bin-by-bin acceptances calculated from tables 24 and 34 the expected number of events was calculated for the various values of $\hat{c}$. Before this could be compared to the measured result the expected background events had to be added to the theoretical number of events requiring some assumption to be made about the background shape. The background was primarily a combination of K$\pi$3 and radiative K$\pi$2. The data prior to the application of the overlapping photon cuts was dominated by K$\pi$3 with a flat tail above the K$\pi$3 cutoff of 133MeV/c, however,

Table 41: Fraction of $K_e live$ With 100< $P_{\pi^+}$ <180MeV/c

| $\hat{c}$ | Fraction |
|---|---|
| -5 | 0.3025 |
| -4 | 0.2823 |
| -3 | 0.3045 |
| -2 | 0.3694 |
| -1 | 0.4526 |
| -0.5 | 0.4896 |
| 0 | 0.5187 |
| +0.5 | 0.5437 |
| +1 | 0.5604 |
| +2 | 0.5830 |
| +3 | 0.5944 |
| +4 | 0.5978 |
| +5 | 0.6002 |
| +7 | 0.5999 |
| +9 | 0.5978 |

K$\pi$3 had 4 photons as compared to the 3 of radiative K$\pi$2 and so was more heavily suppressed by these cuts. The data suggested a flat background after the overlapping cuts, however, for the shape analysis two assumptions were used. One was a flat background, the other used the shape observed before application of the overlapping cuts, i.e. a background dominated by K$\pi$3. For this K$\pi$3-like background shape the background was divided so that the first three momentum bins, 100-130MeV/c, contained the overlapping backgrounds with $P_{\pi^+}$ <133MeV/c (1.92±1.80 from table 19), while the higher bins, 130-180MeV/c contained the overlapping background with $P_{\pi^+}$ >133MeV/c (2.64±2.74 from table 19 and the non-overlapping background of 0.58±0.13). The relative weights within these two regions, 100-130 and 130-180MeV/c, were still determined by the observed spectrum shape (table 42).

The probability distribution relating the real and theoretical number of events for each of the 8 momentum bins was then simply Poisson statistics:

$$f(x_i,\alpha) = f(N_i^D,\hat{c}) = (N_i^T(\hat{c}))^{N_i^D} e^{-N_i^T(\hat{c})}/(N_i^D)! \quad (49)$$

where;

$$N_i^T(\hat{c}) = N_K A_i(\hat{c}) f_e B(\hat{c}) + N_i^B \quad (50)$$

$$n = \text{the number of bins}$$

Table 42: Background Distributions Used in the Maximum Likelihood Test

| Momentum | Flat Background | | K$\pi$3-Like Background | |
|---|---|---|---|---|
| Bin(MeV/c) | Weight | Events | Weight | Events |
| 100-110 | 0.125 | 0.6425±1.1591 | 0.121 | 0.23±0.63 |
| 110-120 | 0.125 | 0.6425±1.1591 | 0.327 | 0.63±1.03 |
| 120-130 | 0.125 | 0.6425±1.1591 | 0.551 | 0.551±1.34 |
| Total | | 1.9275±2.0076 | - | 1.92±1.80 |
| 130-140 | 0.125 | 0.6425±1.1591 | 0.364 | 1.17±1.65 |
| 140-150 | 0.125 | 0.6425±1.1591 | 0.170 | 0.55±1.13 |
| 150-160 | 0.125 | 0.6425±1.1591 | 0.222 | 0.71±1.29 |
| 160-170 | 0.125 | 0.6425±1.1591 | 0.170 | 0.55±1.13 |
| 170-180 | 0.125 | 0.6425±1.1591 | 0.074 | 0.24±0.75 |
| Total | | 3.2125±2.5918 | - | 3.22±2.74 |

$N_i^D$ = the number of real events in bin i

$N_K$ = the kaon flux

$A_i(\hat{c})$ = the measured $\pi\gamma\gamma(2)$ acceptance in bin i for a particular $\hat{c}$

$f_s$ = the kaon stopping fraction

$B(\hat{c})$ = the measured branching ratio for a particular $\hat{c}$

$N_i^B$ = the number of background events in bin i

Substituting this function into $\mathcal{L}$ and plotting $\ln\mathcal{L}$ vs $\hat{c}$ gives the curves in figure 101 for the two background shapes. After interpolating the data to yield the best value of $\hat{c}$, $\hat{c}_{max}$, the range of $\hat{c}$ values within $s$ standard deviations of the best value can be determined by finding the values of $\hat{c}$ where $\ln\mathcal{L}(\hat{c}) = \ln\mathcal{L}(\hat{c}_{max}) - s^2/s$. Table 44 below lists the best value of $\hat{c}$ and also the range of allowed $\hat{c}$ for a confidence level of one standard deviation (68.3%), 90% and two standard deviations (95.5%). These correspond to $s = 1, 1.64$ and 2.

All of the above considered only statistical errors. It was possible for systematic errors to enter through either the background subtraction or the acceptance measurement. From the background UMC studies the overlapping photon background could have been underestimated by 2.93 events, it was not clear if this was the case or not but it was included as a possible systematic error. The error in the non-overlapping background subtraction was ignored since that portion of the background was much smaller than the overlapping background. The other potential error was indicated by the

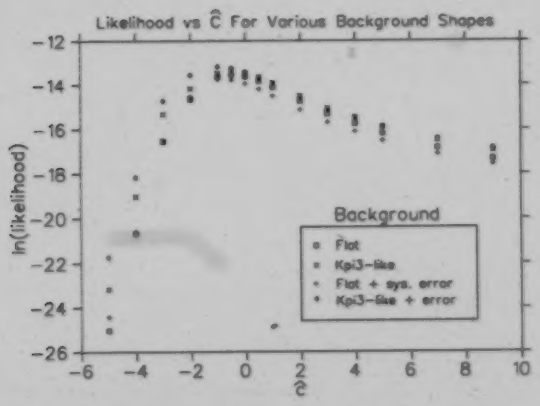


Figure 101: $\ln \mathcal{L}$ vs $\hat{c}$ for flat or K$\pi$3-like background shapes with and without systematic error in the background estimate.

K$\pi$2 branching ratio measurement. The calculated value was 11% below the true value. Although this may have been an overestimate of the acceptance error for $\pi\gamma\gamma(2)$ to be conservative the full 11% was included. It was interesting to note that these two errors were almost exactly the same magnitude but acted in opposite directions, an underestimate of the background resulted in too large a branching ratio while overestimating the acceptance resulted in too small a branching ratio. Because of this the two numbers were combined and just expressed as a systematic error of $\pm$11%. Table 43 lists both total and partial branching ratios including systematic error for the values of $\hat{c}$ studied. The theoretical partial branching ratio was just the theoretical total branching ratio multiplied by the factor in table 41 used to calculate the real partial branching ratio.

Any systematic error would also affect the maximum likelihood measurement performed above. Since the expected number of events used the measured acceptance and branching ratio, changing the overall acceptance did not affect $\mathcal{L}$. However, changing the number of background events would have had an effect and this was tested by increasing the background the amount indicated in table 19, the new likelihood curves are shown in figure 101, with the corresponding $\hat{c}$ values in table 44. The best $\hat{c}$ value was the same regardless of whether the flat or K$\pi$3 background hypotheses were used and even with the addition of the systematic error to the background estimate the optimal $\hat{c}$ did not change by a large amount. Considering then only the flat background and the 90% confidence limits and using the values

Table 43: $\pi\gamma\gamma(2)$ Final Branching Ratios Including Systematic Errors

| | Branching Ratio-$10^{-6}$ | | | |
|---|---|---|---|---|
| | Total | | Partial | |
| $\hat{C}$ | Measured | Predicted | Measured | Predicted |
| -5 | 1.938±0.487±0.213 | 0.56 | 0.586±0.147±0.064 | 0.17 |
| -4 | 2.326±0.585±0.256 | 0.43 | 0.657±0.165±0.072 | 0.12 |
| -3 | 2.344±0.589±0.258 | 0.37 | 0.714±0.179±0.079 | 0.11 |
| -2 | 1.875±0.471±0.206 | 0.38 | 0.693±0.174±0.076 | 0.14 |
| -1 | 1.409±0.354±0.155 | 0.44 | 0.638±0.160±0.070 | 0.20 |
| -0.5 | 1.256±0.316±0.138 | 0.50 | 0.615±0.155±0.068 | 0.24 |
| 0 | 1.148±0.289±0.126 | 0.58 | 0.596±0.150±0.066 | 0.30 |
| +0.5 | 1.067±0.268±0.117 | 0.67 | 0.580±0.146±0.064 | 0.36 |
| +1 | 1.017±0.256±0.112 | 0.77 | 0.570±0.143±0.063 | 0.43 |
| +2 | 0.948±0.238±0.104 | 1.03 | 0.553±0.139±0.061 | 0.60 |
| +3 | 0.911±0.229±0.100 | 1.36 | 0.542±0.136±0.060 | 0.81 |
| +4 | 0.894±0.225±0.098 | 1.74 | 0.534±0.134±0.059 | 1.04 |
| +5 | 0.881±0.221±0.097 | 2.20 | 0.528±0.133±0.058 | 1.32 |
| +7 | 0.870±0.219±0.096 | 3.29 | 0.522±0.131±0.057 | 1.97 |
| +9 | 0.864±0.217±0.095 | 4.64 | 0.517±0.130±0.057 | 2.77 |

for -0.5 and ±2 rather than -0.6 and ±2.2, which data wasn't generated for, the partial and total $\pi\gamma\gamma(2)$ branching ratios were:

$$BR(K^+ \to \pi^+\gamma\gamma, 100 < P_{\pi^+} < 180\text{MeV/c}) = 0.62 \pm 0.16 \pm 0.07 \pm 0.07 \times 10^{-6},$$
$$BR(K^+ \to \pi^+\gamma\gamma) = 1.26 \pm 0.32 \pm 0.14 + 0.62 - 0.31 \times 10^{-6},$$

where the first error is statistical, the second is systematic due to the background and acceptance measurements and the third error is due to the range of accepted $\hat{c}$.

The branching ratio also in principle could be used to limit $\hat{c}$ since there was a strong theoretical branching ratio dependence on the value of $\hat{c}$ (table 43). In fact it would seem that the branching ratio measurement should have more resolving power than the likelihood analysis. However, as was mentioned earlier in section 2.5 the branching ratio was more sensitive to the details of the chiral perturbation calculation than the spectrum shape and a recent measurement of $K^+ \to \pi^0\gamma\gamma$ gave a branching ratio approximately 3 times larger than that expected from chiral perturbation theory.

Table 44: $\hat{c}$ values from the maximum likelihood analysis for both background shapes with and without systematic background errors.

| Confidence | Background Shape | | | |
|---|---|---|---|---|
| Level | Flat | Flat+error | K$\pi$3-Like | K$\pi$3-Like+error |
| Best | -0.6 | -0.9 | -0.6 | -0.9 |
| 1 $\sigma$ (68.3%) | -1.5 – +0.9 | -1.7 – +0.6 | -1.6 – +1.0 | -2.2 – +0.5 |
| 2 $\sigma$ (95.5%) | -2.6 – +3.4 | -2.7 – +3.1 | -3.0 – +3.8 | -3.2 – +3.2 |
| 90% | -2.2 – +2.2 | -2.4 – +1.9 | -2.7 – +2.4 | -2.9 – +1.9 |

Because of this the results based on the spectrum shape were considered more reliable. However, considering the branching ratio values shown in table 43 and accepting any values of $\hat{c}$ which yielded a branching ratio within two statistical standard deviations of the measured value and also allowing the chiral perturbation value to be up to a factor of three too low then the allowed range of $\hat{c}$ was -2 to +3 with the best agreement at +2. Although the optimum values differed the range is quite similar to the $\pm 2.2$ returned by the likelihood analysis. Using the branching ratio at +2 and the range -2 to +3 the partial and total branching ratios were:

$$BR(K^+ \to \pi^+\gamma\gamma, 100 < P_{\pi^+} < 180\text{MeV/c}) = 0.55 \pm 0.14 \pm 0.06 + 0.14 - 0.01 \times 10^{-6},$$

$$BR(K^+ \to \pi^+\gamma\gamma) = 0.95 \pm 0.24 \pm 0.10 + 0.93 - 0.04 \times 10^{-6}.$$

# 8 Conclusion

A search was conducted for $K^+ \to \pi^+\gamma\gamma$ decays below the K$\pi$2 peak in the $\pi^+$ momentum range $100 < P_{\pi^+} < 180$MeV/c. The lower limit on the momentum range was the momentum where a significant fraction of charged tracks would reach RS layer A making acceptance measurements practical, while the upper momentum limit was designed to exclude K$\pi$2. There were four possible background processes in two distinct classes. Decays with more than two photons, radiative K$\pi$2 and K$\pi$3, where the events passed because photons overlapped in the BV giving the illusion of only two photons being present. And decays where the correct number of photons were present but the event kinematics was incorrectly reconstructed due to nuclear interactions, resolution effects or mismeasured variables. This background was dominated by K$\pi$2 and K$\mu$3 but could also have included radiative K$\pi$2 and K$\pi$3 if the extra photons were unobserved.

A total of $31 \pm 5.57$ events were in the final sample with an estimated background contamination of $4.56 \pm 3.28$ (overlapping) plus $0.58 \pm 0.13$ (non-overlapping). The overall $\pi^+$ momentum (or photon invariant mass) spectrum was definitely in agreement with chiral perturbation theory predications. The total K*live* flux was $(1.0111 \pm 0.0004) \cdot 10^{11}$, with the $K^+ \to \pi^+\gamma\gamma$ - acceptance being on the order of $10^{-3}$ before including spectrum information (table 34). The effect of the $\pi\gamma\gamma(2)$ spectrum on the acceptance was dependent on the choice of the unknown chiral perturbation theory parameter $\hat{c}$ (table 24). The measured and expected total branching ratio were given in table 40. The strong dependence of the measured total branching ratio on $\hat{c}$ was due to the dependence of the acceptance on the $\pi^+$ decay spectrum. This dependence was reduced by considering the partial branching ratio for $100 < P_{\pi^+} < 180$MeV/c and figure 98 shows that all of the measured partial branching ratios were within one standard deviation of each other.

To determine the value of $\hat{c}$ which gave the best agreement with the experimental results, two pieces of information were available, the shape of the $\pi\gamma\gamma(2)$ spectrum and the magnitude of the branching ratio. Comparing the observed to the expected number of events in each bin as a function of $\hat{c}$ using a maximum likelihood analysis gave the results listed in table 44. Due to the reported difference[38] between the measured $K^0 \to \pi^0\gamma\gamma$ branching ratio and the theoretical value found using chiral perturbation theory to $O(p^4)$ it was not clear how best to compare the observed $K^+ \to \pi^+\gamma\gamma$ branching ratio to the theoretical values (table 43). However, although the 'best estimate' of $\hat{c}$ differed between the branching ratio and likelihood methods the range of allowed $\hat{c}$ at the 90% confidence level were similar, with the range

being roughly $|\hat{c}| \leq 2.2$.

Inclusion of the $O(p^6)$ unitarity correction increased the predicted branching ratio, at a given value of $\hat{c}$, up to about $\hat{c} = +2$ after which it predicted a lower branching ratio (figure 10). In principle this improved the agreement between the $\hat{c}$ value favored by the branching ratio and shape analysis, since the predicted branching ratio in the region $-1 < \hat{c} < +1$ was lower than that measured (table 43). In practice, because the $O(p^4)$ and $O(p^6)$ branching ratio predictions happened to converge in the region of $\hat{c}$ which gave the best theoretical and experimental branching ratio agreement, the change in the 'best' value of $\hat{c}$ was small. Use of the unitarity corrections in the shape analysis of $\hat{c}$ shifted the preferred value upward from about $\hat{c} = -0.6$ to $+0.7$. This was closer to the $+1$ to $+2$ range coming from the branching ratio analysis, but because of the large uncertainty on the $\hat{c}$ prediction it was well within the range of $-2.2 < \hat{c} < +2.2$ listed above. The data suggested that the unitarity corrections did improve the correlation between theory and experiment but in this case did not significantly change the experimental conclusions.

The final result was that using both the shape of the distribution and the magnitude of the branching ratio the data suggested $\hat{c}$ was in the range -1 to +3. This was in better agreement with the weak deformation model prediction of $\hat{c} = 0$ than the naive factorization value of $\hat{c} = -2.3$. The best estimate of the partial branching ratio was:

$$BR(K^+ \to \pi^+\gamma\gamma, 100 < P_{\pi^+} < 180\text{MeV/c}) = (0.58 \pm 0.15 \pm 0.06 \pm 0.06) \cdot 10^{-6},$$

where the errors are statistical, systematic from the acceptance and background subtraction, and systematic from the uncertainty in $\hat{c}$ respectively. The total branching ratio was more difficult to establish since it varied strongly with $\hat{c}$ even over the range of $\hat{c}$ which the data supported. The branching ratio measured for $\hat{c}$=0 was used as a central value and the best estimate was determined to have been:

$$BR(K^+ \to \pi^+\gamma\gamma) = (1.15 \pm 0.29 \pm 0.13 \pm 0.26) \cdot 10^{-6},$$

where the description of the various errors is as mentioned earlier.

## References


[1] M.S. Atiya *et al.*, Phys. Rev. Lett. **65** (1990) 1188.

[2] R.M. Barnett *et al.*, Phys. Rev. D **54** (1996) 404.

[3] Quantum field theory lecture notes. UBC Phys 508 (unpublished).

[4] G. Ecker, LANL Preprint Archive. hep-ph/9501357.

[5] M. Gell-Mann, *The Eightfold Way: A Theory of Strong Interaction Symmetry*, California Institute of Technology Report CTSL-20 (1961).

[6] Y. Ne'eman, Nucl. Phys. **26** (1961) 222.

[7] ed. N.G. Cooper and G.B. West, *Particle Physics: A Los Alamos Primer*, (Cambridge University Press, Cambridge 1988).

[8] V.E. Barnes *et al.*, Phys. Rev. Lett. **12** (1964) 204.

[9] R.H. Dalitz, ed. C de Witt and M. Jacob, *High Energy Physics*, (Gordon and Breach, New York 1965).

[10] E. Fermi, Nuovo Cimento **11** (1934) 1.

[11] E. Fermi, Z. Phys. **88** (1934) 161.

[12] T.D. Lee and C.N. Yang, Phys. Rev. **104** (1956) 254.

[13] C.S. Wu *et al.*, Phys. Rev. **105** (1957) 1413.

[14] R.P. Feynman and M. Gell-Mann, Phys. Rev. **109** (1958) 193.

[15] I.J.R. Aitchison and A.J.G. Hey, *Gauge Theories in Particle Physics*, (Adam Hilger. Bristol, England 1989).

[16] N. Cabibbo, Phys. Rev. Lett. **10** (1963) 531.

[17] J. Schwinger, Ann. Phys. **2** (1957) 407.

[18] S.L. Glashow, Nucl. Phys. **22** (1961) 579.

[19] P.W. Higgs, Phys. Rev. **145** (1966) 1156.

[20] A. Salam, ed. N. Svartholm, *Elementary Particle Theory*, (Almqvist, Stockholm 1968).

[21] S. Weinberg, Phys. Rev. Lett. **19** (1967) 1264.

[22] F.J. Hasert *et al.*, Phys. Lett. **46B** (1973) 138.

[23] S.L. Glashow, J. Iliopoulos and L. Maiani, Phys. Rev. **D2** (1970) 1285.

[24] M. Kobayashi and T. Maskawa, Prog. Theor. Phys. **49** (1972) 282.

[25] L. Littenberg and G. Valencia, LANL Preprint Archive. hep-ph/9303225.

[26] A. Manohan, LANL Preprint Archive. hep-ph/9606222.

[27] J. Goldstone, Nuovo Cimento **19** (1961) 154.

[28] G. Ecker, LANL Preprint Archive. hep-ph/9501357.

[29] B.R. Holstein, LANL Preprint Archive. hep-ph/9510344.

[30] A. Pich, LANL Preprint Archive. hep-ph/9502366v2.

[31] J. Gasser and H. Leutwyler, Nucl. Phys. **B250** (1985) 465,517,539.

[32] G. Ecker, LANL Preprint Archive. hep-ph/9608226.

[33] G. D'Ambrosio, G. Ecker, G. Isidori and H. Neufeld, LANL Preprint Archive. hep-ph/9411439.

[34] E. deRafael, LANL Preprint Archive. hep-ph/9312327v2.

[35] E. Witten, Nucl. Phys. **B223** (1983) 422.

[36] G. Ecker, A. Pich and E. deRafael, Nucl. Phys. **B291** (1987) 692.

[37] G. Ecker, A. Pich and E. deRafael, Nucl. Phys. **B303** (1988) 665.

[38] G.D. Barr *et al.*, Phys. Lett. **B242** (1990) 523.

[39] G. D'Ambrosio and J. Portoles, LANL Preprint Archive. hep-ph/9606213.

[40] G. Ecker, J. Kambor and D. Wyler, Nucl. Phys. **B394** (1993) 101.

[41] S. Fajfer, LANL Preprint Archive. hep-ph/9505280.

[42] M.S. Atiya *et al.*, Nucl. Instrum. Methods Phys. Res. **A321** (1992) 129.

[43] T. Nakano, Y. Kuno. E787 Technical Note TN256.

[44] T. Nakano, R. Soluk. E787 Technical Note TN310.

[45] R. McPherson. E787 Technical Note TN304.

[46] A. Turcot. E787 Technical Note TN281.

[47] S. Adler. E787 Technical Note TN303.

[48] J. Roy. E787 Technical Note TN296.

[49] R. Soluk. E787 Technical Note TN293.

[50] S. Weinberg. *The Quantum Theory of Fields II*, (Cambridge University Press, 1996).

[51] S. Coleman, J. Wess and B. Zumino. Phys. Rev. **177** (1969) 2239.

# IMAGE EVALUATION
# TEST TARGET (QA-3)

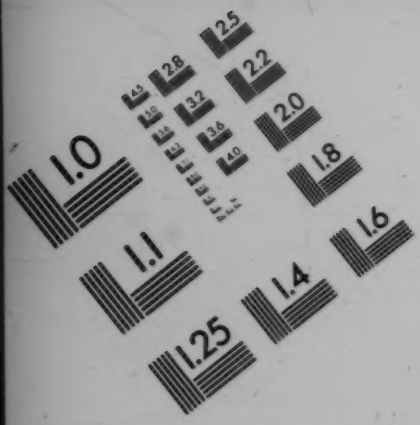

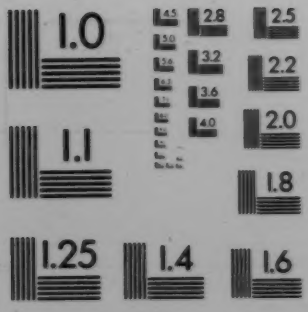


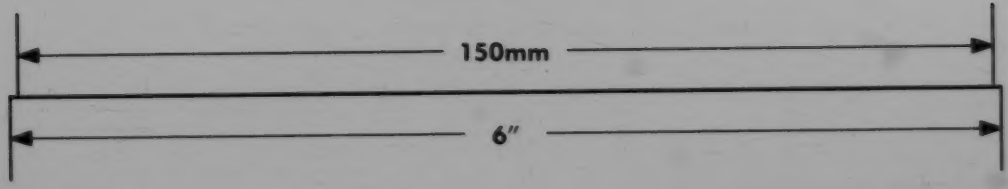


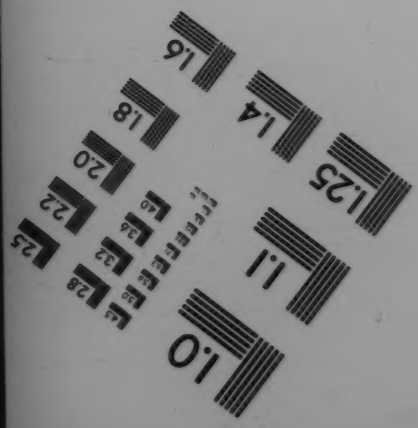


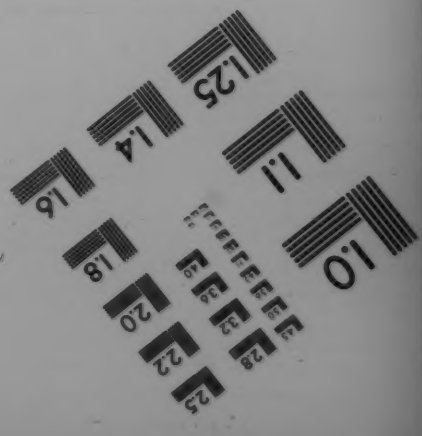


APPLIED IMAGE, Inc
1653 East Main Street
Rochester, NY 14609 USA
Phone: 716/482-0300
Fax: 716/288-5989

© 1993, Applied Image, Inc., All Rights Reserved